Modeling Solar Particle Receivers with the Discrete Element Method

Modellierung von solaren Partikelreceivern mit der Diskreten Elemente Methode

Von der Fakultät für Maschinenwesen der Rheinisch-Westfälischen Technischen Hochschule Aachen zur Erlangung des akademischen Grades eines Doktors der Ingenieurwissenschaften genehmigte Dissertation

vorgelegt von

Johannes Grobbel

Berichter: Universitätsprofessor Dr.-Ing. Robert Pitz-Paal
Universitätsprofessor Dr.-Ing. Harald Kruggel-Emden

Tag der mündlichen Prüfung: 12. Dezember 2019

Acknowledgements

This thesis was created during my time at the Institute of Solar Research at the German Aerospace Center (DLR) in Jülich.
I want to thank Univ.-Prof. Dr.-Ing. Robert Pitz-Paal, whose lecture first aroused my interest in solar energy and who then gave me the opportunity to write my master thesis and this dissertation in this very interesting research area. His precise analysis and assessment of my overall roadmap and his view of the big picture always helped me to keep focus. Additional credit goes to the second examiner Prof. Dr.-Ing. Harald Kruggel-Emden, who has given very fruitful and frequent feedback to heat transfer models and to the DEM in general since the beginning of this thesis. Furthermore special thanks is attributed to Dr.-Ing. Stefan Brendelberger for his moral support in problematic situations, for the many discussions of my models and results, for the help with the vacuum experiment and for the critical review of my publications and this dissertation.
Likewise I would like to express my gratitude to my department leader Prof. Dr. Christian Sattler and my long-time group leader Dr. Martin Roeb for appreciating my work and creating a productive environment for it. This also applies to my later group leaders Dr.-Ing. Henrik von Storch and Dennis Thomey, who always supported me.
Many other colleagues contributed to this work: Dr.-Ing. Jan Felinks with helpful hints in the beginning, Sebastian Richter and Alon Lidor by proof-reading, the solar furnace team in Cologne with their help during experiments, Matthias Henninger and Luiz Aguinsky through their student theses, Dr.-Ing. Reiner Buck and Dr.-Ing. Lars Amsbeck by providing experimental data and by discussions about particle receivers, Dr.-Ing. Hannes Stadler and Dr.-Ing. Robert Flesch through the administration of the compute cluster, Justin Lapp by the joint work on a vacuum particle receiver and the fellow researchers from SANDIA National Labs by providing ceria particles. In particular I would like to thank Sebastian Richter, Gkiokchan Moumin and Henrik von Storch for the many nice moments in our shared office. I also gladly look back to the lunch breaks and free-time activities with the other doctorate candidates, students and colleagues, who have not been mentioned so far. You all created a great atmosphere, in which we had so many creative discussions and fun.
Finally I am grateful for my friends, who had to bear with me in difficult phases but always stood by my side and helped me to find new motivation. This also applies to my family, who I owe my greatest gratitude. You supported me my entire life and were always there when I needed you. Thank you so much!

Abstract

Particles are envisaged as a redox material in solar-thermochemical fuel production processes and as well as a heat transfer medium in solar thermal power plants. They are heated in solar particle receivers, which have mostly been evaluated with continuum models so far, even though the Discrete Element Method (DEM) usually describes the particle motion more accurately. Reasons are the lack of heat transfer models needed for a particle receiver, missing contact model parameters for potential particle types proposed for solar receivers and little experience with the method in the solar thermal research community. In the present work these hurdles are addressed, with the ultimate aim that the method will be part of the methodology toolbox for future researchers. Several models were developed: one for the conductive heat transfer through the contact point and void space between two particles, one for the same heat transfer modes between a particle and a wall, a radiation model based on Monte Carlo ray tracing, a wall conduction model and a model for the chemical reduction of ceria, which occurs in concepts for solar-thermochemical fuel production. The inter-particle conduction model includes a pressure dependence as it is based on the extended Zehner-Bauer-Schlünder model for the thermal conductivity of packed beds. The applicability of this continuum model under vacuum and high temperature conditions was validated in a vacuum experiment in a solar simulator. Also the other models were successfully compared against solutions of various test cases. In context of the model developments, a critical time step limit for the common particle temperature updating process in the DEM was derived for the first time and proven to be reasonable in a stability test. Additionally, contact parameter sets for five particle types envisaged in solar receivers have been determined by a custom calibration approach. It is based on five bulk experiments, which are used to calibrate the contact parameters in three stages. More precisely, the DEM models of the respective experiments in each stage are described by surrogate (Kriging) functions, whose inputs are then optimized to match the experiments and thus find the contact parameters. The calibration was also performed for increased particle diameters to provide parameters for coarse-grained and therefore faster simulations. Finally, the application of the models as a whole is demonstrated by a simulation of the prototype CentRec particle receiver. Mass flow fluctuations observed in experiments could be reproduced and were analyzed in detail. The simulated particle outlet temperature and the receiver efficiency were in good agreement with their experimental counterparts. In summary, the DEM has been shown to be a very useful method for the analysis and the design of solar particle receivers and should be used for this purpose in the future.

Zusammenfassung

Partikel sollen zukünftig sowohl in solar betriebenen thermochemischen Kreisprozessen als Redoxmaterial, als auch in solarthermischen Turmkraftwerken als Wärmeträgermedium eingesetzt werden. In diesen Anlagen werden sie in sogenannten Partikelreceivern mittels konzentrierter Solarstrahlung erhitzt. Diese Partikelreceiver wurden bisher meist mit Kontinuumsmodellen beschrieben, obwohl die Diskrete Elemente Methode (DEM) die Partikelbewegung wesentlich genauer beschreiben kann. Der Grund, dass diese Methode kaum eingesetzt wird, liegt in fehlenden Wärmeübertragungsmodellen für solare Partikelreceiver, fehlenden Kontaktparametern für die angedachten Partikelsorten sowie einer geringen Erfahrung mit dieser Methode im solarthermischen Umfeld. In der vorliegenden Arbeit sollen diese Punkte addressiert werden und die DEM als alternative und ergänzende Methode zur Simulation von solaren Partikelreceivern etabliert werden. Dazu wurden mehrere Modelle entwickelt: eines für den Wärmeübergang zwischen benachbarten Partikeln durch Wärmeleitung durch die Kontaktfläche und den Gaszwischenraum, eines für dieselben Transfermechanismen zwischen Partikel und Wand, ein Strahlungsmodell basierend auf Monte-Carlo Strahlverfolgung, ein Modell für den Wärmetransport durch Wände sowie ein Modell für die chemische Reduktion von Ceroxid, wie sie in Konzepten zur solaren Brennstoffproduktion anzutreffen ist. Das Modell für den Partikel-Partikel-Wärmeübergang besitzt eine Druckabhängigkeit durch die Herleitung aus dem erweiterten Zehner-Bauer-Schlünder-Modell für Festbetten. Die Anwendbarkeit dieses Festbettmodells im Vakuum bei gleichzeitig hohen Temperaturen wurde in einem Vakuumexperiment gezeigt. Auch die anderen Modelle wurden erfolgreich anhand von verschiedenen Testfällen validiert. Für den verwendeten und in DEM-Codes weit verbreiteten Algorithmus zur Berechnung der Partikeltemperatur wurde der kritische Zeitschritt hergeleitet und durch Testsimulationen zur Stabilität bestätigt. Neben den Modellenwicklungen zum Wärmetransport wurden außerdem Kontaktparameter für fünf verschiedene, potentiell in Partikelreceivern zum Einsatz kommende Partikelsorten über einen eigens entwickelten Kalibrationsansatz bestimmt. Dieser basiert auf fünf Experimenten am Partikelkollektiv, die in drei Stufen zur Kalibrierung genutzt werden. Dabei werden die Kontaktparameter anhand von Ersatzfunktionen (Kriging-Modellen) der DEM-Modelle optimiert. Die Kalibrierung wurde auch mit vergrößerten Partikeldurchmessern durchgeführt, um Parameter für schnellere Coarse-Graining-Simulationen zur Verfügung zu stellen. Abschließend wurde die Gesamtheit der Modelle in einer Simulation des Prototyps des CentRec-Partikelreceivers demonstriert. Zum ersten Mal konnten so die im Experiment auftretenden Fluktuationen des Massenstroms in der Simulation abgebildet werden. Die simulierte Partikelaustrittstemperatur und der ermittelte thermische Wirkungsgrad des Receivers stimmten ebenfalls gut mit den Experimenten überein. Insgesamt konnte gezeigt werden, dass die DEM ein nützliches Werkzeug für die Analyse und das Design von solaren Partikelreceivern ist und in Zukunft dafür genutzt werden sollte.

Contents

List of Figures

List of Tables

Nomenclature

Latin Symbols

a	radius of contact area
a	thermal diffusivity
A	area
B	deformation parameter in ZBS model
Bi	Biot number
c	damping coefficient
c_p	heat capacity
$\tilde{c}_\mathrm{p}$	artificial heat capacity accounting for chemical reaction
C_f	shape factor in ZBS model
CG	coarse graining factor
$C_\mathrm{cutoff,HT}$	distance in which neighbor particles participate in DEM heat transfer, in particle diameters
d	diameter
$d_{10,0}$	10 % quantile of particle size distribution
$\overline{d}_{jk}$	ratio of moments
D'_{ij}	diffuse-specular radiation distribution factor
$\mathbf{d}_{(0,0,1)}$	direction of ray in hemisphere with zenith vector (0,0,1)
e	restitution coefficient
E	emissive power
E_tot	total energy
$\mathbf{e}$	unit vector
f	surrogate model function
F_{ij}	view factor from surface i to surface j
$\mathbf{F}$	force vector
G	shear modulus
$\mathbf{g}$	gravity vector
h	convection coefficient
h	height
H_c	thermal conductance by solid contact between two particles
H_g	thermal conductance of gas void space between two particles
H_l	thermal conductance of liquid bridges between two particles
H_t	total thermal conductance between two particles
I_lamp	electric current of solar simulator lamp

$\bar{\bar{\mathbf{I}}}$	inertia tensor
k	spring stiffness
k_{core}	relative core conductivity in ZBS model
k_{G}	relative conductivity by conductive gas transfer in ZBS model
k_{p}	relative conductivity of solid particle phase in ZBS model
k_{rad}	relative conductivity by radiation in ZBS model
k_{R}	torsional spring stiffness
K_{pp}	particle-particle heat transfer model calibration constant
$\mathbf{k}$	rotation axis in Rodrigues' rotation formula
l	modified mean free path in ZBS model
l	thickness of wall
L	length of cylindrical test case in axial direction
m	mass
MRD	mean relative difference
$\mathbf{M}_{\mathrm{R}}$	rolling friction torque
n	amount of substance
n_x,n_y,n_z	components of vector $\mathbf{n}$
N	number
N_{refl}	Number of reflected rays
N_{con}	number of contacting particles
N_{HT}	number of neighbor particles participating in DEM heat transfer
$N_{\mathrm{wall,tri}}$	Number of neighbor particles of a triangular mesh element, relevant for heat transfer
$\mathbf{n}$	vector of surface normal
$\mathbf{n}$	zenith vector of rotated hemisphere
$\mathbf{O}$	ray origin
p	pressure
p_{ch}	main vacuum chamber pressure
p_{pre}	pre-chamber pressure in vacuum experiment
$\mathbf{p}$	vector with contact parameters
Q	heat
$\dot{Q}_{\mathrm{tri}}$	radiation heat source for triangular mesh elements
$\dot{Q}_{\mathrm{chem}}$	chemical heat source
$\dot{Q}_{\mathrm{cond}}$	heat flow by conduction through gas or solid
$\dot{Q}_{\mathrm{em,surr}}$	emission to the surroundings
$\dot{Q}_{\mathrm{ray}}$	power of a single ray in MCRT code
$\dot{Q}_{\mathrm{solar}}$	radiation entering the aperture
$\dot{Q}_{\mathrm{src}}$	heat source term from separate C++ program for extended LIGGGHTS® software
r	radial coordinate in cylindrical coordinate system

R	particle radius
R	thermal resistance
Res	residual
$\mathbf{r}_{ij,c}$	vector from center of gravity of particle i to contact point with particle j
s	separation distance between two spheres in ray tracing test case
$\mathbf{s}$	position vector
t	time
$t100$	time to reach 100 g on scale in horizontal conveyor experiment
$t_{c,0}$	time when particles come in contact
$\overline{T}$	mean temperature
T	temperature
T_0	initial temperature
T_∞	free stream fluid temperature
$\overline{T_{\text{out}}}$	energy-averaged particle temperature at collection ring outlet
T_{outside}	temperature at the outside side of the wall
T_{ref}	reference temperature
$\mathbf{T}_{\text{walls}}$	Vector with temperatures of the triangular mesh elements
U	perimiter
v	velocity
V	volume
$\mathbf{v}_{\text{t,rel}}$	relative tangential velocity vector
$\mathbf{V}$	position vector of triangle vertex
x	coordinate in cartesian coordinate system
$\mathbf{x}$	general position vector
y	coordinate in cartesian coordinate system
y_{Exp}	target value of experiment
Y	Young's modulus
z	collision frequency
z	coordinate in cartesian coordinate system

Greek Symbols

α	angle of repose
α	heat transfer coefficient from wall to entire bed in Schlünder model
α_{bed}	bed penetration heat transfer coefficient in Schlünder model
$\alpha_{\text{bed},t}$	instant bed penetration heat transfer coefficient in Schlünder model
α_{PP}	area-specific heat transfer coefficient between two particles
α_t	time-dependent total heat transfer coefficent in Schlünder model

α_{WP}	wall-particle heat transfer coefficient in Schlünder model
α_{WS}	heat transfer coefficient in Schlünder model
β	rotation angle in Rodrigues' rotation formula
δ	particle overlap
δ	reduction extent of ceria
$\boldsymbol{\delta}_{\mathrm{t}}$	shear vector (tangential overlap vector)
δ_{s}	surface roughness of particle in Schlünder wall model
Δh_{R}	molar reaction enthalpy
Δt	time step
$\Delta t_{\mathrm{coupl}}$	coupling time step between DEM and seperate C++ software
Δt_{crit}	critical time step
Δx	spatial discretization step
ε	emissivity
η	efficiency
γ	accomodation coefficient in ZBS model
λ	parameter in ray equation
λ	thermal conductivity
λ_{eff}	effective thermal conductivity of continuum
λ_{g}	thermal conductivity of interstitial gas
λ_{w}	thermal conductivity of wall
μ	sliding friction coefficient
μ_{R}	rolling friction coefficient
ν	Poisson's ratio
φ	flattening coefficient in ZBS model
ϕ	azimuth angle in spherical coordinate system
ϕ	bed void fraction
ϕ	circumferential angle in CentRec receiver
Ψ	circularity
ρ	density
ρ_{bulk}	bulk density
σ	Stefan-Boltzmann constant
σ	standard deviation
θ	polar angle in spherical coordinate system
$\boldsymbol{\Theta}$	vector with rotation angles of particle
ξ	area share covered by particles in Schlünder wall model
ξ	random variable
ξ_{α}	Random variable to determine if ray is absorbed

Reoccurring Sub- and Superscripts

bed	particle bed
bot	at the bottom

d	referred to the directional vector of the ray
Exp	obtained in experiment
fluid	fluid
glued	on surface with glued particles on it
i	general index for an element
j	general index for an element
$j \rightarrow i$	from element j to i
LR	long range
max	maximum
min	minimum
n	in normal direction
n	n-th time step
O	with respect to the ray origin on a sphere
out	at the outlet of the collection ring of the CentRec receiver simulations
p	particle
pf	between particle and fluid
pp	between two particles
Ps	projected surface
pw	between particle and wall
rad	Radiation
red	reduced or effective mechanical property
rel	releative
S	steel
sph	sphere
Sim	obtained in simulation
SR	short range
$*$	coarse grained
t	in tangential direction
th	thermal
top	at the top
w	wall
ww	between two walls

Abbreviations

BVH	Bounding Volume Hierarchy
CAD	Computer Aided Design
CDT	Constant Directional Torque model
CS	control surface
CSP	Concentrated Solar Power
DEM	Discrete Element Method

DOM	Discrete Ordinate Method
EPDS2	Modified Elastic Spring Dashpot model
HC	horizontal conveyor
IR	infrared
LHS	Latin Hypercube Sampling
LIGGGHTS®	Open source DEM software
MCRT	Monte Carlo Ray Tracing
PV	Photovoltaics
RPM	revolutions per minute
SPRAY	universal tool for ray tracing simulations of CSP systems in Fortran, developed at DLR
STRAL	solar Tower Ray Tracing Laboratory, Monte Carlo ray tracing software developed at DLR
TC	thermocouple
TMR	temperature measurement ring (in CentRec prototype receiver)
TPM	Thermal Particle Method
ZBS	Zehner-Bauer-Schlünder

1 Introduction

In 2016, human mankind had increased their primary energy need by a factor of 2.5 compared to 1971 and still covered the majority (81 %) of it by fossil fuels like coal, gas and oil [1]. Correspondingly, the CO_2 emissions from fossil fuels and industrial processes have more than doubled between 1970 and 2010 [2]. As CO_2 accounts for most of the greenhouse gas emissions [2], many governments desire to replace fossil fuels by renewable energy sources. However, the International Renewable Energy Agency (IRENA) states in their recent report from 2018 that this transition needs to happen six times faster than currently to fulfill the Paris Climate Agreement [3].
Regarding electricity generation, the report proposes a roadmap for 2050 with an 85 % share of renewables. Wind and solar photovoltaics (PV) are expected to provide 58 % of the electricity in this scenario. However, both technologies can only deliver intermittent and varying power. To maintain grid stability, energy storage capabilities, demand side management or flexible power generation units are required, which are also renewable in a best case scenario. Promising candidates for countries with a high direct solar irradiation are concentrated solar power (CSP) plants equipped with a thermal storage unit [4]. Figure 1.1 shows a tower system, where the sun rays are concentrated on a central receiver by heliostats. In this receiver a heat transfer medium is heated

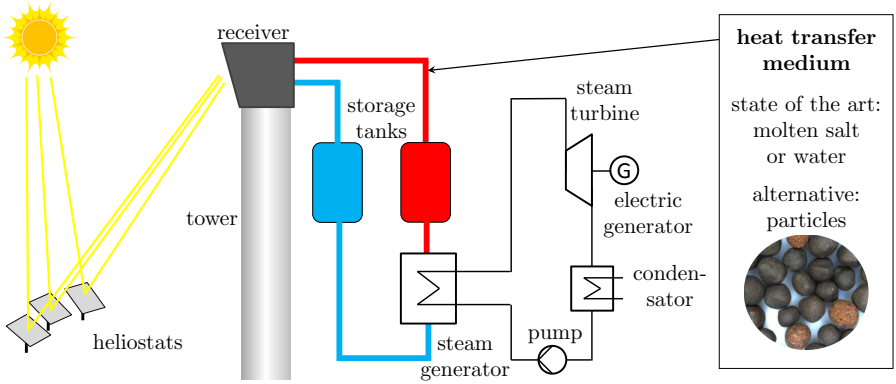

Figure 1.1: Solar tower CSP plant

and later releases its heat in a steam generator to drive a steam cycle. Tanks enable the storage of the hot heat transfer medium, so that steam can be produced in off-sun hours and the plant can continue to operate. While the integration of electricity storage units in a plant usually increases the costs, the thermal storage in a CSP plant decreases the electricity generation costs by increasing the capacity factor[1] [5]. Since a CSP plant has a steam turbine like a conventional power plant, it can help to control the grid frequency in the same manner like these plants. These characteristics assure CSP a place in the electricity systems scenarios: the IRENA roadmap foresees a share of 4 % on the worldwide electricity generation provided by CSP [3]. With current costs as low as US$0.07 per kWh and learning rates[2] above 20 % [6], it is more and more economically viable to replace fossil fuel base load technologies by CSP, especially as fossil fuels are expected to become more expensive due to fuel shortage in the future.

To meet the climate goals, the transportation sector has to undergo a significant transformation as well [3]. Here concentrating solar systems can provide high temperature process heat for the production of biofuels [7], hydrogen [8, 9] or synthetic fuels produced via the Fischer-Tropsch process [10]. Besides the fuel production, there are numerous other industrial processes in which concentrating solar systems can provide high temperature heat and replace fossil fuels. Examples are steam generation, aluminum recycling [11], coal gasification [12] or lime production [13].

In many of these solar driven processes, granular or particulate material needs to be treated, for example biomass, shredded metal, coal or limestone. Aside from these inherently particulate processes, particles are an emerging heat transfer medium for the aforementioned central receiver CSP plants for electricity generation [14] and appear as redox material in solar thermochemical processes for solar fuel production [15, 16].

The designs of corresponding solar particle receivers, which are the devices capturing the concentrated sunlight, are essentially different from designs employing fluids. This is due to the special flow behavior of particulate media and the different thermal characteristics particles have compared to fluids. Often the designs are inspired by ones from other industries, so that adapted fluidized beds, rotary kilns, horizontal conveyors or moving beds can be found as solar particle receiver designs.

[1] The capacity factor is the ratio between actual electricity generation per year and the generation as if the plant would have run at rated power continuously

[2] The learning rate in this context is defined as the "investment cost reduction for each doubling of installed capacity" [6]

1.1 Research Questions and Objective

To be able to model the thermal phenomena in such a solar particle receiver, it is crucial to describe the particle motion accurately. Especially in vacuum environments, as proposed in concepts for solar thermochemical fuel production, heat transfer between particles is greatly reduced so that the convective heat transport by particle motion is essential. However, most current models treat the particles as a continuous phase and can only inaccurately describe this particle motion. As a result an important aspect for the design of particle receivers, the heat transfer to and between the particles, is difficult to estimate and often remains an open question for many different receiver types. The Discrete Element Method (DEM) is considered to describe the particle motion better than the continuum methods. The method has been applied extensively in the field of particle technology for more than a decade and has become an established approach [17]. Especially for dense particle flows, like in moving bed solar receivers or heat exchangers, the interaction between particles is important and the method is clearly superior to others [18]. However, it was not used for particle receivers before 2016. Due to this and the fact that the method is in general mostly applied to cold particle flows, there is a lack of heat transfer models needed for the simulation of a solar particle receiver [18]. All DEM studies of solar receivers in literature either did not include heat transfer at all [18–21], neglected radiation [22] or used the ANSYS model with several limitations, for example with no conductive particle-particle heat transfer [23–26]. Additionally, in all studies arbitrary parameters for the contact force models were used, probably because there are no parameter sets available for particles envisaged in solar receivers.

The objective of this work is to provide all necessary models and parameters to enable the DEM simulation of a solar particle receiver with heat transfer, including radiation. In particular, the pressure influence on the heat transfer should be included to be able to describe heat transfer under vacuum conditions. To accomplish this, the open-source DEM software LIGGGHTS® [27] is extended by a particle-particle heat transfer model, which is based on the Zehner-Bauer-Schlünder (ZBS) continuum model and which includes a temperature and pressure dependence. Additionally, a separate program performing ray tracing, particle-wall conductive heat transfer and interior wall heat transfer is written and coupled to the extended LIGGGHTS® code.

The thesis starts with a review of particle receiver designs and models in section 2. In chapter 3 the fundamentals of the Discrete Element Method are presented and the choice of existing models and settings is discussed. This refers to mechanical models; with respect to heat transfer, an overview of existing models is given and their weaknesses concerning the simulation of so-

lar particle receivers are identified. Addressing these shortcomings, new heat transfer models are developed and described in chapter 4. In chapter 5 a methodology to calibrate contact model parameters by a number of particle flow experiments is developed and parameter sets for five different kinds of particles envisaged in solar receivers are obtained. The model approaches presented in chapter 4 are tested and validated in chapter 6. For the inter-particle conduction model, first the proposed relation between the thermal conductivity of the continuum and the discrete inter-particle conductivity is checked for validity. Then, the applicability of the ZBS continuum model under vacuum conditions and high temperatures is proven in a vacuum receiver experiment in the DLR High-Flux Solar Simulator. For the radiation model, the Monte Carlo ray tracing is validated by several test cases and by comparison to a simpler model; the particle-wall model by replicating a test case from literature and the interior wall model by comparison to a test case with an analytic solution. Finally the model is applied to the CentRec receiver prototype in chapter 7 to demonstrate the feasibility and to point out the method's power to describe experimental findings which could not be covered before. The findings are summarized and an outlook is given in chapter 8.

2 Review of Solar Particle Receiver Designs and Models

2.1 Solar Particle Receivers

Solar receivers in which granular media is heated by means of concentrated solar radiation are called solar particle receivers. In the following it is explained why they are considered for solar thermal power generation and for solar thermochemical fuel production. An overview on particle receiver designs is given.

2.1.1 Power generation

According to the SolarPaces CSP database [28], the vast majority of solar power towers for electricity generation currently use either water or molten salt as heat transfer medium. The latter is found in almost all plants under construction and therefore can be considered as state of the art. However, this molten nitrate solar salt, mostly a mixture of 60 % $NaNO_3$ and 40 % KNO_3, has low thermal conductivity, is corrosive, requires trace heating due to its high melting point of 290°C and has an upper temperature limit of 580°C [29]. This is why other heat transfer media are investigated, among them halide and carbonate salts, air, liquid sodium or liquid metals like lead-bismuth [14]. Another promising heat transfer medium are ceramic particles, which have several advantages:

- **Very high temperature range possible.** Modern, commercially available steam turbines are designed for steam temperatures up to 650°C at the inlet and 670°C for reheat (General Electric STF-D1050 [30]), while turbines operating above 700°C are under development [31]. With the higher temperatures comes greater efficiency of the steam cycle. While these advancements in steam turbine technology cannot be used with currently available solar salt, ceramic particles can withstand temperatures above 1000°C without decomposition or corrosion [14]. With these temperatures, a Brayton cycle with gas temperatures above 1000°C could be driven as well [32]. Even for steam power plants it is beneficial to heat

the particles to temperatures around 1000°C, thus allowing to decrease the size of the storage unit and steam generator, which in turn lowers the levelized costs of electricity [33].

- **Low Price.** Most particle receiver concepts for power generation propose to use bauxite proppants, which come from the fracking industry and are produced in large amounts, making them cheaply available for about 1US$/kg [34]. Sand, which is also considered in some concepts [35, 36], would be even cheaper. Ho [34] states that both the receiver and the storage will be cheaper for particle receiver systems than for other technologies.

- **Direct irradiation.** Molten salt, steam or liquid sodium is heated in tubular receivers, whose tubes are irradiated by solar radiation. Overheating of these tubes is a serious problem in these receivers [37, 38], thus restricting the maximum allowed solar flux density on their surface. The necessary temperature difference over the tube wall is an exergy loss. In contrast, particles can be irradiated directly with basically unlimited flux density. This results in smaller receiver sizes and therefore less reradiation, convection and conduction losses, so that a very high receiver efficiency can be reached.

- **Storage.** Bauxite proppants have a density of 3560 kg m^{-3}[39] and a heat capacity of 1184 J $kg^{-1}K^{-1}$ at 560 °C [40]. Compared with solar salt having a density of 1731 kg m^{-3} and a heat capacity of 1557 J $kg^{-1}K^{-1}$ at this temperature [41], this gives a similar volumetric heat capacity if a particle bed void fraction of 0.4 is assumed (2.53 MJ $m^{-3}K^{-1}$ for bauxite particles and 2.70 MJ $m^{-3}K^{-1}$ for solar salt). However, if one takes into account the wider temperature spread possible with particles, the volume of the storage can be even smaller than for molten salt. Additionally, due to the missing corrosion, the tanks for the particles can be built from cheaper materials [34].

- **Non-corrosive and non-hazardous.** Bauxite or sand particles are not as corrosive as molten salt or especially as halide salts or lead-bismuth mixtures [14]. Moreover, there are no safety issues with these particles unlike with liquid sodium [29].

- **No solidification.** When using molten salt, liquid sodium or liquid metal, trace heating is necessary to avoid solidification. This is not needed for particles.

The potential of particles as heat transfer medium in solar thermal power plants was already seen by researchers in the early 80s and several particle

receivers for power generation have been proposed and tested since then. A classification is given in table 2.1.

Table 2.1: Particle receiver concepts for power generation

Receiver type	Advantages	Drawbacks	Ref.
falling film			
direct absorption 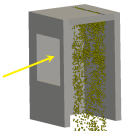	• scalable • no moving parts	• low residence time • particle loss • ambient air entrainment, convective losses [42]	[43–58]
obstructed flow			
direct absorption 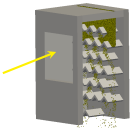	• increased residence time • less wind influence and ambient air entrainment • less particle loss [34]	• wear on obstructions • higher complexity and cost than falling film	[18–20, 59–62]
enclosed 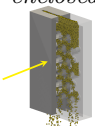	• no particle loss • controlled atmosphere, no ambient air entrainment	• wall as additional heat transfer resistance • flux limitations	[63–66]
fluidized particles			
direct absorption 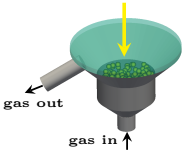	• very good heat transfer • good residence time	• particles are usually not heat transfer fluid • parasitic losses • complexity • scalability	[23–26, 67–80]
enclosed 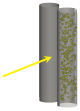	• no particle loss • scalability	• parasitic losses • complexity • flux limitations	[63, 64, 81–83]
centrifugal			
direct absorption 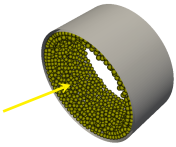	• controlled residence time • high flux and temperatures • walls entirely covered by particles • high efficiency	• parasitic losses • complexity	[40, 84, 85]

After Flamant published his dissertation about the first *fluidized particle receiver* in 1978 [67], this type of receiver was one of the first to be investigated, especially in France [69–71], but also in the US [68] and few years later in Germany [72, 73]. Due to its excellent heat transfer but also mass transfer characteristics this receiver has also been seen in context with chemical processes, historically [67, 86] but also today [24–26, 79]. For power generation, both direct absorption designs [74, 75, 78] and enclosed designs [83] are currently investigated. In many prototypes, particles are just used to enhance the heat transfer to air, which is in fact the actual heat transfer medium, so that the storage advantage of particles is not exploited. The reason might be the complexity of the system, which is a challenge beside the reduction of parasitic losses generated by the blowers.

Apart from the fluidized particle receivers, research organizations (mainly from the US) focused on *falling film particle receivers* in the 80s [43–50]. In this concept a particle curtain is directly irradiated. The comparatively simple and cheap design allows scale-up to large dimensions. The drawback is the very short falling time of the particles, so that they cannot be heated to high temperatures unless they have a very small diameter in the range of 0.1 mm and the particle film is not too thick, which can be seen from straightforward energy balances. With small particles though, the convection losses increase and additionally particles can be blown out of the receiver [52]. To reach higher temperatures, concepts with recirculating particles within the receiver were proposed [54, 55].

Another way to increase the residence time of the particles are obstructions, which should slow down the particle flow, like porous foams [61], wire-mesh screens [18–20], hexagonal tubes [22, 65] or chevron-shaped mesh structures [53, 62, 87]. The latter are depicted in figure 2.1. The obstructions also lower the convection losses, since they greatly reduce natural convection by decreasing the Grashof number and because they impede forced convection by wind. Particle loss is expected to be smaller than in the falling film receiver. As visible in figure 2.1(b), overheating of the obstructions and mechanical wear are a problem. In other designs, obstructions and walls create an enclosed space for the particles, which are therefore not directly irradiated by solar radiation, but are heated through the irradiated enclosing structure [65, 88]. This implies an additional heat transfer resistance through the walls, but eliminates particle loss and can further increase the residence time.

The *centrifugal particle receiver* (CentRec) was patented 2010 by DLR researchers [89], tested in a solar simulator [90] and recently also in larger scale (300 kW) at the solar tower in Jülich, Germany. Figure 2.2 shows the installation of the receiver at the tower in Jülich and the working principle. The particles are fed into a rotating drum via a feeding cone and accelerated to

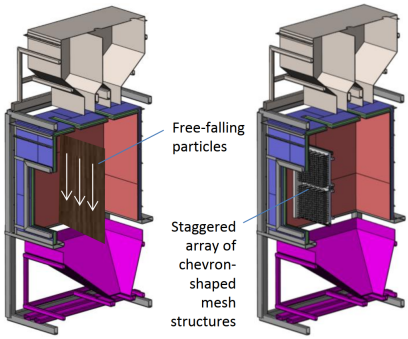

(a) Falling film receiver (left) and obstructed flow receiver (right)

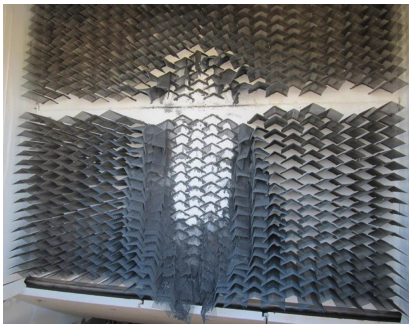

(b) Melted obstructions

Figure 2.1: Falling film and obstructed flow particle receiver, images from Ho et al. [53], republished with permission of ASME

such a degree, that the centrifugal force overcomes the gravitational force and a particle film is formed on the drum walls. The rotation axis is inclined, so that the gravity force partly acts in the axial direction. By adapting the rotation speed, the residence time and film thickness can be adjusted. Since the particles cover the cavity walls, very high flux and temperatures above 1000°C are possible. The convection losses are reduced by the inclination of the receiver [40, 91, 92]. In addition, the aperture is relatively small due to the high incoming flux density, which also reduces the convection losses, but in particular the radiation losses. This results in possible thermal receiver efficiencies around 90 % [40]. The main drawbacks are parasitic losses and the complexity of the design. The receiver is a central research topic at DLR at the moment and is going to be tested in upcoming projects and in larger scale.

2.1.2 Fuel production

Many of the aforementioned particle receiver types are also proposed for solar fuel or hydrogen production, in particular for so called solar thermochemical redox cycles. In these cycles, in the first step a metal oxide is reduced in an endothermic reaction driven by concentrated solar energy:

$$\mathrm{MO_{ox}} \rightleftharpoons \mathrm{MO_{red}} + \frac{1}{2}\mathrm{O_2} \quad . \tag{2.1}$$

In the second step, the reduced metal oxide is oxidized by water, carbon dioxide or both and respectively hydrogen, carbon monoxide or a mixture of them,

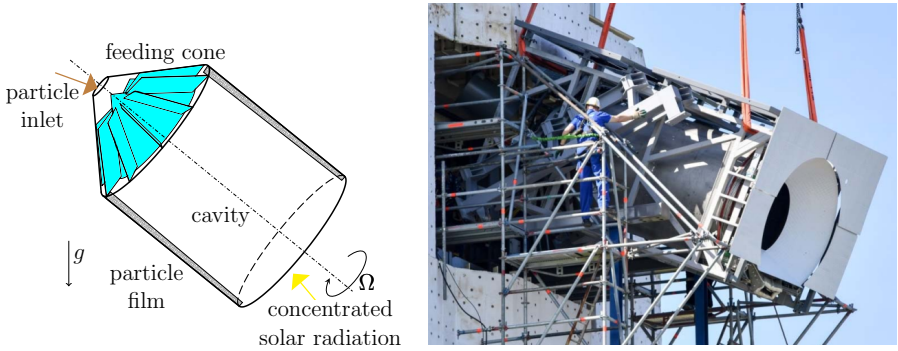

(a) Working principle (b) CentRec500 installation at solar tower Jülich

Figure 2.2: Centrifugal Particle Receiver (CentRec)

syngas, is produced in a slightly exothermic reaction:

$$MO_{red} + H_2O + CO_2 \rightleftharpoons MO_{ox} + H_2 + CO \quad . \tag{2.2}$$

Syngas can be further processed to synthetic fuels via the Fischer-Tropsch synthesis [10]. According to Le Chatelier's principle, the reduction extent during the reduction reaction (2.1) is increased by high temperatures and by low oxygen partial pressure. To obtain the latter, either a purge gas [93] or a vacuum [16, 94, 95] can be used. During the oxidation reaction, lower temperatures and a higher pressure are favorable. This means that the redox material needs to be cycled between two thermodynamic states with different atmospheres and temperatures. The optimal temperature difference depends on the redox material and other process design choices, but has the order of several hundred Kelvin [96] and heat recovery between the two steps is essential to obtain high efficiency [9].

These process characteristics let the requirements for the solar receiver differ in some aspects compared to receivers for power generation. First, there is the need for higher temperatures (above 1400°C in the case of ceria, the most commonly used redox material to date [10, 97]), which exceed the limits of steel, requiring the interior of the receiver to be made of ceramics. Second, there is the need to control the atmosphere, which complicates the receiver construction, especially when using vacuum. Third, the redox material needs to be cycled between two temperatures and heat recovery must be realized.

So far, this led to designs with redox material in the shape of porous monoliths [98, 99], reticulated foams [94], honeycombs [100] or rotating rings [101, 102]. Since in the latter the redox material is moving, continuous operation

and heat recovery by radiative transfer could be realized. If the redox material is fixed, both the reduction and oxidation needs to happen in the same location. This requires the change of gas flows and temperature, so that the receiver-reactor has to be operated in a batch mode. Heat recovery is difficult in these designs. Having the redox material in particulate form brings several advantages aside from the storage possibility and high temperatures already mentioned for power generation:

Continuous operation. The particles can be moved in a cycle instead of cycling the gas flows and temperatures. This allows a continuous operation of the reduction and oxidation at different locations; the respective reactors can be designed and sized according to the needs of the respective step, for example the oxidation reactor can be made out of steel as an enclosed device, so that radiation losses are avoided.

Less thermal shock and less thermally induced tension problems. Due to the continuous operation, the receiver structure stays at fairly the same temperature once the system is in operation. In contrast, batch receivers undergo periodic temperature swings, which induce thermal tension. In continuously operating particle receivers, only the redox material itself experiences high thermal shocks. However, as the material is in particulate form, the effects are way less severe as for large blocks like in the CR5 rotating ring receiver, where thermal tension caused serious problems [102].

Avoidance of temperature hysteresis. If the redox material is a large solid structure, bringing it to a uniform temperature in a reasonable time is nearly impossible and parts of the redox material are below or above the desired temperature. This strongly affects the reduction extent due to its nonlinear dependence on temperature and therefore also affects the efficiency. Parts of the redox material can differ in reduction extent by an order of magnitude [103]. In contrast, particles in the sub-millimeter scale can be heated to uniform temperature within a few seconds [104].

Replacement of redox material. The performance of the redox material itself is crucial for the process to be competitive [105]. With particulate media, it is possible to easily change the redox material in an existing receiver when a better redox material is available.

These advantages encouraged investigation of particle receivers for solar thermochemical redox cycles, including fluidized particle receivers [106–108] and the falling film receiver [109]. Besides these types, which are known from power generation, other concepts like gravity-driven inclined plate receivers [32, 110]

have been developed. Ermanoski et al. suggested a new, innovative vacuum reactor concept where a packed bed of particles serves as a pressure separation between the different steps of the cycle [15]. It was shown that cascading pressures are advantageous for the reduction step [95]. The concept was realized in the Solar Thermochemical Hydrogen Production Research Project (STCH) of the Department of Energy (DoE) of the United States. The key component, a patented [111] vacuum particle receiver-reactor designed by DLR, is shown in figure 2.3. In this receiver, the particles are transported on an oscillating

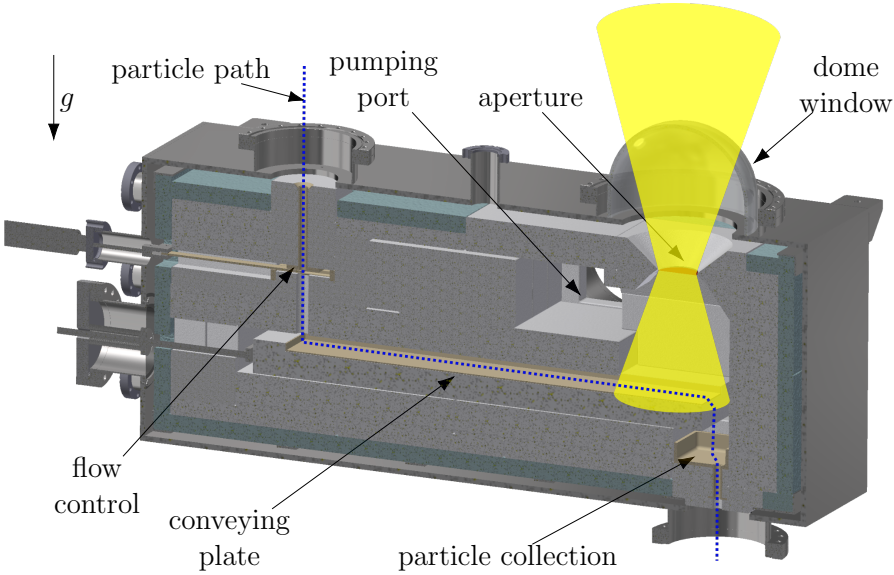

Figure 2.3: Vacuum particle receiver

conveying plate into a cavity, where they are directly irradiated by concentrated radiation entering through the aperture below a dome-shaped quartz window. The mass flow on the plate is controlled by a linear actuator and the oxygen released during the reduction is removed through a port by a vacuum pump. The design allows controlling the residence time and the particle layer thickness very accurately, which is hardly the case in a gravity-driven inclined plate receiver.

2.1.3 Heat Transfer to the Particles as a Limiting Factor

The described vacuum receiver of the STCH project in figure 2.3 is an example of a receiver where the heat transfer to the particles might be a limiting factor.

If the particle layer on the conveying plate in the receiver is assumed to have the conductivity of a packed bed, figure 2.4 shows that the conductivity is very low, in particular under vacuum conditions. At both the design pressures

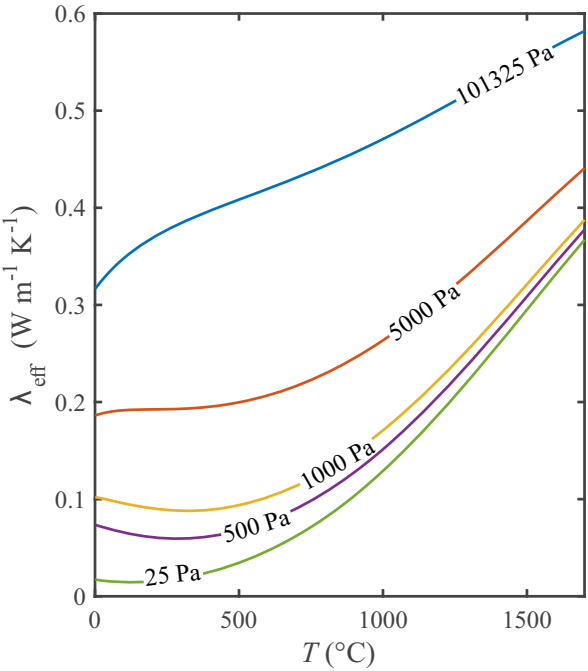

Figure 2.4: Effective thermal conductivity of a fixed bed composed of ceria particles used in the STCH vacuum receiver (278 µm), calculated as a function of temperature for various pressures by the Zehner-Bauer-Schlünder model described in section 4.2.1.2. Image from Grobbel et al. [112], properties of ceria particles are found in table A.1 in the appendix

of the two receivers in the project (1000 and 25 Pa), the effective thermal conductivity of a packed particle bed is an order of magnitude lower than at ambient pressure. An 1-D heat transfer model of the bed coupled to a 3D-radiation model of the cavity showed this can indeed be a limiting factor, even though the particle layer has a thickness of just a few millimeters. However, a definite conclusion could not be drawn, as the effect of convection by particle motion in the bed is expected to have a significant impact but at the same time it is hard to predict. Only some extreme cases could be investigated. In this sense the treatment of the thin particle layer as a packed bed is conservative,

since the void fraction will be higher in reality and radiation will penetrate easier into the thin layer than into a dense packed bed. Details of the model are published by the author of this thesis in [16].
In another concept for solar thermochemical fuel production, inert particles are heated in a solar receiver and then mixed with reactive particles in a vacuum reactor to exchange heat [113–115]. The reactive particles are reduced and after exiting the reactor they are separated from the inert particles by sieving. An arrangement of multiple stages of these particle-mix reactors can emulate a counter-current flow heat exchanger and heat recuperation can be realized, which is essential for high system efficiency [9]. Felinks found in his dissertation that even under ambient conditions heat transfer from the inert to the reactive particles is a limiting factor, so that the quality of the mixture is very important. Due to the reduced thermal conductivity, the mixing is even more important for the operation under vacuum conditions.
These are two examples for the immense impact of the particle motion on the heat transfer in particle receivers. Unless very thin particle layers are irradiated, convective heat transport by particle motion is crucial for sufficient heat transfer to the particles. The attempts to model the motion and the heat transfer in particle receivers are reviewed in the following.

2.2 Models for Solar Particle Receivers

As explained in the previous section, the correct representation of the particle motion is a necessary prerequisite for an accurate thermal description of solar particle receivers. Existing models for particle receivers were reviewed and grouped in table 2.2 by the way the particles are treated.
In the first group of models, the particles as a bulk have *prescribed positions and velocities*, given by explicit equations. In some cases these equations are just definitions of the particle position since the focus was not on particle motion [40], in other cases they are empirical correlations for the specific case [32, 55]. The particle motion calculation is very fast and therefore whole system simulations can be performed in a reasonable time. However, the models are only valid for a very specific case and are often based on a lot of assumptions, which not always hold in reality. In case of the falling film receiver for example, experiments show that the particle curtain affects the fluid velocity, so that the particles in the curtain fall faster than a single, isolated particle [58]. In the model of Röger et al. [55] this effect is not covered, as described by Gobereit [58].
This is why she and many other researchers [51, 54, 56–58, 109, 116–121] use a *dispersed phase model* for the falling film receiver; mostly the commercial

software ANSYS was used where the model is called discrete phase model. In this Euler-Lagrange model the motion of each particle is described by a force balance on the particle, which includes the force coming from an eulerian fluid field. A two-way coupling allows the inclusion of the aforementioned reduced drag effect in the falling film receiver. Convective heat transfer can also be investigated by heat source terms for the eulerian phase and the particles, which are calculated by Nusselt number correlations. As the model does not capture particle-particle interactions, it is limited to dilute particle flow; the ANSYS documentation states a maximum particle volume fraction of about 10 %.

Particle receivers with higher particle volume fraction like fluidized bed or obstructed flow receivers as well as a moving bed particle heat exchanger have been addressed by the so called two-fluid or Euler-Euler approach, in which the particles are treated as an *Eulerian phase*. This means it is modeled as a continuum by Navier-Stokes equations, which are modified to mimic granular behavior. As the model inherently has no discrete nature, it performs good if the particles behave similar like a fluid, but it can hardly describe typical granular phenomena like bridge building, for example.

Discrete Element methods (DEM) cover these effects well, as they provide a more accurate physical description of the granular flow. Similar to the *disperse phase model*, a force balance is applied to each particle, but this time also the interactions between particles are included. They are described by spring-dashpot models, which require a small time step, so that the method is computationally expensive. However, only a few microscopic parameters are needed and once these are found, the method can be applied to all sorts of granular flow problems, while mostly giving superior results than other models. Hence it is often used for the validation of continuum models, as it was done in the first DEM study of a solar receiver performed by Morris et al. in 2016 [22]. While Morris et al. investigated an enclosed obstructed flow receiver, Zanino et al. presented a preliminary DEM study of a falling film receiver in the same year [21]. Starting in 2017, Bellan and colleagues published multiple DEM studies of a fluidized bed receiver [23–26]. They used the DEM parcel approach of the ANSYS software, in which the parcels represent a group of particles. Recently, Sandlin compared the Euler-Euler two-fluid model with the DEM for an obstructed flow receiver with wire-mesh screens in his dissertation [18] and published two papers in 2018 where he focused on the influence of input parameters [19, 20]. It was concluded that the DEM performed better than the Euler-Euler model, which could be expected for a flow through wire-mesh screens as close to the mesh the particle flow does not behave like a fluid. Beside for solar receivers, the DEM is also used in another solar thermal context: for the calculation of thermal stresses in heat storage

tanks [126, 127].
In summary, the DEM can be considered the most accurate method to describe the particle motion in the receiver. The fact that there was no publication at the beginning of this thesis in which it had been applied to solar particle receivers gave rise to further investigate it. This view is confirmed by the recent publications of other researchers on such topic. The method is expected to give new insights and be able to tackle previously unsolvable modeling problems. In the next chapter, its fundamentals will be outlined and the choice of methods and models in scope of solar particle receiver modeling is discussed.

Table 2.2: Particle treatment in solar particle receiver models

Particle representation	Characteristics	Receivers modeled in literature
Prescribed positions or velocities	Particle phase is assumed to be a continuum and position or velocity is given by correlations or analytic expressions	falling film [55], centrifugal [40], inclined plate [32, 110]
Dispersed Phase	Low particle volume fraction (<10 %), no particle-particle interaction, lagrangian description of particle motion by force balance on each particle or particle parcels, coupling with eulerian fluid phase	Falling film [51, 54, 56–58, 109, 116–121], entrained flow [106], recirculating particles [78]
Eulerian Phase (granular fluid)	Eulerian particle phase shares grid cell with fluid phase; separate, but fluid-like momentum, energy and mass balance equations; artificial pressure of particle phase derived from kinetic theory; coupling between the two phases by exchange terms	Fluidized bed [77, 122–124], Obstructed flow [18–20, 22, 60, 61, 65], Moving bed heat exchanger [125]
Discrete Elements	Most physical representation. Lagrangian force balance on discrete particles or particle parcels. Particle-particle interaction by microscopic contact models. Coupling to eulerian fluid by averaging and mapping properties to a grid cell	Fluidized bed [23–26] (parcels), obstructed flow [22] *without heat transfer:* Falling film[21], obstructed flow [18–20]

3 The Discrete Element Method

Parts of this chapter have been published by the author of this thesis:
Grobbel, J., Brendelberger, S., et al. "Calibration of parameters for DEM simulations of solar particle receivers by bulk experiments and surrogate functions." In: *Powder Technology* (2019). DOI: `10.1016/j.powtec.2019.11.028`.

In this chapter the fundamentals of the Discrete Element Method (DEM) are given. The selection of established model approaches is discussed. In addition, an overview of existing heat transfer models is provided in preparation for the heat transfer model development in chapter 4.

3.1 Equations of Motion

The DEM is a lagrangian approach. Each particle is tracked individually by solving its equations of motion, which are the force

$$m_i \ddot{\mathbf{s}}_i = \sum_{j=1}^{N_{\text{con}}} \mathbf{F}_{j\to i,\text{n}} + \sum_{j=1}^{N_{\text{con}}} \mathbf{F}_{j\to i,\text{t}} + m_i \mathbf{g} + \mathbf{F}_{i,\text{fluid}} \tag{3.1}$$

and torque

$$\begin{aligned} \bar{\bar{\mathbf{I}}}_i \ddot{\boldsymbol{\Theta}}_i = & \underbrace{\sum_{j=1}^{N_{\text{con}}} \mathbf{r}_{ij,\text{c}} \times \mathbf{F}_{j\to i,\text{n}}}_{=0 \text{ for spherical particles}} \\ & + \sum_{j=1}^{N_{\text{con}}} \mathbf{r}_{ij,\text{c}} \times \mathbf{F}_{j\to i,\text{t}} + \mathbf{M}_{i,\text{R}} + \underbrace{\mathbf{r}_{i,\text{fluid}} \times \mathbf{F}_{i,\text{fluid}}}_{=0 \text{ for spherical particles}} \end{aligned} \tag{3.2}$$

balances in each direction [27, 129]. The forces are visualized in figure 3.1. In the balance equations, m_i denotes the mass of particle i, $\mathbf{s}_i$ its position vector, $\bar{\bar{\mathbf{I}}}_i$ its inertia tensor and $\boldsymbol{\Theta}_i$ a vector with its angles to the coordinate axes. The

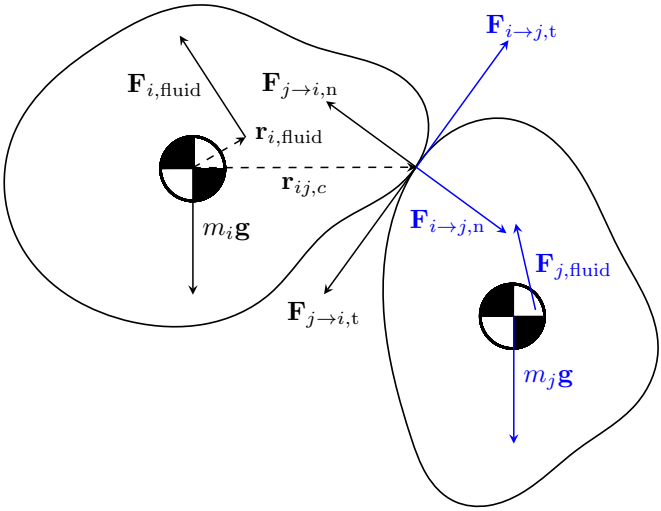

Figure 3.1: Forces on two particles in contact with each other

forces acting on a particle are the sum of the normal and tangential contact forces $\sum \mathbf{F}_{j\to i,\mathrm{n}}$ and $\sum \mathbf{F}_{j\to i,\mathrm{t}}$, gravity $m_i\mathbf{g}$ and in case a fluid is present the force from the fluid on the particle $\mathbf{F}_{i,\mathrm{fluid}}$. In this work gravity is the only body force; in other contexts, also other ones like electrostatic or magnetic forces could be present. The fluid interaction force $\mathbf{F}_{i,\mathrm{fluid}}$ is neglected for the DEM simulations in this thesis as no cases with forced fluid flow are considered and the magnitude of this force is assumed to be small. In other cases though, $\mathbf{F}_{i,\mathrm{fluid}}$ can be the dominating force, for example in fluidized beds.
In the torque balance, $\mathbf{r}_{ij,\mathrm{c}}$ is the vector from the center of the particle to the point of contact force application (contact point with particle j). For spherical particles, only the tangential force component $\mathbf{F}_{i,\mathrm{t}}$ can exert a torque on the particle, since the normal component goes through the center of gravity. The same is true for fluid forces. Rolling friction is taken into account with the term $\mathbf{M}_{i,\mathrm{R}}$.
In this thesis the calculation of the individual forces and moments was performed in the open source DEM software LIGGGHTS®, which is a derivate of the molecular dynamics software LAMMPS [130]. The software is available for no charge, can be modified without restrictions, has a good documentation, an active user base and good parallel performance. In addition it can be coupled to the CFD software OpenFOAM, which is used by other researchers at DLR so that special models for solar receivers could potentially be utilized. The open source nature allows a precise documentation of the models, which will

be done in the following. Even though some implementation details might be specific for this software, the described models are not and they may be found in other DEM codes as well.

3.2 Contact Force Model

To compute the contact forces, the particles are allowed to overlap as depicted in figure 3.2. The resulting force is modeled by a spring for the elastic and a damper for the dissipative part of the contact. Thus the force $\mathbf{F}_{j\to i,\mathrm{n}}$ in normal direction $\mathbf{e}_\mathrm{n}$ is

$$\mathbf{F}_{j\to i,\mathrm{n}} = \left[k_\mathrm{n}\delta_\mathrm{n} - c_\mathrm{n} v_{\mathrm{n,rel}}\right]\mathbf{e}_\mathrm{n} \quad , \tag{3.3}$$

where δ_n denotes the normal overlap and $v_{\mathrm{n,rel}}$ the relative normal velocity of the two particles i and j in contact. In a *linear viscoelastic* or *linear spring dashpot (LSD)* model the spring stiffness k_n and the damping parameter c_n do not depend on the overlap δ_n. This allows to analytically solve for the collision time and the restitution coefficient, which are independent of the impact velocity in this model [131, 132]. In *non-linear viscoelastic* models, the spring stiffness k_n and the damping parameter c_n are themselves functions of the normal overlap δ_n. They are usually derived from Hertzian theory of elastic contact and hence predict a more realistic collision time than the linear viscoelastic model. This could potentially be relevant for later heat transfer simulations, so that the nonlinear Hertz model of Tsuji et al. was selected in this work [133]. In the model the spring stiffness k_n is itself a function of the normal overlap:

$$k_\mathrm{n}(\delta_\mathrm{n}) = \frac{4}{3} Y_\mathrm{red}\sqrt{R_\mathrm{red}\delta_\mathrm{n}} \quad . \tag{3.4}$$

The damping parameter is also a function of the overlap, it scales with $\delta_\mathrm{n}^{\frac{1}{4}}$ and according to Antypov and Elliott it is connected to the restitution coefficient e [134]:

$$c_\mathrm{n}(\delta_\mathrm{n}) = -2\sqrt{\frac{5}{6}}\frac{\ln(e)}{\sqrt{\ln^2(e)+\pi^2}}\sqrt{m_\mathrm{red} 2 Y_\mathrm{red}\sqrt{R_\mathrm{red}\delta_\mathrm{n}}} \quad . \tag{3.5}$$

The equations for the reduced or "effective" Young's modulus Y_red, the reduced particle radius R_red and reduced particle mass m_red are documented in appendix A.1. To better see the nonlinear behavior in δ_n, one can rewrite equation (3.3) with the new constants $\tilde{k}_\mathrm{n}$ and $\tilde{c}_\mathrm{n}$:

$$\mathbf{F}_{j\to i,\mathrm{n}} = \left[\tilde{k}_\mathrm{n}\delta_\mathrm{n}^{\frac{3}{2}} - \tilde{c}_\mathrm{n}\delta_\mathrm{n}^{\frac{1}{4}} v_{\mathrm{n,rel}}\right]\mathbf{e}_\mathrm{n} \quad . \tag{3.6}$$

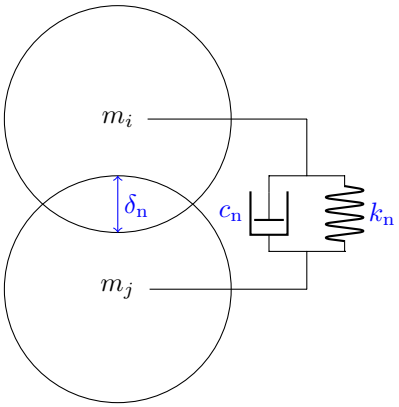

Figure 3.2: Two particles in contact, overlapping by δ_n in normal direction (exaggerated for better visualization). The normal contact force is represented by a network of a spring and a dashpot

For the tangential force component $\mathbf{F}_{j\to i,\mathrm{t}}$ the "tangential history model" was selected in LIGGGHTS®. According to the documentation, it originates from publications of Di Renzo and di Maio [135, 136], Ai et al. [137], Brilliantov et al. [138], Schwager and Pöschel [139], Silbert et al. [140] and Zhang and Makse [141]. In the model the shear vector $\boldsymbol{\delta}_\mathrm{t}$ is defined as the sum of the incremental displacements since the initial contact at time $t_{\mathrm{c},0}$ given by the relative tangential velocity at the contact point $\mathbf{v}_{\mathrm{t,rel}}$ and the time increment $\mathrm{d}t$:

$$\boldsymbol{\delta}_\mathrm{t} = \int_{t_{\mathrm{c},0}}^{t} \mathbf{v}_{\mathrm{t,rel}} \mathrm{d}t \quad . \tag{3.7}$$

From that, the tangential contact force is calculated according to

$$\mathbf{F}_{j\to i,\mathrm{t}} = \begin{cases} -k_\mathrm{t}\boldsymbol{\delta}_\mathrm{t} - c_\mathrm{t}\mathbf{v}_{\mathrm{t,rel}} & \text{if } k_\mathrm{t}\left|\boldsymbol{\delta}_\mathrm{t}\right| \leq \mu\left|\mathbf{F}_\mathrm{n}\right| \\ -\frac{\boldsymbol{\delta}_\mathrm{t}}{\left|\boldsymbol{\delta}_\mathrm{t}\right|}\mu\left|\mathbf{F}_\mathrm{n}\right| & \text{if } k_\mathrm{t}\left|\boldsymbol{\delta}_\mathrm{t}\right| > \mu\left|\mathbf{F}_\mathrm{n}\right| \text{ (sliding)} \end{cases} , \tag{3.8}$$

where μ denotes the sliding friction coefficient between the materials. During sliding, the tangential displacement vector is rescaled to have a magnitude of

$$\left|\boldsymbol{\delta}_\mathrm{t}\right|_\mathrm{max} = \frac{\mu\left|\mathbf{F}_\mathrm{n}\right|}{k_\mathrm{t}} \quad . \tag{3.9}$$

The tangential spring stiffness k_t and the tangential damping parameter c_t are again functions of the normal overlap δ_n:

$$k_\mathrm{t} = 8G_\mathrm{red}\sqrt{R_\mathrm{red}\delta_\mathrm{n}} \tag{3.10}$$

$$c_\mathrm{t} = -2\sqrt{\frac{5}{6}}\frac{\ln(e)}{\sqrt{\ln^2(e)+\pi^2}}\sqrt{m_\mathrm{red}k_\mathrm{t}} \quad . \tag{3.11}$$

The formula for the reduced shear modulus G_red is found in appendix A.1. The description of the tangential history model in equation (3.8) slightly differs from the usually cited equation given by Kloss et al. [27], because it more precisely describes the actual implementation in LIGGGHTS® 3.8.0. In case of small shear $|\boldsymbol{\delta}_\mathrm{t}|$ and high relative tangential velocity $|\mathbf{v}_{\mathrm{t,rel}}|$, the actual implementation allows $|\mathbf{F}_{j\to i,\mathrm{t}}|$ to exceed $\mu\,|\mathbf{F}_\mathrm{n}|$, while in the documentation it is stated otherwise[1].

3.3 Particle Shape and Rolling Friction Model

In the vast majority of practical applications, particles are no perfect spheres and vary in dimensions. The shape can be accounted for in the DEM, for example by polyhedrons, by continuous function representations like ellipsoids or superquadrics or by composite particles consisting of simple geometries like spheres of different sizes [142]. However, these methods require more computational resources than the single sphere representation, because usually the contact detection is more difficult (i.e. nonlinear equations must be solved for superquadric particles) or the number of elements increases significantly (in case of the multi-sphere method) [143]. Therefore it is in many cases a good practice to model each particle by a perfect sphere. This will be done throughout this thesis, because the considered particles have a high sphericity which will be seen in section 5.1. The diameter of the spheres could be different to mimic the particle size distribution of the real particles, but in this work mono-sized spheres are used and the diameter is set to the mean Sauter diameter of the real particles. This reduces the number of particles and allows more efficient contact detection [144], so that it lowers the simulation runtime. One weakness of the perfect sphere representation is that spherical particles will roll substantially easier than the real, nonspherical particles. A rolling friction model tries to compensate for this effect by applying an artificial rolling

[1] In practice, $\mathbf{v}_{\mathrm{t,rel}}$ often does not change direction much during the contact, so that $|\boldsymbol{\delta}_\mathrm{t}|$ increases with $\left|\mathbf{v}_{\mathrm{t,rel}}\right|$ according to equation (3.7). This and the small time step lead in most cases to only a marginal difference to the description of Kloss et al. [27] and $|F_{j\to i,\mathrm{t}}|$ can only slightly exceed $\mu\,|\mathbf{F}_\mathrm{n}|$.

friction torque $\mathbf{M}_\mathrm{R}$ on the particle. LIGGGHTS® offers four different rolling friction models. The modified elastic-plastic spring dashpot (EPSD2) model [137, 145] was chosen in this thesis after some initial tests with angle of repose simulations, which showed creeping bulk behavior for the constant directional torque (CDT) model, as reported in the literature [137, 145]. The name of the EPSD2 model is misleading, because in the modified version in LIGGGHTS® there is no dashpot part like in the original model, but only the spring part. The rolling friction is calculated by the numerical integration of

$$\dot{\mathbf{M}}_\mathrm{R} = -k_\mathrm{R}\dot{\boldsymbol{\Theta}}_\mathrm{rel} \tag{3.12}$$

with the torsional spring stiffness

$$k_\mathrm{R} = k_\mathrm{t}(R_\mathrm{red})^2 \tag{3.13}$$

and the relative rotation of the contact partners $\boldsymbol{\Theta}_\mathrm{rel}$. The variable R_red is the reduced particle radius (see appendix A.1). As the artificial torque is equivalent to a tangential force for a spherical particle, it is reasonable to limit it in a similar way as the tangential force in the contact model described in chapter 2.1:

$$|\mathbf{M}_\mathrm{R}| \leq \mu_\mathrm{R} R_\mathrm{red} |\mathbf{F}_\mathrm{n}| \quad . \tag{3.14}$$

In the EPDS2 model the rolling friction coefficient μ_R hence only affects the maximum possible rolling friction torque. Below this limit, it is only influenced by the stiffness of the particles via k_t and by the relative angular velocity $\dot{\boldsymbol{\Theta}}_\mathrm{rel}$.

3.4 Contact Detection

So far the forces and torques on contacting particles have been described, but one needs to know which particles are in contact to each other in the first place. In general, the condition for a particle i with radius R_i and position $\mathbf{s}_i$ to be in contact with particle j with radius R_j and position $\mathbf{s}_j$ is

$$|\mathbf{s}_i - \mathbf{s}_j| \leq R_i + R_j \quad . \tag{3.15}$$

One could check all particles against each other, but this is computationally very costly as it would scale with the square of the particle number [129]. A better way is to build neighbor lists, which contain the IDs of particles in the vicinity of a particle [130]. They are constructed in specified time intervals by dividing the simulation domain into bins of a certain width and mapping the particles to them. This is done based on the particles coordinates and

therefore does only scale linearly with the particle number [130, 144]. The bin width and neighbor list update frequency strongly influence the simulation runtime [144]. A small bin size has the advantage of quick checking particles against each other within a bin, but it also requires building the neighbor lists more often. There is no general optimum for the bin size as it is computer system dependent [27]. In the molecular simulation software LAMMPS [130] and also in its derivate LIGGGHTS®, the neighbor cutoff distance is the sum of the force cutoff distance and the so called skin distance, which is set to one particle diameter in this work. As a consequence the neighbor list bins have a width of three particle diameters, because the force cutoff distance is always one particle radius due the fact that only contact interaction forces are considered. This is a rather small bin width so that it was decided to update the neighbor lists every time step. This assures that no neighbor particles are missed in the computation, which is considered to be particularly important for the model validation simulations in this work. A less frequent update and hence less runtime would probably be possible in some cases, but this would require preliminary studies to make sure it would not affect the results.

3.5 Critical DEM Time Step

The equations of motion (3.1) and (3.2) are integrated in an explicit velocity verlet scheme. The time step must be small enough so that only the current positions and velocities of the contacting particles influence the motion of the considered particle but not the positions and velocities of the other particles. In other words, the forces should not propagate further than one particle diameter within one time step. The force propagation speed can be estimated by the speed of Rayleigh waves, which describe the wave propagation along the surface of a solid body [146]. From these waves the Rayleigh time step is deduced [147]:

$$\Delta t_{\mathrm{crit,Rayleigh}} = \frac{\pi R_{\min}}{b}\sqrt{\frac{\rho}{G}} \quad , \tag{3.16}$$

where b is one of the roots of

$$\left(2-b^2\right)^4 = 16\left(1-b^2\right)\left[1-b^2\frac{1-\nu}{2(1-\nu)}\right] \tag{3.17}$$

and ν denotes Poisson's ratio. The relevant root is approximated by [147]

$$b = 0.8766 + 0.1631\nu \quad . \tag{3.18}$$

The critical DEM time step has shown to be a fraction of this Rayleigh time step, values between 10 % [148] and 30 % [149] have been found in the literature. In this thesis, values between 15 and 20 % of the Rayleigh time step were

used. Because the time step is inversely proportional to the square root of the shear modulus G, it is a common practice to artificially reduce G to save simulation time [150]. This usually does not affect the overall motion of the particles very much, but it still should be applied with caution [151]. In this thesis Young's modulus Y of the particles, from which G is calculated, was reduced to 5 MPa, the lowest value allowed by the LIGGGHTS® software as it was also done by other researchers [19]. In context of sensitivity studies in section 5.2 this was shown to be a good simplification, as the particle stiffness showed negligible influence on the respective test cases.
The particle collision time is dependent on the impact velocity if the Hertz model is used [132]. However, the Rayleigh time step is not affected by the velocity. To still make sure that the collision can always be resolved, it was assured that the timestep does not exceed 10 % of the Hertz collision time derived by Timoshenko [152]:

$$\Delta t_{\mathrm{crit,Hertz}} = 2.87 \left(\frac{m_{\mathrm{red}}^2}{R_{\mathrm{red}} Y_{\mathrm{red}}^2 v_{\max}} \right)^{0.2} \quad . \tag{3.19}$$

The maximum impact velocity $v_{\max}$ is the maximum relative velocity between two contact partners. In LIGGGHTS® it is estimated by twice the maximum absolute particle velocity (upper limit for relative velocity of two particles) and by the maximum of relative velocity between the walls and the particles. Many heat transfer models rely on correct collision times and contact areas, which are affected by the softening of the particles when the modulus is decreased. Corrections proposed by Morris et al. [153] can eliminate this problem. For the heat transfer model developed in this thesis the corrections are not needed though.

3.6 Coarse Graining

A particle receiver with several meters of aperture size may contain several millions of particles. This causes long run time of the DEM simulations with real size particles and thus can make them unfeasible. To circumvent this problem, a typical approach is to use larger particles in the simulation than in reality to reduce the number of computational particles. This is often referred to as *coarse graining* or *coarse-grain method* [17, 154–157], *similar particle assembly (SPA) model* [158, 159] or *parcel-based approach* [160]. The underlying assumption is that a number of small particles can be represented by fewer and larger coarse-grain particles. This is depicted in figure 3.3. Already without coarse-graining the particles were assumed to be mono-sized spheres with mean Sauter diameter $d_{\mathrm{p}} = \overline{d}_{32}$ in this work, which is a simplification of their

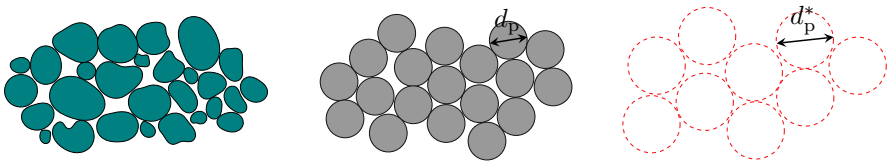

Figure 3.3: Representative particles of the real particles in the DEM simulation

real shape and size. With coarse-graining, the diameter of the mono-sized spheres is increased by the coarse-graining factor CG:

$$d_p^* = CG \cdot d_p = CG \cdot \overline{d}_{32} \tag{3.20}$$

The other geometric dimensions of the problem are kept the same, so that the particle number decreases with the third power of the coarse-graining factor CG. The scaling requires the modification of the particle interaction models, their parameters or both of them. Several ways how this should be done are proposed in literature, a review is given by Hilton and Cleary [157]. Basically all authors conduct dimensional analyses, but as pointed out by Feng and Owen, the procedure is not straightforward and often tailored to specific applications, which results in different scaling laws [161]. Most studies conclude both for linear and nonlinear viscoelastic contact models that the density and the sliding friction coefficient should remain unaffected by coarse graining [17, 155, 156, 160, 162–168]. The restitution coefficient for a damped Hertzian model with cohesion was derived to be invariant by Bierwisch [167] based on conservation of energy density. Later publications follow this approach and come to the same conclusion for the LSD model [160] and the damped Hertzian model also used in this work [168]. However, other studies expect the restitution coefficient to decrease with coarse graining factor [156, 157, 166], which will be discussed in more detail in section 5.2.5.
Even with contact model and parameter adaptations, granular flows which inherently depend on the particle size like the flow through small orifices can hardly be described by classical coarse-graining [157]. A recently published multi-level coarse graining approach with adequate coarse-graining factors for certain geometry regions could avoid this problem in the future [168].
As coarse graining is considered to be essential to be able to simulate large scale particle receivers, it is also investigated in this thesis. To account for its effect on the particle motion, adapted parameters are calibrated in section 5.2.5. The necessary modifications of the developed heat transfer model for coarse-grained

simulations are discussed in section 4.4.

3.7 Heat Transfer

3.7.1 Overview of DEM heat transfer models

Initially, the DEM was developed by Cundall and Strack in 1979 solely to describe particle motion [169]. Since then, the method has emerged as one of the most important ones to model granular matter. However, until the 2000s it had not been used to model heat transfer, as a literature search on the combined terms "discrete element method" and "heat transfer" on the Scopus database[2] revealed. As indicated in figure 3.4, heat transfer can be called a niche topic in the early stages, but in the last couple of years it became more popular; The number of papers in 2017 was already reached after 7 months in 2018. DEM simulations with heat transfer were applied in numerous areas, for example: Drying [170–175], Xerography printing [176], waste and biomass [177, 178], nuclear power [179], metallurgy [180, 181], limestone production [182], insulation design [183], geothermal power [184], food [185], dust explosion [186], combustion [187, 188], calcination [189, 190], ballistics [191], road construction [192], agriculture [193] or polymerization [194]. Relevant heat transfer phenomena in these fields of application are visualized in figure 3.5. They comprise

- convective transport by a fluid
- conduction in between particles (inter-particle)
  - through the solid contact
  - through the gas void space, both inside and outside of the contact region
  - through liquid bridges in case both liquid and gas phase are present
- conduction within the particle (inner-particle conduction)
- radiation, in particular at high temperatures
- heat generation, for example by chemical or nuclear reactions
- surface processes, for example evaporation, oxidation or mechanical friction in the contact area

[2] http://www.scopus.com, results retrieved on August 6th, 2018

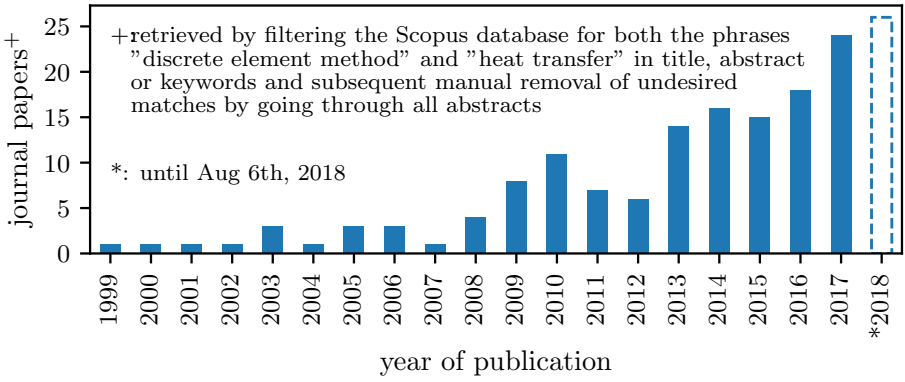

Figure 3.4: Journal articles on heat transfer and the discrete element method

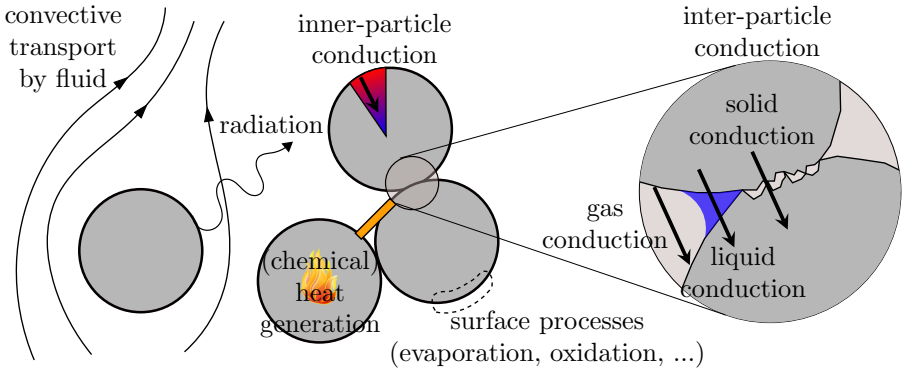

Figure 3.5: Illustration of heat transfer phenomena in granular media

3.7.1.1 Fluid convection

The convective heat transport to a fluid is usually captured by coupling the DEM to a CFD simulation, as it was done in early publications for a fluidized bed by Kaneko et al. [194] or for pipe flows by Li and Mason [195], who extended the pure CFD-DEM coupling introduced by Tsuji et al. [196] by the energy equation. The approach is depicted in figure 3.6. If the size of the CFD mesh cells (blue) is chosen several magnitudes smaller than the particle size, the flow between the particles and the boundary layers can be resolved. Then microscopic heat transfer can be investigated, for example by direct numerical simulation (DNS) from which Nusselt number correlations can be obtained [197, 198]. However, for practical applications with many particles

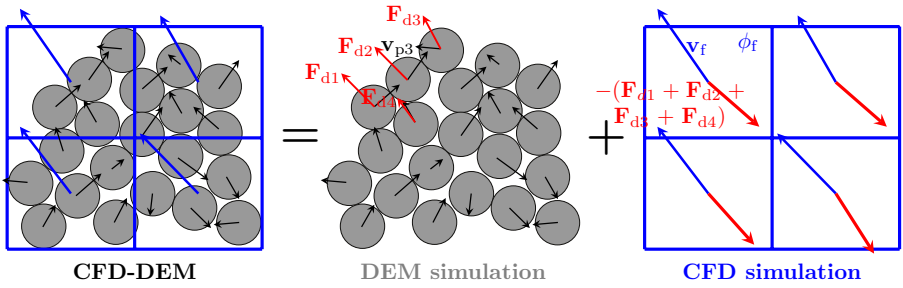

Figure 3.6: Coupling of DEM with CFD. Drag force $\mathbf{F}_{\mathrm{d}i}$ calculated from fluid velocity in cell $\mathbf{v}_{\mathrm{f}}$ and velocity of particle $\mathbf{v}_{\mathrm{p}i}$

the resolved approach is currently not feasible and instead the CFD mesh cell is usually selected so large that it may contain multiple particles as it is shown in the figure. In this case the DEM particle data is mapped to the CFD mesh and averaged to obtain macroscopic properties like the fluid fraction ϕ_{f} or the superficial particle temperature of each cell. The mass, momentum and energy conservation equations of the CFD model are formulated only for the fluid volume in each cell. Source terms from the coupling between the fluid and the particles are included. They are calculated both from the effective properties of each cell and particle-specific data [27]. An example is the drag force in figure 3.6, which is calculated from the fluid velocity $\mathbf{v}_{\mathrm{f}}$ and particle velocity $\mathbf{v}_{\mathrm{p}i}$ by a drag correlation for each particle. These forces are summed for all particles in a cell to give the negative force acting on the fluid. In an analogous way the heat source terms can be calculated by Nusselt correlations for each particle and then they contribute to the energy equation of the fluid in the respective CFD mesh cell.

3.7.1.2 Inter-particle conduction

For the conductive inter-particle heat transfer, Vargas and McCarthy presented the Thermal Particle Method (TPM) for stagnant interstitial fluids [199, 200]. Their model makes use of the resolution of the particle contact, which is available from the DEM method. Heat is conducted through the contact surface and through the interstitial gas and liquid as visualized in figure 3.7. A uniform particle temperature is assumed and the heat flow $\dot{Q}_{ij}$ from particle j to particle i is

$$\dot{Q}_{j\to i} = (\underbrace{H_{\mathrm{c}} + H_{\mathrm{g}} + H_{\mathrm{l}}}_{H_{\mathrm{t}}})(T_j - T_i) \quad . \tag{3.21}$$

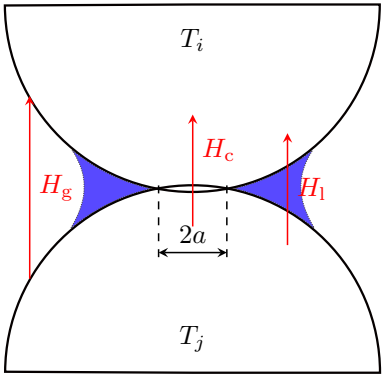

Figure 3.7: Thermal particle method (TPM) developed by Vargas and McCarthy for the inter-particle conduction [200]. Heat is conducted through the contact surface with radius a, through the interstitial gas and through the interstitial liquid

The change of internal energy of particle i is the sum of the heat flows from the contacting neighbors:

$$m_i c_{\mathrm{p},i} \frac{\mathrm{d}T_i}{\mathrm{d}t} = \sum_{j=1}^{N_{\mathrm{con}}} \dot{Q}_{j \to i} \quad . \tag{3.22}$$

The difficulty is to find accurate expressions for the thermal conductance of the solid contact H_{c}, the one in the gas void space H_{g} and the one of the interstitial liquid H_{l}. In the original paper of Vargas and McCarthy, H_{c} is expressed as

$$H_c = \lambda_{\mathrm{p}} 2a \quad , \tag{3.23}$$

where a is the radius of the contact area. This relationship was derived by Batchelor and O'Brien from Hertz theory for two spheres with a large circular contact area, where the gas conduction through the void space could be neglected [201]. Strictly speaking equation (3.23) is not correct once conduction through interstitial liquid or gas is present. However, besides for solely solid conduction [202–207] the model is also widely used when conduction through the gas void space is included [200, 208, 209]. It should be noted that neglecting interstitial gas conduction is in most cases not justified as it is often the main conduction mechanism [210]. This is due to the small solid-solid contact area compared to the area where the solid-fluid-solid conduction is happening. It often outweighs the fact that the conductivity of the fluid is usually

lower than the one of the particle. Cheng et al. presented a modified version of the Batchelor and O'Brian model, where the conduction through the stagnant fluid is included, also when the particles are not in contact [211]. Other studies [171, 187, 195, 212, 213] use the analytically derived model of Sun and Chen, which takes the collision time into account and which is applicable to short collisions [214]. Zhou et al. combined both approaches by choosing the Sun and Cheng model for short contact times and the modified Batchelor and O'Brian model by Cheng et al. for long contact times [215]. In consecutive publications of the same group the model was further extended to correct for particle softening [216] and to handle ellipsoids [217, 218]. Oschmann et al. [219] also apply this sophisticated model for the inter-particle conduction. A weakness of most models is the assumption of a purely solid contact in the contact region, which in fact is rather a combination of small solid and gas contacts due to the surface roughness as indicated in figure 3.5. This is only addressed by some authors in their models [220, 221].

3.7.1.3 Inner-particle conduction

Inner-particle conduction is not considered in the majority of studies, which is reasonable if it is significantly faster than the other heat transfer modes. To evaluate if this is the case and a uniform particle temperature assumption is applicable, Vargas and McCarthy defined a modified Biot number, which relates the inter-particle heat conduction to the inner-particle conduction [199]:

$$Bi_{\mathrm{Vargas}} = \frac{H_\mathrm{t}}{\lambda_\mathrm{p} \frac{A_\mathrm{p}}{r_\mathrm{p}}} = \frac{1}{\pi} \frac{H_\mathrm{t}}{R \lambda_\mathrm{p}} \quad . \tag{3.24}$$

This definition should be extended here by radiative and convective heat flows which also affect the total heat flow at the particle surface:

$$\begin{aligned} Bi_\mathrm{p} :=& \frac{2\sigma(T^4 - T_\mathrm{p}^4)A_\mathrm{p} + H_\mathrm{t}(T - T_\mathrm{p}) + 2h(T - T_\mathrm{p})A_\mathrm{p}}{\lambda_\mathrm{p} \frac{A_\mathrm{p}}{R}(T - T_\mathrm{p})} \\ =& \frac{2R\sigma(T^2 + T_\mathrm{p}^2)(T + T_\mathrm{p})}{\lambda_\mathrm{p}} + \frac{H_\mathrm{t}}{\pi R \lambda_\mathrm{p}} + \frac{2hR}{\lambda_\mathrm{p}} \end{aligned} \tag{3.25}$$

Here A_p denotes the projected surface area of the particle and h the convective heat transfer coefficient. For $Bi_\mathrm{p} \ll 1$ it is justified to assume a uniform particle temperature. If the Biot number is near or above unity, conduction within the particle becomes important. This is treated by resolved particle models in the literature [178, 219, 222–228].

3.7.1.4 Radiation

Radiation has been widely ignored in the majority of DEM heat transfer models in literature. If it was included, a local average temperature and Stefan Boltzmann's law was the most sophisticated model for a long time [215]. More recently, methods based on view-factors [226, 229] and Voronoi cells [230] have been applied. A Monte Carlo ray tracing approach was presented as well [231]. However, all these models only took short-range radiation phenomena into account.

3.7.1.5 Heat generation

In literature, heat source terms have been included for coal combustion reactions [187, 213], nuclear fission [179], evaporation [178] or for heat generation by friction [232]. In solar particle receivers heat generation is important in solar-chemical applications, when the particles undergo a chemical reaction.

3.7.2 Available models in LIGGGHTS

A lot of the previously described models are implemented in custom codes of the respective researchers, which are often not available to the public. The only available heat transfer model in the current LIGGGHTS® version 3.8 is a modified version of the Thermal Particle Method (TPM) developed by Vargas et al. [199]. The LIGGGHTS® documentation cites a paper from Chaudhuri et al. [233] instead, where the TPM was just applied. The model only covers solid-solid heat conduction through the contact area. This area is either given or calculated from the contact model. It should be noted that the conduction through the fluid void space between the particles is not covered, even though it is under most circumstances the main heat transfer mechanism [234].
Heat transfer to a wall is realized by the same heat transfer model as in between particles, which can be justified for the current implementation where only the solid contact heat transfer is taken into account. If conduction through the void space should be added, the model should be different because the gap between wall and particle is different to the one between two particles. Another limitation of the current wall heat transfer model is that an entire mesh can only be set to a single, fixed temperature. Thus it behaves as an isothermal heat source or sink with infinite conductivity, which is an unrealistic assumption for solar receiver walls.
Convective fluid-particle heat transfer can be added by coupling LIGGGHTS® to the CFD software OpenFOAM, which is done in the CFDEM® project [235]. In this case a source term is added on the right hand side of equation (3.22).

When it comes to radiation, it can be stated that there is no available and working radiation model in LIGGGHTS® or CFDEM®, even though the release notes of CFDEM® version 3.7.0 mention one. A closer look at the source code shows that only the radiation models of OpenFOAM were activated by including a single header file and the interaction with the particle phase seems to be missing. A Monte Carlo ray tracing model between particles was implemented in LIGGGHTS® [231], but the code is not available to the public and only calculates radiation between neighbors in a neighbor list, meaning long range radiation or radiation to walls is not covered. These phenomena are also not taken into account in a recently published, novel algorithm to calculate particle-particle radiation by view factors [229].

3.7.3 Summary

Despite the increased interest in DEM heat transfer models in recent years, there is still a lot of potential to improve them. Some topics like the particle shape and size influence on the heat transfer [218], the particle-wall heat transfer [219] or improved radiation models [229] were addressed just very recently. Not yet treated at all is long-range radiation and there are still many open questions concerning the inter-particle conduction. Examples are the influence of surface roughness in the contact area on the solid-solid conduction, but also the conduction through the gas void space. The respective models are only validated at ambient pressure, even though the pressure can have a large influence on the thermal conductivity of granular media [210].
In addition, many models require own implementation, as they have not yet found their way in available software packages. In LIGGGHTS® for instance, the existing heat transfer models neither include radiation nor conduction through the gas void space and the wall heat transfer model is very simple.
It is concluded that currently there is no comprehensive DEM modeling framework for solar particle receivers and heat transfer models need to be developed, as also mentioned in literature [18]. These developments will be described in the next chapter.

4 Model Development

Section 4.2.1.2 has already been published by the author of this thesis: **Grobbel, J., Brendelberger, S., et al. "Heat transfer in a directly irradiated ceria particle bed under vacuum conditions." In: *Solar Energy* 158 (2017), pp. 737–745. DOI:** `10.1016/j.solener.2017.10.022`.

As outlined in the previous chapter, the research on heat transfer models for the DEM has just started in the last couple of years. The method has just recently been applied to solar receivers as described in chapter 2.2. Hence no comprehensive modeling framework for solar particle receivers is available and heat transfer models need to be developed [18]. This is done in the following.

4.1 Particle Energy Balance

In a solar particle receiver, the energy balance of a particle is affected by various mechanisms, which are visualized in figure 4.1. The particles exchange heat with other particles via gas and solid conduction ($\dot{Q}_{\mathrm{cond,pp}}$), but also via radiation ($\dot{Q}_{\mathrm{rad,pp}}$). They also do this with walls ($\dot{Q}_{\mathrm{cond,pw}}$ and $\dot{Q}_{\mathrm{rad,pw}}$) and with the fluid in the receiver ($\dot{Q}_{\mathrm{pf}}$). In most particle receiver concepts the particles are directly irradiated to receive a heat flow $\dot{Q}_{\mathrm{solar}}$, while losing some energy $\dot{Q}_{\mathrm{em,surr}}$ to the surroundings by emission through the aperture. Radiative heat transfer can either have short range (index SR) or long range (index LR). If a chemical reaction is present, it will contribute to the particles energy balance with the source term $\dot{Q}_{\mathrm{chem}}$. Then the overall energy balance of particle i is

$$m_i c_{\mathrm{p},i} \frac{\mathrm{d}T_i}{\mathrm{d}t} = \underbrace{\dot{Q}_{\mathrm{chem}} + \dot{Q}_{\mathrm{cond,pp}}}_{\text{in extended LIGGGHTS}} + \underbrace{\dot{Q}_{\mathrm{rad,pp}} + \dot{Q}_{\mathrm{pw}} + \dot{Q}_{\mathrm{solar}} + \dot{Q}_{\mathrm{em,surr}}}_{\dot{Q}_{\mathrm{src}}\text{, calculated in separate C++ program}} + \dot{Q}_{\mathrm{pf}} \,. \tag{4.1}$$

For certain receiver types, some of the terms in equation (4.1) can be crossed out or neglected. For indirect concepts like the one from NREL [65], $\dot{Q}_{\mathrm{solar}}$ and

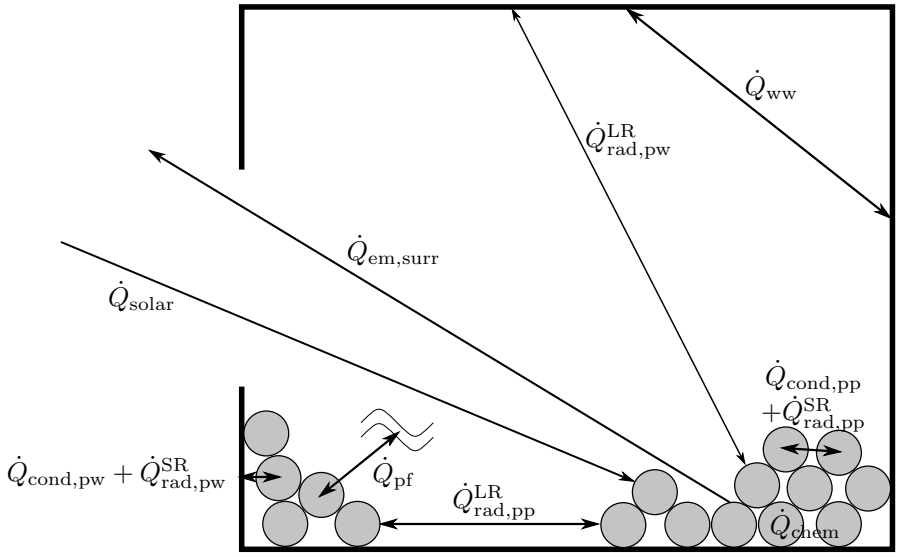

Figure 4.1: Ways of heat transfer in a solar particle receiver

$\dot{Q}_{\mathrm{em,surr}}$ are zero. For a vacuum receiver, the fluid might be neglected, so that $\dot{Q}_{\mathrm{pf}}$ can be dropped. This was done in this thesis, as a vacuum receiver for the reduction of ceria and a vacuum particle mix reactor were foreseeable applications of the models. In this case a chemical source term $\dot{Q}_{\mathrm{chem}}$ is present, while it can be omitted for receivers for power generation, which usually use inert Bauxite particles. Even though convection was omitted in this thesis, it could later be incorporated in OpenFOAM via CFDEMcoupling®.

In LIGGGHTS®, only a heat transfer model for $\dot{Q}_{\mathrm{pp}}$ and $\dot{Q}_{\mathrm{pw}}$ is available. The model is the same for both particle-particle and particle-wall heat transfer and only a single, fixed temperature can be given to the mesh. The implemented correlation for the thermal conductance was considered to be insufficient for the simulation of solar particle receivers as it does not include the conduction through the gas void space. Radiation is not modeled at all. Therefore, own models have been developed for the respective terms in equation (4.1).

A model for $\dot{Q}_{\mathrm{cond,pp}}$ and $\dot{Q}_{\mathrm{chem}}$ was added to LIGGGHTS®, for the other terms and also the particle-particle radiation $\dot{Q}_{\mathrm{rad,pp}}$ a separate C++ program was developed, which is coupled to the extended LIGGGHTS® software as depicted in figure 4.2. It is provided by LIGGGHTS® with the current particle positions, mesh positions and temperatures. The terms $\dot{Q}_{\mathrm{rad,pp}}$, $\dot{Q}_{\mathrm{pw}}$, $\dot{Q}_{\mathrm{solar}}$ and $\dot{Q}_{\mathrm{em,surr}}$ are calculated, added and returned to LIGGGHTS® as particle

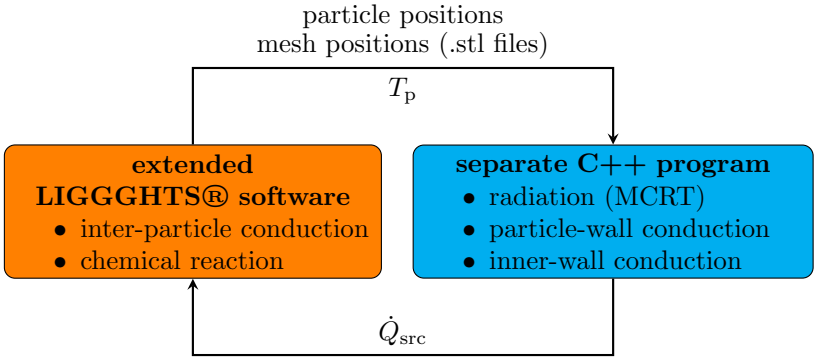

Figure 4.2: Coupling of extended LIGGGHTS® software and separate C++ program

heat sources $\dot{Q}_{src}$. The time integration of equation (4.1) is then performed in the extended LIGGGHTS® software. In the seperate C++ program radiation is calculated by Monte Carlo ray tracing (MCRT), also radiation exchange between walls $\dot{Q}_{ww}$. Besides that, the code also contains a simple 1D heat transfer model for each wall element and calculates the heat transfer through the wall and between the particles and the wall. The details of the models are described in the following.

4.2 Models added to LIGGGHTS

4.2.1 Inter-particle conduction model

The standard heat transfer model in LIGGGHTS® is the Thermal Particle Method (TPM), which is described in section 3.7.1.2. In difference to the original model of Vargas et al., it only accounts for solid conduction through the contact area of touching particles, so that H_t=H_c in equation (3.21). In most cases however, the heat transferred by this mechanism is essentially lower than the solid-gas-solid conduction through the void space [236]. Also, radiation between particles is not taken into account, which is especially important for solar particle receivers due to the high operating temperatures.
To include these effects, an ansatz essentially different from the ones found in the literature should be applied here: a total particle-particle thermal conductance H_t is calculated from a continuum model for the effective bed conductivity λ_{eff}. Instead of trying to model the heat transfer mechanisms at particle scale by some kind of thermal resistance network, a method to calculate the

particle-particle total thermal conductance from the effective bed conductivity is proposed. The advantage of this approach is that it indirectly includes the influence of particle roughness and shape, pressure and temperature via the model for the bed conductivity. In addition, the model can be calibrated directly by thermal conductivity measurements and the large amount of both theoretical and experimental studies on the effective thermal conductivity of particle beds can be utilized.

4.2.1.1 Connection between continuum and discrete model

To relate a continuum model to the discrete heat transfer between the particles in the DEM, heat transfer in one direction is investigated as visualized in figure 4.3.

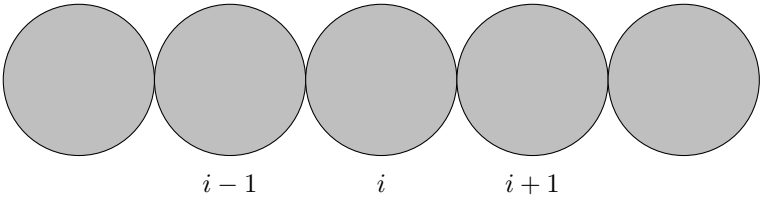

Figure 4.3: Hypothetical particle arrangement in one dimension

In this case the explicit Euler integration of equation (3.22) gives

$$mc_p T_i^{n+1} = mc_p T_i^n + H_\mathrm{t} \Delta t \left(T_{i+1}^n - T_i^n + T_{i-1}^n - T_i^n \right) \quad . \tag{4.2}$$

This can be written as

$$\frac{T_i^{n+1} - T_i^n}{\Delta t} = \frac{H_\mathrm{t} \Delta x^2}{mc_p} \frac{T_{i+1}^n - 2T_i^n + T_{i-1}^n}{\Delta x^2} \quad . \tag{4.3}$$

It is the Euler-forward, central difference discretization of the differential equation

$$\frac{\partial T}{\partial t} = \frac{H_\mathrm{t} \Delta x^2}{mc_p} \frac{\partial^2 T}{\partial x^2} \tag{4.4}$$

and hence similar to the heat diffusion equation for a continuous phase

$$\frac{\partial T}{\partial t} = \frac{\lambda_\mathrm{eff}}{\rho c_p} \frac{\partial^2 T}{\partial x^2} \quad . \tag{4.5}$$

Therefore, one can expect that

$$\frac{H_\mathrm{t}\Delta x^2}{mc_p} \sim \frac{\lambda_\mathrm{eff}}{\rho_\mathrm{bulk}c_p} \quad . \tag{4.6}$$

In this simplified one dimensional case, each particle has only two other particles to exchange heat with and additionally all particles are in line. In a general three-dimensional case, this is not the case and the particle exchanges heat with N_HT particles, which are located around the particle. As also gas conduction is considered, not only the physically contacting particles are expected to exchange heat, but also more distant ones. Therefore a particle j is considered a neighbor of particle i in terms of conductive heat transfer, if the condition

$$|\mathbf{s}_i - \mathbf{s}_j| < (R_i + R_j)\, C_\mathrm{cutoff,HT} \tag{4.7}$$

is fulfilled. In the original model from Vargas et al. only directly contacting particles are considered ($C_\mathrm{cutoff,HT} = 1$), by choosing $C_\mathrm{cutoff,HT} > 1$ more distant ones are included. One can assume that the effective thermal conductivity of such an arrangement is proportional to N_HT

$$\lambda_\mathrm{eff} \sim N_\mathrm{HT} \quad . \tag{4.8}$$

Combining the assumptions (4.6) and (4.8) one obtains

$$\frac{H_\mathrm{t}N_\mathrm{HT}\Delta x^2\rho_\mathrm{bulk}}{\lambda_\mathrm{eff}m} = \mathrm{const.} \tag{4.9}$$

The characteristic length Δx should scale with the particle diameter d_p, the bulk density ρ_bulk can be approximated by $(1-\phi)\rho_\mathrm{p}$ and the particle mass can be expressed by ρ_p and d_p. This leads to the hypothesis

$$\frac{H_\mathrm{t}N_\mathrm{HT}\,(1-\phi)}{\lambda_\mathrm{eff}d_\mathrm{p}} = \mathrm{const.} = K_\mathrm{pp} \tag{4.10}$$

for a fixed heat transfer cutoff distance. In section 6.1.1, this hypothesis is checked, a heat transfer cutoff distance $C_\mathrm{cutoff,HT}$ is chosen and K_pp is calibrated. This allows to calculate H_t from the effective bed conductivity λ_eff:

$$H_\mathrm{t} = \lambda_\mathrm{eff}\frac{d_\mathrm{p}K_\mathrm{pp}}{N_\mathrm{HT}\,(1-\phi)} \quad . \tag{4.11}$$

It should be reflected upon the assumptions made for equation (4.11) and the differences to other approaches to determine H_t. In contrast to the most

sophisticated models in literature [215, 226], where H_t is dependent on the collision time and where the conduction through the gas void space is a function of the particle distance, in the current model the same value of H_t is used for all particle pairs within the cutoff distance. The dependency on particle distance indirectly comes into play by the number of neighbors and by the void fraction, which occurs in equation (4.11) and in the model for λ_eff. In this way the presented approach takes the complex three-dimensional structure of the void space between the particles into account. Meanwhile common literature models are based on two particles in contact and it is not considered whether the void volume between two particles is reduced by other particles occupying this space. It should be noted that the selected continuum model shows some similarity to existing discrete models, as it is also derived by considering two discrete particles in contact. However, influences coming from the arrangement of particles are taken into account as well, as it will be explained in the next section. It will be shown that the continuum model also accounts for pressure, particle shape and surface roughness. In some way it can even compensate for the inaccurate uniform particle temperature assumption in case of thermally thick particles (high Biot number Bi_p). Hence the proposed ansatz in equation (4.11) offers some advantages over existing DEM heat transfer models and is worth being investigated.

4.2.1.2 Continuum model for the effective bed conductivity

For λ_eff in equation (4.11) the model from Zehner, Bauer and Schlünder [234, 236, 237] was implemented because it is widely used [238] and was found to be the best one in an extensive review by Antwerpen [239], who compared numerous analytic models for the effective conductivity of particle beds. Additionally, the model includes pressure dependence and radiation, which is considered important for a solar receiver. It is based on a unit cell which consists of a cylindrical core with two touching semi-particles and an outer cylindrical shell containing only gas, see figure 4.4. The unit cell can be seen as a network of a gas resistance in parallel with a series resistance of gas and solid. In the gas phase conduction and radiation are considered. Convection is not covered by the model; it is expected to be treated separately as it is dependent on the imposed flow conditions [236]. The shape of the model particles is defined by the deformation parameter B and is not meant to represent the real shape of the particle, instead the shape should account for non-parallel heat flow lines [238]. The deformation parameter B is chosen to match the unit cell porosity with the real porosity of the particle bed. Volume integration of the

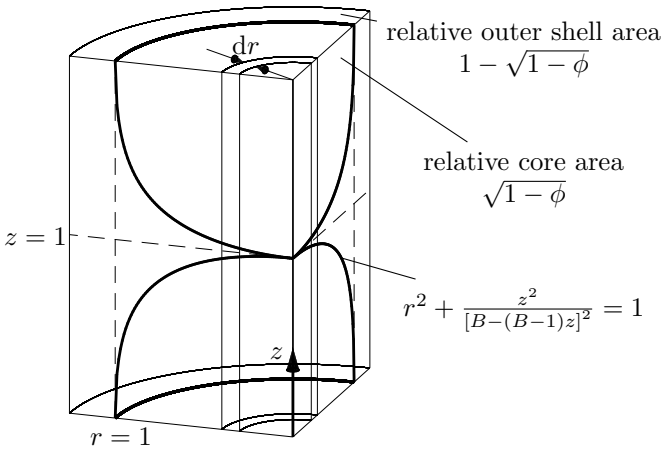

Figure 4.4: Unit cell in Zehner-Bauer-Schlünder model

unit cell and fitting the result to a simpler expression gives

$$B = C_\mathrm{f}\left[\frac{1-\phi}{\phi}\right]^{\frac{10}{9}} \tag{4.12}$$

with $C_\mathrm{f} = 1.25$ and the bed porosity ϕ. The shape factor C_f is different when working with other particle shapes, for example with cylinders or rings [238]. The outer shell represents the gas conduction through the fluid voids, a path which is always existent in a 3D arrangement of particles. Its equivalent in mass transfer is the diffusion path. Therefore, the percentage of the cylindrical shell area on the entire cross-sectional area of the unit cell is taken from mass diffusion experiments, which give a share of $1-\sqrt{1-\phi}$ [237]. In the core with an area share of $\sqrt{1-\phi}$ heat is transferred through the solid and gas phase in series. As the share of the gas phase varies with the radius, the resulting relative core conductivity k_core is calculated via integration over the radius. In the unit cell the contact between the particles is a point contact. To take pure solid conduction between particles into account, the core cell of the unit model is split again and a small percentage φ of the core cell area is assigned to solid conduction, the remainder $1-\varphi$ to the solid-gas-solid heat transfer as described before. The factor φ is called flattening coefficient. This leads to the relative effective bed conductivity

$$\begin{aligned} k_\mathrm{eff} = \frac{\lambda_\mathrm{eff}}{\lambda_\mathrm{f}} = \left(1-\sqrt{1-\phi}\right)\phi\left[\left(\phi - 1 + k_\mathrm{G}^{-1}\right]\right)^{-1} + k_\mathrm{rad}\right] \\ +\sqrt{1-\phi}\left[\varphi k_\mathrm{p} + (1-\varphi)k_\mathrm{core}\right] \quad . \end{aligned} \tag{4.13}$$

The result of the integration for the solid-gas-solid path in the core is [238]

$$k_{\mathrm{core}} = \frac{2}{N}\left\{\frac{B(k_{\mathrm{b}}+k_{\mathrm{rad}}-1)}{N^2 k_{\mathrm{G}} k_{\mathrm{p}}}\ln\left(\frac{k_{\mathrm{p}}+k_{\mathrm{rad}}}{B\left[k_{\mathrm{G}}+(1-k_{\mathrm{G}})(k_{\mathrm{p}}+k_{\mathrm{rad}})\right]}\right)\right. \\ \left. +\frac{B+1}{2B}\left[\frac{k_{\mathrm{rad}}}{k_{\mathrm{G}}}-B\left(1+\frac{1-k_{\mathrm{G}}}{k_{\mathrm{G}}}k_{\mathrm{rad}}\right)\right]-\frac{B-1}{N k_{\mathrm{G}}}\right\} \tag{4.14}$$

with the abbreviation

$$N = \frac{1}{k_{\mathrm{G}}}\left(1+\frac{k_{\mathrm{rad}}-Bk_{\mathrm{G}}}{k_{\mathrm{p}}}\right)-B\left(\frac{1}{k_{\mathrm{G}}}-1\right)\left(1+\frac{k_{\mathrm{rad}}}{k_{\mathrm{p}}}\right) \quad . \tag{4.15}$$

Due to the solid segments, the relative solid conductivity $k_{\mathrm{p}} = \lambda_{\mathrm{p}}/\lambda_{\mathrm{f}}$ comes into play. This in some way compensates for the assumption of a uniform particle temperature in equation (3.22). In the gas phases of the model, the heat transfer is a combination of conduction and radiation. The radiation part is based on the radiation between parallel plates

$$k_{\mathrm{rad}} = \frac{\lambda_{\mathrm{rad}}}{\lambda_{\mathrm{f}}} = \frac{4\sigma}{\frac{2}{\varepsilon}-1}T^3\frac{d_{\mathrm{p}}}{\lambda_{\mathrm{f}}} \quad . \tag{4.16}$$

The radiation term was only included when the ray tracing between the particles was deactivated, which can be useful for some receiver types to save simulation time as described in section 4.3.1.4. The conduction part includes the Smoluchowski effect, which describes the reduction of gas conductivity when the mean free path of the gas molecules approaches the size of the pores, or in other words when the Knudsen number is large:

$$k_{\mathrm{G}} = \frac{\lambda_{\mathrm{G}}}{\lambda_{\mathrm{f}}} = \frac{1}{1+\frac{l}{d_{\mathrm{p}}}} \quad . \tag{4.17}$$

In the context of heat transfer, the modified mean free path

$$l = \frac{2\frac{2-\gamma}{\gamma}\sqrt{\frac{2\pi \mathrm{R}T}{M_{\mathrm{f}}}}\lambda_{\mathrm{f}}}{p\left(2c_{\mathrm{p,f}}-\frac{\mathrm{R}}{M_{\mathrm{f}}}\right)} \tag{4.18}$$

is used [238]. In [240] it is suggested to calculate the accommodation coefficient γ as

$$\gamma = \left(10^{0.6-\frac{1000}{T}+1}{2.8}+1\right)^{-1} \quad . \tag{4.19}$$

The model has been tested by various authors. Bauer [236] and Nasr [241] compared it in extensive studies with experimental data for high temperatures and ambient pressures, and ambient temperatures and low pressures and found good agreement. However, no data for high temperature and low pressures at the same time is available. Therefore, the model was validated for these conditions in section 6.1.2.
It can be summarized that the bed conductivity in the ZBS model is a function of particle diameter d_p, temperature T, pressure p, void fraction ϕ, particle emissivity ε, particle solid thermal conductivity λ_p, interstitial gas type, flattening coefficient φ and shape factor C_f:

$$\lambda_\mathrm{eff} = f(d_\mathrm{p},T,p,\phi,\varepsilon,\lambda_\mathrm{p},\text{gas type},\varphi,C_\mathrm{f}) \quad . \tag{4.20}$$

Particle diameter, temperature and solid conductivity of the particle are known in the DEM code; emissivity, gas type, flattening coefficient and shape factor are global constants given by the user. In this work also the pressure is assumed to be constant, as it was also done by other researchers for solar vacuum particle receivers [242]. The remaining necessary parameter is the void fraction, which is a continuum and no particle property. Therefore its local value needs to be approximated in the discrete model; this was done by a correlation between N_HT and ϕ, which is determined in section 6.1.

4.2.2 Chemical reaction

If the particles undergo a chemical reaction in the particle receiver, the term $\dot{Q}_\mathrm{chem}$ in equation (4.1) must be modelled. As the models are potentially being used in context of thermochemical water splitting, the reduction reaction for ceria

$$\mathrm{CeO_2} \rightleftharpoons \mathrm{CeO_{2-\delta}} + \frac{\delta}{2}\mathrm{O_2} \tag{4.21}$$

happening in the solar receiver was implemented. This reaction has very fast kinetics [105, 243], so that equilibrium was assumed. The reduction extent δ can be described as a function of temperature and oxygen partial pressure [244]:

$$\begin{aligned} \delta(T,p_{\mathrm{O_2}}) =& \frac{0.35 C_1}{1+C_1} \quad , \\ & C_1 = 105808 p_{\mathrm{O_2}}^{-0.217} \exp\left(-\frac{195600\mathrm{J/mol}}{\mathrm{R}T}\right) \mathrm{Pa}^{0.217} \, . \end{aligned} \tag{4.22}$$

Then the chemical source term is

$$\dot{Q}_\mathrm{chem} = \Delta h_\mathrm{R} n_{\mathrm{CeO_2}} \dot{\delta} \quad . \tag{4.23}$$

Here Δh_R denotes the reaction enthalpy per oxygen atom leaving the ceria lattice. For a vacuum receiver, oxygen is the only gas in the receiver after a certain time and the pressure in the receiver is held at the desired level by controlling a vacuum pump. In this case, the reduction extent will only change with temperature, so that the derivative can be written as

$$\dot{\delta} = \frac{\mathrm{d}\delta}{\mathrm{d}t} = \frac{\mathrm{d}\delta}{\mathrm{d}T}\frac{\mathrm{d}T}{\mathrm{d}t} \quad . \tag{4.24}$$

As equation (4.1) shows, the chemical reaction can then be incorporated by simply modifying the heat capacity of the particles to an "artificial" heat capacity $\tilde{c}_\mathrm{p}$:

$$m_i c_{\mathrm{p},i}\frac{\mathrm{d}T_i}{\mathrm{d}t} = (...) + \dot{Q}_\mathrm{chem} \Leftrightarrow m_i \underbrace{\left(c_{\mathrm{p},i} - \frac{\Delta h_\mathrm{R}}{M_i}\frac{\mathrm{d}\delta_i}{\mathrm{d}T_i}\right)}_{\tilde{c}_\mathrm{p}}\frac{\mathrm{d}T_i}{\mathrm{d}t} = (...) \tag{4.25}$$

To implement equation (4.25), the heat capacity was changed from a global to an atom property in the LIGGGHTS® source code. This was in any case necessary to include a temperature dependence of the heat capacity. The temperature derivative of the reduction extent is determined analytically and the artificial heat capacity is updated every time step if this chemical reaction is activated in the simulation.

4.2.3 Integration and time step limit

The feature to integrate the particle temperature is already available in the software LIGGGHTS®. However, equation (3.22) was modified by adding the source term from the coupled C++ program, by extending the amount of participating particles from the touching ones N_con to the ones in a certain surrounding N_HT and by changing the heat capacity from $c_{\mathrm{p},i}$ to $\tilde{c}_{\mathrm{p},i}$:

$$m_i \tilde{c}_{\mathrm{p},i}\frac{\mathrm{d}T_i}{\mathrm{d}t} = \underbrace{\sum_{j=1}^{N_\mathrm{HT}} \dot{Q}_{ji}}_{\dot{Q}_{\mathrm{pp},i}} + \dot{Q}_{\mathrm{src},i} \quad . \tag{4.26}$$

This equation is discretized in an Euler-forward scheme:

$$T_i^{n+1} = T_i^n + \frac{\sum_{j=1}^{N_\mathrm{HT}} H_\mathrm{t}\left(T_j^n - T_i^n\right)}{m_i \tilde{c}_{\mathrm{p},i}}\Delta t + \frac{\dot{Q}_{\mathrm{src},i}}{m_i \tilde{c}_{\mathrm{p},i}}\Delta t \quad . \tag{4.27}$$

Only the nearest neighbors are taken into account in the summation, which is only a valid approach if the time step in the integration in equation (4.26) is

not too large to make sure the thermal perturbations do not propagate further than about one particle distance within one iteration [199]. No literature was found where this time step limit was quantified. Therefore a limit should be derived for the case without source terms. In the special case when particles are aligned in one direction like in figure 4.3, the numerical integration is the same as if the thermal diffusion equation (4.6) would be discretized. For this equation, the stability limit is widely known and it follows in this case

$$\Delta t_{\max} = \frac{mc_p}{2H_{\mathrm{t}}} \quad . \tag{4.28}$$

For the general case of N_{HT} particles exchanging heat with particle i, one finds

$$\Delta t_{\max} = \frac{mc_p}{N_{\mathrm{HT}} H_{\mathrm{t}}} \tag{4.29}$$

via the von-Neumann analysis, which is shown in detail in Appendix A.2 and checked in section 6.1.4. Usually the acceptable thermal DEM time step is significantly larger than the critical mechanical DEM time step from equation (3.16), so that the explicit integration in equation (4.27) is not problematic. Nevertheless, it is useful to know this limit in the case of stagnant, non-moving beds when particle motion is deactivated. In such a case, a time step close to the limit should be selected so that the computation time is reduced significantly. It should be kept in mind that this stability limit is not related to the truncation error introduced by the discretization of equation (4.26) by equation (4.27). It scales with Δt^2 for every step in the Euler method and accumulated after many time steps with Δt [245]. Thus a smaller time step still gives higher numerical accuracy. If particle motion is activated, the time step could be selected higher than the one for the particle mechanics. However, this could affect the choice of neighbor particles for the heat transfer simulation, which would then depend on the time step. It might be acceptable to decrease simulation time in this way in many situations, but in this thesis the time step was set equal to the mechanical time step to avoid this inaccuracy.

4.3 Models in Separate C++ Program

The remainder of the heat transfer calculations were performed in a standalone C++ program, which was coupled to the extended LIGGGHTS® software via a Bash script. In the following it is described how radiation, particle-wall conduction and conduction within the receiver walls is covered by this program.

4.3.1 Radiation model

For central receivers of solar power plants, radiation is one of the main heat transfer modes since high temperatures are reached. This is especially true for particle receivers, which aim for particle temperatures of about 1000°C (power generation [85]) or even for more than 1400°C (thermochemical redox cycles [16]). In the literature, radiation in particle receivers is mostly modeled by discrete ordinate methods (DOM) [58]. Monte Carlo ray tracing (MCRT) is sometimes used to calculate the incoming flux profiles [40]. In the DOM the radiative transport equation is solved on a volume mesh. For the simulation of a particle receiver an attenuation coefficient needs to be calculated for each mesh cell containing particles. The accuracy of the approach is strongly dependent how this is realized. As a volume mesh is needed, coupling to OpenFOAM would be necessary. The advantage is that the speed of the radiation calculation is not dependent on the number of particles. In contrast, in MCRT the speed decreases with the number of elements. However, MCRT can be considered the most accurate way to calculate radiation. Therefore it can also serve as a validation method for other radiation models, including the DOM. Since this thesis should be the basis for further model developments and since the radiation calculation should also work without a coupling to OpenFOAM, it was decided to follow the ray tracing approach.
Amberger et al. [246] already implemented a ray tracing algorithm for the LIGGGHTS® software, but the code is not available to the public and it covers only the short-range radiation but neither the long-range radiation nor the radiative heat transfer to walls. Therefore an own ray tracing code was developed. The simplified flow sheet of the program is shown in figure 4.5. It can trace rays between spheres and triangles. With the spheres the particles are modeled and with the triangles complex shaped walls can be assembled.

4.3.1.1 Ray generation

After reading the necessary data and settings from text files, rays are generated by selecting a random origin on the sphere or triangle accompanied by a random direction. For a sphere, the random ray origin is generated by creating the polar angle

$$\theta_{\mathbf{O}} = 2\pi\xi_\theta \tag{4.30}$$

and the azimuth angle

$$\phi_{\mathbf{O}} = \mathrm{acos}(\xi_\phi) \tag{4.31}$$

with the random variable ξ_θ from the interval [0,1] and ξ_ϕ from the interval $[-1,1]$, generated with the Mersenne-Twister pseudorandom number generator

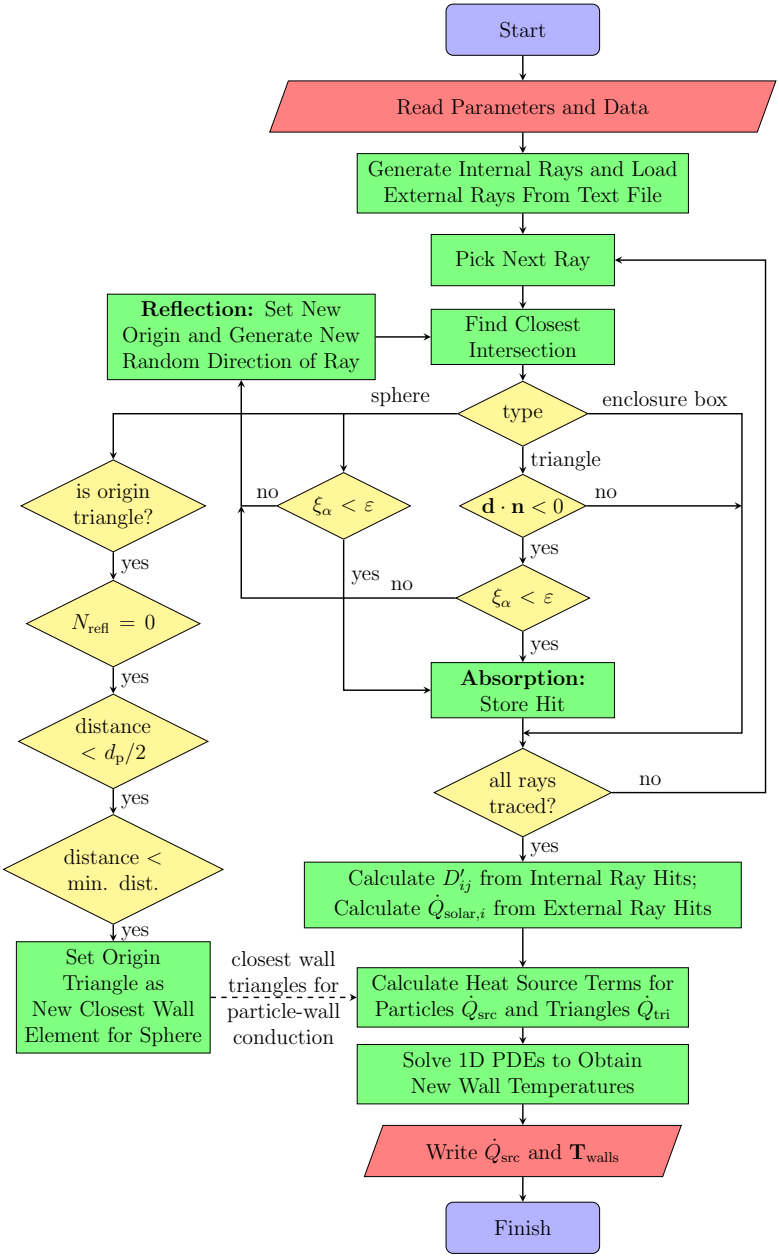

Figure 4.5: Flow chart of the separate C++ program

from the `std` C++ library. Then the ray origin is

$$\mathbf{O} = \mathbf{s}_{\text{sph}} + R_{\text{sph}} \begin{pmatrix} \cos(\theta_{\mathbf{O}}) \sin(\phi_{\mathbf{O}}) \\ \sin(\theta_{\mathbf{O}}) \sin(\phi_{\mathbf{O}}) \\ \cos(\phi_{\mathbf{O}}) \end{pmatrix} \quad . \tag{4.32}$$

For a triangle spanned by vertex position vectors $\mathbf{V}_0$, $\mathbf{V}_1$ and $\mathbf{V}_2$, the ray origin is

$$\mathbf{O} = \mathbf{V}_0 + \xi_1(\mathbf{V}_1 - \mathbf{V}_0) + \xi_2(\mathbf{V}_2 - \mathbf{V}_0) \tag{4.33}$$

with the random numbers ξ_1 and ξ_2 from the interval [0,1] and with the condition $\xi_1 + \xi_2 \leq 1$.
From the origin of both the spheres and the triangles, the rays are shot into an hemisphere whose zenith is the surface normal at the origin point of the ray. To obtain the direction of the ray, a random direction vector in a hemisphere with zenith vector (0,0,1) is created and then transformed into the desired, rotated hemisphere with zenith vector $\mathbf{n}$.
Diffuse reflection and emission is assumed. Then the random direction in the (0,0,1)-hemisphere is [247]

$$\mathbf{d}_{(0,0,1)} = \begin{pmatrix} \cos(\theta_{\mathbf{d}}) \sin(\phi_{\mathbf{d}}) \\ \sin(\theta_{\mathbf{d}}) \sin(\phi_{\mathbf{d}}) \\ \cos(\phi_{\mathbf{d}}) \end{pmatrix} , \quad \theta_{\mathbf{d}} = 2\pi\xi_\theta , \quad \phi_{\mathbf{d}} = \operatorname{asin}\left(\sqrt{\xi_\phi}\right) \tag{4.34}$$

with random numbers ξ_θ and ξ_ϕ from the interval [0,1]. The transformation into the rotated hemisphere was realized by Rodrigues' rotation formula

$$\mathbf{d} = \mathbf{d}_{(0,0,1)} \cos(\beta) + \mathbf{k}(\mathbf{k} \cdot \mathbf{d}_{(0,0,1)}) \left(1 - \cos(\beta)\right) + \sin(\beta) \left(\mathbf{k} \times \mathbf{d}_{(0,0,1)}\right) \tag{4.35}$$

which rotates $\mathbf{d}_{(0,0,1)}$ around axis $\mathbf{k}$

$$\mathbf{k} = \frac{\mathbf{e}_z \times \mathbf{n}}{|\mathbf{e}_z \times \mathbf{n}|} \tag{4.36}$$

by an angle β, whose sine and cosine are be expressed by

$$\sin(\beta) = |\mathbf{e}_z \times \mathbf{n}| = n_x^2 + n_y^2 \qquad , \qquad \cos(\beta) = \mathbf{e}_z \cdot \mathbf{n} = n_z \tag{4.37}$$

The number of rays generated per element has to be defined in a settings file by the keywords `mesh_num_rays` and `sph_num_rays`. Besides these rays, external rays can be loaded by the keyword `externalRays_datafile` followed by the name of the data file containing the origins, directions and energies of the external rays. In this way incoming solar radiation can be provided, for example from a STRAL [248] heliostat field simulation or from a SPRAY[1]

[1] STRAL and SPRAY are both in-house ray tracing software from DLR, which can be obtained for a license fee

simulation, as it was done in chapter 7.

4.3.1.2 Tracing the rays

The generated rays are traced by checking all spheres and triangles for a ray intersection and picking the element with the closest distance. To avoid checking all elements, a bounding volume hierarchy (BVH) tree traversal algorithm was tested in a supervised master thesis but was found to be slower than the brute-force approach [249].
The intersection with a particle is determined by substituting the ray equation

$$\text{ray} : \mathbf{x} = \mathbf{O} + \mathbf{d}\lambda \qquad , \qquad \lambda \geq 0 \tag{4.38}$$

into the sphere equation

$$(\mathbf{x} - \mathbf{x}_{\text{sph}}) \cdot (\mathbf{x} - \mathbf{x}_{\text{sph}}) = R_{\text{sph}}^2 \quad , \tag{4.39}$$

which gives

$$\lambda^2 \underbrace{\mathbf{d} \cdot \mathbf{d}}_{1} + 2 \underbrace{(\mathbf{O} - \mathbf{x}_{\text{sph}}) \cdot \mathbf{d}}_{b} \lambda + \underbrace{(\mathbf{O} - \mathbf{x}_{\text{sph}}) \cdot (\mathbf{O} - \mathbf{x}_{\text{sph}}) - R_{\text{sph}}^2}_{c} = 0 \quad . \tag{4.40}$$

This quadratic equation has the solutions

$$\lambda_{1,2} = -b \pm \sqrt{b^2 - c} \quad . \tag{4.41}$$

In case the determinant $b^2 - c$ is negative, these solutions are complex which means the sphere is not hit. If all solutions are real but negative, which happens to be the case for $b > 0$, the ray points away from the sphere and does not hit. Therefore, as suggested by Eberly [250], in the implementation of the algorithm it is first checked if the determinant is not negative and then if the ray has the right direction before actually calculating the solution of the equation. The intersection of a ray with a triangle was determined by the Möller-Trumbore algorithm [251].
Finally, the algorithm for the intersection with a box was adapted from [252]. The speed of this algorithm is important if the BVH tree traversal approach is used. However, the brute-force approach was surprisingly found to be faster [249] and therefore used instead of the BVH approach. This means it is not necessary to check for any boxes except for the enclosure box. Therefore, the performance of the ray-box intersection algorithm is not critical and details are omitted here.

If the closest intersection of the ray is one with a triangle, it is tested from which side the triangle is hit. If the ray direction vector points in the same direction as the normal vector of the triangle, the ray is discarded. If the ray hits the other side of the triangle or intersects a sphere, a random number ξ_α in the interval [0,1] is generated and compared to the absorptivity of the intersected element. In this thesis the walls and particles are assumed to be gray, so that the absorptivity equals the emissivity ε. If the random number is smaller than the absorptivity, the ray is absorbed at the intersected element and the hit is stored. If it is greater, the ray is reflected: a new ray origin on the intersected element and a new ray direction is generated and the ray is traced again. This is repeated until the ray is absorbed or discarded because it has hit the back face of a triangle or the enclosure box.
Since the rays do not interfere with each other, the ray generation and ray tracing can easily be parallelized, which was done using OpenMP. The computation speed scales almost linearly with the number of processors [249].

4.3.1.3 Radiative heat flows

Once all rays are traced, the stored hits of the external rays (loaded from a text file) are used to calculate the external radiation source

$$\dot{Q}_{\mathrm{solar},i} = \sum_{n=1}^{N_{\mathrm{hits}}} \dot{Q}_{\mathrm{ray}} \quad . \tag{4.42}$$

This summation is the common way how ray tracing is used in the field of solar engineering. Each ray transports a power bundle $\dot{Q}_{\mathrm{ray}}$ from its origin to its absorption location [248, 253]. For the internal rays, however, a different approach was applied. These rays do not carry energy bundles but their hits on surface patches (spheres and triangles) are used to calculate the total diffuse-specular radiation distribution factor D'_{ij}, which is defined as [254]

$$D'_{ij} = \frac{\begin{array}{c}\text{radiation emitted diffusely by surface} \\ \text{patch } i \text{ which is absorbed by patch } j, \\ \text{after all diffuse or specular reflections}\end{array}}{\begin{array}{c}\text{total radiation emitted diffusely by} \\ \text{surface patch } i\end{array}} \approx \frac{\begin{array}{c}\#\text{rays emitted by } i \\ \text{and absorbed by } j\end{array}}{\#\text{rays emitted by } i} \quad . \tag{4.43}$$

In contrast to the widely known view factor, it does not only contain information about the geometric arrangement of the surface patches, but also information about their optical properties. As it includes all reflections, the radiation transported from surface i to surface j can simply be calculated from the emission E_i of surface i

$$\dot{Q}_{\mathrm{rad},ij} = E_i A_i D'_{ij} = \sigma T_i^4 \varepsilon_i A_i D'_{ij} \quad . \tag{4.44}$$

This is an advantage over the calculation by view factors, which would require a matrix inversion. Different to the energy bundle method the ray tracing does not need to be repeated if only the surface emissions change and the geometric arrangement of the surface patches remains the same. Instead equation (4.44) directly gives the new heat flows. This is especially useful if one would like to find a steady-state solution of a receiver without particles or with one with stagnant particles, for example to find initial particle and wall temperatures for a dynamic simulation. Even though diffuse reflections and grey surfaces are assumed in this thesis, the method could be extended to include specular reflections and wavelength-dependent optical properties [254]. The method also allows to speed up the radiation calculation for certain receiver types as explained in the following.

4.3.1.4 Speedup of radiation solution for certain receiver types

The more particles are in a simulation, the more elements need no be checked for ray intersections. Additionally, rays need to be emitted from each new particle, so that also the number of rays increases, which results in a roughly quadratic increase of ray tracing simulation time with particle number. For certain receiver types, this quadratic scaling can be reduced to a linear scaling. This is done by only tracing rays from the walls, so that the number of rays does not increase if the particle number increases. In this way the radiation from walls to the particles is addressed and also the one vice versa by using the relationship

$$\varepsilon_i A_i D'_{ij} = \varepsilon_j A_j D'_{ji} \tag{4.45}$$

which can be derived from the net exchange between two patches i and j at equilibrium. The particle-particle radiation exchange is then included by the radiation term (4.16) in the inter-particle model in the extended LIGGGHTS® software. Equation (4.1) changes to

$$\begin{aligned} m_i c_{\mathrm{p},i} \frac{\mathrm{d}T_i}{\mathrm{d}t} = & \underbrace{\dot{Q}_{\mathrm{chem}} + \dot{Q}_{\mathrm{cond,pp}} + \dot{Q}_{\mathrm{rad,pp}}}_{\text{in extended LIGGGHTS®}} \\ & + \underbrace{\dot{Q}_{\mathrm{pw}} + \dot{Q}_{\mathrm{solar}} + \dot{Q}_{\mathrm{em,surr}}}_{\text{in separate C++ program}} + \dot{Q}_{\mathrm{pf}} \,. \end{aligned} \tag{4.46}$$

The reason why this is only applicable to certain receiver types is the long range particle-particle radiation $\dot{Q}^{\mathrm{rad}}_{\mathrm{pp,LR}}$. This part of the term $\dot{Q}_{\mathrm{rad,pp}}$ exists in receivers where particles see each other over a long distance. As these particles are not neighbors, they do not exchange heat in the particle-particle model in LIGGGHTS®, so that $\dot{Q}^{\mathrm{rad}}_{\mathrm{pp,LR}}$ can not be covered in this way. This means that

this simplification should not be applied to receivers where particles see each other over long distances, for example for solar rotary kilns, but also not for the DOE-STCH receiver in figure 2.3 as particles can see each other over long distances by reflections over the walls. Possible receiver types where the model can be applied are tubular particle receivers and obstructed flow receivers with a dense moving bed. The short range particle-particle radiation $\dot{Q}^{\mathrm{rad}}_{\mathrm{pp,SR}}$ can be covered well by a radiation term in the particle-particle model [208], since the penetration distance of radiation in a dense particle bed is only about three particle layers [255]. An assessment of the accuracy of this approach is made in section 6.2.2 by a comparison to the MCRT solution.

4.3.2 Particle-wall heat transfer

4.3.2.1 Motivation

Radiation between particles and walls is calculated by ray tracing as described previously. For particles in the vicinity of a wall, not only radiation but also conduction through the gas and the contact area is important. This effect can be modelled in LIGGGHTS® with a very simple particle-wall model. One can set a fixed temperature for an entire mesh and then use the same heat transfer model as in between particles. This model was considered not to be sufficient as it has major limitations:

- The wall temperatures are not updated. Therefore they act as a heat source or sink with infinite capacity. Cooling or heating effects by cold or hot particles are not represented by the model.
- As there is only one temperature assigned to the entire mesh, a realistic receiver with a wall temperature distribution can only be modeled by splitting the mesh into hundreds of smaller ones, which is very inconvenient.
- The heat transfer phenomena between walls and particles are only similar to the phenomena in between particles but not the same. Therefore two different models are desirable.

To overcome these limitations, an own wall heat transfer model was developed. The model was added to the separate C++ program instead of the LIGGGHTS® code for several reasons. First, the way how walls are handled in LIGGGHTS® is a very basic feature and in the first place developed for the mechanical interaction with particles. Therefore a change in these models affects a lot of the source code and the entire concept how walls are treated, making it a very difficult task. Second, the heat transfer calculations can be

done with a much larger time step than the DEM time step. Third, the walls are already loaded for the ray tracing in the separate C++ program and also distance information from the ray tracing is available.

4.3.2.2 The model

A thickness, heat capacity, thermal conductivity and density is assigned to each mesh, which is provided in .stl-format (consisting of triangles). Each triangle of the mesh is virtually expanded by the wall thickness to a prism as visualized in figure 4.6 for 4 elements. An one-dimensional heat conduction

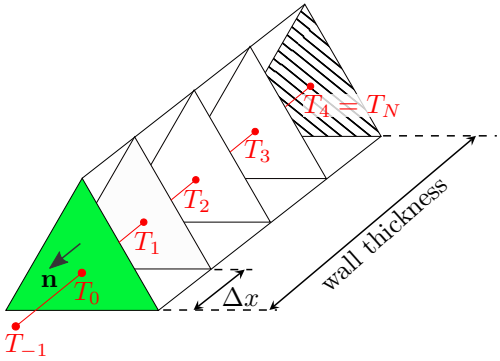

Figure 4.6: Triangle mesh element (green) virtually expanded to the wall thickness by 4 elements to model conductive heat transfer through the wall

equation is solved for elements within the wall with a forward Euler scheme:

$$T_i^{n+1} = T_i^n + \frac{a\Delta t}{\Delta x^2}\left(T_{i-1}^n - 2T_i^n + T_{i+1}^n\right) \quad . \tag{4.47}$$

Here a is the thermal diffusivity of the wall:

$$a = \frac{\lambda_\mathrm{w}}{\rho c_p} \quad . \tag{4.48}$$

For the outward-facing side of the wall (hatched in figure 4.6), four different boundary conditions can be selected by the user:

- Fixed temperature, $T_N = T_\mathrm{outside}$
- Adiabatic, $T_N = T_{N-1}$

- Convection, $T_N = \frac{\zeta}{h+\zeta} T_{N-1} + \frac{h}{h+\zeta} T_\infty$ with $\zeta = \frac{\lambda_\mathrm{w}}{\Delta x}$ and convection coefficient h
- Coupled Wall, $T_N^A = T_N^B$ with the two meshes A and B

The coupled wall boundary condition can be used to mimic conduction through an interior wall, which exchanges radiation on both sides. This is accomplished by shifting mesh A by a certain distance and inverting the normal vectors to generate mesh B, which is then coupled to A.
For the inward side facing the particles (green in figure 4.6) a Neumann boundary condition is used to set the heat flux:

$$\dot{Q}_\mathrm{w} = -\lambda_\mathrm{w} A_\mathrm{w} \frac{T_1 - T_{-1}}{2\Delta x} \quad . \tag{4.49}$$

A second-order discretization with the ghost element T_{-1} was used here, as the first order discretization was found to be too unstable. The heat flux to the wall $\dot{Q}_\mathrm{w}$ consists of the radiation source term from the ray tracing and a term due to conduction:

$$\dot{Q}_\mathrm{w} = \dot{Q}_\mathrm{tri} + \dot{Q}_\mathrm{cond,pw} \quad . \tag{4.50}$$

The radiation source term is the sum of the radiative flows from all other elements (spheres and triangles):

$$\dot{Q}_\mathrm{tri} = \sum_i \dot{Q}_{\mathrm{rad},i\to\mathrm{tri}} \quad . \tag{4.51}$$

The conduction term is modeled similar to the particle-particle model as a product of a total conductance H_w and the temperature difference between particle and wall:

$$\dot{Q}_\mathrm{cond,pw} = \sum_{i=1}^{N_\mathrm{wall,tri}} H_\mathrm{w} \left(T_{\mathrm{p},i} - T_\mathrm{w}\right) \quad . \tag{4.52}$$

To decide if heat is exchanged via conduction between a particle and a triangle wall element, distance information from the ray tracing is used. If a ray from a triangle hits a particle within a distance of one particle radius, the particle is considered to conduct heat to this triangle. If a particle is close to two triangles, the closest one is chosen. In the flow sheet in figure 4.5 these steps are shown in the branch on the very left side.
The conductance H_w is calculated a-priori from the pressure dependent relationship given by Schlünder [256]

$$\alpha_\mathrm{wp} = \frac{4\lambda_g}{d_\mathrm{p}} \left[\left(1 + \frac{2\left(l + \delta_\mathrm{s}\right)}{d_\mathrm{p}}\right) \ln\left(1 + \frac{d_\mathrm{p}}{2\left(l+\delta_\mathrm{s}\right)}\right) - 1 \right] \quad . \tag{4.53}$$

In this equation, λ_g is the conductivity of the interstitial gas, l the modified mean free path (see equ. 4.18) and δ_s the surface roughness of the particles. As α_{wp} is an area-specific quantity, the conductance is obtained by multiplication with the projected particle area:

$$H_w = \frac{\alpha_{wp}\pi d_p^2}{4} \quad . \tag{4.54}$$

4.4 Model Adaptions for Coarse Graining

If coarse graining is applied, the heat transfer models need to be adapted. For the particle-particle heat transfer model the real particle diameter d_p is replaced by the coarse-grained diameter d_p^*:

$$H_t^* = K_{pp}\frac{d_p^*}{N_{con}\,(1-\varphi)}\lambda_{eff} \quad . \tag{4.55}$$

The effective thermal conductivity λ_{eff} should be evaluated with the real radius d_p. In the same way α_{wp} has to be calculated with the real diameter in the particle-wall model and d_p is replaced with d_p^* in equ. (4.54):

$$H_w^* = \frac{\alpha_{wp}\pi\left(d_p^*\right)^2}{4} \quad . \tag{4.56}$$

Radiative heat transfer in particle beds increases with particle size, because the distance between the particle surfaces in the void space becomes larger [257]. Hence the radiative heat transfer in particle beds is overestimated in coarse-grained simulations unless the radiative heat transfer model is adapted. An idea how this could be done is visualized in figure 4.7. Artificial, small spheres would be introduced in void spaces of particle beds in coarse-grained simulations and would participate only in the ray tracing. Their heat source terms and temperatures would be assigned to nearby coarse-grained particles. In this way the radiation penetration distance could be reduced to the one of a bed with real-sized particles. Additionally only a few changes in the ray tracing algorithm would be needed. However, significant modeling work would be required to determine where artificial spheres need to placed, what size they should have and to which particle they should be assigned to. This is postponed to later studies and ray tracing model is not adapted for coarse-grained simulations in this work.

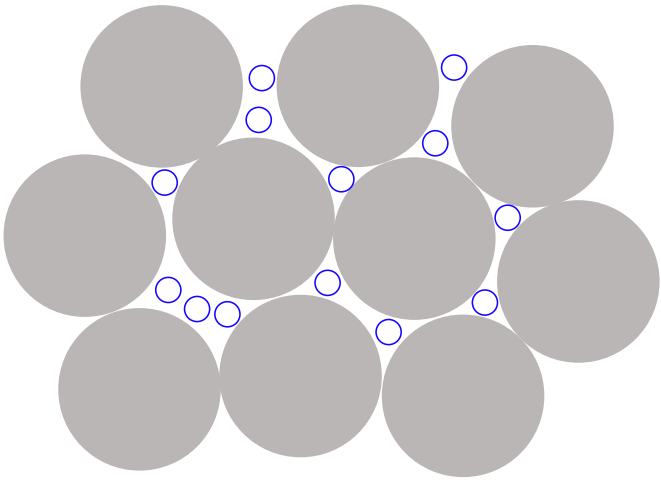

Figure 4.7: Proposed artifical sphere insertion for ray tracing in coarse-grained simulations. Artificial spheres (blue) fill the void spaces between coarse-grained particles (grey) during the ray tracing process

5 Determination of Model Parameters

A major part of this chapter has been published by the author of this thesis: **Grobbel, J., Brendelberger, S., et al. "Calibration of parameters for DEM simulations of solar particle receivers by bulk experiments and surrogate functions." In: *Powder Technology* (2019). DOI:** `10.1016/j.powtec.2019.11.028`.

For the models described in the preceding two chapters, both thermal as well as mechanical properties of the considered particles are required, namely particle size, density, emissivity, heat capacity and thermal conductivity. They are determined by measurements or acquired from literature in section 5.1. In addition, parameters for the contact force model and for the rolling friction model are needed. They were obtained by a custom calibration approach based on bulk experiments presented in section 5.2. The investigated particle types are on the one hand several types of bauxite particles, which are currently favored for particle receivers for power generation [34] and which are used in chapter 7 for the demonstration of the models. Microscope images of these particles are shown in figure 5.1.
On the other hand, the properties of ceria particles were also determined as they were used in in the vacuum experiment in section 6.1.2. They are depicted in figure 5.2.

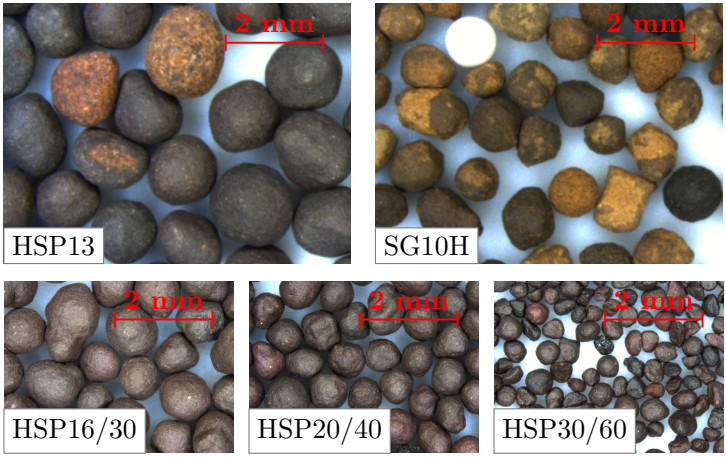

Figure 5.1: Microscope images of investigated bauxite particles. The white alumina particle between the SG10H particles is a tracer used for particle tracking

5.1 Particle Properties

5.1.1 Particle size

The particle size was determined with an optical method similar to the one used by Felinks [113]. Digital images of particles on cardboard were taken from the top and analyzed with the free image processing software ImageJ [258]. The images were converted to grayscale ones, the particles were separated from the background by setting an appropriate threshold for the grayscale value, touching particles were separated by the watershed algorithm and then the projected areas and perimeters of the detected particles were further processed. The diameter of particle i is calculated from the projected (index P) surface (index s) area:

$$d_{\mathrm{Ps},i} = \sqrt{\frac{4A_{\mathrm{P},i}}{\pi}} \quad . \tag{5.1}$$

The circularity is defined as the ratio between the perimeter of a circle with radius $d_{\mathrm{Ps},i}$ and the detected perimeter U

$$\Psi_{\mathrm{Ps},i} = \frac{\pi d_{\mathrm{Ps},i}}{U} \quad . \tag{5.2}$$

From these two quantities, characteristic particle statistics were deduced, which are diameters at the end of the 10 %, 50 % and 90 % quantiles of the particle size distribution, named $d_{10,0}$, $d_{50,0}$ and $d_{90,0}$ and the ratios of moments

$$\overline{d}_{jk} = \frac{\sum\limits_i d_{\mathrm{Ps},i}^j}{\sum\limits_i d_{\mathrm{Ps},i}^k} \quad . \tag{5.3}$$

Here $\overline{d}_{10}$ is the arithmetic mean diameter, $\overline{d}_{21}$ the length-weighted diameter, $\overline{d}_{32}$ the area-weighted mean or Sauter diameter and $\overline{d}_{43}$ the volume-weighted mean or DeBroukere diameter [259]. Accordingly, $\overline{\Psi}_{10}$ is the arithmetic mean and $\Psi_{50,0}$ the median of the circularity.
As the ceria particles have white to yellow color, they were poured onto black cardboard and 57 images were taken with an optical microscope, one of these images is shown in 5.2 before (left) and after particle detection by image processing (right). The measurements with the bauxite proppants were conducted

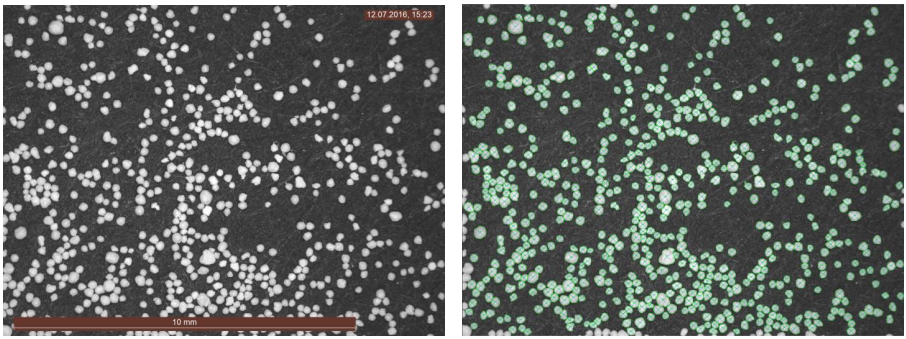

(a) original with scale (b) after image processing

Figure 5.2: Microscope image of ceria particles

in a similar way, except that white cardboard was used and the images were taken with a digital camera instead of a microscope. This was done since the bauxite particles have dark color and because they are significantly larger than the ceria ones. The particle statistics of the investigated particles are depicted in table 5.1. The bauxite particles were provided by Saint Gobain ("SG") and by CarboCeramics ("Carbo"). Two types of them were already used in other studies, so that the naming was adopted. The ceria particles were custom made for the DOE-STCH receiver. For the Carbo HSP particles the manufacturer also provided a sieving analysis, which agreed very well with the results

Table 5.1: Particle size statistics, diameters in µm

Name	$\overline{d}_{10}$	$\overline{d}_{21}$	$\overline{d}_{32}$	$\overline{d}_{43}$	$d_{10,0}$	$d_{50,0}$	$d_{90,0}$	$\overline{\Psi}_{10}$	$\Psi_{50,0}$	N_p
Carbo HSP13*†	1553	1574	1595	1617	1344	1547	1774	0.941	0.945	1783
SG10H‡†	1175	1188	1201	1215	1019	1176	1322	0.94	0.945	2107
Carbo HSP16/30	1068	1085	1101	1117	917	1052	1247	0.948	0.951	2253
Carbo HSP20/40	807	816	826	836	703	800	919	0.954	0.956	3797
Carbo HSP30/60	584	593	603	614	496	578	677	0.957	0.96	5273
Ceria§	254	265	277	291	199	245	324	0.931	0.936	12115

† : used in the dissertation of Trebing [260]
* : used in the dissertation of Wu [40]
‡ : used for cold tests in CentRec receiver [85]
§ : used in DOE-STCH receiver (figure 2.3) and in this thesis in the vacuum experiment

gathered via the optical method. In this work, particles were assumed to be mono-sized in the simulations. As a representative diameter the Sauter diameter $\overline{d}_{32}$ was selected because it is often used for empirical flow correlations, in the Beverloo equation for silos for example. The high sphericity justifies the assumption of spherical particles in section 3.3 to reduce the simulation time.

5.1.2 Density

The density of the ceria particles was averaged from four pycnometer measurements to give a value of 6636.1 kg/m^3 with a standard deviation of 96.6 kg/m^3. For the bauxite proppants, the density is given by the manufacturers. As they only differ in size and shape but have a very similar composition, their density is almost the same and does not deviate more than 2 % from the mean value of 3560 kg/m^3, which was used for all bauxite particles for simplicity.

5.1.3 Emissivity and absorptivity

In the radiation heat transfer model grey surfaces are assumed, so that the emissivity is set equal to the absorptivity. For the bauxite particles, this is no far fetched assumption, as wavelength-dependent measurements indicate. They were conducted by Siegel and are shown in the appendix in figure A.1. Both emissivity and absorptivity lay in a band between 0.84 and 0.95. Wu [40] used an absorptivity of 0.89 and an emissivity of 0.82. In this work, an intermediate value of $\varepsilon = \alpha = 0.86$ was used for the bauxite proppants. For the ceria particles, the emissivity jumps at a temperature of about 800 °C to a

value of about 0.9, as measurements from literature indicate. They are shown in figure A.2 in the appendix. As emission scales with the forth power of the temperature and temperatures above 800 °C are expected in the vacuum experiment in section 6.1.2, this high value of 0.9 was used here both for the absorptivity and emissivity.

5.1.4 Heat capacity

The heat capacity of the bauxite proppants was also measured by Siegel. A fit to the measurements for 25 °C ≤ T ≤ 1000 °C given by Wu [40] was applied here:

$$\begin{aligned} c_{p,\mathrm{bauxite}}(T) = [&- 2.853 \times 10^{-9} (T/^\circ\mathrm{C})^4 + 7.059 \times 10^{-6} (T/^\circ\mathrm{C})^3 \\ &- 5.795 \times 10^{-3} (T/^\circ\mathrm{C})^2 \\ &+ 2.439 \times (T/^\circ\mathrm{C}) + 677.0] \ \mathrm{J\,kg^{-1}\,^\circ C^{-1}} \quad . \end{aligned} \tag{5.4}$$

For ceria, a fit to literature data [261] shown in the appendix in figure A.3 was made:

$$c_{p,\mathrm{ceria}}(T) = \begin{cases} \left[235.2 \ (T/\mathrm{K} - 229.6)^{0.09955}\right] \ \mathrm{W\,kg^{-1}\,K^{-1}} & \text{for } T < 1000\,\mathrm{K} \\ [0.05362 \cdot T/\mathrm{K} + 402.8] \ \mathrm{W\,kg^{-1}\,K^{-1}} & \text{for } T \geq 1000\,\mathrm{K} \end{cases} \tag{5.5}$$

5.1.5 Solid thermal conductivity

The thermal conductivity of the ceria particles was assumed to be identical to the pure material. Temperature-dependent data is provided in [262] near room temperature and at high temperatures above 1000 °C as depicted in the appendix in figure A.4. To obtain values in between, a fit of the form $A \cdot T^B$ was applied:

$$\lambda_{\mathrm{p,ceria}} = \frac{19070}{(T/\mathrm{K})^{1.3}} \ \mathrm{W\,m^{-1}\,K^{-1}} \quad . \tag{5.6}$$

This was motivated by the fact that the intrinsic thermal conductivity of zirconia, a similar ceramic, scales with the reciprocal of the temperature [263]. For the bauxite, no temperature-dependent data could be found. Therefore, a solid thermal conductivity of 10 $\mathrm{W\,m^{-1}\,K^{-1}}$ was assumed, which is in the range of similar ceramics like alumina.

5.2 Calibration of Mechanical DEM Parameters

For the contact model and the rolling friction model described in chapter 3.2 and 3.3, the parameters in table 5.2 are required. Among these parameters, the density was measured directly as described in section 5.1.2. Poisson's ratio ν was set to the typical value of 0.3 for bauxite [264] and Young's modulus E to the constant value of 5 MPa, the minimum value allowed by LIGGGHTS®. This is significantly lower than the actual modulus; this softening of the particles is a common approach to reduce the simulation time by increasing the time step according to equation (3.16)[151]. The two parameters ν and E are excluded from the calibration under the assumption that they have only a minor influence on the particle motion. This assumption is examined later in a sensitivity analysis. The remaining, unknown parameters are particle-particle and particle wall restitution coefficients, friction coefficients and rolling friction coefficients. To obtain these parameters, there are basically two approaches:

Table 5.2: Parameters required for DEM contact model

Symbol	Name	Value
Y	Young's modulus	5 MPa
ν	Poisson's ratio	0.3
ρ	Particle density	see section 5.1.2
e_{pp}	Coefficient of restitution for particle-particle interaction	calibrated
e_{pw}	Coefficient of restitution for particle-wall interaction	calibrated
μ_{pp}	Coefficient of friction for particle-particle interaction	calibrated
μ_{pw}	Coefficient of friction for particle-wall interaction	calibrated
$\mu_{\mathrm{R,pp}}$	Coefficient of rolling friction for particle-particle interaction	calibrated
$\mu_{\mathrm{R,pw}}$	Coefficient of rolling friction for particle-wall interaction	calibrated

measure them directly on particle scale *(Direct Measuring Approach)* or calibrate them to the outcome of bulk experiments *(Bulk Calibration Approach)* [150, 265]. In this work the latter approach was chosen, because the particles investigated were rather small and no perfect spheres. Therefore experiments on a particle scale were considered to be significantly more difficult than bulk

experiments. Marigo et al. state that direct measurement is mainly applied to particles in the millimeter range [265]. Additionally, parameters obtained by the bulk calibration approach can be seen as "adjustment parameters" [150], which can compensate for model inaccuracies, for example for the assumption of spherical particles. Here the lack of rolling resistance is compensated by a rolling friction model [145], so that the rolling friction coefficient can be considered a "purely empirical parameter", which cannot be measured directly [150]. Coarse-graining can also be interpreted as a model inaccuracy, which can be accounted for by adapted parameters. The parameters for a coarse-grained simulation can be obtained by the bulk calibration approach without making new experiments.

5.2.1 Calibration experiments

In the selection of the bulk experiments for the parameter calibration, the following aspects should be taken into account:

- Each of the parameters in the calibration should be sensitive to at least one experiment
- Measurement of data from the experiments should be simple and the measurement uncertainties should be low.
- The experiment should be easy to reproduce in a DEM setup.
- The particle number should be kept as low as possible to reduce the computational load and the duration of the calibration.

Considering these points, the following five experiments have been designed for the calibration:

1. Static angle of repose on particles laminated on cardboard
2. Static angle of repose on a flat surface (steel or Al_2O_3)
3. Transport of particles on a horizontal conveyor (HC) laminated with particles
4. Transport of particles on a horizontal conveyor with flat surface (steel or Al_2O_3)
5. Impact of particles on an inclined plate (steel or Al_2O_3)

These experiments were performed with the bauxite particles listed in Table 5.1. Two typical wall materials in a solar receiver were tested: steel and a porous alumina (Al_2O_3) insulation board. Experiments 2.) and 4.) were performed in scope of a supervised bachelor thesis [266]. In the coming sections, the experiments are described in more detail.

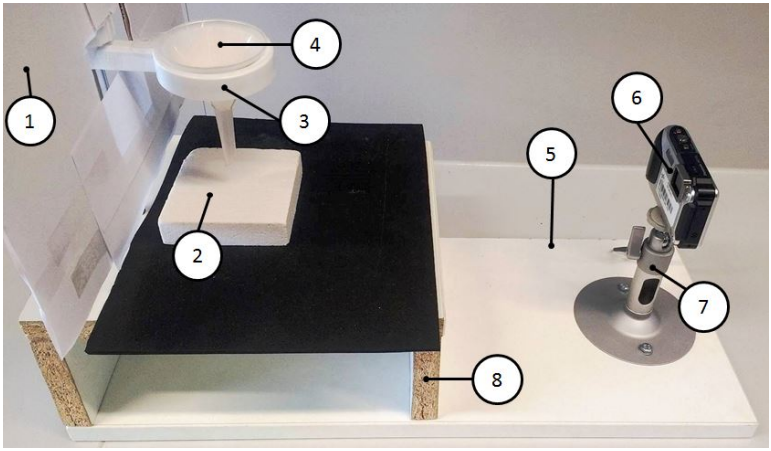

Figure 5.3: Experimental setup of angle of repose experiment, image from [266]

5.2.1.1 Static angle of repose experiment

The setup of the angle of repose experiment is shown in figure 5.3. The static angle of repose was measured by pouring the particles through a funnel (4) on a plate of the respective contact material (2), taking a picture with a digital camera (6) and analyzing this picture via image processing with the opencv package in Python. To conduct experiment 1.), the plate of contact material was replaced by a cardboard covered by a layer of particles, fixed by double-sided duct tape and shown in figure 5.4. The whole setup including the funnel was reproduced in LIGGGHTS®; a restart file with a filled funnel was created to reduce simulation time. For the simulations with the glued particles on the cardboard, the sliding and rolling friction coefficients of the contact material were set to the extremely high value 1000.
A typical measurement overlayed with lines from the image processing is depicted in figure 5.5 alongside with the image processing of the DEM result. The measured angles α are listed in table 5.3. The experiments on the flat surfaces were repeated 15 times, so that the standard error of the mean is lower than for the experiments on fixed particles, which were only repeated four or five times.

5.2.1.2 Horizontal conveyor experiment

The third and fourth experiment are closely related to the vacuum particle receiver-reactor, which was developed at DLR and which is shown in fig-

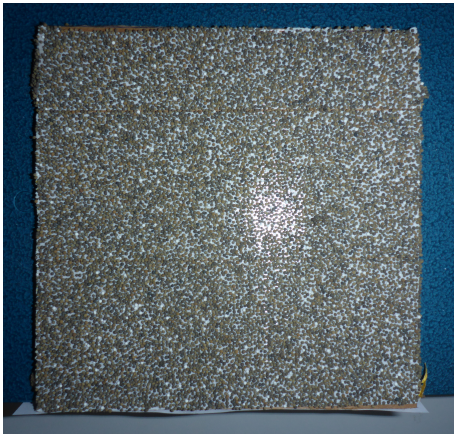

Figure 5.4: Cardboard laminated with SG10H particles

Table 5.3: Mean value of angle of repose measurements and standard error of the sample mean. Angle on steel α_S, on alumina α_{Al2O3} and on glued particles α_{glued}

Name	α_S	α_{Al2O3}	α_{glued}
Carbo HSP13	28.23° ± 0.09°	29.40° ± 0.14°	30.50° ± 0.31°
SG10H	32.18° ± 0.14°	34.16° ± 0.13°	33.93° ± 0.27°
Carbo HSP16/30	30.68° ± 0.12°	31.54° ± 0.17°	31.84° ± 0.27°
Carbo HSP20/40	28.82° ± 0.29°	30.40° ± 0.11°	30.25° ± 0.22°
Carbo HSP30/60	31.42° ± 0.06°	31.45° ± 0.22°	31.79° ± 0.26°
Ceria	31.73° ± 0.18°	31.19° ± 0.21°	31.75° ± 0.29°

ure 2.3. Both experiments are conducted with the same apparatus depicted in figure 5.6. It consists of a horizontally oscillating plate (1) mounted on a slider (5), which is driven by a stepper motor (9) along a rail (6). Particles are poured through the funnel (3) onto the plate (1) and are transported alongside the plate by the oscillation until they fall onto the scale (2). The time between opening of the funnel and the moment when 100 g of particles is on the scale is measured and denoted as $t100$. To measure the different contact surfaces, they are attached to the plate. In case of experiment 3.), cardboard is laminated with particles and fixed on the plate as shown in figure 5.8.
The particles on the horizontal conveyor are transported by the following mechanism: During the slowly accelerated forward motion of the plate, the particles

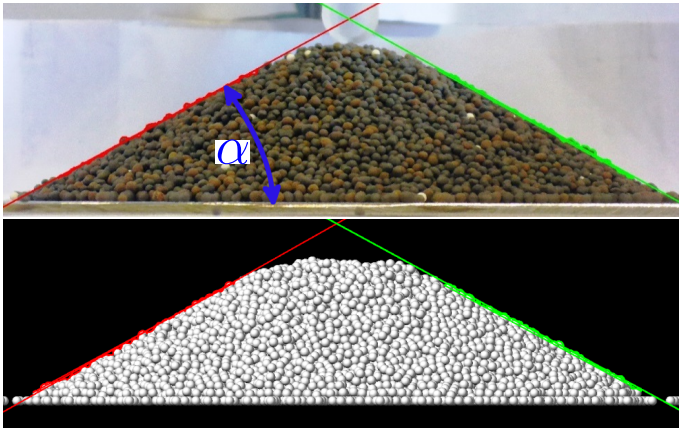

Figure 5.5: Analysis of the experimental (top) and simulated (bottom) angle of repose of Carbo HSP13 on steel, modified image from [266]

stick to it and are moved forward. Then the plate is stopped and moved back with a high acceleration, so that the particles slip. Their forward motion is decelerated, depending on the accelerations and the particle friction they could even be transported backwards at some point in this stage. However, over an entire cycle the net motion is positive and they are transported forward. The acceleration and position profile for the plate was created in a MATLAB Simulink/Stateflow program, which assumes the particles to move as a solid body on the plate, similar as it was done by Lim [267]. To check if the plate follows the desired motion, high speed camera videos were analyzed for the case of experiment 3.), where the plate is laminated with particles as shown in figure 5.8. In figure 5.7 the extracted plate and glued particle positions are plotted alongside the desired position profile which was given to the controller. The plate follows the desired profile with some minor deviations, mainly the period is a little longer than defined. The glued particles make the same motion as the plate, so that they can be considered to be glued sufficiently to the plate. In LIGGGHTS®, the motion profile is defined as a sum of cosine functions. That is why there is a slight deviation between the desired profile and the profile of the plate in the DEM. To realize the lamination in LIGGGHTS®, the particle-wall sliding friction and rolling friction coefficients were set to the value of 1000, so that the particles basically make the same motion as the plate in the DEM (dotted lines). A restart file with the laminated plate was created by running a simulation until no particles were leaving the plate anymore. The same was done in the experiment: particles were initially

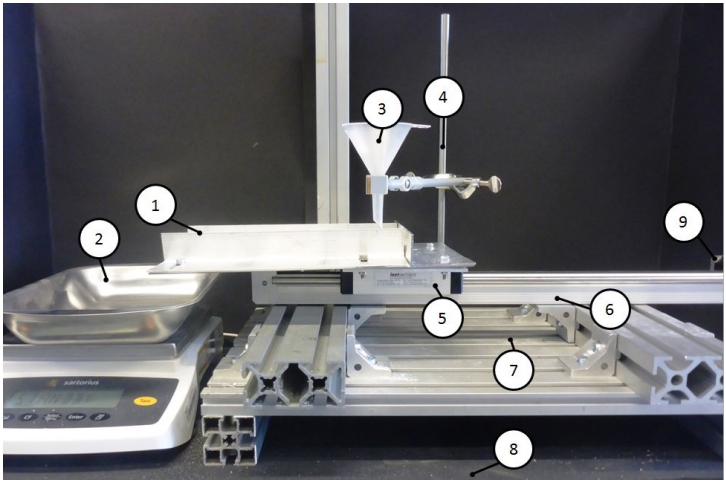

Figure 5.6: Setup of horizontal conveyor experiment, image from [266]

poured on the plate and it is kept running before each experiment until only a negligible amount of particles leaves the plate. Before each experiment also a spirit level was used to ensure that the plate is horizontal. After the plate motion had been activated, the plug closing the funnel was removed and the weight on the scale was recorded over time. A typical result is shown in figure 5.9 for Carbo HSP13 particles moving on a plate laminated with the same particles. After the first particles reach the end of the plate, the mass on the scale almost linearly increases. The slope of the line shows that the mass flow is only slightly lower than the one coming out of the funnel. Obviously this funnel mass flow strongly influences the outcome of the experiment, therefore it was measured beforehand; the mass flows are listed in appendix A.6. The results of the horizontal conveyor experiments on the different plate surfaces are summarized in table 5.4 alongside with the standard errors of the mean which were gathered by repeating all experiments five times. Since the mass flow through the funnel is different for all particle types, it is difficult to generally draw conclusions from comparisons between them. The tendency that $t100$ decreases with particle size could be caused by the higher mass flow through the funnel for smaller particles.

The comparison between the contact surfaces clearly shows that they have an influence on the transport speed. The residence time of the particles increased for all particle types with increasing roughness of the plate. It should be noted that the Al_2O_3 surface is an insulation board, which is perceptibly rougher

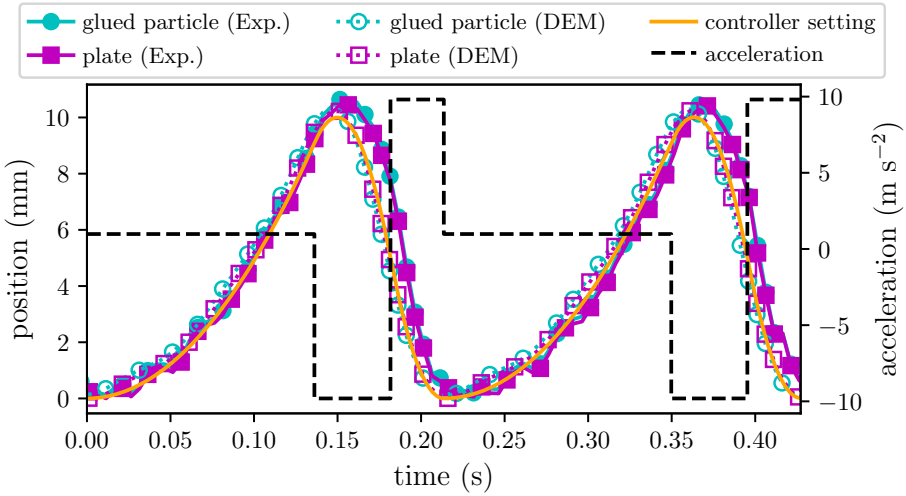

Figure 5.7: Motion profile of horizontal conveyor

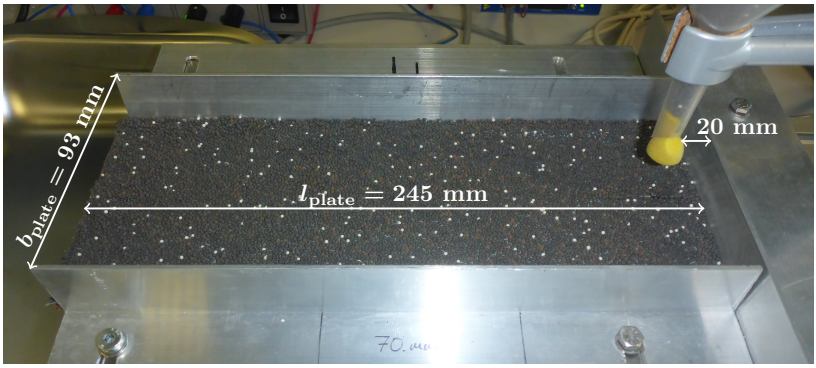

Figure 5.8: Horizontal conveyor laminated with SG10H particles

than the steel plate.

5.2.1.3 Plate impact experiment

As it will be shown in section 5.2.2, the previous experiments are almost insensitive to particle-particle or particle-wall restitution coefficients. Therefore an experiment was designed to be especially sensitive to these two parameters. Figure 5.10 shows the apparatus of the experiment on the left and the

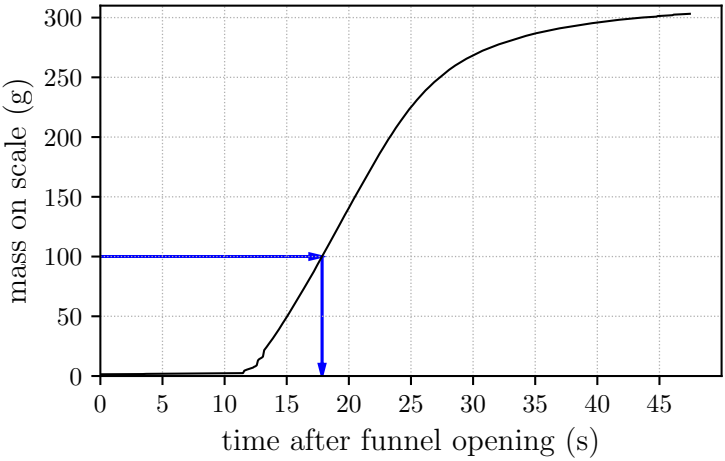

Figure 5.9: Mass of Carbo HSP13 particles on scale, after transporting them via the horizontal conveyor (laminated with the same particles)

Table 5.4: Results of horizontal conveyor experiments. Time to reach 100 g on scale for a plate surface made of steel ($t100_{\mathrm{S}}$), made of alumina ($t100_{\mathrm{Al2O3}}$) and made of fixed particles ($t100_{\mathrm{glued}}$)

Name	$t100_{\mathrm{S}}$ [266]	$t100_{\mathrm{Al2O3}}$ [266]	$t100_{\mathrm{glued}}$
Carbo HSP13	10.13 s ± 0.06 s	11.59 s ± 0.10 s	17.90 s ± 0.02 s
SG10H	9.99 s ± 0.06 s	12.71 s ± 0.11 s	15.99 s ± 0.12 s
Carbo HSP16/30	9.73 s ± 0.07 s	11.87 s ± 0.04 s	15.55 s ± 0.13 s
Carbo HSP20/40	9.31 s ± 0.07 s	11.18 s ± 0.02 s	14.22 s ± 0.06 s
Carbo HSP30/60	9.18 s ± 0.01 s	11.40 s ± 0.07 s	13.39 s ± 0.06 s

corresponding DEM model with the dimensions on the right. The examined particles are filled into the funnel (1), fall through the pipe (2) and hit a 45° inclined plate of the wall material (3). The particles are deflected by the plate and fall either in one of the four plastic boxes (4) or beside them. The masses in the respective boxes are weighted. Every experiment is repeated five times to determine the standard error of the mean. The results are listed in table 5.5. Experiments on the porous alumina insulation board were only conducted with the Carbo HSP13 particles. The other particle types were omitted because the calibration results on steel indicated that the restitution coefficients will not

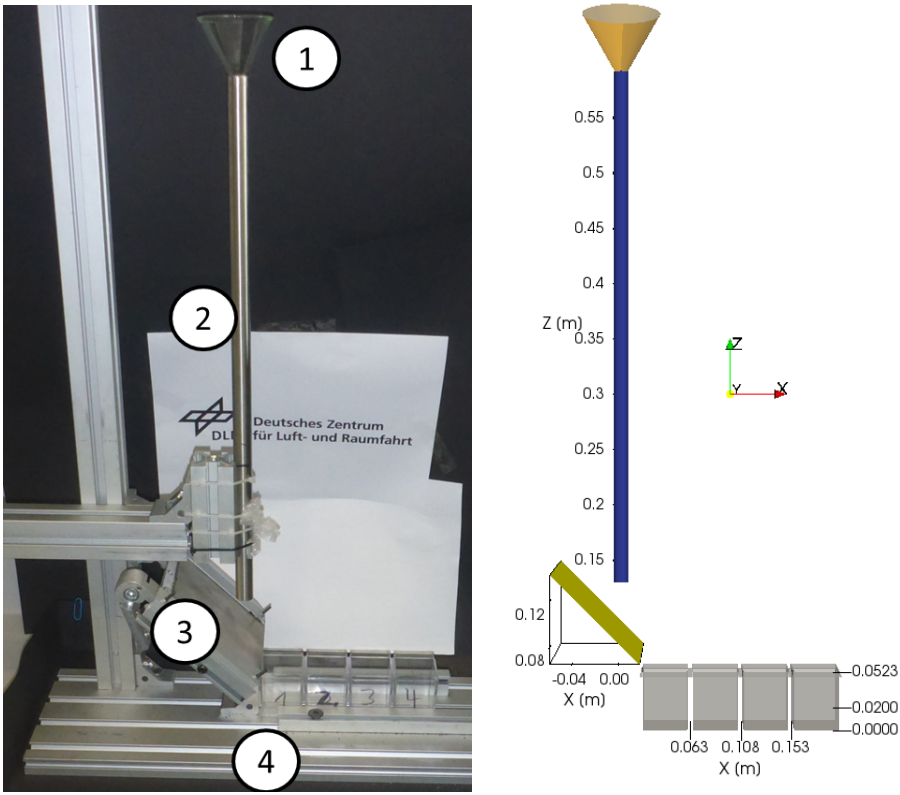

Figure 5.10: Setup of plate impact experiment (left) and simulation (right)

differ much between particle types.
In the DEM representation of the experiment, it was assured to exactly reproduce the geometry of the collection boxes. For the simulations one has to assume a restitution coefficient between the particles and the plastic boxes, which is a possible error source. To assess its influence, the restitution coefficient of the plastic was varied in preliminary simulations and the impact was found to be negligible.

5.2.2 Sensitivity studies

To develop a calibration procedure, sensitivity studies with the DEM models of each experiment were conducted for the Carbo HSP13 particles. The

Table 5.5: Results of plate impact experiments

Particles	Wall	Initial mass (g)	m_1 (g)	m_2 (g)	m_3 (g)	m_4 (g)
Carbo HSP13	steel	68.73	30.21 ±0.15	8.5 ±0.09	2.74 ±0.04	0.55 ±0.03
SG10H	steel	33.79	12.79 ±0.09	6.3 ±0.05	1.58 ±0.05	0.25 ±0.01
Carbo HSP16/30	steel	34.83	10.9 ±0.18	6.34 ±0.04	2.57 ±0.14	0.61 ±0.05
Carbo HSP20/40	steel	30.87	12.47 ±0.09	4.94 ±0.02	1.42 ±0.03	0.26 ±0.01
Carbo HSP30/60	steel	17.64	5.84 ±0.08	4.46 ±0.03	1.17 ±0.07	0.14 ±0.01
Carbo HSP13	Al2O3	68.73	38.12 ±0.24	7.89 ±0.08	1.26 ±0.03	0.3 ±0.03

parameters were set to the baseline values in table 5.6 and then each of the parameters was varied while the others were kept constant.

Table 5.6: Baseline parameters for sensitivity study of calibration experiments, for a description of the parameters see table 5.2

Y	ν	e_{pp}	e_{pw}	μ_{pp}	μ_{pw}	$\mu_{\mathrm{R,pp}}$	$\mu_{\mathrm{R,pp}}$
5 MPa	0.3	0.6	0.6	0.35	0.35	0.2	0.2

5.2.2.1 Angle of repose

The sensitivity of the angle of repose simulation on the contact parameters is shown in figure 5.11 for the case where particles are glued to the ground (left) and for a flat ground of steel or alumina (right). Particle-wall coefficients are not shown if particles are glued to the ground, because then particles are only in contact with other particles and hence the particle-wall coefficients are irrelevant. All curves are not very smooth due to a natural variation in the angle of repose, which occurs because single particles can cause avalanches slightly changing the resulting angle [268]. Both on the glued particles and on the flat surface, the restitution coefficients have significant smaller influence on the angle of repose (AOR) than the friction coefficients. The fact that the influence of the particle-particle restitution coefficient e_{pp} is stronger on glued

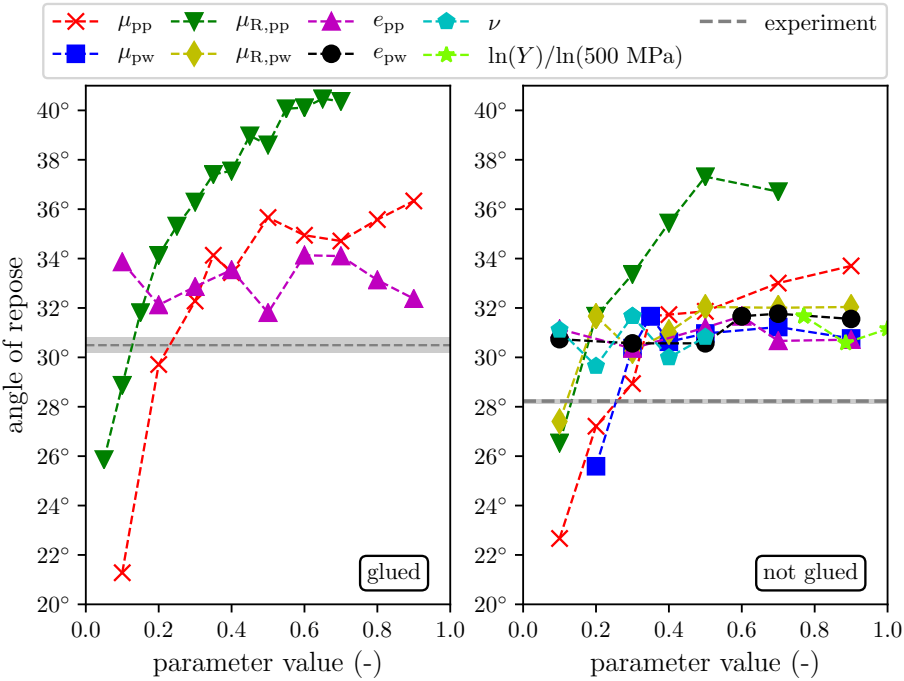

Figure 5.11: Sensitivity of angle of repose simulations to contact parameters. Left: with particles glued to the ground, right: particles on flat ground (not glued). Experimental values of Carbo HSP13 particles shown for comparison

particles could be explained by the immobility of the first particle layer. The particles in this layer cannot obtain momentum so that more momentum stays with impacting particles than it would be the case if the particles were not glued to the ground.

The strong influence of both the rolling and static friction coefficients could be expected from findings in the literature [145, 269]. The rolling friction was found to be essential to build a pile. Without rolling friction no pile could be formed. This is also reported by Grima et al., who state that a particle-particle rolling friction value of 0.2 is necessary [149]. A minimum particle-wall friction coefficient was also required to build a pile. This is interesting, as in many studies in literature, only the particle-particle contact parameters are calibrated and the respective ones between particles and walls are arbitrary. In the review of Coetzee [150], 21 of the listed papers containing a form of the

angle of repose experiment had the particle-particle sliding friction coefficient as a calibration parameter, but only three the particle-wall sliding friction coefficient.
Since there is a dependence on all friction coefficients, several combinations of them exist to match the measured angle. To constrict the variables, the shape of the pile [149] or the funnel discharge rate [269] could be added as target values. The alternative is to add additional experiments [150], also sensitive to friction values, as it was done here with the horizontal conveyor experiment.

5.2.2.2 Horizontal conveyor

Figure 5.12 shows the sensitivity of the horizontal conveyor simulation to the model parameters. The case with the glued particles on the plate is shown on the left and the case of particles on a the flat surface on the right. In this

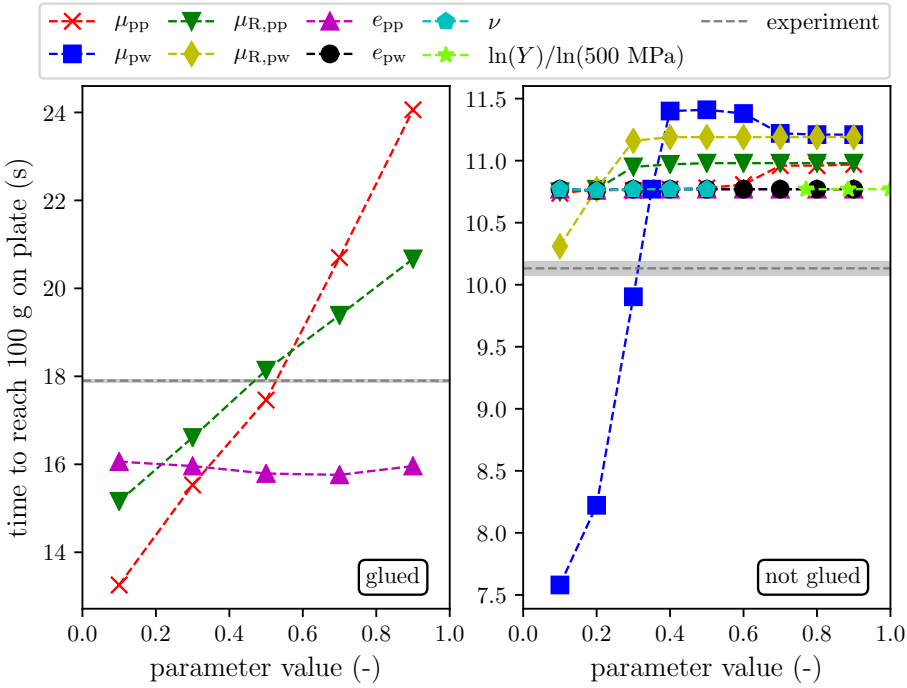

Figure 5.12: Sensitivity of horizontal conveyor simulations to contact parameters. Left: with particles glued to the plate, right: particles moving on a flat surface. Experimental values of Carbo HSP13 particles shown for comparison

case the time to transport 100 g to the scale is taken as an indicator for the influence of the contact parameters on the simulation. Both with particles glued to the ground and on a flat conveyor surface the restitution coefficients e_{pp} and e_{pw} have basically no influence on the transportation speed. If particles are glued to the plate, increasing the particle-particle sliding friction μ_{pp} or rolling friction $\mu_{\mathrm{R,pp}}$ leads to an increasing particle residence time on the plate, whereas these coefficients only barely have an influence if particles are transported on a flat surface. In this case the strong sensitivity on the particle-wall friction coefficient μ_{pw} is obvious. The other friction coefficients show very little influence, mostly the particle-wall rolling friction $\mu_{\mathrm{R,pw}}$ in the range between 0.1 and 0.3.
These results are reasonable, as particles on oscillating plates often behave similar to a solid body [267]. If the plate surface is smooth, the bulk of particles slides along this surface, so that mostly the particle-wall coefficient influence the transport speed. In case of a rough surface, a layer of particles on the wall is established and the remaining bulk of particles glides on this first layer. This was also seen in experiments performed with sandpaper on the plate. With the glued particles to the plate this behavior is ensured.

5.2.2.3 Plate impact

In the sensitivity study of the plate impact setup the dependence of the masses in the boxes on the restitution coefficients e_{pp} and e_{pw} is clearly visible, as depicted in figure 5.13. For the mass in the first box, both the restitution coefficients e_{pp} and e_{pw} have a strong influence, while for the mass in the other boxes the particle-particle restitution coefficient e_{pp} has a negligible influence in contrast to the particle-wall coefficient e_{pw}. This behavior makes sense, as above the first box particle-particle contacts are significantly more frequent than above the other boxes. The pure change of direction caused by a particle-particle hit makes it very unlikely for a particle to reach boxes 2-4, regardless of the restitution coefficient e_{pp}, whereas for box one e_{pp} clearly affects if the particle will fall into the box or not. One can also see a steep peak in the particle-wall restitution curves for box 2-4. With increasing e_{pw} the particles first do not reach the box until they hit the closer box wall and some of the particles fall into the box. This corresponds to the left side of the peak. When the particles hit the center of the box, the top of the peak is reached and on the decreasing slope the particles tend to hit rather the back wall of the box and more and more particles fly too far.
Beside the particle-wall restitution coefficient, for boxes 2-4 a strong dependence on the particle-wall friction coefficient stands out, which is not the case for the first box. A possible reason for this behavior is the change of energy,

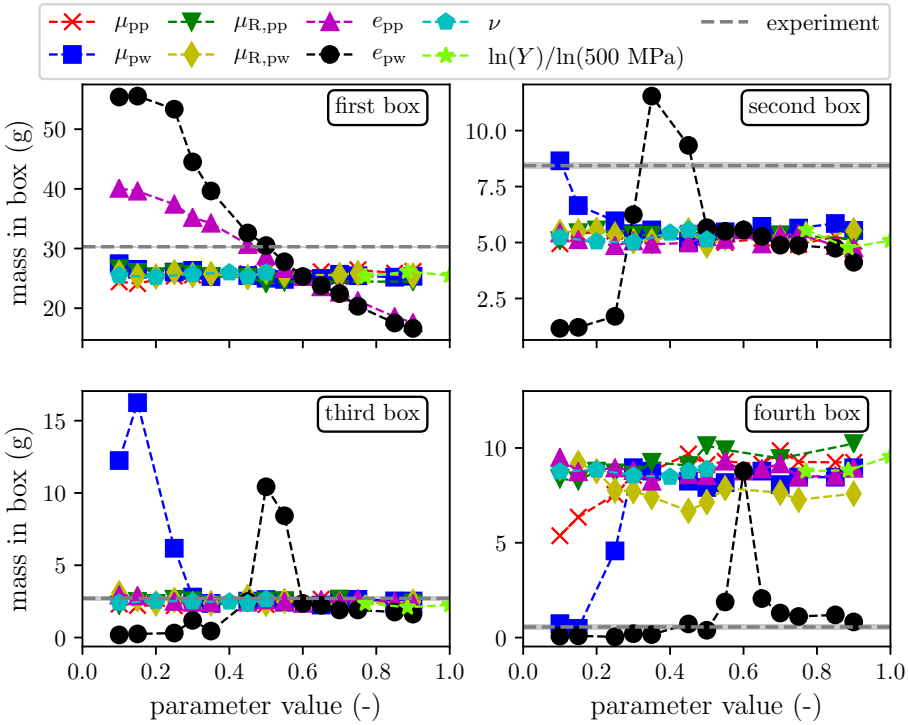

Figure 5.13: Sensitivity study of plate impact simulations to contact parameters, experimental value of Carbo HSP13 particles on steel shown for comparison

which is dissipated both at the walls of the tube during the fall of the particles and at the plate during the impact. However, this strong dependence is only seen for very low friction values, which lay in a rather unrealistic low range, as one can expect from the horizontal conveyor sensitivity study. Therefore we have four target values depending in a different way on two parameters so that this experiment is well suited to isolate the restitution coefficients.

5.2.2.4 Influence of Young's modulus and Poisson's ratio

Figures 5.11, 5.12 and 5.13 also show the sensitivity of the numerical experiments on the modulus Y and on Poisson's ratio ν. For the angle of repose setup, the sensitivity is not exceeding the natural variation caused by the avalanches and also for the other setups the sensitivity to these parameters

is very small. Therefore the softening of the particles is a valid approach to reduce the simulation time and it is justified to exclude Y and ν from the calibration. It is assumed that also a solar receiver simulation will not be very sensitive to these parameters.

5.2.3 Calibration procedure

To perform the actual calibration, many approaches exist. The most naïve one would be to cover the whole parameter space with DEM simulations and choose the parameter set which fits best to all experiments. But if many parameters are involved, the parameter space is very large and this approach is not feasible. More intelligent approaches are based on neural network [270] or genetic algorithms [271]. The calibration procedure in this work was inspired by the calibration framework DEcalioc [272], which was made available to the public. This tool performs a multi-variable, multi-objective optimization in two steps: first, an optimization with surrogate models built by Latin hypercube sampling (LHS) of the DEM models; second, a Levenberg-Marquardt optimization with the real DEM models and the results of the first optimization stage as the starting point. The framework was tested in a preliminary study [266]. It was found that the first optimization stage already provides a good parameter set and the second stage of the optimization shows little or no improvement at all. This was explained by the discrete character of the DEM simulations which can lead to steep gradients or no gradient at all when the optimization algorithm builds the Jacobian matrix within the Levenberg-Marquardt algorithm. Besides the little benefit of the second stage it is computationally costly as it requires DEM model evaluations to calculate the derivatives in the Jacobian matrix and new function values.

Therefore it was decided to follow an own calibration approach, which is depicted in figure 5.14. It consists of three stages, in each of these stages two of the six unknown contact parameters are determined. Each stage starts with a Latin hypercube sampling (LHS) of the respective DEM models. In the LHS, the possible range of each parameter is split into the same number of subintervals and samples are randomly created in a way that each subinterval contains only one sample point. In two dimensions like here, it can be visualized by a chess board with rooks, which cannot take each other. From the results at the sample points surrogate models of the DEM models, more precisely Kriging models of the contact parameters $\mathbf{p}$, are created. This is done in the same way as in DEcalioc (universal Kriging with linear trend and anisotropic Matérn-Covariance, for more details see [272]). From the surrogate models $f_i(\mathbf{p})$, the residuals Res_i to the experiment for the i-th target value $y_{\mathrm{Exp},i}$ are

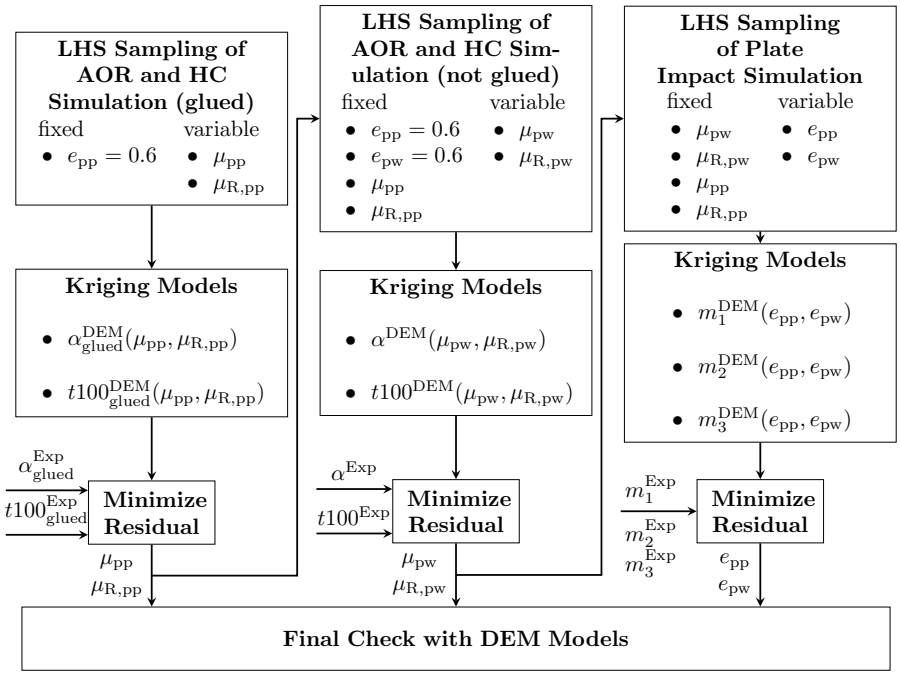

Figure 5.14: Calibration procedure

constructed:

$$Res_i = \frac{f_i(\mathbf{p}) - y_{\mathrm{Exp},i}}{y_{\mathrm{Exp},i}} \quad . \tag{5.7}$$

Their quadratic sum is then minimized to give the contact parameters at each stage.

In the first stage, these contact parameters are the particle-particle sliding and rolling friction coefficients μ_{pp} and $\mu_{R,pp}$. The angle of repose and horizontal conveyor experiments with the glued particles are mainly dependent on these parameters, so that their results are taken as target values and surrogate functions of DEM models of these experiments are created. The only remaining parameter needed for the simulations of the experiments is the particle-particle restitution coefficient e_{pp}, which is kept constant at this stage as it only has a minor influence.

In the following second stage the angle of repose and the horizontal conveyor experiment on a flat surface is used to determine the particle-wall rolling and sliding friction coefficients μ_{pw} and $\mu_{R,pw}$. The particle-particle friction coef-

ficients are taken from the first calibration stage. The restitution coefficients have no influence as shown in the sensitivity analysis, so that it is reasonable to keep their values fixed.
In the final third stage, the plate impact experiment delivers the particle-particle and particle-wall restitution coefficients e_{pp} and e_{pw}. In contrast to the two previous stages, where there were two target values to determine two parameters, the plate impact experiment offers the four masses in the boxes as target values to determine two parameter values. As we will see in the result section, we need three of them. As the mass in box four has the highest measurement uncertainty, the masses in the first three boxes were chosen.
The presented calibration approach in stages has the following advantages over the simultaneous calibration:

- Significantly less simulations are needed to build accurate two-dimensional surrogate models than 6D models.
- The 2D surrogate models can be visualized easily which is not possible with 6D models.
- The global search for initial values for the minimization of the residuals is computationally very expensive in six dimensions.

The only disadvantage of the calibration in stages is the assumption of certain parameters to be constant in each stage. For example, the particle-particle restitution coefficient e_{pp} has an minor influence on the outcome of the angle of repose and horizontal conveyor simulations, but is kept constant in the first two stages. Besides this, for both the simultaneous and the stage approach the use of surrogate models instead of the DEM models for the minimization introduces an error. Therefore, at the end of the calibration process, the results are checked by running the DEM models with the gathered parameters and the deviations from the target values are determined.

5.2.4 Calibration results

In calibration stage one, a LHS of the angle of repose and horizontal conveyor experiment with glued particles was conducted with 100 sampling points in the parameter range $[\mu_{\mathrm{pp}}, \mu_{\mathrm{R,pp}}] \in [0.1, 0.8] \times [0.05, 0.6]$ to obtain the Kriging functions shown in figure 5.15. The contour plot of the angle of repose simulation is similar to the one shown by Wensrich et al. [145]. The angle of repose increases with both rolling and sliding friction coefficients, even extreme angles can be obtained with high values of these coefficients. The horizontal conveyor simulation mainly shows a dependence on the sliding friction coefficient

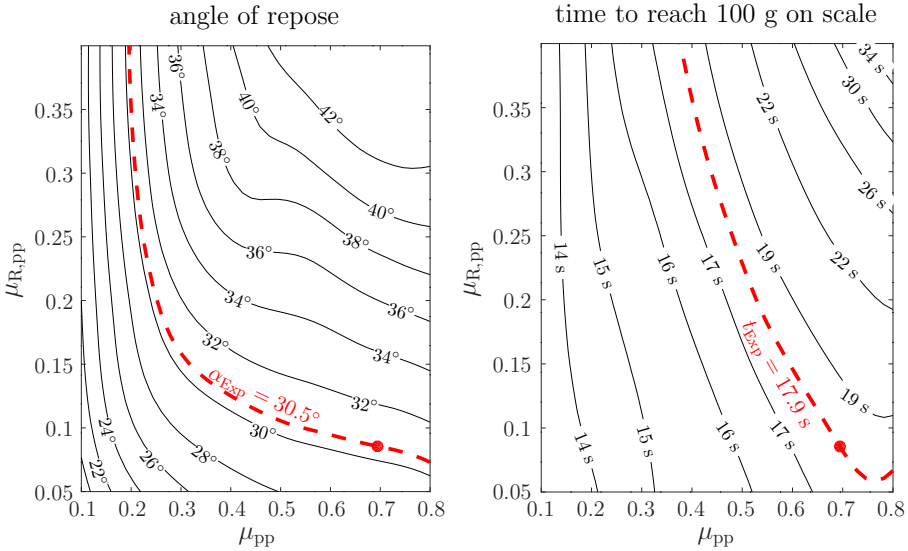

(a) Angle of repose on a surface laminated with particles

(b) time to transport 100 g to the scale via the horizontal conveyor with glued particles on its surface

Figure 5.15: Contour lines of the two Kriging functions in calibration stage 1 for Carbo HSP13 particles, each function generated from 100 sample points of the respective DEM simulation. The intersection point of the dashed experimental target value contour lines is marked with a dot

as expected from the sensitivity study. However, for higher sliding friction coefficients the rolling friction coefficients have more and more importance.
The contour lines of the experimental target values are highlighted with the dashed red lines. The intersection of these lines from the angle of repose and horizontal conveyor experiment gives the rolling and sliding friction coefficients between the particles, indicated by a red dot. The curves only intersect at one point and measurement errors would not alter this intersection point very much. It can be concluded that this first calibration stage with the glued particle surfaces is well suited to determine μ_{pp} and $\mu_{R,pp}$.
The experiments and models for the second stage are the same, except that no particles are glued to the contact surfaces. Thus the sliding and rolling friction coefficients μ_{pw} and $\mu_{R,pw}$ between the particles and the contact surfaces affect the result. Based on the LHS of the DEM models, the Kriging func-

tions created this time had these two coefficients as variables. The respective ones for the angle of repose and the for the transport time on the horizontal conveyor are shown in figure 5.16 for the Carbo HSP13 particle size. The particle-particle parameters were taken from the first calibration stage and the restitution coefficients were set to the fixed value of 0.6, as they have minor influence.

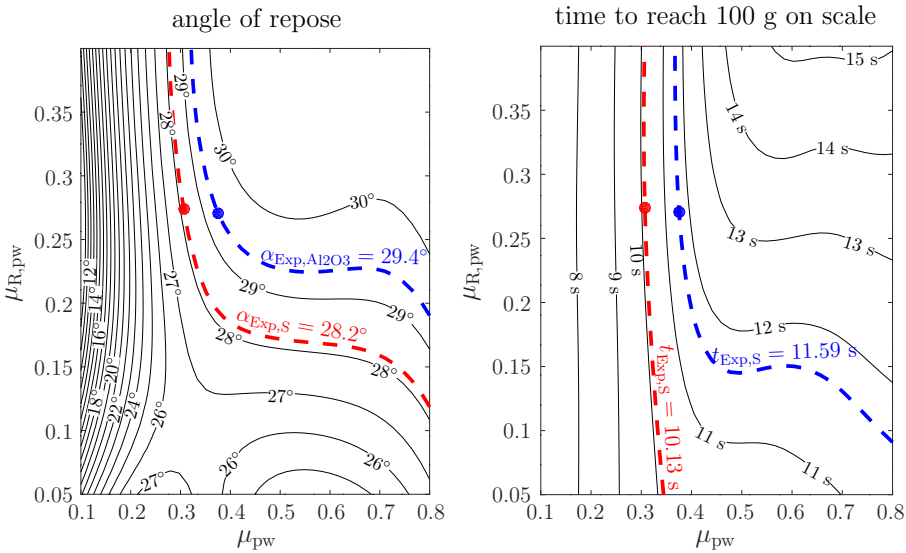

(a) Angle of repose on a flat surface

(b) time to transport 100 g to the scale via the horizontal conveyor with flat surface

Figure 5.16: Contour lines of the two Kriging functions in calibration stage 2 for Carbo HSP13 particles, each function generated from 100 sample points of the respective DEM simulation. The intersection point of the dashed experimental target value contour lines is marked with a dot

The contour plot for the angle of repose shows some different characteristics than the previous plot for a glued particle surface and the particle-particle coefficients. In general, if both the particle-wall sliding and rolling friction coefficient are high, the base of the pile is stable and the pile angle is determined by the particle-particle friction coefficients μ_{pp} and $\mu_{R,pp}$. Here, for example, the maximum angle is just above 30.5°, which is the target value of calibration stage one. If one decreases either μ_{pw} or $\mu_{R,pw}$ below a certain value, the base of the pile breaks down and the wall parameters have an impact on the

angle of repose. This happens most noticeably for sliding friction coefficients $\mu_{\mathrm{pw}} < 0.3$, where the rolling friction $\mu_{\mathrm{R,pw}}$ has minor influence. Above a value of 0.3 the impact of μ_{pw} is not so dominant anymore and the rolling friction $\mu_{\mathrm{R,pw}}$ stronger influences the angle of repose.
The horizontal conveyor simulation is barely influenced by $\mu_{\mathrm{R,pw}}$ if the sliding friction μ_{pw} is below about 0.35. If the sliding friction is above this value, increasing the rolling friction leads to a higher particle residence time on the plate and the sliding friction has only minor influence.
The DEM models are the same for different contact surfaces, so that both the target values for steel and alumina are drawn as dashed lines into the same plot. Both intersection points are in a region where the gradient of both the angle of repose and the transport time on the plate is bigger in the direction of the sliding friction coefficient μ_{pw} than in the direction of the rolling friction coefficient $\mu_{\mathrm{R,pw}}$. Therefore the reliability of the gathered sliding friction coefficient can be considered higher than the one of the rolling friction coefficient. Nevertheless, the rolling friction value is almost the same for both contact materials, which can make sense, as both contact surfaces are flat and the particle shape is also the same.
In the third calibration stage, a LHS of the plate impact simulation was performed with restitution coefficients $[e_{\mathrm{pp}},e_{\mathrm{pw}}] \in [0.2,0.9] \times [0.2,0.9]$. For the Carbo HSP13 particle size this leads to the Kriging functions for the box masses shown in figure 5.17. As expected from the sensitivity analysis, the Kriging surface for the first box looks essentially different from the Kriging surfaces of the other boxes. In the entire parameter range, the mass in the first box is reduced if either the particle-particle or the particle-wall restitution coefficient is increased. This is not the case for the other boxes; here only the particle-wall restitution coefficient e_{pw} is the deciding parameter. Also, there is a steep peak in the Kriging surfaces for theses boxes. The experimental target value, in this case for steel and indicated by a dashed red line, is always close to this peak and could be on either side of it. To decide on which side, two of the boxes 2-4 need to be included in the analysis. Here boxes 2 and 3 were taken and it is clear, that this leads to a particle-wall restitution coefficient around 0.43. As the mass in box 1 is sensitive to e_{pp}, it was possible to determine both restitution coefficients with this experiment.

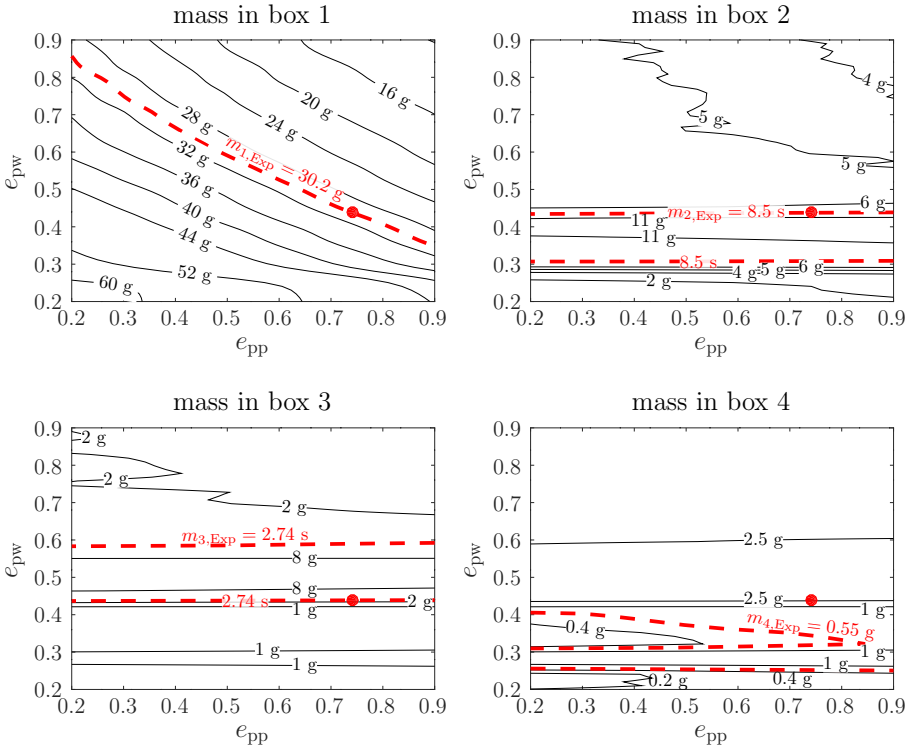

Figure 5.17: Contour lines of the Kriging functions in calibration stage 3: masses in the boxes of the plate impact simulation, shown for Carbo HSP13 particles. Generated from 300 sample points of the plate impact DEM simulation. The intersection point of the dashed experimental target value contour lines for steel as wall material is marked with a dot

The calibration results of all particles are summarized in table 5.7. The rolling friction values of all particles are by about a factor of 3 lower between the particles than between a particle and a wall. This makes sense, as one can imagine that a particle rolls easier on the convex surface of another particle than on flat ground. As mentioned, the particle wall rolling friction $\mu_{R,pw}$ is hard to determine in calibration stage two; above a value of about 0.3 the simulations are not very sensitive to this parameter anymore, which is considered the reason of the variation in $\mu_{R,pw}$ between particle types. In some cases, the contour lines of the angle of repose and the horizontal conveyor simulation did not intersect

Table 5.7: Results of the three-stage parameter calibration process

		μ_{pp}	μ_{pw}	$\mu_{R,pp}$	$\mu_{R,pw}$	e_{pp}	e_{pw}
Carbo HSP13	Steel	0.69	0.31	0.09	0.27	0.74	0.44
	Al2O3		0.38		0.27	0.78	0.30
SG10H	Steel	0.53	0.31	0.16	0.38*	0.46	0.43
	Al2O3		0.41		0.40†		
Carbo HSP16/30	Steel	0.61	0.30	0.12	0.42	0.77	0.44
	Al2O3		0.38		0.30		
Carbo HSP20/40	Steel	0.71	0.29	0.09	0.45*	0.89	0.45
	Al2O3		0.36		0.49†		
Carbo HSP30/60	Steel	0.72	0.30	0.13	0.50*	0.82	0.44
	Al2O3		0.39		0.42		

* : no intersection of contour lines

† : simulation of AOR was in all points too low

in calibration stage two. The values of μ_{pw} and $\mu_{R,pw}$ are obtained by taking the closest distance between the contour lines in this case. Due to the high sensitivity of the horizontal conveyor experiment to μ_{pw} (almost vertical line in figure 5.16) its value could still be determined accurately. There was also no intersection point or better not even an experimental AOR contour line when the target angle of repose from the experiment could not be reached by the surrogate model. This happened when the measured angle of repose on the alumina board was slightly higher than on the surface with the glued particles. In both of these experiments the base of the pile is stable and the pile angle is only controlled by particle-particle friction. As μ_{pp} and $\mu_{R,pp}$ come from the first calibration stage, the maximum angle of repose in the second calibration stage ideally is the target angle from stage one.

The sliding friction coefficient to a wall μ_{pw} is very similar among different particle types. With a value between 0.36 and 0.41 it is for all particles higher on the alumina insulation board than on steel with a value between 0.29 and 0.31. This was expected from the sensitive roughness of the materials. The sliding friction between the particles μ_{pp} is essentially higher than between particles and both wall materials μ_{pw}. This could be assumed from the horizontal conveyor experiments without glue, because no fixed first particle layer developed. It is hard to tell what causes the large difference between μ_{pp} and μ_{pw}. The particles have a ceramic surface as the alumina board, probably their shape has an impact on the sliding friction coefficient, too. Interesting to note is the relatively large difference in μ_{pp} between the SG10H particles from the company Saint Gobain to the other particles produced by CarboCeramics.

This is attributed to the different surfaces of the particles, which can be seen in the microscopic images in figure 5.1.

The particle-wall restitution coefficients e_{pw} on steel are with values between 0.43 and 0.45 very similar between the different particle types. As e_{pw} did not change significantly between particle types for steel as contact parameter, for the alumina insulation board it was decided to calibrate it only for the Carbo HSP13 particles. On the insulation board e_{pw} has a value of 0.3, which is clearly lower than on steel with 0.44. The results are in accordance with preliminary high-speed camera tests with single particles, which also showed a lower restitution coefficient on the insulation board.

The particle-particle restitution e_{pp} shows more variation between particle types than e_{pw}. There is a significant difference between the SG10H particles from Saint Gobain and the other particles from Carbo Ceramics: The Carbo Ceramics particles have a particle-particle restitution coefficient between 0.74 and 0.89, while it is 0.46 for the SG10H particles. This probably relates to the different surface as discussed above for the particle-particle friction coefficient. Ideally, both the calibration with steel and with the insulation board as contact partner should result in the same particle-particle restitution coefficient e_{pp}. Here the value of 0.776 for the Carbo HSP13 particles on the insulation board is close to 0.742 on steel, which confirms the results.

Since the calibration was done in stages and based on surrogate models, the results were finally checked with the DEM models. DEM simulations of the calibration experiments were conducted with the final parameter sets and the deviations from the experimental values were obtained. They are listed in table 5.8. For the angle of repose and the horizontal conveyor experiments both with and without glued particles to walls they are mostly below 4 %, the maximum is a angle of repose deviation of −8.4 %. It must be noted that the angle of repose has some natural variance, as avalanches can be formed and single particles can cause the angle to differ noticeably. The mass in box 1 in the plate impact experiment also shows little deviation, whereas the masses in boxes 2 and 3 significantly differ, in one case by almost 60 %. This is caused by the high gradient with respect to the wall restitution coefficient e_{pw} in the DEM model for boxes 2 and 3, which can be seen in figure 5.17 for the Carbo HSP13 particles. The target value from the experiment is just on the edge of the peak; a small change in e_{pw} causes a large increase or decrease in the mass in the boxes. This high sensitivity to e_{pw} was a desired feature of the plate impact experiment. It is expected that the surrogate model for the masses in boxes 2 and 3 has large deviations from the DEM model near the peak position, because the peak is very narrow and hence only sampled by a few points during the Latin hypercube sampling. However, the high sensitivity also implies that large deviations in the masses in boxes 2 and 3 can be accepted as

long as the peak position is represented correctly. This is expected to be the case for the given deviations if one compares their magnitude with the contour levels in figure 5.17. Hence the obtained values for e_{pw} are considered to be reliable.

Table 5.8: Final check of calibration results: deviations of DEM simulations of the calibration experiments from the experimental values when the simulations are conducted with the final parameter sets

		angle of repose		transport time on horizontal conveyor		masses in boxes in plate impact simulation		
particles	wall	α_{glued}	α	$t100_{\mathrm{glued}}$	$t100$	m_1	m_2	m_3
Carbo HSP13	Steel	1.4 %	0.1 %	−1.3 %	−0.2 %	0.7 %	40.5 %	−52.3 %
	Al2O3		−2.9 %		0.1 %	−0.4 %	−19.2 %	2.1 %
SG10H	Steel	3.1 %	−3.5 %	−1.2 %	1.5 %	−3.4 %	59.2 %	14.0 %
	Al2O3		−3.0 %		−0.1 %			
Carbo HSP16/30	Steel	1.2 %	−3.3 %	−1.3 %	2.0 %	1.0 %	12.4 %	0.5 %
	Al2O3		−3.5 %		−0.2 %			
Carbo HSP20/40	Steel	−1.4 %	−0.0 %	−4.0 %	2.0 %	−5.2 %	−30.1 %	−5.6 %
	Al2O3		−8.4 %		0.1 %			
Carbo HSP30/60	Steel	0.1 %	−6.2 %	−2.8 %	1.1 %	−10.2 %	−19.3 %	−10.1 %
	Al2O3		−1.7 %		−0.1 %			

5.2.5 Coarse graining

As described in section 3.6 coarse graining is useful to speed up the simulation. The contact parameters must be adapted in this case.
This was done here by increasing the particle diameter in the DEM setups leading to the Kriging functions in the calibration. Some phenomena are difficult to describe by coarsed grained particles, especially the flow within narrow gaps, for example through the funnel of the angle of repose experiment. In the simulations the funnel was therefore replaced by an insert region with the same mass flow and exit velocity as the funnel. All simulations were performed with exactly the same masses and mass flows. If the coarse-graining factor

$$CG = \frac{d_{\mathrm{Sim}}}{\overline{d}_{32,\mathrm{Exp}}} = \frac{d_{\mathrm{p}}^*}{d_{\mathrm{p}}} \tag{5.8}$$

is high, it causes some inaccuracies in the post processing, for example in the angle of repose determination as the pile surface is not so smooth anymore. Therefore only moderate CG factors were investigated: particle diameters d_{p}^* of 2 mm, 2.5 mm and 3 mm were used for the calibration of the Carbo HSP13 particles instead of the real size diameter d_{p} of 1.6 mm.

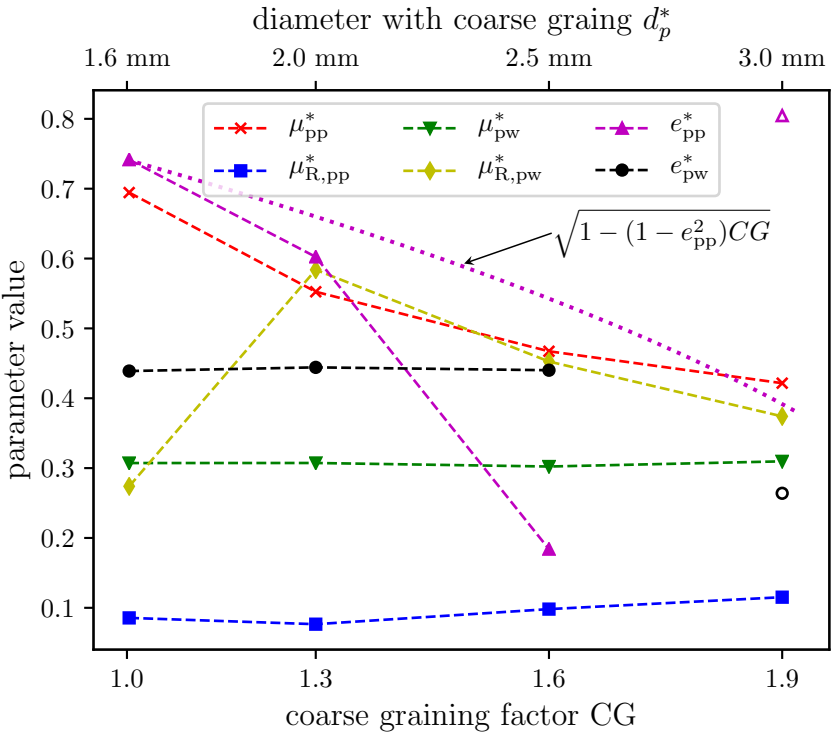

Figure 5.18: Calibration results with coarse-grained particle size

The resulting parameters visualized in figure 5.18 show that the particle-particle sliding friction coefficient μ_{pp}^* drops with increasing CG factor. This is intuitive as bigger particles harder glide above each other in the laminated horizontal conveyor experiment, similar to a surface with higher coarseness. To match the target residence time of the real sized particles, μ_{pp}^* has to decrease with the CG factor accordingly. To still meet the angle of repose then, the particle-particle rolling friction coefficient $\mu_{R,pp}^*$ has to increase, which is overall the case.

The particle-wall sliding friction coefficient μ_{pw}^* basically does not change if coarse graining is applied. This was expected, since this coefficient also barely changed between particle sizes; the particles behave in an arrangement similar to a rigid body on the horizontal conveyor and the size of the particles therefore has little influence on μ_{pw}^*. It also agrees with the literature [157]. Like in the case of real size particles, the particle-wall rolling friction coefficient $\mu_{R,pw}^*$ is

hard to calibrate exactly because the simulations are barely sensitive to $\mu^*_{\mathrm{R,pw}}$ for values above 0.3, so that the trend in the points for $\mu^*_{\mathrm{R,pw}}$ has no special physical meaning.
The particle-particle restitution coefficient e^*_{pp} drops with the CG factor due to less frequent collisions in the coarse-grained case, which should be explained by the kinetic gas theory in the following. The collision frequency of a single particle in the kinetic gas theory is [273]

$$z = \pi d_{\mathrm{p}}^2 \overline{v} \frac{N}{V} \quad , \tag{5.9}$$

where $\overline{v}$ is the average particle velocity and N the number of particles in a volume V. The average particle velocity is assumed to be the same in the coarse-grained simulation to preserve kinetic energy. Since d_{p} scales with CG and N with $1/CG^3$, z scales with $1/CG$. The collision frequency of all N particles is then proportional to $1/CG^4$. The energy dissipation over time due to particle-particle collisions is proportional to the collision frequency of all particles and the energy dissipation per collision, which scales with $1 - e^2_{\mathrm{pp}}$ and the mass of the particle. It follows

$$\frac{\text{energy dissipation due to p-p collisons}}{\text{time}} \sim \frac{1 - e^2_{\mathrm{pp}}}{CG} \quad , \tag{5.10}$$

because the mass of each particle scales with CG^3. If one assumes that energy dissipation over time should remain the same for coarse-grained simulations, e^*_{pp} has to follow the relationship

$$e^*_{\mathrm{pp}} = \sqrt{1 - (1 - e^2_{\mathrm{pp}}) \cdot CG} \quad , \tag{5.11}$$

which is indicated by a dotted line in figure 5.18. The same expression was derived by Lu et al. with similar reasoning [156, 166]. The formula predicts a decline of e^*_{pp}, but less pronounced as it is seen in the curve obtained by the calibration. By the collision frequency with a wall it can be shown in a similar way, that the particle-wall restitution coefficient e^*_{pw} should be independent of CG. This is clearly seen in the results, e^*_{pw} does not alter noticeably when coarse-graining is applied. It should be noted that in other studies the restitution coefficient is considered invariant [160, 168], following the derivation from Bierwisch [167]. In this derivation it is stated that the number of collisions per volume and time scales with $1/CG^3$, which is questionable. The decreasing particle-particle restitution coefficient with coarse graining factor in the present work supports the expectation mentioned in [157] and the derivation by Lu et al. [156, 166].

For a coarse-graining factor of 1.9, the solution of the optimization problem for the plate impact simulation jumps from the valley between peaks of masses m_2 and m_3, which look similar to the ones shown in figure 5.17, to a lower value of e^*_{pw}, because further lowering e^*_{pp} is not possible. It is very questionable if e^*_{pp} and e^*_{pw} would describe other experiments well in this case, so that their values are shown as unconnected, empty markers in figure 5.18.

5.2.6 Concluding remarks

In summary, DEM parameters for two wall materials and five different sorts of bauxite particles were determined with the developed three-stage calibration procedure. Only moderate variations in the resulting parameters were observed among particle types, in particular the sliding friction μ_{pw} and particle-wall restitution e_{pw} barely differed. With ceramic insulation board as contact partner, the particle-wall friction was higher and the particle-wall restitution coefficient lower than on steel, as it was expected. Rolling friction was found to be necessary to describe the motion behavior of the investigated particles. The rolling friction coefficient between a particle and a wall $\mu_{\mathrm{R,pw}}$ is confined to a value above ≈ 0.3, but a precise value can hardly be determined with the calibration approach. In general, the obtained parameters are considered to be reliable due to the consistency of the calibration results with the sensitivity study and findings from literature.
Additionally a study was conducted to provide parameters for coarse-grained simulations. The particle-wall sliding friction μ_{pw} and the particle-wall restitution coefficient e_{pw} were found to be invariant to coarse-graining, while particle-particle friction μ_{pp} and particle-particle restitution e_{pp} decreased with increasing coarse-graining factor. As the restitution coefficient e_{pp} is often assumed to be invariant to coarse graining in the literature, the results were analyzed in detail and could be explained by kinetic particle theory.
The determined parameters for both the real size and coarse-grained particles can be useful for other researchers, as no calibrated parameters for bauxite particles have been published before. If other than Bauxite particles should be used, the developed calibration procedure can be applied to them as well.
Besides the calibration, knowledge about the motion behavior on the horizontal conveyor was gained, which will be useful for future experiments with the receiver shown in figure 2.3.

6 Model Validation and Verification

The content in subsection 6.1.2 of this chapter has already been published by the author of this thesis:
Grobbel, J., Brendelberger, S., et al. "Heat transfer in a directly irradiated ceria particle bed under vacuum conditions." In: *Solar Energy* 158 (2017), pp. 737–745. DOI: `10.1016/j.solener.2017.10.022`.

In this chapter the developed models were tested. The inter-particle conduction model, the radiation model and the particle-wall heat transfer model were validated, meaning that simulation results obtained with the models were compared to experimental results or analytical solutions. The implementation of the chemical reaction model was verified by checking the energy balance in a test case.

6.1 Inter-Particle Conduction Model

The inter-particle conduction model described in section 4.2.1 is validated in multiple steps: First, the proposed way to connect a continuum model with the discrete element method is checked and the constant K_{pp} in the model is determined. Then the applicability of the selected continuum model was validated for a solar receiver environment in a vacuum receiver experiment for low pressures and high temperatures. Finally the coarse graining modifications described in section 4.4 are tested and the validity of the derived time step limit is demonstrated.

6.1.1 Connection between continuum and discrete model

In section 4.2.1 an approach to connect the ZBS continuum model for the effective thermal conductivity of a packed bed with the discrete element method was introduced. The proposed hypothesis in equation (4.10) should be checked here and K_{pp} should be determined for various thermal cutoff distances $C_{\mathrm{cutoff,HT}}$.

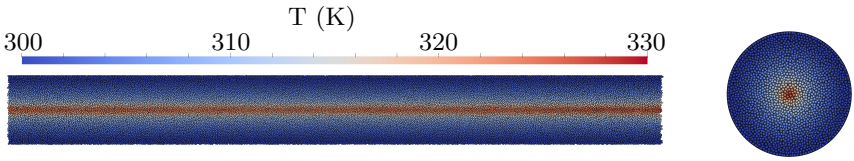

Figure 6.1: Cylindrical bed test case

The cylindrical test case for this purpose is shown in figure 6.1. It consists of a cylindrical particle bed, which has a diameter of $20d_\mathrm{p}$ and a bed height to bed diameter ratio of 10. An artificial heat source is set to all particles in the center region of the particle bed, located within a radius of two particle diameters. All particles in the outside region of the bed, located at a distance more than $17d_\mathrm{p}$ to the center, are set to the fixed temperature 300 K. The top and bottom of the bed are adiabatic, as external radiation is not activated. Due to the high height to diameter ratio and the adiabatic axial ends, it can be assumed that the heat only propagates in radial direction. For this case, the effective thermal conductivity in radial direction can be determined from the steady state case:

$$\lambda_\mathrm{eff} = \frac{\dot{Q} \ln\left(\frac{r_1}{r_2}\right)}{2\pi L \left(T_2 - T_1\right)} \quad . \tag{6.1}$$

In this equation, T_1 and T_2 are temperatures averaged within a thin slab at radius $r_1 = 6d_\mathrm{p}$ and $r_2 = 13d_\mathrm{p}$, which are both neither in the central heat source region nor in the outer fixed temperature region. The heat flow $\dot{Q}$ is obtained by summing up all artificial heat sources of the central particles. Tests with different total conductivities H_t, particle diameters d_p and heat transfer cutoff distances were conducted. The effective thermal conductivities determined by equation (6.1) are shown in figure 6.2 for various particle diameters and a heat transfer cutoff distance of 1.1 particle diameters. As one can see, λ_eff is proportional to H_t as expected for a fixed particle diameter and particle arrangement. The slopes of these curves are extracted and K_pp in equation (4.10) is calculated for various diameters and heat transfer cutoff distances. The mean values averaged over the particle diameters and the deviations to the mean value are shown in figure 6.3 over the particle diameter. The maximum deviation from the mean is about 2 %, so that the hypothesis for K_pp to be constant for a specified heat transfer cutoff distance is considered to be an accurate and reasonable approach.
To be able to compute H_t from the previously calibrated K_pp and the effective bed conductivity λ_eff according to equation (4.10), one needs to know the

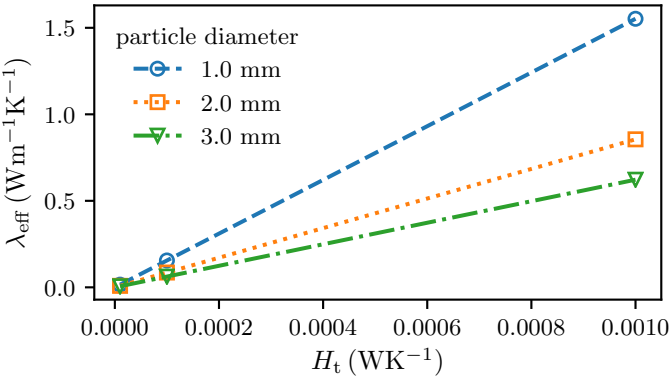

Figure 6.2: Effective thermal conductivity of the bed for various particle-particle total conductances and particle diameters

void fraction. However, as it is a bulk property, it is not available in the DEM software during the computation. Therefore, the local void fraction is obtained from the number of neighbors within the heat transfer cutoff range, which is available anyway so that no costly additional computation is needed. Figure 6.4 shows the correlation between number of neighbors within the heat transfer cutoff range and the void fraction. A linear regression describes the correlation sufficiently. It is also observed that the void fraction decreases with increasing particle diameter. This is because the same contact parameters were used for all particle diameters. As rolling friction has a higher impact on the smaller particles, this causes the packing to be less dense than the packing composed of larger particles.

6.1.2 Continuum model under vacuum and high temperature conditions

In the preceding section it was shown that equation (4.10) is a valid approach to connect a continuum model with the discrete element method. However, the continuum model itself needs to be validated. The selected ZBS continuum model is widely applied and established, but it has never been tested under simultaneous vacuum and high temperature conditions. However, these conditions appear in solar receivers for thermochemical fuel production as described in section 2.1.2. Therefore, the ZBS model was validated for these conditions in scope of this work by comparing temperatures from an irradi-

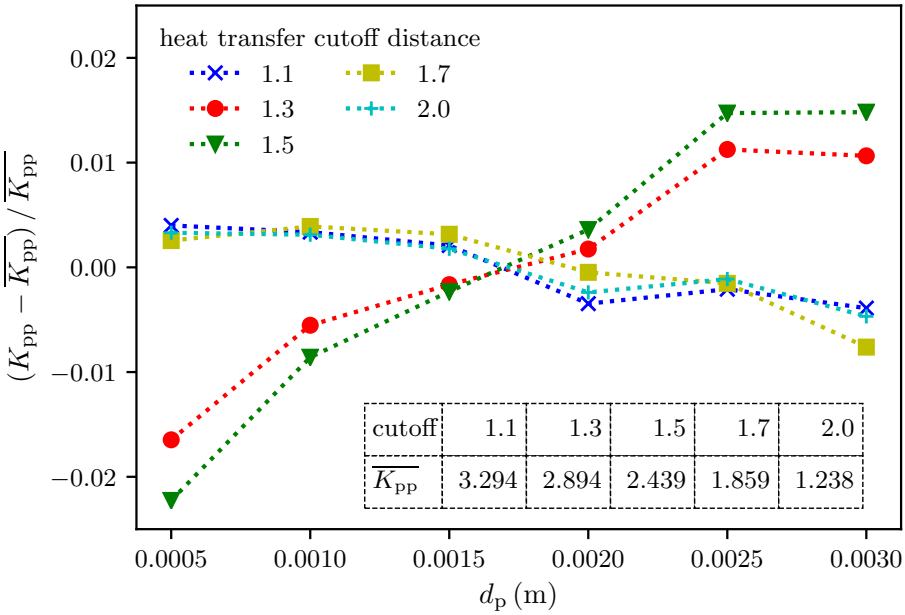

Figure 6.3: Normalized calibration factor over particle diameter for various heat transfer cutoff distances

ated bed experiment with the ones obtained by a continuum simulation using the ZBS model for the bed conductivity. Major parts of this section have been published in [112].

6.1.2.1 Experimental setup

A packed bed of the ceria particles, whose properties have been determined in section 5.1, was placed in a vacuum chamber and irradiated by the DLR high-flux solar simulator in Cologne, Germany. A schematic of the experimental setup is shown in figure 6.5. The concentrated flux of the solar simulator hits a water cooled mirror and is directed downwards through a 32 mm thick quartz glass window into the main vacuum chamber. Within this chamber the flux impinges on a cylindrical bed of ceria particles, which is surrounded by vacuum-formed alumina insulation of cylindrical shape. The insulation itself is surrounded by a water cooled black enclosure to maintain well defined boundary conditions and to protect the vacuum chamber from overheating.

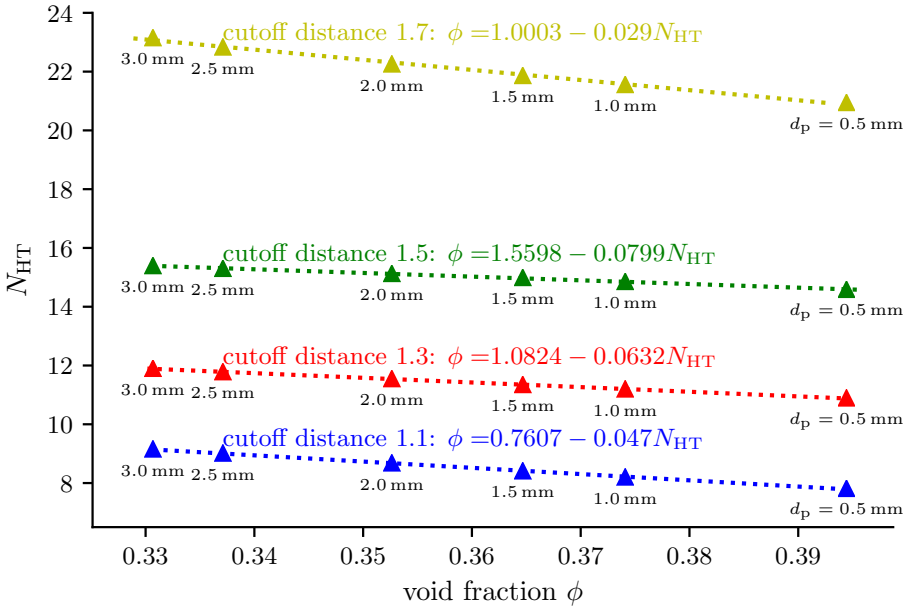

Figure 6.4: Correlations between the number of particles participating in heat transfer N_{HT} and void fraction for different cutoff distances

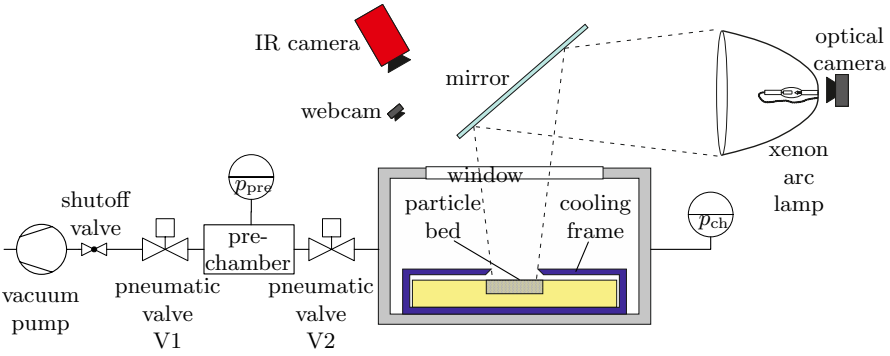

Figure 6.5: Schematic of the experimental setup for the validation of the ZBS continuum model under vacuum and high temperature conditions

Within the particle bed the temperature is measured at various positions in the vertical and radial direction as depicted in figure 6.6. For TC 1 and TC 2 alumina-sheathed type R thermocouples were used, for the others steel-

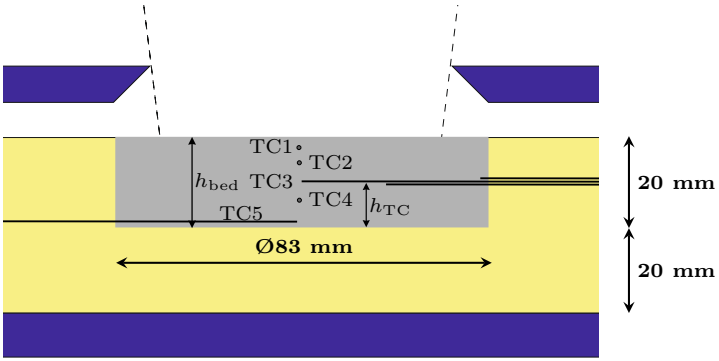

Figure 6.6: Positioning of thermocouples within the particle bed, more dimensions in table A.1

sheathed type K thermocouples with a diameter of 1 mm. They were placed horizontally in the bed and at a circumferential angle of 90° to each other to reduce their influence on the temperature distribution in the bed. The connection to the data acquisition system was established via an electrical feedthrough; therefore the cold junction compensation was made at the plug within the vacuum chamber. To check the complete measurement chain, all thermocouples were tested with a thermocouple calibrator at temperatures of 600, 900 and 1200°C, once before the experiments and once after the experiments to check for temperature drifts. No significant drift was observed and the difference to the reference thermocouple was always below 1 % for all thermocouples used in this study. The vertical positions of the steel-shielded thermocouples in the bed were measured before and after the experimental campaign with a caliper, the uncertainty in the measurement was assumed to be ±0.5 mm. As the fixation of the ceramic-shielded type R thermocouples was more difficult, the uncertainty in their position was expected to be higher. Pictures without particles present were taken over the mirror by an optical camera placed sideways behind the xenon arc lamp to determine the thermocouple positions in the lateral directions relative to the cooling frame. With the same camera pictures and videos of the particle bed surface were taken during irradiation through a radiation protection glass. The bed surface and the cooling frame were monitored by a webcam. Additionally an infrared camera with a filter for glass windows measured the surface temperature of the particle bed. With the filter the camera operates in a spectral range where the window transmissivity is high, so that temperatures of objects behind the window can be determined. To verify that the measurement through the win-

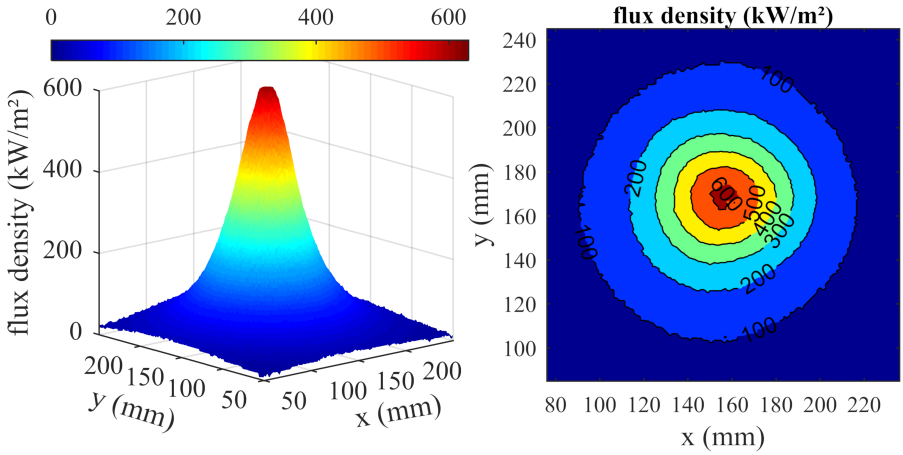

Figure 6.7: FMAS radiation flux measurement for a lamp current of 165 A

dow is possible, preliminary tests were conducted where the temperature of ceria particles in an oven was measured with and without the window present in the optical path; the temperature of the IR camera was also compared with the temperature of a thermocouple which was placed into the particle bed in the oven. These pre-tests showed in general good measurability through the window; for temperatures below 1000 °C the deviation between thermocouple measurement and IR measurement was between 0 and 5 %. However, for higher temperatures the deviations were higher, with a maximum of 13 % for one measurement at an oven temperature of 1350 °C. Therefore it was decided to use the IR measurements just as a qualitative measure and not investigate the deviations further.

Radiation flux measurement A single xenon arc lamp of the solar simulator was used for all experiments. It was driven with three different currents: 100 A, 140 A and 165 A, corresponding to a respective peak flux density of 271, 469 and 602 kW/m^2 or total flux of 0.57 kW, 1.32 kW and 1.84 kW. Two-dimensional flux density profiles were measured with the FMAS measurement system [274] in the plane of the bed surface prior to the actual vacuum experiment, without the reactor or window present. figure 6.7 shows the measured radiation flux for a lamp current of 165 A. As the Xenon arc lamps need some time to heat up and reach their maximum power, the time dependent behavior of the profiles was recorded with a radiometer.

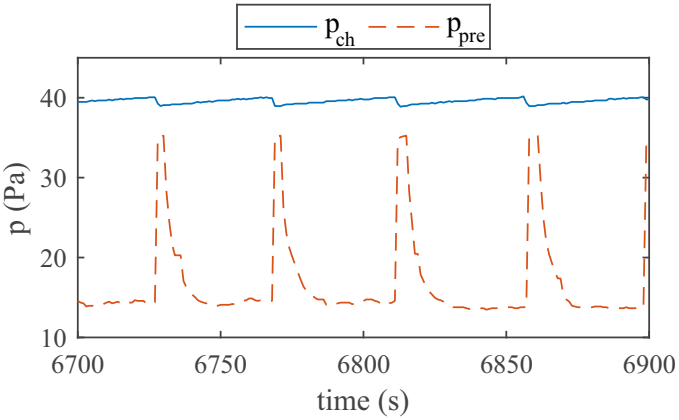

Figure 6.8: Pressure in main chamber and pre-chamber for a target pressure of 40 Pa

Pressure control system The pressure in the main vacuum chamber was measured with two pressure gauges; first, with a Pfeiffer PKR 251 in the full pressure range up to ambient pressure with an accuracy of ±30 %. Second, with an Inficon Porter CDG020D having an accuracy of ±1 % in the pressure range 10-1000 Pa; data from this gauge was always used when the pressure was in its operational range. The main chamber pressure was controlled by a bang-bang control method. Therefore, a second vacuum chamber, here called pre-chamber, was installed between the main vacuum chamber and the vacuum pump. The pressure in this chamber was also measured with a CDG020D gauge. The pre-chamber has about 6 % of the main chamber volume and can be closed on both sides by the pneumatic valves V_1 and V_2. In normal operation, the vacuum pump works continuously and the pumped flow is controlled by the valves. First, the pre-chamber is evacuated and only V_1 is open. If the pressure in the main chamber is above the desired value, both valves are closed. Shortly after that V_2 is opened and the pressures in the pre-chamber and the main chamber equilibrate. The pressure in the main chamber drops by a small amount, while it increases in the pre-chamber by a large amount. After the equilibration, the cycle starts again and repeats until the target pressure is reached in the main chamber. With this control mechanism, the pressure in the main chamber fluctuated around the target pressure in a defined bandwidth, which was set to 3 Pa for the experiments. An example with a target pressure of 40 Pa is shown in figure 6.8. With the pressure control mechanism also the gas flow rate could be measured. The leakage rate at ambient temperature

and vacuum was around 0.1 µmol s^{-1}. When heating the bed under vacuum with pressures below 500 Pa, the gas flow increased to about 1.5 µmol s^{-1} for the 100 A cases, 3 µmol s^{-1} for the 140 A cases and to 6 µmol s^{-1} for the 165 A cases. During heating these rates slowly decreased. After switch-off of the simulator, a pressure drop was observed in the chamber. If this happens, the control mechanism simply leaves valve V2 closed. Converting the pressure drop over time into a molar flow by the ideal gas law resulted in a peak with similar magnitude as the flows during heating. In the end, the gas flows could not clearly be identified as gas coming from the reduction of the ceria particles and can rather be attributed to water condensation or insulation outgassing.

Measuring procedure In each experiment the pressure was set to a certain target pressure with the pressure control system. After reaching the target pressure, video recording with the optical camera and infrared camera was started and the solar simulator was switched on. Pictures of the webcam were stored by a LabView program every 15 seconds; temperatures, pressures and other data from the control cabinet every second. Most experiments were stopped before the temperatures within the bed reached steady state, as steady state is not necessary to compare with the transient simulations. After each experiment the bed was irradiated with a lamp current of 100 A at ambient pressure to oxidize possibly reduced particles at temperatures below 900 °C. This was done in preparation for the next experiment to have the same initial state.

6.1.2.2 Continuum simulation model for packed bed

To check whether the ZBS continuum model is applicable under high temperature and low pressure conditions, the idea is to reproduce the experimental setup in a continuum simulation deploying the ZBS model and to compare the measured temperatures with the simulated ones. Therefore a transient thermal analysis was carried out in ANSYS Mechanical. The simulation domain comprises the insulation, the particle bed and the thermocouples only; the particle bed is assumed to be a continuous body. The thermocouples were incorporated because they had a noticeable influence on the temperature distribution for the very low bed conductivities arising at low pressures. This made three-dimensional simulations necessary. For the thermal conductivities of all materials, temperature dependent values were used.
The particle bed was meshed with tetrahedral elements with maximum edge length 2 mm, the insulation with maximum edge length 10 mm. A mesh refinement by a factor of two changed the temperature at all thermocouples at all times not more than 0.2 %, so that the mesh was considered to be fine

enough. Automatic time stepping was chosen, but the time step size was limited in certain time regions. For example, around switch on and switch off time of the solar simulator, the time step was restricted to 1 s. To check for the influence of the time step limits on the results, all time step limits were halved for one case. The maximum change in temperature at thermocouple 5 was at all times below 0.7 %. A fixed temperature boundary condition is applied to the bottom and outer circumferential surface of the insulation. It was set according to the measured temperatures in the experiment. Radiation, natural convection to the surroundings and an incoming radiative heat flux is specified as the boundary condition for the top surface of both the particle bed and the insulation. For the heat transfer coefficient a correlation for a horizontal plane from Churchill as cited in [238] was used. The chemical reaction of ceria is not included in the simulation, because the energy consumed by the reaction is at all times expected to be lower than 1 % of the heat conducted into the bed, which is shown in detail in [112].

The incident radiative heat flux on the particle bed equals the transmitted flux of the solar simulator through the window. Hence the measured flux profiles shown in figure 6.7 were preprocessed to use them in the ANSYS software: under the good assumption of being axisymmetric they were averaged in circumferential direction and were multiplied by the total transmissivity of the window. This transmissivity was determined from wavelength-dependent attenuation and reflection data as described in [275]. The solar simulator was assumed to have a spectrum of a black body at 5777 K. This resulted in a total transmissivity of 0.90 for the 32 mm thick window. A gain factor from the calorimeter measurement was used to incorporate the startup-behavior of the lamps. In figure 6.9 the flux profiles are shown immediately after switch on and after 6 minutes (steady state) for the lamp currents 100 A, 140 A and 165 A. The total flux on the bed for the respective currents is 0.51 kW, 1.19 kW and 1.66 kW in steady state. Small misalignments of the simulator beam were detected by image processing of optical camera pictures. Pictures taken over the mirror during the heat up phase were analyzed to determine the center of the simulator beam relative to the cooling frame. One picture without particles was taken before the experiments to know the positions of the thermocouples. The gathered positions of the thermocouples and the beam position were incorporated in the simulation setup. Technically, for each experiment a two dimensional flux profile was exported from MATLAB and imported in ANSYS as external data, which was scaled with a time-dependent factor to include the lamp startup behavior and to switch off the lamp. The simulation parameters are summarized in table A.1 in the appendix. The table also contains an estimation of the uncertainty in each parameter. How these uncertainties could affect the simulation results is shown in figure A.5 in the appendix.

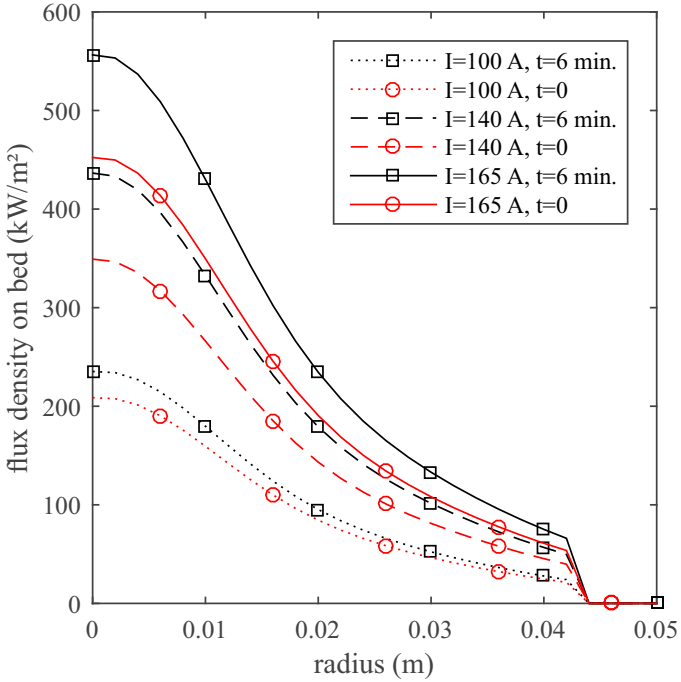

Figure 6.9: Extracted radiation profiles from flux measurement which were used for the simulations, including the transmission of the window. Grey curves with circles: immediately after switch on of simulator, black curves with squares: after reaching steady state

6.1.2.3 Results

In figure 6.10 an example for the measured bed temperatures is shown for a lamp current of 165 A and a pressure of 40 Pa. The simulator lamp was switched on at time 0 and switched off after 5550 s, indicated by the vertical line. For the type R thermocouple TC1 located about 3 mm below the bed surface only temperatures above 500 °C can be read with the data acquisition system. Due to its proximity to the bed surface, this thermocouple reached the highest temperature, in this case 1252 °C. This is in good agreement with the IR camera measurements, which showed bed surface temperatures above 1300 °C. Thermocouple TC2 indicates a maximum temperature of 1190 °C. At the center of the bed, 10.4 mm above the bottom, the temperature of thermocouple TC3 was 1115 °C at shutoff time. Thermocouples TC4 placed 7.8 mm above bottom and TC5 placed 2.1 mm above bottom showed maximum tem-

peratures of 925 °C and 511 °C, respectively. Since the heat needs some time to travel through the bed, there is some delay between lamp switch on/off and temperature response, most noticeable for thermocouple TC5. The tempera-

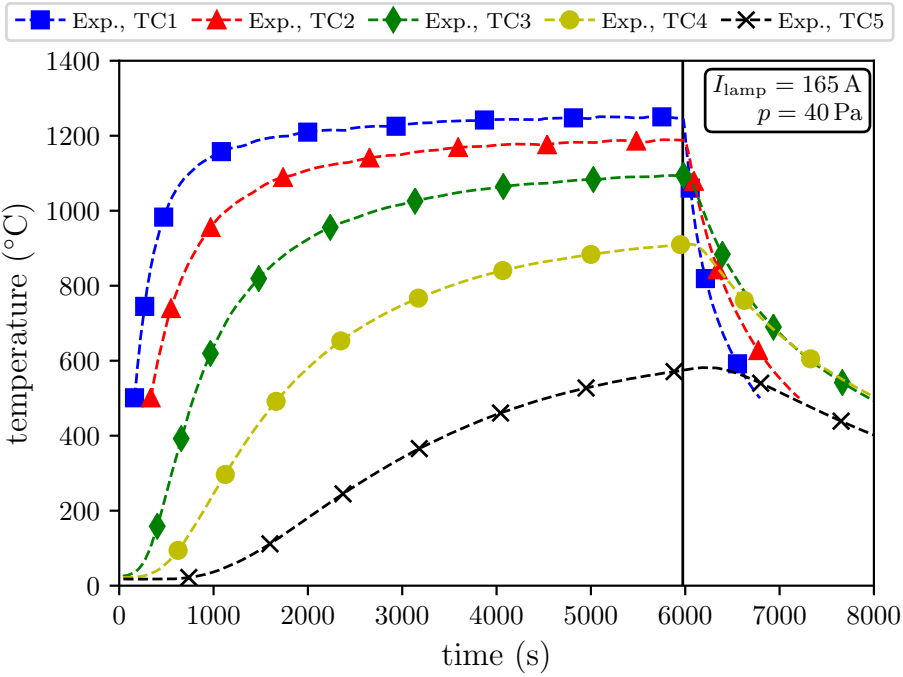

Figure 6.10: Temperature at various thermocouple locations for highest lamp current of 165 A and pressure of 40 Pa. Vertical line marks lamp shutoff

ture of this thermocouple is influenced by the particle layers above with their respective temperature and thermal conductivity. Therefore it can be seen as an indicator how well the heat is conducted overall and thus will be used to compare the experiment and simulation in the following. The temperature of TC5 is shown for lamp currents of 100 A, 140 A and 165 A in figure 6.11, figure 6.12 and figure 6.13, respectively. Both the experiment and simulation are shown for various pressures. The lamp switch off is indicated with a grey light bulb. The expected pressure dependence of the thermal conductivity was clearly seen in the experiments. The time delay at switch on and switch off increased with lower pressures; the inclination of the temperature curves was lower at lower pressures and the time to reach steady state also increased.

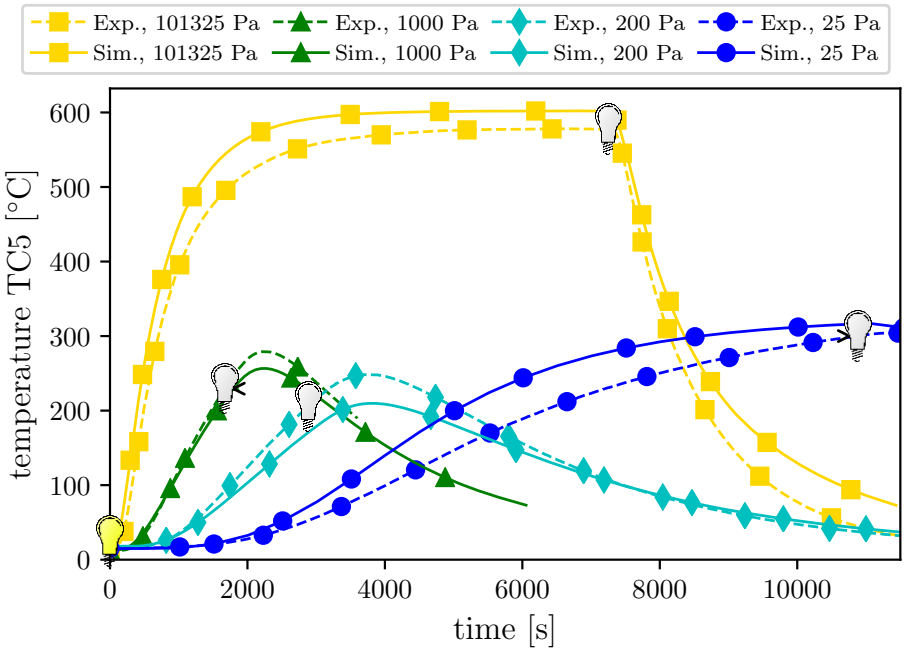

Figure 6.11: Temperature of thermocouple TC5 at various pressures and a lamp current of 100 A. Results from experiments and simulations; light bulbs indicate when the solar simulator was switched on (yellow) and off (grey)

For example, for the lowest pressure steady state was still not reached after 3 hours, while it was reached after about 1 hour for the ambient pressure case, see figure 6.11. The simulations show good agreement with the experiments in general, the deviation between experiment and simulation is in almost every case within the error band of the simulations, which is given in an exemplary case in appendix A.5. To obtain a quantitative measure of the agreement, the mean relative difference between simulation and experiment was calculated for each thermocouple. Twenty equally spaced sample times t_i were used, 10 during the heat up phase and 10 during the cool down phase. The mean relative difference (MRD) is then

$$\mathrm{MRD} = \frac{\sum_{i=1}^{20} \left| 1 - \frac{T_{\mathrm{Sim}}(t_i)}{T_{\mathrm{Exp}}(t_i)} \right|}{20} \quad . \tag{6.2}$$

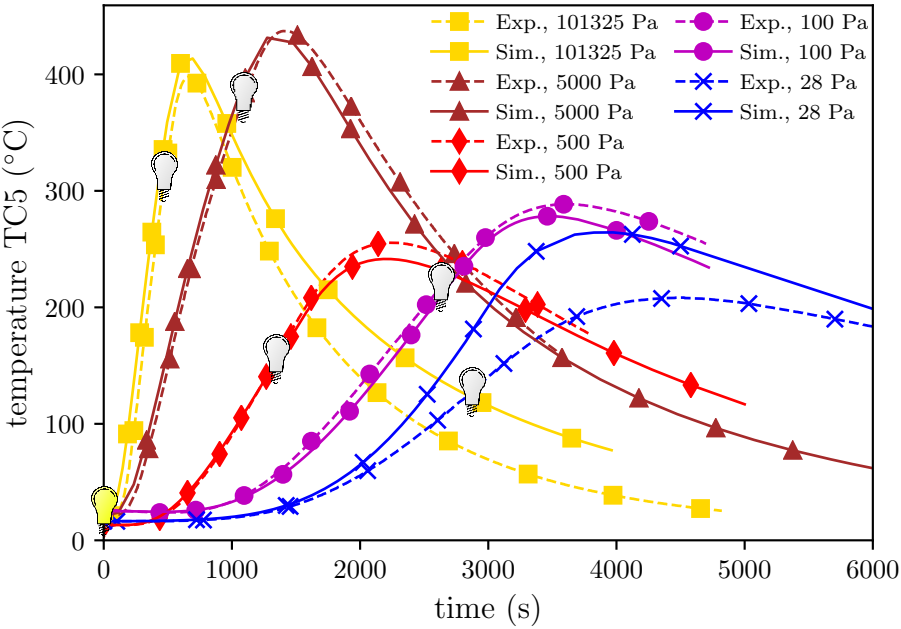

Figure 6.12: Temperature of thermocouple TC5 at various pressures and a lamp current of 140 A. Results from experiments and simulations; light bulbs indicate when the solar simulator was switched on (yellow) and off (grey)

Averaged over all experiments the MRD was 4.2 % for thermocouple TC5. For thermocouples TC4, TC3, TC2 and TC1 the average MRD was similar with 4.1 %, 7.5 %, 8.8 % and 6.6 %, so that curves for the other thermocouples are not shown in figure 6.11, 6.12 and 6.13. At ambient pressure, a larger deviation can be observed in the cool down phase for all lamp currents. Here the temperature in the experiment decreases faster than in the simulation, even though the model fits the experiment well in the heat up phase. This leads to a maximum deviation in temperature of about 50 °C for all lamp currents. At first sight, one could consider boundary conditions or bed conductivity as the reason for this deviation. However, wrong boundary conditions would also affect the simulations at lower pressures, but they show good agreement with the experiment, also in the cool down phase. Wrong bed conductivity would affect both the heat up and the cool down phase, but the heat up phase matches well. A possible reason could be the insulation material which conducts more heat than expected. This effect is most important at ambient

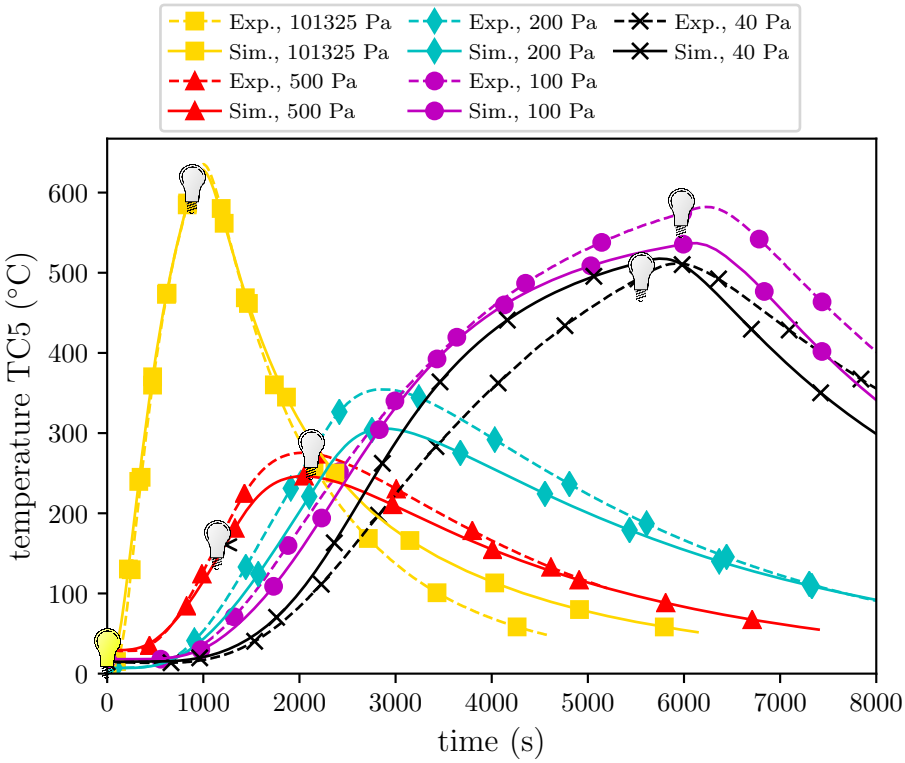

Figure 6.13: Temperature of thermocouple TC5 at various pressures and a lamp current of 165 A. Results from experiments and simulations; light bulbs indicate when the solar simulator was switched on (yellow) and off (grey)

pressure as the heat propagation in the bed is an order of magnitude faster than at vacuum conditions and heat flux reaching the insulation is higher than at vacuum conditions.

Below ambient pressures, the simulated temperatures match the experimental ones or are slightly lower, except for the lowest pressure case at each lamp current. The qualitative behavior is the same when a pressure was measured at multiple lamp currents, which is a good indicator for the validity of the results. The 5000 Pa, 1000 Pa, 500 Pa and 100 Pa cases for the respective lamp currents show a very good agreement between model and experiment. The biggest underestimation of the temperature by the model happens at 200 Pa. The biggest overestimation occurs for all lamp currents at the lowest pressure,

namely at 25 Pa, 28 Pa and 40 Pa. To investigate the low pressure cases further, the data of the experiment with a lamp current of 140 A and a pressure of 28 Pa is plotted in figure 6.14 in more detail. Besides thermocouple TC5 also the other thermocouples are shown, which are located above TC5 in the bed, as indicated in figure 6.6. For all thermocouples a good agreement between model and experiment is observed, also during the cool down phase. For TC4 and TC5 the temperatures are slightly overestimated by the model, while they are slightly underestimated for TC3, TC2 and TC1. This behavior was observed for each lowest pressure case at the respective lamp current; with the exception that at the highest lamp current of 165 A also the maximum temperature at TC4 is underestimated. Additionally the underestimation in TC3, TC2 and TC1 is bigger than for the other lamp currents. As the bed temperature is higher overall due to the higher flux on the bed the temperature of TC4 at 165 A is similar to the one of TC3 at a lamp current of 140 A. This indicates that the effective bed conductivity under these vacuum conditions is slightly underestimated by the ZBS model at high temperatures, while it is slightly overestimated at low temperatures. Nevertheless, the deviations are still small considering all the possible influences in simulation and experiment. Thus it can be stated that the ZBS model performs well under vacuum conditions and high temperatures for an irradiated ceria particle bed.

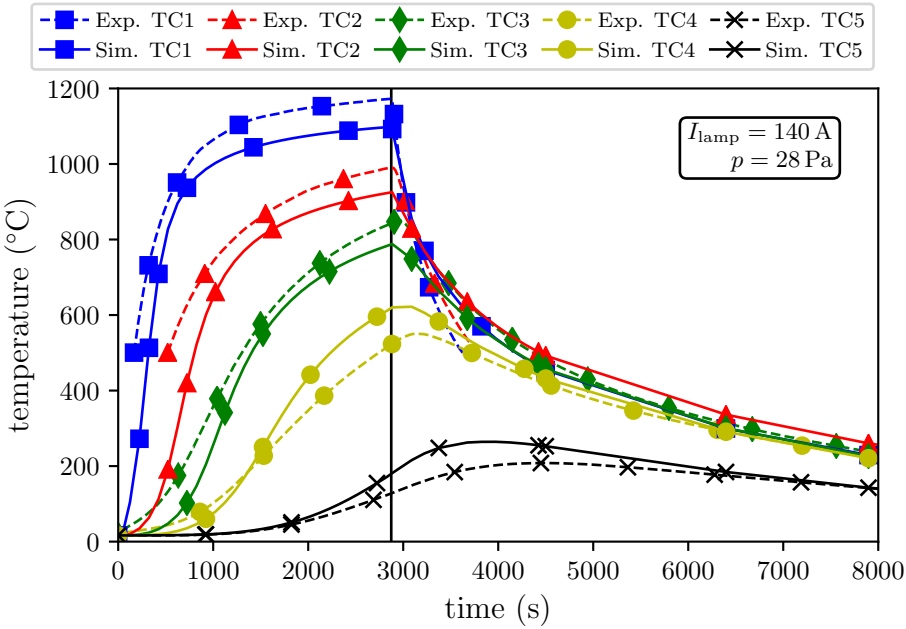

Figure 6.14: Temperatures in experiment and simulation with a lamp current of 140 A and a pressure of 28 Pa at three different thermocouple positions. Vertical line marks lamp shutoff

6.1.3 Heat transfer coarse-graining approach

If coarse graining is applied, the coefficients H_t and H_w need to be adapted as described in section 4.4. Here it is tested how well this adaption works for H_t. Therefore the cylindrical test case from section 6.1.1 was simulated, but this time not with a fixed H_t, but with one calculated by the calibrated K_pp and equation (4.55). In this way, also the implementation of the ZBS model into the extended LIGGGHTS® code in general was checked. In figure 6.15 the obtained thermal conductivities calculated from the DEM simulations with coarse-graining are compared with the thermal conductivity calculated by the ZBS model. A good agreement is found, meaning the coarse graining only marginally influences the result and the implementation of the ZBS model in the DEM code can be expected to be correct.

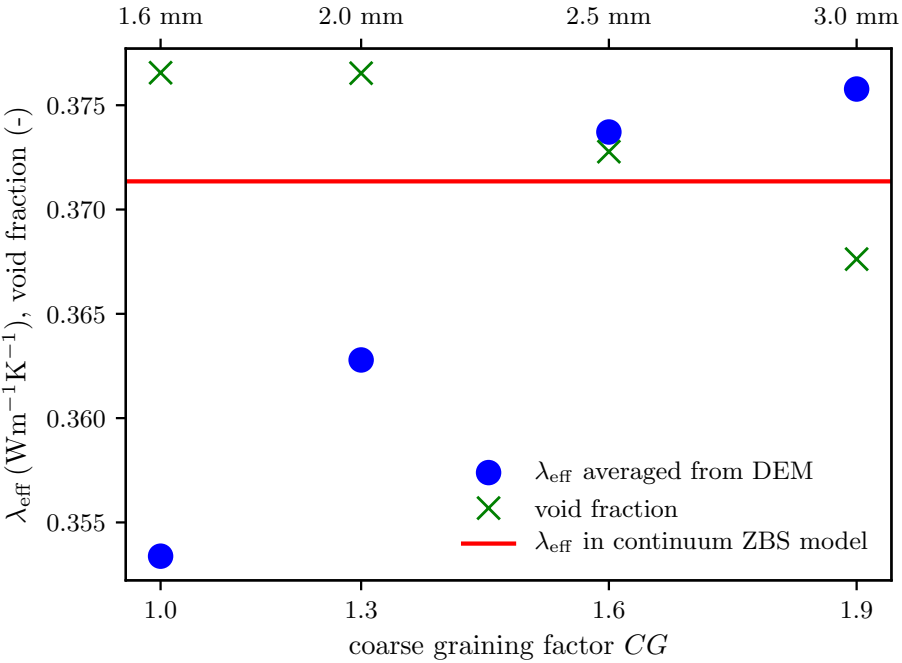

Figure 6.15: Comparison of effective thermal conductivity averaged from DEM simulations with various factors of coarse graining applied. Radiation was deactivated by setting emissivity to zero, fixed temperature of the outer shell particles in the test case is 300 K (center particles slightly above) and red line shows the result of the continuum ZBS model for a void fraction of 0.376557 and particle diameter 1.595 mm

6.1.4 Stability of explicit integration scheme

In section 4.2.3 a stability limit for the numerical integration scheme to update the particle temperature was derived, as no limit was found in literature even though this scheme is used in the majority of DEM codes. Since estimates are used during the derivation and local perturbations can also cause instabilities (for example because not all particles have the same number of neighbors), the derived time step limit via the van Neumann analysis is not a sharp one and should be checked here. Therefore the cylindrical test case in figure 6.1 was tried to be solved with different time steps, starting with a large one and decreasing it until a steady state solution could be obtained. This was

done for three thermal cutoff distances $C_{\text{cutoff,HT}}$ and two total particle-particle conductances H_{t}. The results and the limit calculated from equation (4.29) are shown in figure 6.16. The prediction of the critical time step by equation (4.29)

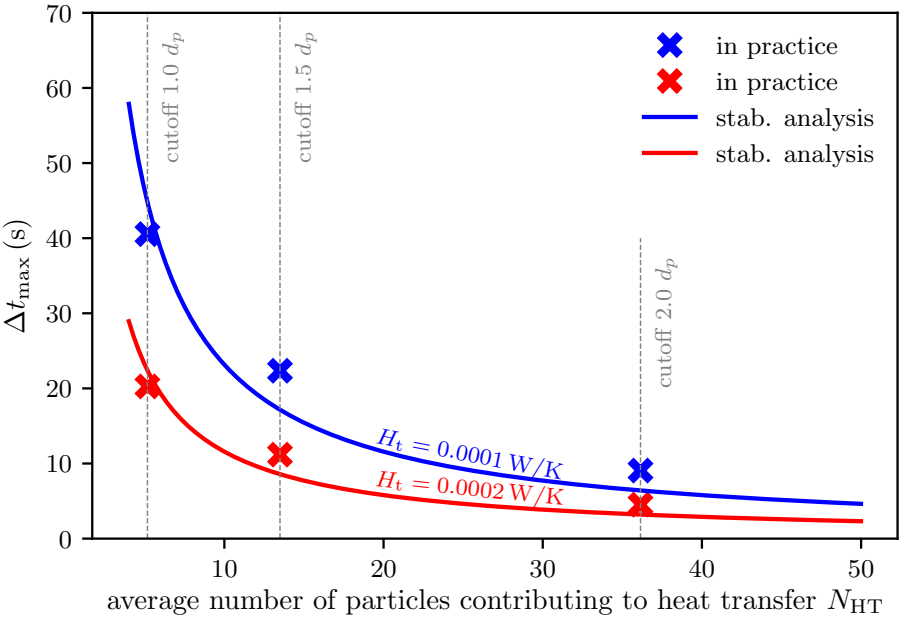

Figure 6.16: Stability test for the simulation of the cylindrical test case shown in figure 6.1

is in good agreement with the one seen in the actual simulations. It can be concluded that the derived limit is well suited to estimate a time step. This gives the possibility to increase the speed of DEM heat transfer simulations with non-moving particles significantly.

6.2 Radiation Model

To check the implemented MCRT model for the radiation calculation, the results of basic test cases are compared to analytical solutions and for a more complex test case of a packed bed with many particles the results are compared to another radiation model.

6.2.1 Basic test cases

The basic test cases are shown in figure 6.17. For these test cases the emissivity was set to unity, so that the diffuse-specular radiation distribution factor D'_{ij} is equal to the view factor or configuration factor F_{ij}. In test case (a) the view

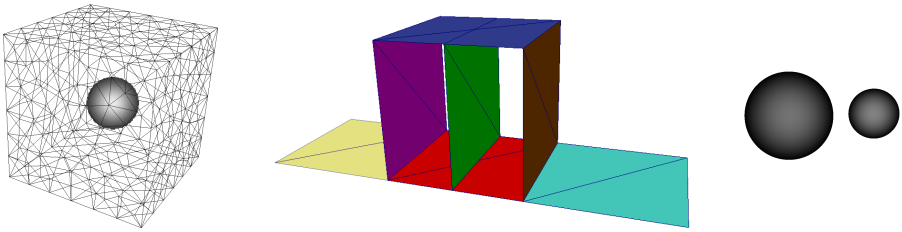

(a) Sphere in enclosure [249]

(b) Various wall combinations

(c) Two spheres of different size

Figure 6.17: Basic test cases for separate C++ program

factor from the sphere to each of the 6 walls of the cube should be 1/6 due to symmetry. Each wall of the cube was discretized into 100 triangles and the sum of the view factors from the sphere to each of these triangles indeed converged to 1/6 [249]. To check radiation between walls, various combinations of the squares in figure 6.17(b) consisting of two triangles were simulated. Wall-to-wall view factors matched with the correlations from literature. It was assured that shadowing is taking place, for example in a test case with the purple, green and brown surfaces the brown one should not see the purple one. By changing the surface orientations it was also verified that the directional requirements are fulfilled, for example that the ray is only counted on a surface if it is hit on the front side. Finally the view factor between two spheres of different size was calculated for various distances between them [249] and compared to data from the literature as shown in figure 6.18. The MCRT solution coincides with the literature data in all cases.

6.2.2 Comparison with a continuum model for a packed bed

To check the radiation model for an arrangement of many particles, the radiation in a cylindrical packed bed similar to the one in figure 6.1 was simulated. An additional heat source was set for particles in the center of the cylinder and the temperature of particles located outside a certain cylinder radius was fixed. The particle-particle heat transfer was deactivated in LIGGGHTS® by

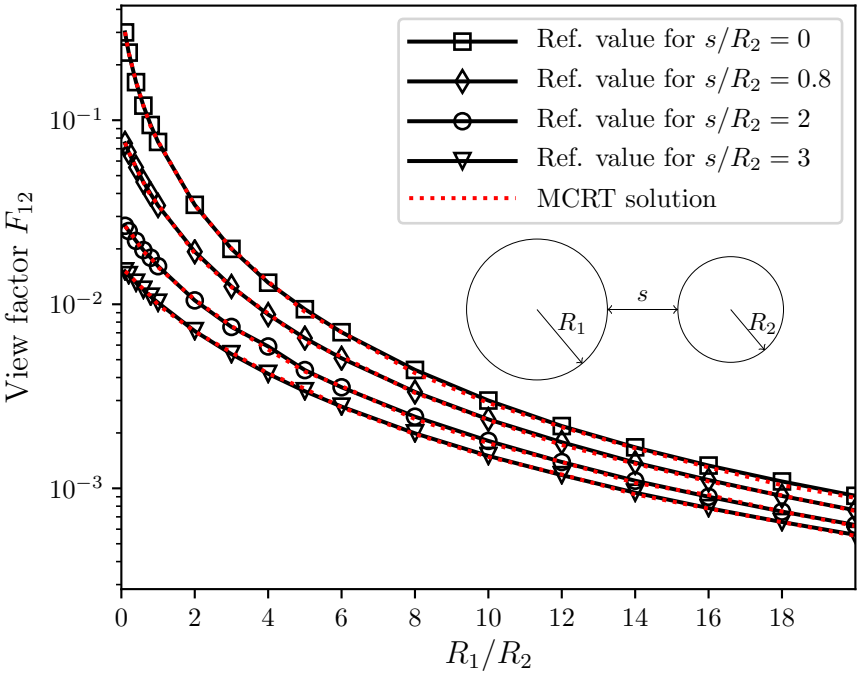

Figure 6.18: View factor between two spheres of different size at various distances to each other. Comparison of reference values from [276] with ones calculated by the Monte-Carlo ray tracing of the C++ program developed in this work

setting H_t to zero. Radiation source terms were calculated with the separate C++ program by shooting 10 rays per sphere and updated in an appropriate time interval, which had to be smaller for higher temperatures. The simulation was stopped when a steady radial temperature profile was reached and the effective conductivity was determined according to equation (6.1). The results for various temperatures are shown in figure 6.19 for an emissivity of (a) $\varepsilon = 1.0$ and (b) $\varepsilon = 0.7$. Also shown is the effective bed conductivity of the ZBS model with the parameters corresponding to the test case, which are

- $k_p \to \infty$, since the LIGGGHTS® model has a uniform particle temperature
- $p \to 0$ for no conductive gas heat transfer
- $\varphi = 0$ for no conduction heat transfer between particles through the

contact point

- Void fraction 0.4013, calculated from the DEM data

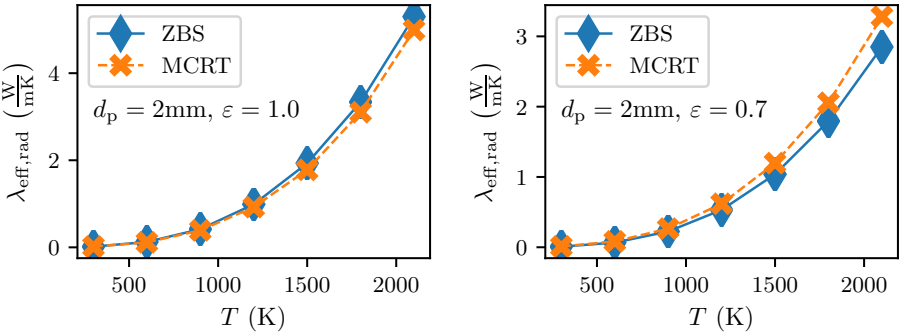

(a) $\varepsilon = 1$ (b) $\varepsilon = 0.7$

Figure 6.19: Effective particle bed conductivity due to radiation for $d_p = 2$ mm. Comparison between Monte Carlo Ray Tracing (MCRT) and Zehner-Bauer-Schlünder model (ZBS)

The MCRT solution shows an remarkable agreement with the ZBS model, considering the simplicity of the ZBS model approach. As expected, the effective radiative conductivity of the bed decreases for a lower emissivity; here it is interesting that the ZBS model predicts a higher effective bed conductivity than the MCRT code for $\varepsilon = 1.0$, while the opposite is true for $\varepsilon = 0.7$. The relative deviation between the models is higher at lower emissivity. A possible reason could be more reflections, which should lead to more inaccuracies in the ZBS model as it is assuming a simple geometric arrangement of particles and as it is derived from the radiative transport in a small gap between parallel plates [234].

In summary, the results of the shown test cases give high confidence that the ray tracing model works as desired. The good agreement with the radiative part of the ZBS model shows that the error in the short-range radiation calculation which is made if one applies the simplifications in section 4.3.1.4 is small. Additionally, the packed bed test case also showed that only a few rays per sphere are sufficient in the MCRT model to reach a steady state in overall heat transfer, if the MCRT calculation is repeated in a short time interval. This is discussed in more detail in the following.

6.2.3 Study on the number of rays and the coupling interval

Monte Carlo ray tracing can never be expected to be exact, because it is a stochastic method. Therefore an accuracy statement should be accompanied with a confidence level [277]. The calculation of the radiation distribution factor D_{ij} can be compared to a biased coin flip and its accuracy at a given confidence increases with the square root of the number of rays [277]. Emitting only 10 rays per sphere like in the previous section means that a high error in the radiation distribution factor between spheres is expected. However, in practice the overall bed temperatures and heat flows are relevant, so that this high error in D_{ij} can be accepted. This was checked by comparing radial temperature profiles of the cylindrical test case from the previous section 6.2.2 for various numbers of emitted rays per sphere. Additionally, two different coupling time intervals between DEM and MCRT code were investigated. The heat source terms of each particle in the central, heated region of the particle bed were increased compared to the previous section to have more pronounced temperature profiles. In figure 6.20 they are shown after 20 s for a fixed outer shell temperature of 1500 K and the same initial temperature of all particles.

Indeed a number of 10 rays per sphere is sufficient to obtain an accurate temperature profile, both for a coupling time of 0.1 s and 0.5 s the curves nearly coincide with the ones with 5 rays per sphere. It should be noted that the number of rays shot per time is inversely proportional to the coupling time. Hence the temperature profile at a coupling time of 0.5 s and 1 ray per sphere shows the largest deviation, followed by the one with 3 rays per sphere. If the coupling time is decreased to 0.1 s, already 1 ray per sphere is enough to sample a proper radial temperature profile in the particle bed.

Averaging the temperature of a number of particles to obtain a radial temperature profile is also a reason why the ray number requirement is so low. Local perturbations are expected to be higher. As an example a single particle in 6 mm radial distance to the bed center at half the bed height is picked. Its temperature after 20 s is calculated first by shooting 1 ray per sphere and coupling every 0.1 s and then also by shooting 5 rays per sphere and coupling every 0.5 s. These calculations are repeated ten times, so that a standard deviation can be given for both calculation ways. The results are depicted in figure 6.21. In both calculation ways, the maximum difference in particle temperature between the samples is about 100 K. Also the sample standard deviation is similar with 30.6 K and 25.5 K. It can be concluded that the amount of rays per sphere and time is important for the accuracy of the result. As the temperature update is usually done in the DEM code to include other heat transfer modes, the coupling time must not be chosen too large and rather a small coupling time and a small number of rays per sphere should be

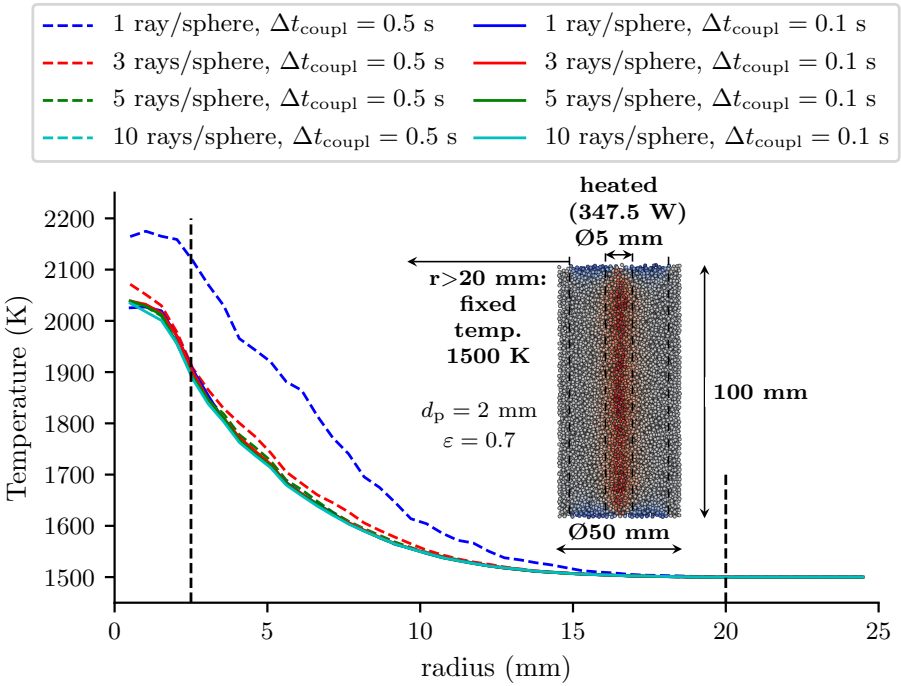

Figure 6.20: Temperature profile of cylindrical test case in radial direction after 20 seconds, shown for various numbers of rays shot per sphere and two different coupling time intervals between the DEM and the MCRT code

selected. If one is not interested in the temperature of each particle but in the one of the agglomerate, 1 ray per sphere and a coupling time of 0.1 s is sufficient.

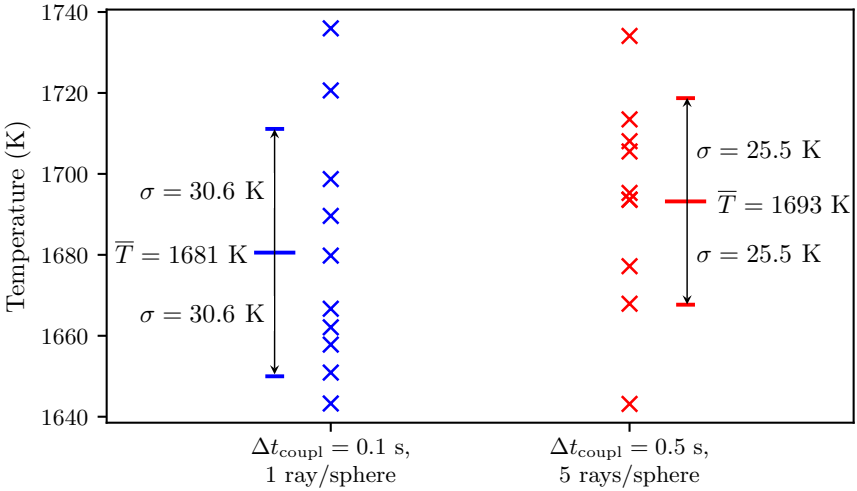

Figure 6.21: Temperature of a single particle in 6 mm radial distance to the bed center at half the bed height after 20 s. Results of ten simulation runs, once with 1 ray per sphere and coupling time 0.1 s and once with 5 rays per sphere and coupling time 0.5 s

6.3 Particle-Wall Model

The particle-wall model was validated in two steps. First, the conduction within the wall was compared with an analytical solution. Second, the wall temperature was fixed and a test case from the literature was reproduced to check the conduction between particles and wall.

6.3.1 Conduction within wall

To test the conduction within the wall, two parallel, quadratic walls of edge length 1 m and separated by a tiny gap of 0.01 mm were generated, as schematically shown in figure 6.22(a). The only heat transfer allowed between these walls was radiation. The emissivity of both walls was set to $\varepsilon_{\text{top}} = \varepsilon_{\text{bot}} = 0.6$, each of their thickness to $l = 0.1$ m and their thermal conductivity to $\lambda_{\text{w}} = 1$ W m^{-1} K^{-1}. The walls were discretized into 20 elements each and a fixed temperature boundary condition was selected, 300 K for the bottom and 1500 K for the top wall. A total of 4 million rays were shot from the two walls for the ray tracing. This setup was chosen since it can be represented by a thermal resistance network depicted in figure 6.22(b), from which the two wall surface temperatures T_1 and T_2 were obtained by itera-

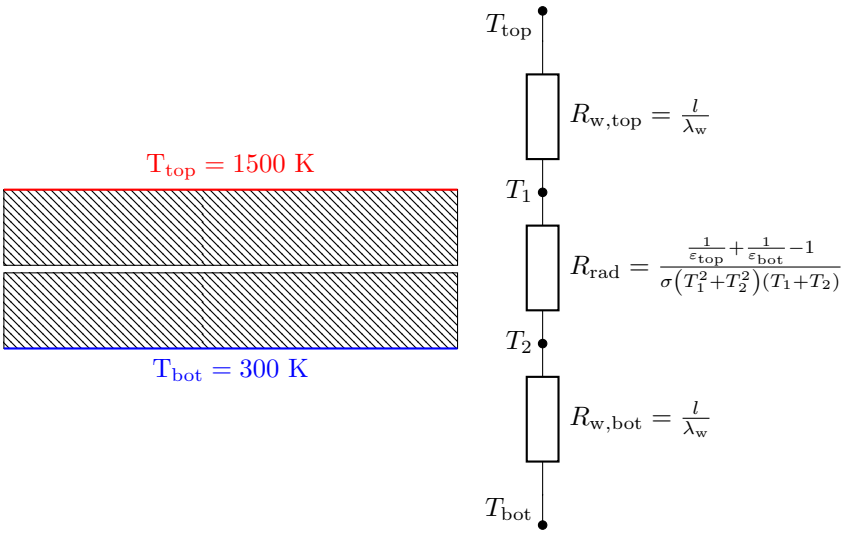

(a) Simulation setup schematic (b) Thermal resistance network

Figure 6.22: Parallel plate test case, not to scale

tion. In table 6.1 they are shown side-by-side to the ones obtained from the wall model and the ray tracing. The deviations are extremely small, also for

Table 6.1: Results of wall conduction test case

Temperature	Iterative solution of resistance network	Solution of ray tracing and wall model	Relative deviation
T_1	939.476 K	939.479 K	−0.00032 %
T_2	860.524 K	860.515 K	−0.00105 %

other temperatures and emissivities not shown here, so that thermal conduction through walls can be considered to be treated correctly by the separate C++ program.

6.3.2 Conduction between particles and wall

For the particle-wall conduction validation, a two-dimensional test case of Kwapisnka et al. [278] was replicated. They investigated the heat transfer from an isothermal wall of 343 K to particles with initial temperature of 293 K in a drum at various rotational speeds. The results were compared to the penetration model of Schlünder [256]. This continuum model describes the heat transfer process as a series of two thermal resistances: a contact resistance $1/\alpha_{\mathrm{WS}}$ and a penetration resistance $1/\alpha_{\mathrm{bed}}$. The penetration resistance can be derived from a semi-infinite body subjected to a sudden wall temperature change, for which the analytical solution

$$\frac{T(x,t) - T_0}{T_{\mathrm{w}} - T_0} = 1 - \mathrm{erf}\left(\frac{x}{4\sqrt{at}}\right) \tag{6.3}$$

can be obtained [279]. For small arguments, the error function can be approximated by

$$\mathrm{erf}(\zeta) = \frac{2}{\sqrt{\pi}}\zeta \qquad , \quad \text{for } \zeta \ll 1 \quad . \tag{6.4}$$

On the wall of the semi-infinite body, Fourier's equation then gives

$$\alpha_{\mathrm{bed},t}\left(T_w - \overline{T}\right) = -\lambda \left.\frac{\partial T}{\partial x}\right|_{x=0} \Rightarrow \alpha_{\mathrm{bed},t} = \frac{T_{\mathrm{w}} - T_0}{T_{\mathrm{w}} - \overline{T}} \frac{1}{\sqrt{\pi}} \frac{\sqrt{\rho c_p \lambda}}{\sqrt{t}} \quad . \tag{6.5}$$

The fraction of temperature differences in the right term tends towards unity in a semi-infinite body, because the average bed temperature $\overline{T}$ tends towards the initial temperature T_0. This leads to the penetration heat transfer coefficient given by Schlünder [256]

$$\alpha_{\mathrm{bed},t} = \frac{1}{\sqrt{\pi}} \frac{\sqrt{\rho c_p \lambda_{\mathrm{bed}}}}{\sqrt{t}} \quad , \tag{6.6}$$

which scales with the inverse square root of time. This time-dependency is indicated with the index t. Considering only conduction and no radiation, the contact heat transfer coefficient α_{WS} is the particle-wall heat transfer coefficient from equation (4.53) times the share of area ξ covered by particles [256]

$$\alpha_{\mathrm{WS}} = \xi \alpha_{\mathrm{WP}} \tag{6.7}$$

and should therefore not change over time. The overall heat transfer resistance from the wall to the particles is then

$$\frac{1}{\alpha_t} = \frac{1}{\alpha_{\mathrm{WS}}} + \frac{1}{\alpha_{\mathrm{bed},t}} \tag{6.8}$$

and the energy balance for the whole bed is

$$mc_p \frac{\mathrm{d}\overline{T}}{\mathrm{d}t} = \alpha_t A \left(T_\mathrm{w} - \overline{T}\right) \quad . \tag{6.9}$$

Through integration, one obtains the time-averaged overall heat transfer coefficient from the wall to the bed [278]:

$$\alpha = \ln\left(\frac{T_\mathrm{w} - T_0}{T_\mathrm{w} - \overline{T}}\right) \frac{mc_p}{A} \frac{1}{t} \quad . \tag{6.10}$$

The validation of the particle-wall model is based on this time-averaged overall heat transfer coefficient. A two-dimensional drum half filled with particles was simulated with the identical parameters as in the study of Kwapinska et al., except for the particle diameter, which was changed from 8 mm to 2 mm. The particle diameter was reduced because the time window where the assumption of a semi-infinite body is valid was found to be very small for the 8 mm particles; this will be discussed later. The parameters are summarized in table 6.2 and a picture of the particle arrangement is shown in figure 6.23.

In accordance to the paper of Kwapinska et al., the case was simulated

Table 6.2: Parameters for the 2D simulation of a stagnant bed in a drum

drum diameter	d_p	ρ_p	c_p	α_PP
0.25 m	2 mm	2500 kg m^{-3}	836 J kg^{-1} K^{-1}	100 W m^{-2} K^{-1}

with wall-particle heat transfer coefficients 500, 1000 and 100000 W m^{-2} K^{-1} and the time-averaged overall heat transfer coefficient was evaluated according to equation (6.10). The results are shown in figure 6.24 in logarithmic axes. While the curve for the extremely high heat transfer coefficient α_WP = 100000 W m^{-2} K^{-1} immediately drops, the other two curves show a constant overall heat transfer coefficient in an initial time span. This is the expected behavior as the heat transfer to the bed is controlled by the particle-wall contact resistance for these short heat transfer durations, until the first layer of particles on the wall has the same temperature as the wall, as indicated by the maximum particle temperature in figure 6.25. For the 1000 W m^{-2} K^{-1} case for example, the asymptotic value of α for short times is 744 W m^{-2} K^{-1}. According to equation (6.7) this corresponds to a wall area coverage of 74 %, a reasonable value as the value for the 3D case is reported to be about 80 % [238]. The curves of α_WP = 100000 W m^{-2} K^{-1} and α_WP = 500 W m^{-2} K^{-1} lead to the same area coverage.

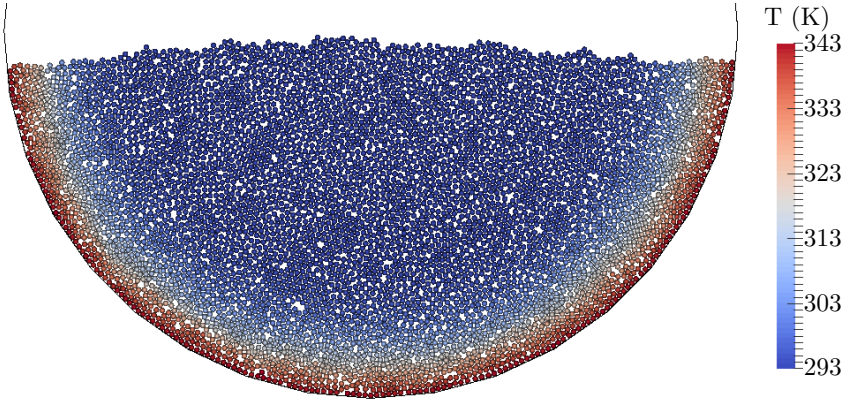

Figure 6.23: Two-dimensional drum filled with 5920 particles. Temperatures are shown for $\alpha_{\mathrm{WP}} = 500$ W m^{-2} K^{-1} after 1000 s

For very long times, all curves fall together and approach the slope of -0.5 in the double logarithmic plot, which was expected from equation (6.6). If one would simulate even longer times, the assumptions of a semi-infinite body would break down at some point as there is no infinite reservoir of spheres at initial temperature in the real case. A smaller particle diameter means less time to heat up the first particle layer, so that there is a larger time span in which the slope should approach -0.5 in the double logarithmic plot. With the original particle diameter from Kwapinska et al., this time span was very short, so that the diameter was decreased as stated previously.
In summary, the developed and implemented particle-wall model showed the expected behavior, both for the heat conduction within the wall itself and for the conduction between particle and wall. Hence it was validated successfully. Additionally the half-filled drum test case served as another validation of the particle-particle model.

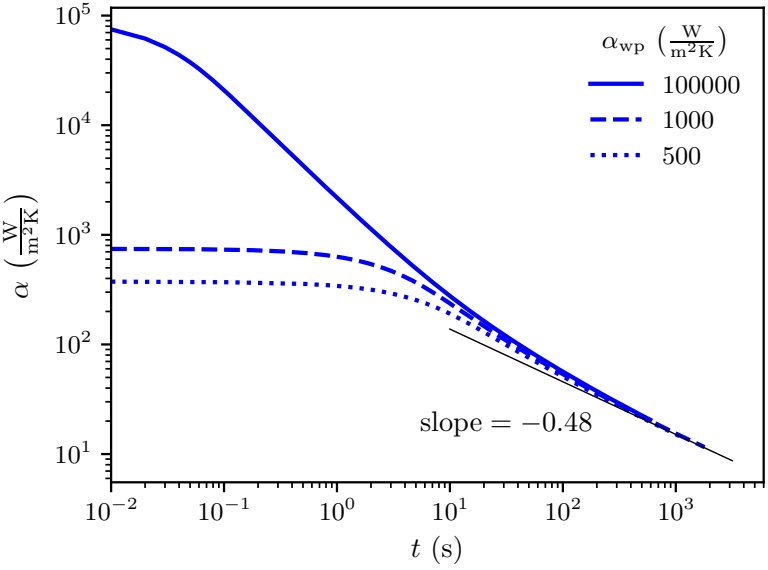

Figure 6.24: Time-averaged overall heat transfer coefficient

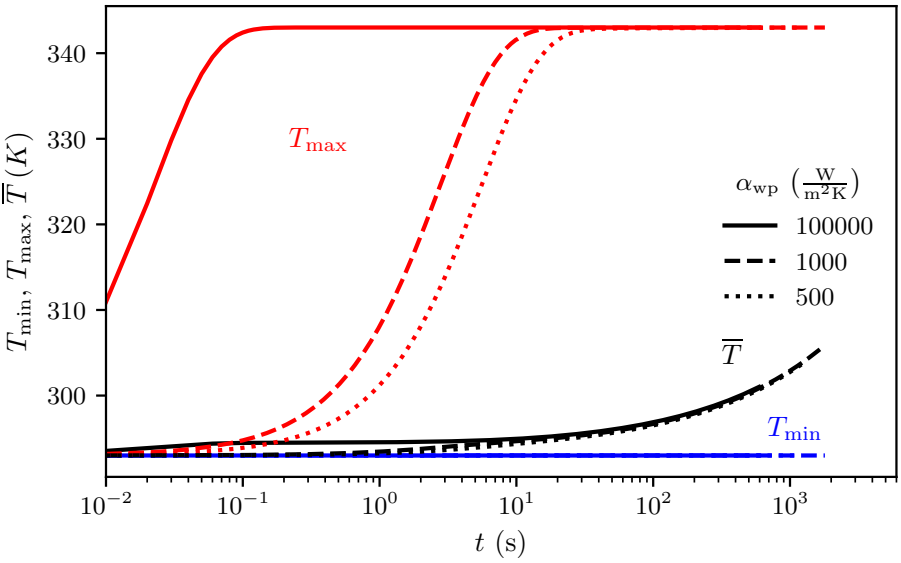

Figure 6.25: Minimum, maximum and average particle temperatures in two-dimensional drum simulation

6.4 Verification of Chemical Reaction Model

The chemical source term for ceria was implemented by modifying the heat capacity of the particle in equation (4.25). To check if this approach works and and if it was implemented correctly, a simple test case shown in figure 6.26 was constructed. It consists of two particles on top of each other, the lower one with a temperature of 2000 K and the upper one with a temperature of 1500 K. The pressure is set to 25 Pa and according to figure (4.22) the particles A and B have the reduction extent δ_A and δ_B.
If the chemical reaction model was implemented correctly, the overall energy E_{tot} should not change when the particles exchange heat between and only between themselves. The components of the overall energy, the total chemical and thermal energy of the two particles should change though, as the reduction extent is an exponential function of temperature. In table 6.3 it can be

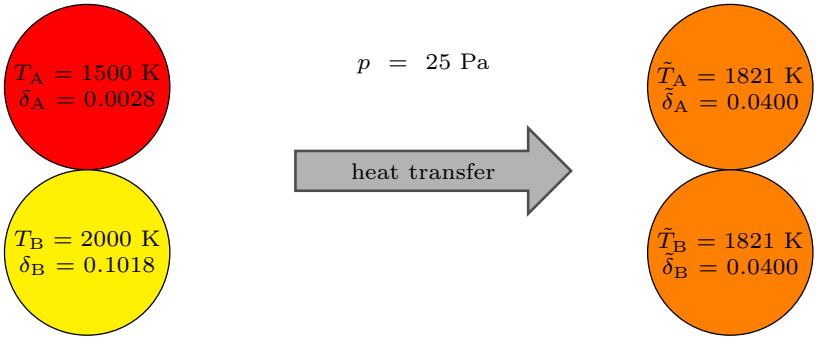

Figure 6.26: Test case for verification of chemical reaction model

seen that this is the case. After the equilibration of the heat transfer, both particles have the same temperature of 1821.2 K, which is above the mean initial temperature. This is because some of the chemical energy from the initial configuration was transformed into thermal energy. The overall energy differs only by 0.007 J, so that the chemical reaction model can be considered to be implemented correctly.

Table 6.3: Results of chemical reaction model verification

	T_{A} (K)	T_{B} (K)	δ_{A}	δ_{B}	Q_{th} (J)	Q_{chem} (J)	E_{tot} (J)
Initially	1500	2000	0.0028	0.1018	334.500	58.114	392.614
After equilibration	1821.2	1821.2	0.0400	0.0400	348.117	44.510	392.627

7 Model Application to the CentRec Particle Receiver Prototype

The aim of this thesis is to enable DEM simulations with heat transfer of solar particle receivers and particle receiver-reactors. In this chapter the model is applied to the prototype of the centrifugal particle receiver (CentRec, section 2.1.1), which was investigated in the dissertation of Wu [40]. The purpose is to demonstrate the full model, its feasibility and the power of the DEM. The CentRec prototype was chosen because of several reasons. First, well documented experimental data is available. Second, the receiver type is considered to be used in multiple future projects. Third, the particle motion in the receiver was only modeled with rheology models so far and these were not coupled with heat transfer [260]. It exists a one dimensional heat transfer model, but it assumes a particle motion in the receiver [40]. A model capturing both the motion and the heat transfer is desired.

7.1 Experimental Setup and Observations

The cross-sectional view of the receiver geometry is shown in figure 7.1. The whole receiver rotates around its centerline, driven by a belt drive (1) and rolling on 4 wheels placed around the perimeter (2). Particles enter the receiver through the feeding tube (3) and are distributed on the receiver walls by the feeding cone (4). The rotation speed Ω is set so high, that the particles build a film on the wall of the cylinder (5) due to the centrifugal force. The cylinder has a length of 0.26 m and an inner diameter of 0.17 m. At the outlet (6) of the receiver, Wu [40] found a tiny barrier half a particle diameter high necessary to establish a stable particle film. The radiation from the solar simulator (10) enters the receiver through the aperture with a diameter of 0.138 m, spillage is captured by the radiation shield (7). The particles leave the receiver through a collection ring (8). The insulation (9) is fixed in the housing.
Wu [40] conducted numerous experiments and varied the input power, the particle mass flow, the rotation speed and the inclination angle of the receiver.

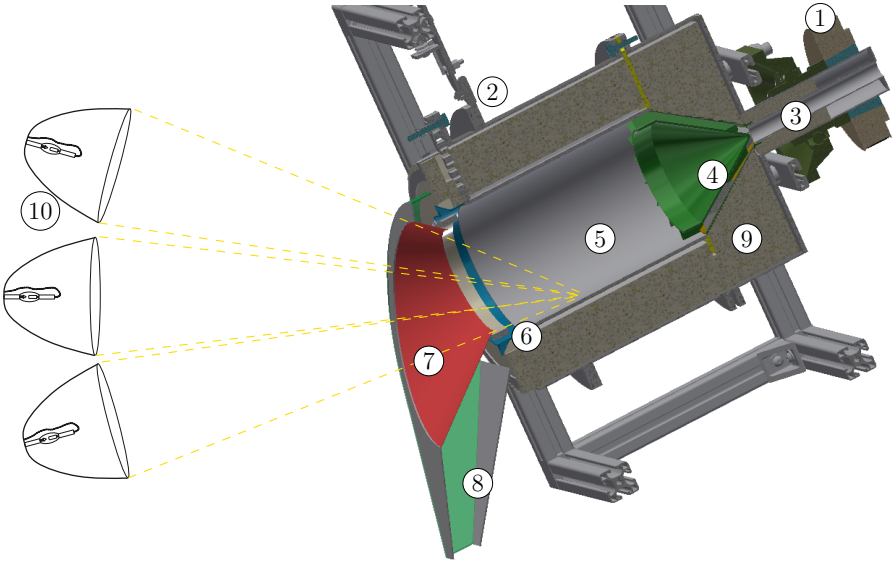

Figure 7.1: Sectional view of the CentRec receiver prototype in the CAD model and indicated irradiation from solar simulator

Due to limitations imposed by the solar simulator, the receiver was tested only at part load with relatively low particle mass flows. Except of the mass flow at the outlet of the collection ring, which was measured by a weighing system, only qualitative observations of the particle motion are available from the experiment. To obtain a particle film on the receiver wall, the particle barrier near the outlet was found to be necessary. In initial experiments particles were accumulating in the upper region of the receiver, until these buildups broke down again, so that a periodic mass flow was measured as depicted in figure 7.2. This undesired behavior was reduced by the introduction of vibrations on the bearing wheels. Temperatures were measured by thermocouples alongside the rotating cylinder and by a temperature measurement ring (TMR). In this TMR, shown in blue near the particle barrier (6) in figure 7.1, particles were collected periodically in small chambers and the temperature was measured in the center of them. In addition to the thermocouples the particle temperature in the cylinder was also measured by an infrared camera. More details on the experimental setup are found in [40].
One of the conducted experiments was selected for simulation with the developed DEM particle receiver model. Specifications of this experiment are displayed in table 7.1. This dataset, as well as all other complete and well

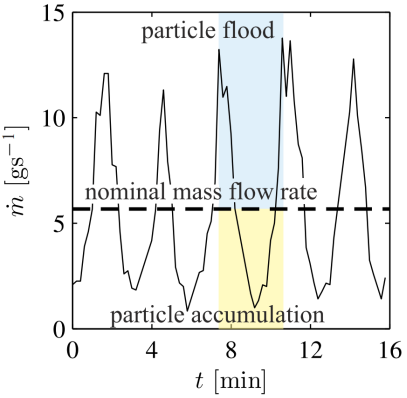

Figure 7.2: Exemplary mass flow fluctuations seen in Wu's experiment, figure from [40]

Table 7.1: Selected experiment from Wu

Property	Value
Mass flow	6 g/s
Incoming Power	5.8 kW
Inclination Angle	45°
Measured outlet temperature	688 °C
Rotation Speed	171 RPM

documented datasets, were obtained while imposing vibrations on the receiver. Unfortunately, no information about these vibrations is available. Due to this lack of information and in order to better understand the periodic mass flow, the vibrations are omitted in the DEM model. It is described in the following section.

7.2 Model Setup

7.2.1 Receiver geometry and particle insertion

From the CAD geometry in figure 7.1 a simplified surface geometry was deduced. It consists of 11 parts which are listed in table 7.2 and make up the receiver shown in figure 7.3. The geometry of the receiver was kept almost exactly the same as in the CAD file, except for the outlet, which had a very

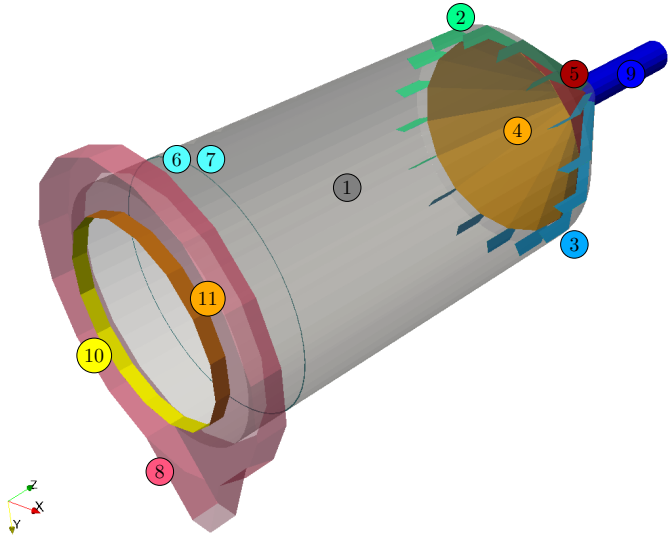

Figure 7.3: Representation of receiver with surface meshes for the simulation environment developed in this work

complex shape. It was replaced by a simple collection ring (8). As the little particle barrier before the outlet was found to be very important in the experiments, it was also included (part 6 and 7). Mesh parts 1-7 were specified as rotating with a period of 0.35 s, which corresponds to 171 RPM like in the experiment. Particles are inserted in a region within the inlet tube at a constant mass insertion rate of $\dot{m} = 6$ g/s every 100 DEM time steps, after an initial filling process during which a mass rate of $\dot{m} = 100$ g/s is filled in within 10 s.

7.2.2 Contact model coefficients

The experiment was conducted with the Carbo HSP13 bauxite particles, whose contact model parameters were calibrated in section 5.2 for smooth, stainless steel as contact partner. Since the interior of the CentRec prototype cylinder has custom-made grooves in the material and is therefore noticeably rougher than the stainless steel plate, modifications of the contact parameters were necessary. It was assumed that all parameters remain the same, except of the wall friction coefficients. To determine them, an additional experiment with the original CentRec prototype cylinder shown in figure 7.4 was conducted. A pile of particles is placed in the empty, horizontal cylinder (figure 7.4(b)).

Table 7.2: Wall boundary conditions

Id	Name	Boundary condition	depth (mm)	ε	c_p $\left(\frac{\text{J}}{\text{kg K}}\right)$	density $\left(\frac{\text{kg}}{\text{m}^3}\right)$	λ_w $\left(\frac{\text{W}}{\text{m K}}\right)$
1	cylinder with conical end	$T_{\text{outside}} = 298$ K	72.5	0.4	1130	400	0.168
2	fins, side A	coupled to 3	1.5	0.4	420	8400	13.4
3	fins, side B	coupled to 2	1.5	0.4	420	8400	13.4
4	feeding cone, side A	coupled to 5	1.5	0.4	420	8400	13.4
5	feeding cone, side B	coupled to 4	1.5	0.4	420	8400	13.4
6	particle barrier, side A	coupled to 7	1.5	0.4	420	8400	13.4
7	particle barrier, side B	coupled to 6	1.5	0.4	420	8400	13.4
8	collection ring	$T_{\text{outside}} = 298$ K	72.5	0.4	1130	400	0.168
9	feeding tube	$T_{\text{outside}} = 298$ K	72.5	0.4	1130	400	0.168
10	aperture, side A	coupled to 11	1.5	0.4	420	8400	13.4
11	aperture, side B	coupled to 10	1.5	0.4	420	8400	13.4

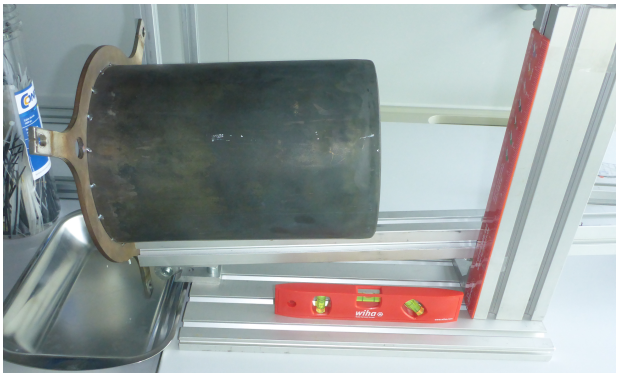

(a) Side view

(b) Front view

Figure 7.4: Experiment to evaluate the roughness of the CentRec prototype

The cylinder is then slowly tilted by manually lifting the 2 meter long bar it is mounted to (figure 7.4(a)). The tilt angle at which all particles have left the cylinder is noted. Due to the high temperatures the cylinder has seen at the particle exit, the roughness is sensibly lower there than at the entrance; this coincides with a color change of the steel. Therefore, two experiments were conducted: one with the pile in the front and one with the pile in the back part of the cylinder. If the particles are placed in the back, the angle at which all particles have left the cylinder is 23°, while it is 19° if the particles are placed in the front part.

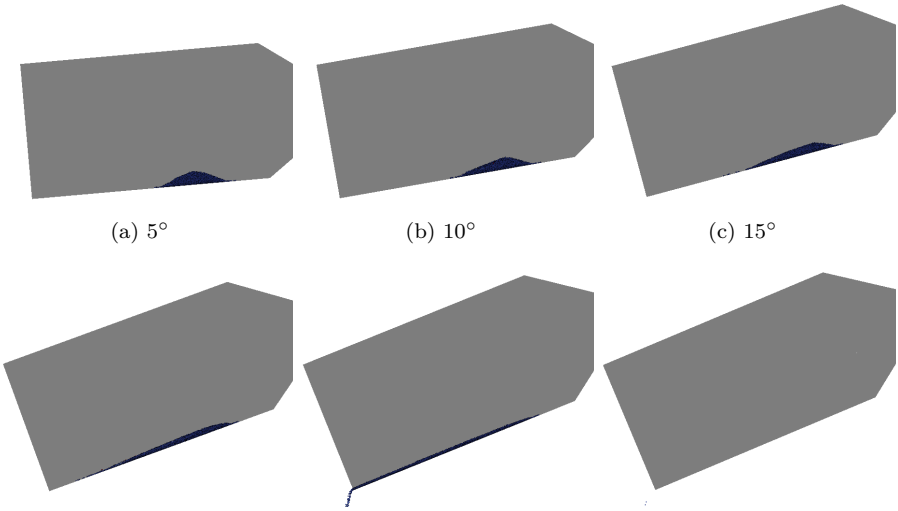

(a) 5° (b) 10° (c) 15°

(d) 20° (e) 22° (f) 22.8°

Figure 7.5: DEM setup of CentRec inclination experiment

The experiment was simulated in LIGGGHTS® as visualized in figure 7.5. The cylinder tilting rotation period was set to 1500 s so that the rotation was sufficiently slow like in the experiment. Figure 7.6 shows the inclination angle at which all particles have left the receiver for various combinations of particle-wall sliding and rolling friction coefficients. It is obvious that the friction parameters determined in figure 5.2 are too low to mimic the behavior in the receiver, which was expected as they were calibrated on the smooth stainless steel surface. It would be desirable to have varying friction values along the length of the receiver. However, in the public version of LIGGGHTS®, only a single rotating geometry can be set which has a single wall friction coefficient. As a compromise it was tried to meet the mean angle of 21°. If sufficiently high, the rolling friction coefficient has little influence on the simulation outcome in the parameter region of interest. A rolling friction value to the wall of $\mu_{\mathrm{R,pw}} = 0.3$ was chosen; this gives a sliding friction of $\mu_{\mathrm{pw}} = 0.37$ to meet the angle of 21°. For simulations with a coarse graining factor of 1.88 the rolling friction value was kept at the original one for smooth steel, $\mu_{\mathrm{R,pw}} = 0.37$. This results in the sliding friction coefficient $\mu_{\mathrm{pw}} = 0.37$, which is the same as in the simulation without coarse-graining. This is consistent with section 5.2, where it was found that coarse graining basically does not affect the particle-wall

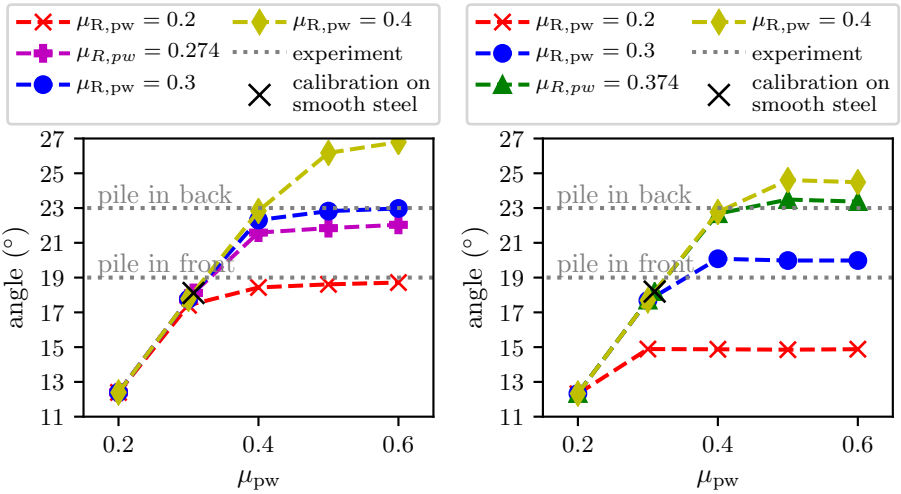

(a) real particle size (b) with coarse graining

Figure 7.6: Inclination angle at which all particles have left the tilted receiver. Shown are DEM simulation results for various particle-wall sliding and rolling friction coefficients and the two experimentally obtained values when the particle pile is placed in either the back or the front part of the receiver

sliding friction coefficient. The final parameter sets for the simulation of the CentRec prototype are given in table 7.3.

Table 7.3: Contact parameters for CentRec prototype simulations

	μ_{pp}	μ_{pw}	$\mu_{R,pp}$	$\mu_{R,pw}$	e_{pp}	e_{pw}
real particle size	0.69	0.37	0.09	0.30	0.74	0.44
coarse grained by factor 1.88	0.42	0.37	0.12	0.37	0.74	0.44

7.2.3 Heat transfer model settings

The boundary conditions for the walls were selected from the possible options described in section 4.3.2.2. For the largest mesh which is the cylinder with the conical end part, a fixed outside temperature condition was selected. This was done to be able to use the effective thermal conductivity of the receiver

walls determined by Wu [40], who assumed this boundary condition for her preliminary heat loss experiments. Because this effective value was available, the rotating cylinder was just modeled by one surface mesh, having the same density and heat capacity as alumina but the optical properties of steel. For all surfaces the emissivity was set to 0.4. The feeding tube and the particle collection ring were given the same properties as the cylinder, because no better information was available and both are rather unimportant regarding the heat losses. All other walls are coupled pairs. A pair is created by copying a surface, moving it a little and inverting the normals, as described in 4.3.2.2. They are necessary to include the solid conduction through the feeding cone with its fins, through the particle barrier and the ring in the aperture. The wall thickness of the steel parts was about 3 mm according to the CAD drawing, so that the thickness of the coupled walls was set to half this value. As no heat capacity and density of the insulation material is given by Wu, values for porous alumina insulation (Altraform KVS 174-400, Rath Group) were used. The steel parts in the receiver were made of Inconel 617 (2.4663), whose properties were obtained from [280]. For the particles, the same heat capacity as in the work of Wu was used (see section 5.1.4). The conductance between wall and particles was calculated according to equation (4.54). As shown in figure 7.7 it is a function of temperature. However, in the current implementation H_w is a constant, so that one value at a specific temperature needs to be selected; here 600 °C was expected to be a reasonable value which gives $H_\mathrm{w} = 0.00156$ W/K for the Carbo HSP13 particles. If coarse-graining with a particle diameter of 3 mm is applied, a value of $H_\mathrm{w}^* = 0.00551$ W/K is obtained from equation (4.56).

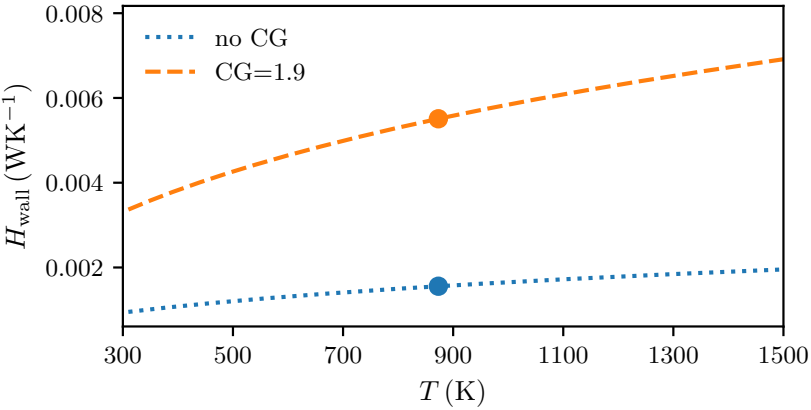

Figure 7.7: Conductance H_w between wall and particle over temperature. Dots indicate the values taken for the simulations

The file with the incoming rays was generated by the in-house ray tracing code SPRAY, which also delivered the input radiation in Wu's work [40]. It traces the rays from the solar simulator and exports the ones which hit the aperture. The flux density in the aperture plane is shown in figure 7.8, once for about 4.5 million rays and once for the number of rays reduced by a factor of 50. The latter was used for the receiver simulations to save computation time.

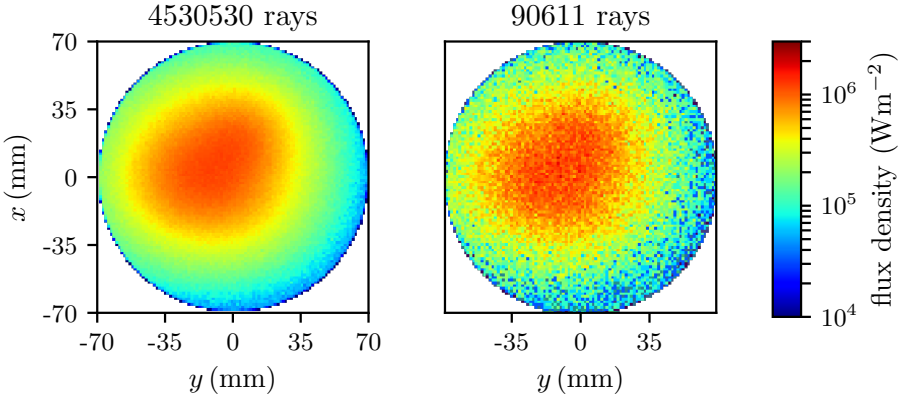

Figure 7.8: Flux density in aperture plane

7.2.4 Coupling

The CentRec prototype rotates with about three rotations per second. This implies a very short coupling time if one would like to calculate the radiation very accurately in every time step, because the positions of the triangles and spheres change rapidly and therefore need to be updated frequently by LIGGGHTS®. However, in most cases we are not interested in temperature changes happening in the millisecond range and therefore we do not require each MCRT step to be accurate, but rather the average of MCRT steps over a longer time period. This enables us to use less rays and a higher coupling time than for an exact radiation solution at every time step. In the simulations presented here the coupling time is 0.05 s, which corresponds to a revolution of 50°. Only one ray per particle is emitted in every MCRT step, which is considered sufficient to describe bulk temperature distributions as discussed in section 6.2.3. The simulations were mostly performed on a machine with two Xeon E5-2697v3 processors and 64 Gb RAM. A 20-minute real time thermal simulation with about 34000 particles of 3 mm diameter needed about 5 days to complete on 16 cores.

7.3 Results and Discussion

7.3.1 Particle flow

Since Wu measured the mass flow at the exit of the collection ring, the same was done in the simulation by counting the particles through a control surface (CS) in a given time interval

$$\dot{m}_{\text{out}} = \frac{1}{\Delta t} \sum_{i=1}^{N_{\text{p,CS}}} m_i \quad , \quad \Delta t = 2 \text{ s} \quad . \tag{7.1}$$

The resulting mass flow is shown in figure 7.9 for the original parameters

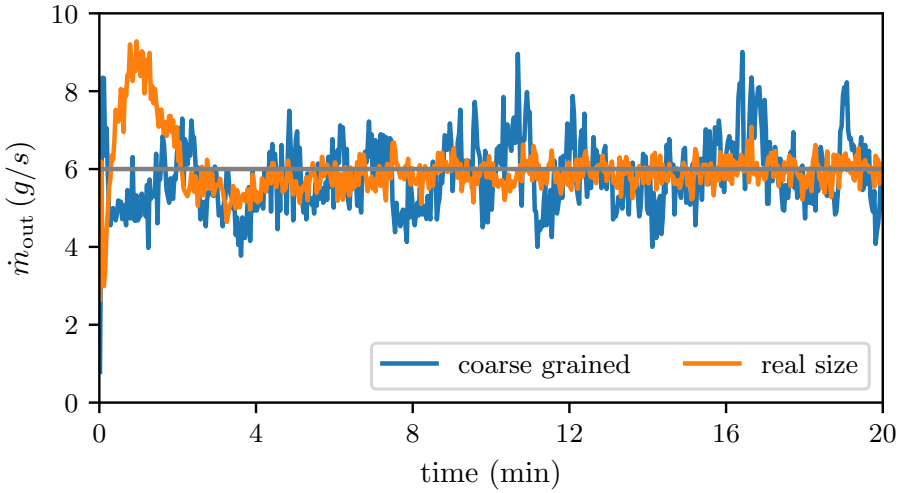

Figure 7.9: Mass flow leaving the receiver collection ring, obtained with original Carbo HSP13 contact parameters calibrated in section 5.2

calibrated in section 5.2. The insertion mass rate of 6 g/s is indicated by the horizontal line. Without coarse graining the mass flow becomes fairly constant after an initial phase which lasts about 4 minutes. If coarse-graining is applied, the mass flow shows more fluctuations, but not like the ones seen in the experiment in figure 7.2. In general the mass flows obtained from coarse grained simulations have more short-time peaks which is reasonable as the mass flow is determined from fewer particles passing the control surface. If the particle-wall friction is increased to account for the rough surface inside the receiver as described in section 7.2.2, both with and without coarse graining the fluctuations of the mass flow increase as depicted in figure 7.10. In the

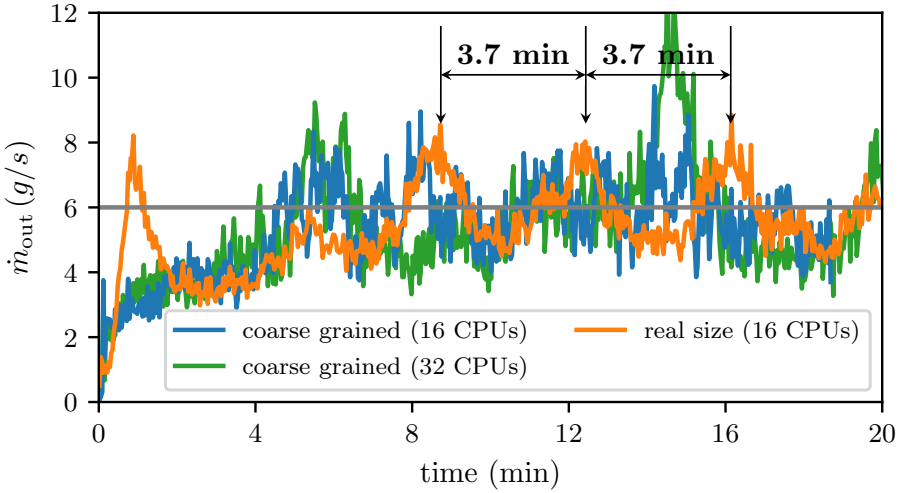

Figure 7.10: Mass flow leaving the receiver collection ring, obtained with modified Carbo HSP13 contact parameters to account for rougher walls according to section 7.2.2. The coarse grained case was calculated two times; once on 16 and once on 32 CPUs.

simulations with real sized particles one can see fluctuations as observed in the experiment, but with lower amplitude. The period is similar, with 3.7 minutes it is only slightly higher than in the exemplary case shown by Wu; in her experimental data one can also find times when the period was 4 minutes and the amplitude was lower. If coarse graining is applied in the DEM simulation, clear periodic oscillations cannot be identified. At many times the mass flows from coarse-graining agree well with the original particle size simulations, but there are also time intervals where this is not the case. No clear pattern can be observed. Interestingly, there are some differences in mass flow when 32 instead of 16 CPUs are used for the calculation of this coarse grained case. This implies that a minor change of particle insertion location as it happened here through the change of processor boundaries affects the particle flow in the receiver significantly. This is in accordance with the general observation that the flow in the receiver is very unstable and minor changes to insertion mass flow or rotation speed can change flow behavior significantly, as it was also observed in initial simulations and in the experiment. The peak occurring in the simulation with the 32 processors is shown in figure 7.11(b) in more detail and shall be investigated in the following.

Therefore the axial mass distribution $m'(z)$ in the receiver was calculated

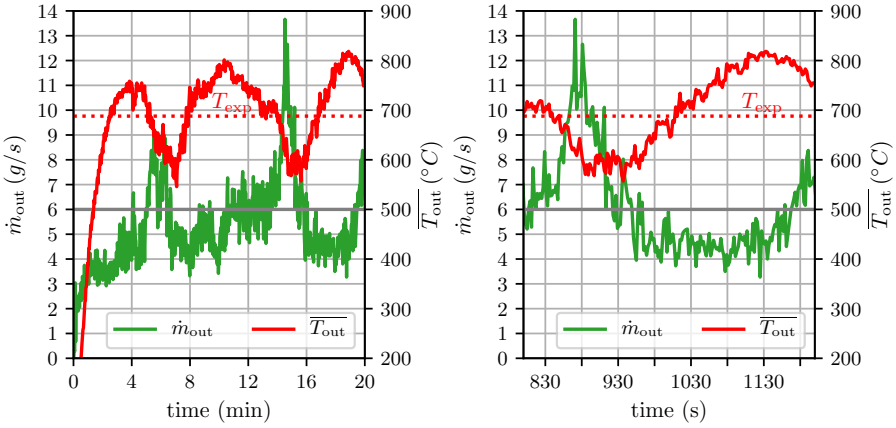

(a) Overview (b) Detail

Figure 7.11: Mass flow and average temperature of the particles leaving the receiver collection ring, obtained from coarse grained simulations with modified Carbo HSP13 parameters from section 7.2.2

according to

$$m'(z) = \frac{1}{\Delta z} \int_{z-\Delta z/2}^{z+\Delta z/2} m(\tilde{z}) \mathrm{d}\tilde{z} \tag{7.2}$$

and shown in figure 7.12 along the normalized receiver axis. The particle barrier is at $z = 0$, the conical part starts at $z = L$. In general, the mass per length and therefore the thickness of the particle film in the receiver decreases on its way to the outlet. At the onset of the peak in figure 7.11(b) at 830 s, it barely changes in the first half of the receiver and then drops towards the particle barrier (the TMR) in a convex curve. Subsequently, the mass near the receiver exit drops at 880 s and the highest outlet mass flow is reached in figure 7.11(b). Interestingly, the film thickness near the receiver entrance remains almost the same. After the outlet mass flow falls below the insertion rate at about 930 s, the film starts to build up again until the mass distribution profile at 1180 s looks similar to the profile at the beginning of the cycle at 830 s.

The magnitude of the axial velocity during these stages is shown in figure 7.14 over the circumferential angle ϕ in the receiver. The circumference was divided into 6° segments in which the axial velocity was averaged during two receiver

revolutions. As expected, at peak outlet mass flow at 880 s the axial velocity is noticeably higher than during the rest of the cycle; this is even true at all circumferential angles. It can also be seen that the circumferential velocity profiles at the different times are similar in shape. For all times the minimum velocity is reached after the lowest point is passed; here gravity acts in the same direction as the centrifugal force, so that the particles are subject to a higher radial force at the wall while the force in the axial direction remains the same. Accordingly the peak velocity is reached after the particles have passed the highest point as gravity and circumferential force act in opposite radial direction. The fact that the minimum and maximum velocities are reached after and not at these respective points is due to the time which is needed for acceleration. As in all stages and all circumferential angles the axial velocity is well below 4 mm/s it can be stated that there is no rapid avalanching going on. This was also seen in the mass distribution, which did not change significantly during one revolution of the receiver. However, we have seen in figure 7.12 that it changes in axial direction over a longer time period. The view in circumferential direction in figure 7.13 shows that the discharge process does not happen uniformly; for example, at 880 s some areas are still completely filled, while for other areas in circumferential direction the film thickness is already significantly reduced. The subsequent buildup of the film is more uniform. Nonuniform distributions mean that there is an unbalance, which imposes undesired forces on the receiver.

It is concluded that even though the particle flow in the receiver is very sensible to small disturbances, i.e. mass flow or rotation speed, the DEM is able to describe the phenomena seen in the experiment, even with coarse-grained simulations. The method enables to analyze the particle motion in the receiver in detail and gives the possibility to quantify expected mass flows and for example unbalances and forces on the receiver, which is hardly possible with other methods.

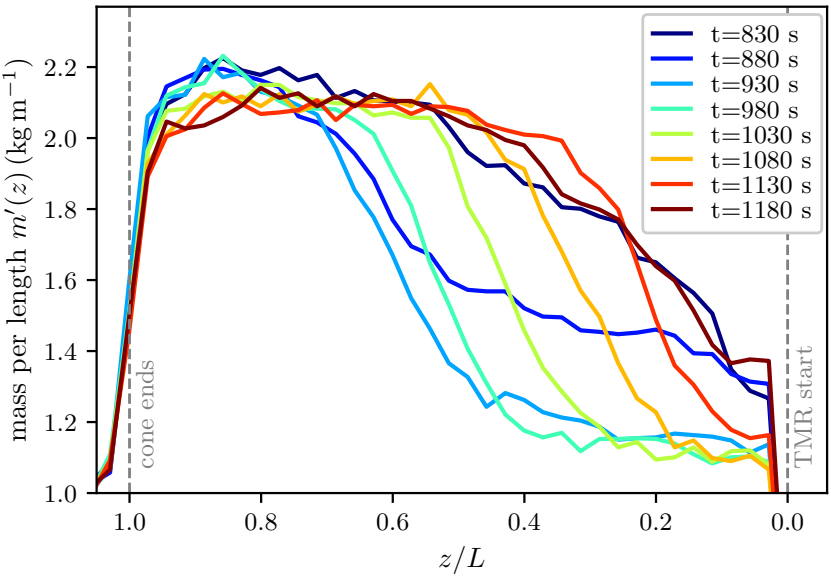

Figure 7.12: Mass distribution along the receiver axis

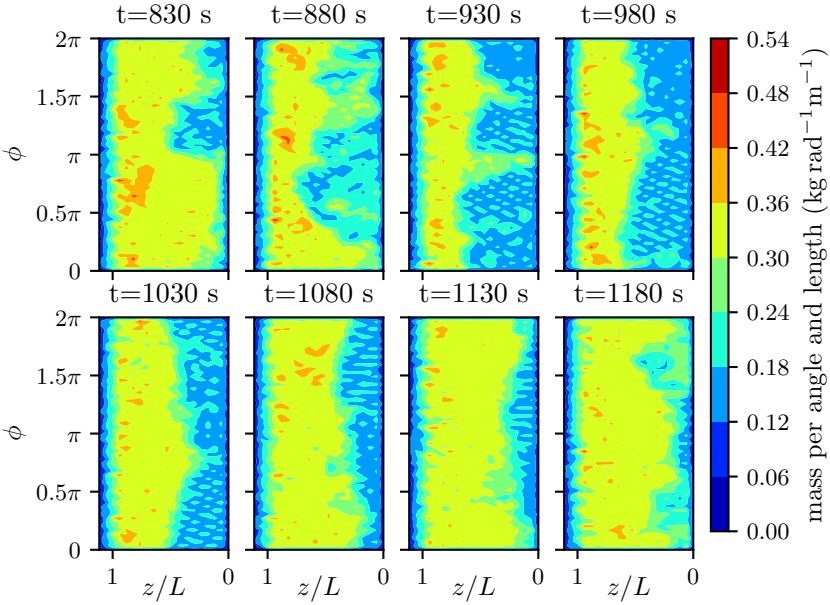

Figure 7.13: Mass distribution on the receiver envelope

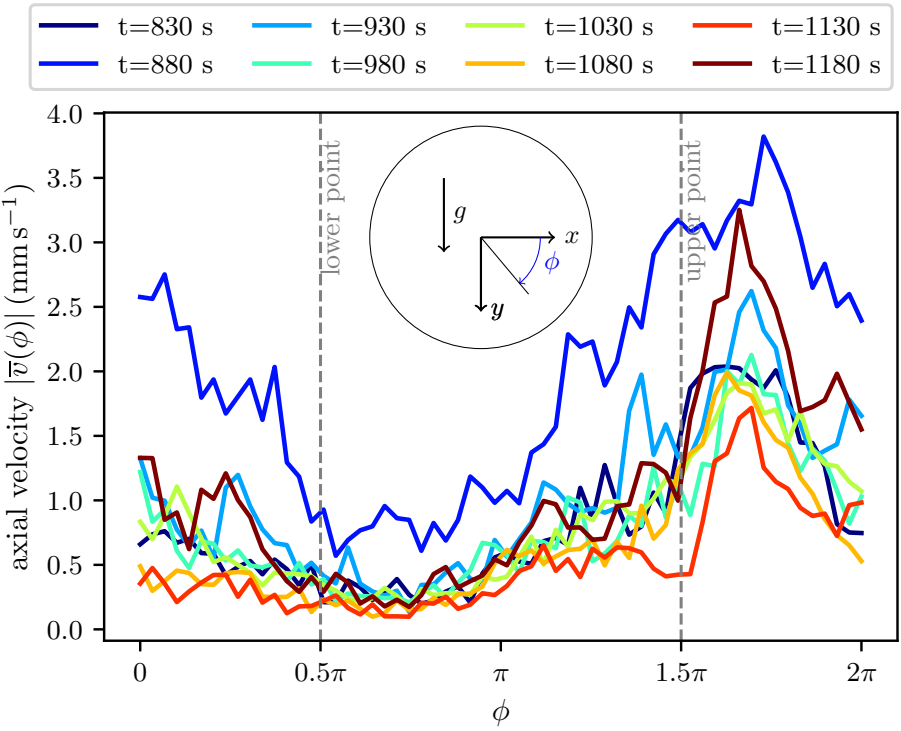

Figure 7.14: Axial particle velocity as a function of the circumferential angle. Averaged over two revolutions

7.3.2 Heat transfer

Regarding heat transfer, Wu's experiment offers the particle outlet temperature, an axial profile of receiver wall temperatures and rather qualitative infrared measurements. This data should be compared to the results obtained with the heat transfer models developed in this work, beginning with the particle outlet temperature, which was measured by the TMR in the experiment. As the particle temperature could equilibrate in this ring, in the simulation the energy-averaged temperature instead of the arithmetic mean was used for comparison. It is calculated by first defining the thermal energy of the particles leaving the collection ring as

$$\dot{Q}_{\mathrm{p,out}} = \frac{1}{\Delta t} \sum_{i=1}^{N_{\mathrm{p,CS}}} m_i \int_{T_{\mathrm{ref}}}^{T_i} c_{p,\mathrm{p}}(\tilde{T})\mathrm{d}\tilde{T} \quad , \quad T_{\mathrm{ref}} = 25^{\circ}\mathrm{C} \tag{7.3}$$

and then interpolating the energy-averaged particle outlet temperature $\overline{T_{\mathrm{out}}}$ from

$$\int_{T_{\mathrm{ref}}}^{\overline{T_{\mathrm{out}}}} c_{p,\mathrm{p}}(\tilde{T})\mathrm{d}\tilde{T} = \frac{\dot{Q}_{\mathrm{p,out}}}{\dot{m}_{\mathrm{out}}} \quad . \tag{7.4}$$

Due to the oscillating mass flow, $\overline{T_{\mathrm{out}}}$ also oscillates as shown in figure 7.11. When the outlet mass flow rises, the outlet temperature drops, which can be expected as the incoming radiative heat flow remains the same. In the experimental data of Wu temperature fluctuations of about 100 K could be observed, but no consistent dataset is available as she reduced the oscillations by the application of uncharacterized vibrations. Therefore the measured steady state outlet temperature is shown as a single value, indicated by a dashed horizontal line. The simulated temperatures oscillate around this line, so that a good agreement between simulation and experiment can be concluded.
In figure 7.16 the heat flows to the walls and to the particles as well as the radiative heat losses by reflection and emission through the aperture are depicted. The corresponding temperatures of particles and wall surfaces are shown in figure 7.15 with the colors and numbering of the receiver parts in figure 7.3. At the beginning of the heating process, there are almost no losses by emission as everything is at ambient temperature. With increasing temperature less input power ends up in the particles and the walls, as more is lost by emission through the aperture. The lost heat by reflection of the incoming radiation remains constant as the receiver is constantly filled with particles and the direction of the incoming irradiation does not change. Already after about 4 minutes the average temperature of the particles and the cylinder walls reaches a plateau and is then mostly influenced by the transient particle

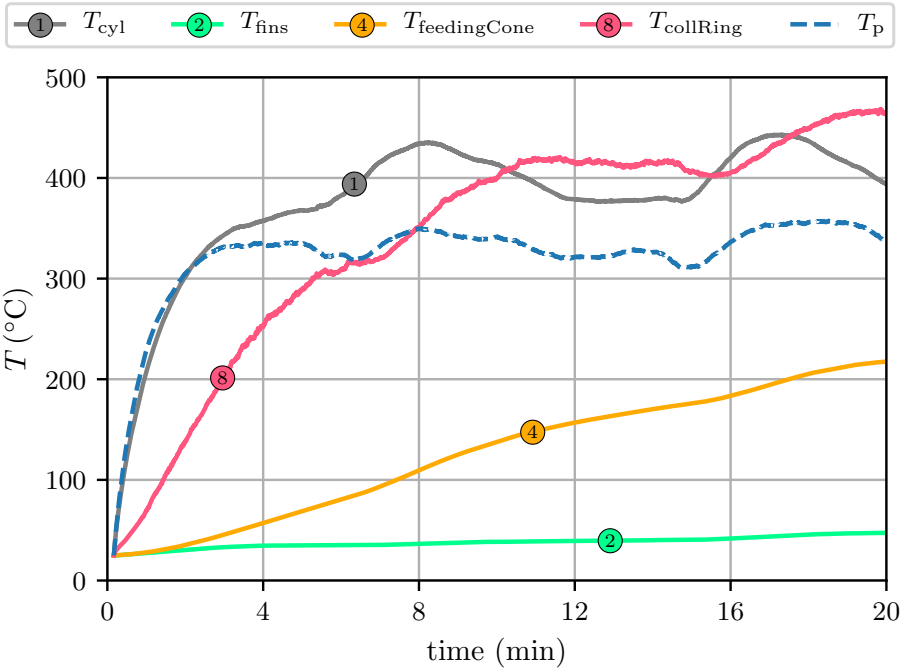

Figure 7.15: Averaged wall and particle temperatures

flow. Since the collection ring is not irradiated directly but is only heated by particles pouring though it or by radiation from other walls, it heats up significantly slower. This is even stronger the case for the feeding cone, which is basically only heated by indirect radiation emitted or reflected from walls or particles. Even though these parts are nowhere near thermal equilibrium, the major insulation losses go into the rotating cylinder.
From the heat flows, the thermal receiver efficiency can be calculated as

$$\eta_{\mathrm{th,Sim}} = \frac{\Sigma \dot{Q}_{\mathrm{p}}}{\dot{Q}_{\mathrm{solar}}} \quad . \tag{7.5}$$

It is in good agreement with the experimentally obtained efficiency of 0.77 by Wu [40], which is indicated by the dashed line in figure 7.16.
If the particle outlet temperature and the average particle temperature in the cylinder are compared, a big difference can be noticed; while the outlet temperature fluctuates around 700 °C with peaks above 800 °C, the average particle temperature in the receiver fluctuates around 330 °C. This is caused

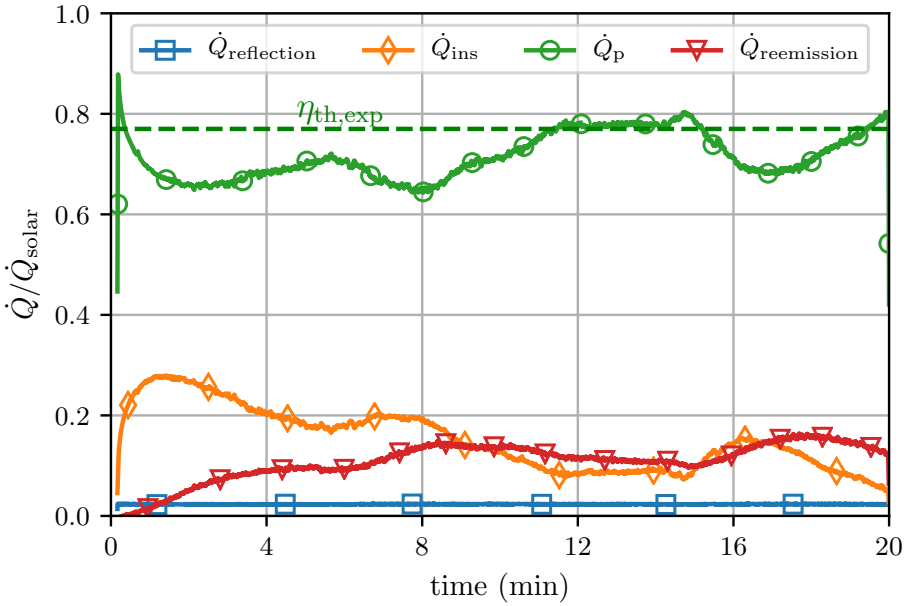

Figure 7.16: Simulated heat flows to walls and particles, simulated and experimental absorption efficiency

by the incoming radiation not reaching the back of the receiver, which can be seen in figure 7.17. It shows the average heat source term for a single particle in axial and circumferential direction. The incoming radiation basically only hits the lower front half of the receiver. Accordingly, the particles remain relatively cold in the back part of the receiver as shown in figure 7.18. Since the particles in front are hot and see the cold particles in the back, they actually cool down by emission when they are in the upper part of the receiver and the heat source term is negative in figure 7.17. However, this does not lead to substantial temperature differences in circumferential direction as the rotational speed of the receiver is very high. This also demonstrates the assumption to couple the DEM code with the separate C++ program only every 0.05 s to be valid.
In the experiment the temperature distribution in the receiver was measured by a staggered array of thermocouples placed on the outer surface of the rotating cylinder, therefore not measuring the particle but wall temperature as visualized in figure 7.19(b). The temperature distribution Wu interpolated from the thermocouples in figure 7.19(a) is in good qualitative agreement with the simulated temperature distributions in figure 7.18. However, the temperature near the outlet is substantially higher in the simulation than in the experiment,

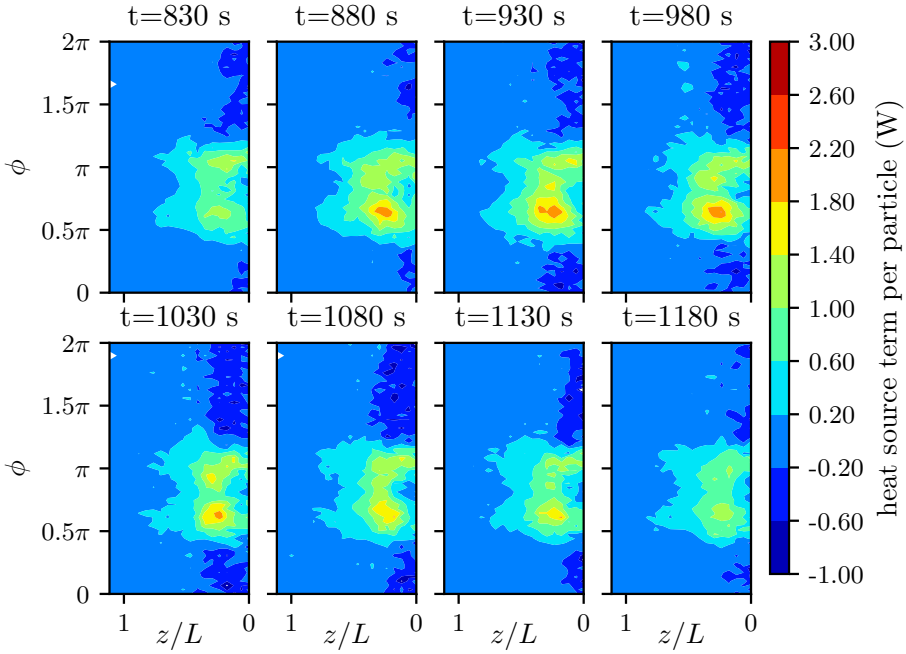

Figure 7.17: Average heat gain of a single particle in the receiver

which is better seen in the axial temperature profile in figure 7.20. The figure shows the measured wall temperature and the particle temperature gathered from averaging the TMR ring measurements. In addition the wall and particle temperature profiles calculated by the thermal DEM model from this work are shown for three different times; also the simulated particle temperatures at the outlet of the collection ring are shown as squares; they are not necessarily in line with the temperature profile as they were energy-averaged as described above, while the other temperatures are arithmetic mean values. While the experiment and simulation agree well in the back part of the receiver, a significant deviation in the front part is observed. This was also seen by Wu when she compared the experimental results to a 1D model of the receiver, which also predicted higher particle temperatures than seen in the experiment.

Wu mentioned several possible reasons for this behavior, for example that the wall temperature is measured, but the particle temperature is simulated in her 1D model. She suspects a difference between these temperatures and also an influence of the particle film thickness. However, the results of the more detailed model presented here show almost no difference between wall tem-

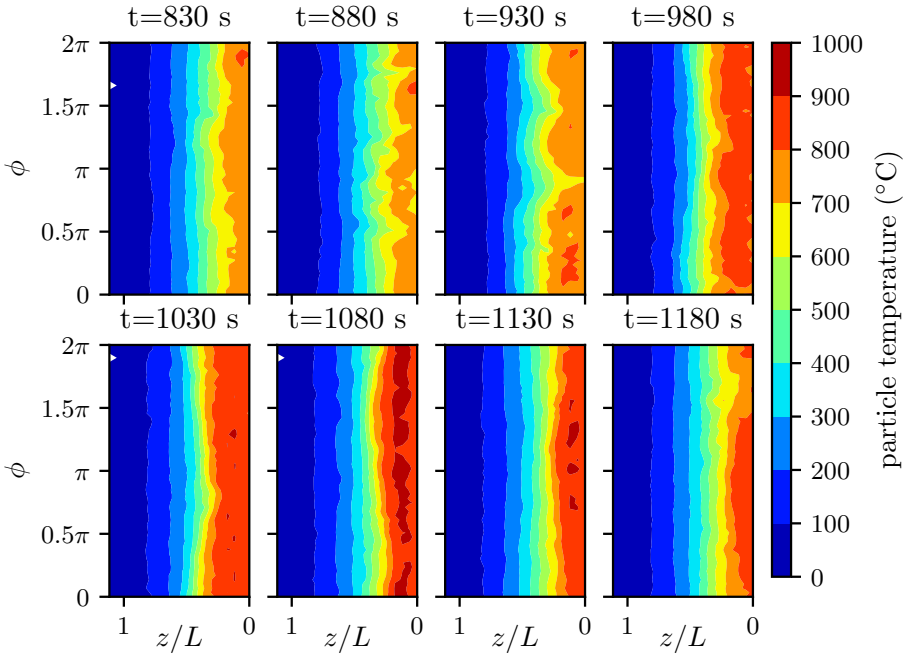

Figure 7.18: Simulated particle temperature distribution in the receiver

perature and particle temperature. Only in the TMR there is a significant difference, which is due to the high axial speed of the particles in this section and therefore the little time to exchange heat with the walls. Wu also mentions the missing capability of her model to capture particle preheating by convection and axial conduction in the particle film. This would in fact decrease the particle temperature in the receiver front, but it should also increase the temperature in the back significantly. As this is not case in the experiment, the most probable reason for the difference between the models and the experiment is expected to be the uncertainty in the incoming heat flux distribution. Wu's error analysis showed that it has a strong influence on the model results and as the same distribution was used in this work, it is also expected to have a strong influence here and the main reason for the deviations.

In summary, the developed heat transfer models were applied successfully to the CentRec particle receiver prototype. A good agreement of the particle outlet temperature and of the receiver efficiency with their experimental counterparts was found. The axial temperature profile deviated in a similar way from the experimental data like the one-dimensional model from Wu, so that

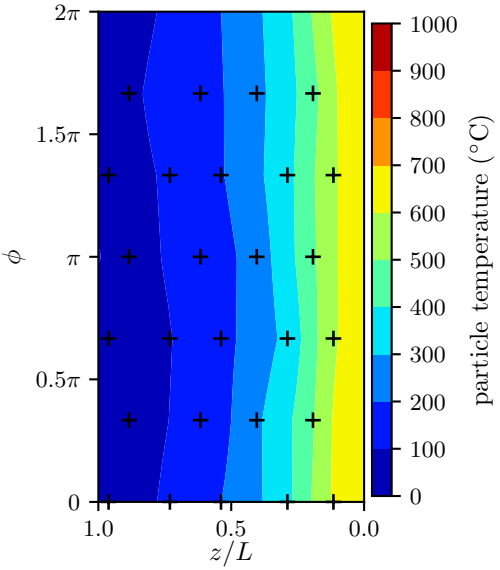

(a) Wall temperature distribution

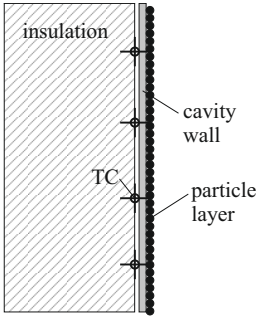

(b) Placement of thermocouples, image from Wu [40]

Figure 7.19: Wall temperature distribution measured and interpolated by Wu [40]. Crosses indicate thermocouple locations

the deviation is suspected to come from an inaccurate radiation profile measurement.

In general the DEM has shown to enable an unmatched, rigorous and in-depth analysis of the mechanisms occurring in the CentRec. The influence of the receiver angle, the mass flow and the rotation speed are just some of the examples to be investigated by a simple application of the developed model in the future[1].

[1] Unfortunately the respective simulations could not be completed in scope of this work because of a severe hard disk and backup system failure of the DLR computer cluster in Jülich

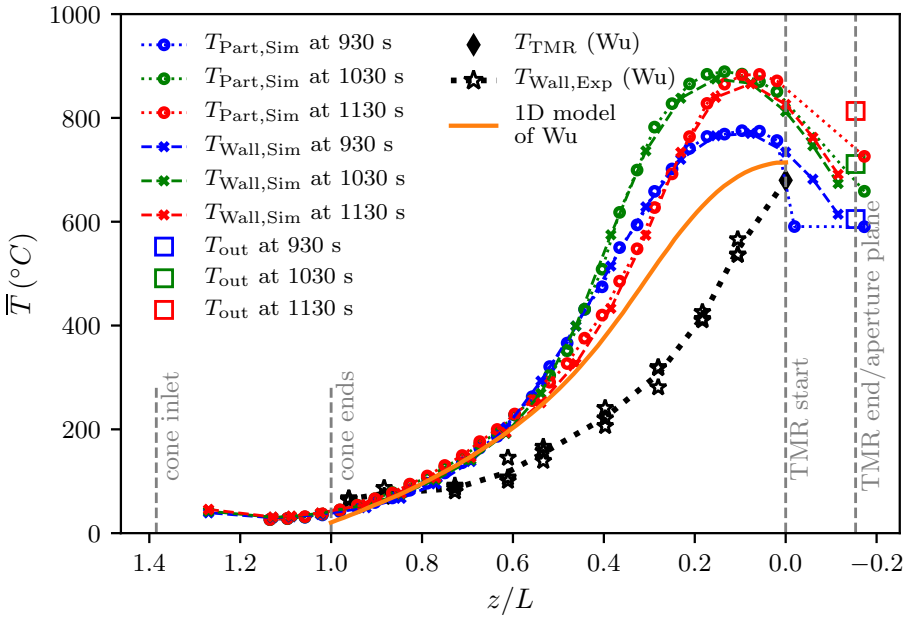

Figure 7.20: Comparison of axial temperature profile to the experiments of Wu [40]

8 Conclusions and Outlook

The objective of this work was the development of models and the determination of parameters to enable the DEM simulation of a solar particle receiver, including heat transfer. Special attention was paid to vacuum receiver-reactors, which are proposed for solar thermochemical redox cycles for fuel production. It was found that the available DEM heat transfer models are not sufficient to accurately describe the phenomena in a solar particle receiver, so that new models were developed in this work. For heat transfer between neighboring particles a relationship connecting the thermal conductivity of a continuous particle bed with the discrete thermal conductance between two particles was developed. In this context it was shown how the usual approach of updating the temperature in DEM relates to the heat diffusion equation of the continuum. Additionally, a critical time step for the temperature update in DEM was derived. Both the connection to the continuum and the stability limit were validated successfully by a cylindrical bed test case.

The approach to connect a continuum model with the DEM makes it possible to use existing and established continuum models for the bed conductivity. In this way, the pressure dependence necessary for vacuum receivers was included by using the model of Zehner, Bauer and Schlünder (ZBS). This model is widely used and accepted, but was never tested at both high temperatures and vacuum. Hence this was done in scope of this thesis in a vacuum experiment in a solar simulator. Transient temperatures in an irradiated particle bed were measured and compared with the temperatures from a continuum simulation including the ZBS model. A good agreement was found for various vacuum pressures; the bed conductivity decreased with the pressure as expected. The mean relative deviation between experimental and simulated temperature averaged over all experiments was between 4.2 % and 8.8 % for the respective thermocouple locations in the bed. These results are within the margin of uncertainties introduced both by model parameters and by measurement errors.

Due to its architecture, each particle can only interact with particles in its neighborhood in the DEM code. This was the main motivation to treat radiation heat transfer in a separate C++ program, as it also occurs over long distances. The program calculates radiative heat exchange by radiation distribution factors, which are determined by Monte Carlo ray tracing (MCRT).

This is beneficial for particle receivers where it can be assumed that particles cannot see each other over long distances. In these cases, only the distribution factors from walls to particles need to be calculated and reciprocity can be used to obtain the distribution factors from particles to walls. Radiative transport between particles can be included in the particle-particle model by using the radiation term of the ZBS model. One does not need to shoot rays from the particles, which reduces the computational cost significantly. The developed program can handle spheres and surface meshes with triangular elements. It was parallelized with OpenMP and shows good parallel performance. To include external radiation, for example from a heliostat field, rays can be loaded from a text file. The radiation calculation was ensured to work correctly by various test cases. A comparison to the radiative part of the ZBS continuum model showed remarkable agreement given the simplicity of the ZBS model approach, which is based on the radiative exchange in a narrow gap between infinite planes.

Beside the radiation calculation, particle-wall heat transfer was also added to the separate C++ program, as the original DEM software only allowed a wall with a constant, uniform temperature. With the added wall model each triangle in the surface mesh has its own temperature and the heat transfer between particle and wall is derived from the Schlünder model dedicated to particle-wall heat transfer. The implemented model was validated by a drum test case from literature. The heat transfer through the wall is modeled by virtually expanding the triangular mesh elements into prisms and solving the one-dimensional heat diffusion equation along them. Several boundary conditions on the outside of the mesh can be selected. The correctness of this model was checked with a test case consisting of two walls with a narrow gap between them. This case can be represented by a thermal resistance network and is also another, indirect test of the radiation model. The deviation of the model from the resistance network solution was about 0.001 %, showing successful validation.

For a DEM simulation of a solar receiver, not only suitable heat transfer models are required, but also parameters for the contact force models. Therefore a calibration approach based on bulk experiments was developed. Five experiments were designed and the sensitivity of each one to the contact parameters was investigated. The results indicated to do the calibration in three stages: first, the determination of the friction coefficients between particles, then between particles and walls and finally the determination of restitution coefficients. In each stage, surrogate models of the DEM model were created by Latin hypercube sampling to speed up the optimization process. In this way contact parameters for five prospective particle types envisaged in solar receivers were calibrated. The calibration was also performed for various coarse-grained par-

ticle diameters to enable faster simulations with fewer particles. The obtained parameter sets are the first ones obtained for these particle types, so that they will be helpful to other researchers who may need them for the simulation of solar receivers.

Finally, the developed models were demonstrated on the CentRec prototype receiver. The outlet mass flow fluctuations observed in experiments could also be seen in the simulations, which were conducted with exactly the same dimensions, rotation speed and mass flow as the experiment. It shows the power of the method, as this oscillation phenomenon could not be covered with other methods before. The results indicate that the appearance and the magnitude of the fluctuations is strongly affected by the friction between particle and wall. In general the flow pattern in the receiver is quite unstable. An analysis of the mass distribution in the receiver showed that the mass flow fluctuations at the outlet go along with periodic slow buildup of film thickness in the front part of the receiver, followed by a faster depletion. In contrast, the film thickness in the back near the feeding cone does not fluctuate that much. The simulations confirmed the expectation that particles do the majority of the axial movement when they are in the upper half of the rotation cycle as in that state the gravity and centrifugal force do not act in the same direction. With respect to heat transfer, the DEM model also gave sound results. The particle outlet temperature fluctuated due to the mass flow oscillations, and it did so around the average temperature obtained in the experiment. Moreover, the thermal receiver efficiency was found to be in good agreement with the efficiency measured during experiments (77 %). However, the axial temperature profile deviated from the measured one quite significantly, but in a very similar way like a previously developed 1D model. This led to the conclusion that the error can be attributed to uncertainties in the incoming flux profile. The uniformity of the temperature profile in circumferential direction with at the same time a very nonuniform input flux profile proved that it was justified to perform ray tracing only about three times per rotation and not in every DEM time step.

In summary, this work paves the way for further DEM simulations of solar particle receivers. As the demonstration of the model has shown, it is possible to simulate a prototype receiver in a reasonable time and to obtain new insights about effects which could not be covered before with other methods. If a real time duration in the order of hours is desired, real-size receivers can only be simulated with the real particle size on large compute clusters. However, even today it is possible to simulate them with a reasonable effort by using coarse-graining; aspects of the operation happening on the time scale of a few minutes can also be captured with real-size particles. In the special case of non-moving particles, the developed models can be applied to simulate radiation and heat

transfer between millions of particles and walls for a duration of multiple hours. This is possible due to the increased time step for heat transfer, whose limit was derived for the first time in this thesis. A scenario where this can be applied is the prototype of a particle-mix reactor, which is currently investigated at DLR. During a mixing process, which lasts a few seconds, a small time step is chosen and particle motion is calculated. Once a mixture is generated and the particles stop moving, motion calculation is deactivated and the time step is increased significantly.

The presented work should be the basis for future model developments and analysis of particle receivers. With the developed MCRT model it is possible to validate other, more inaccurate but faster methods for solving the radiative heat transfer. One of them, the discrete ordinate method, is not dependent on the particle number. Missing coupling terms should be developed and implemented for the coupling of LIGGGHTS and OpenFOAM to be able to use the method. With the CFD-DEM coupling also the convection influence in the CentRec receiver could be tackled, which was omitted in this work. As the method is just being establishing in industry, significant improvements in speed are expected in the future, for example by using GPUs or by approaches like adaptive coarse-graining. Together with hardware improvements this will enable the full simulation of real-size receivers in the near future.

Bibliography

[1] IEA. *World Energy Balances 2018: Overview*. Technical report. Paris, France: International Energy Agency, Aug. 2018.

[2] IPCC. *Climate Change 2014: Synthesis Report. Contribution of Working Groups I, II and III to the Fifth Assessment Report of the Intergovernmental Panel on Climate Change [Core Writing Team, R.K. Pachauri and L.A. Meyer (eds.)]* Technical report. Geneva, Switzerland: IPCC, 2014. 151 pp.

[3] IRENA. *Global Energy Transformation: A roadmap to 2050*. Technical report. Abu Dhabi: International Renewable Energy Agency, 2018.

[4] Forrester, J. "The Value of CSP with Thermal Energy Storage in Providing Grid Stability." In: *Energy Procedia* 49 (2014), pp. 1632–1641. DOI: 10.1016/j.egypro.2014.03.172.

[5] Pitz-Paal, R. "Concentrating solar power: Still small but learning fast." In: *Nature Energy* 2, 17095 (2017), pp. 1–2. DOI: 10.1038/nenergy.2017.95.

[6] Lilliestam, J., Labordena, M., et al. "Empirically observed learning rates for concentrating solar power and their responses to regime change." In: *Nature Energy* 2, 17094 (2017), pp. 1–6. DOI: 10.1038/nenergy.2017.94.

[7] Nzihou, A., Flamant, G., and Stanmore, B. "Synthetic fuels from biomass using concentrated solar energy - A review." In: *Energy* 42.1 (2012), pp. 121–131. DOI: 10.1016/j.energy.2012.03.077.

[8] Muhich, C. L., Ehrhart, B. D., et al. "A review and perspective of efficient hydrogen generation via solar thermal water splitting." In: *Wiley Interdisciplinary Reviews: Energy and Environment* 5.3 (2016), pp. 261–287. DOI: 10.1002/wene.174.

[9] Siegel, N. P., Miller, J. E., et al. "Factors Affecting the Efficiency of Solar Driven Metal Oxide Thermochemical Cycles." In: *Industrial & Engineering Chemistry Research* 52.9 (2013), pp. 3276–3286. DOI: 10.1021/ie400193q.

[10] Marxer, D., Furler, P., et al. "Demonstration of the Entire Production Chain to Renewable Kerosene via Solar Thermochemical Splitting of H2O and CO2." In: *Energy & Fuels* 29.5 (2015), pp. 3241–3250. DOI: 10.1021/acs.energyfuels.5b00351.

[11] Neises von Puttkamer, M., Roeb, M., et al. "Solar Aluminum Recycling in a Directly Heated Rotary Kiln." In: *REWAS 2016: Towards Materials Resource Sustainability.* Ed. by Kirchain, R. E., Blanpain, B., et al. Cham, Switzerland: Springer International Publishing, 2016, pp. 235–240. DOI: 10.1007/978-3-319-48768-7_35.

[12] Piatkowski, N. and Steinfeld, A. "Solar-driven coal gasification in a thermally irradiated packed-bed reactor." In: *Energy & Fuels* 22.3 (2008), pp. 2043–2052. DOI: 10.1021/ef800027c.

[13] Meier, A., Bonaldi, E., et al. "Solar chemical reactor technology for industrial production of lime." In: *Solar Energy* 80 (10 2006), pp. 1355–1362. DOI: 10.1016/j.solener.2005.05.017.

[14] Ho, C. K. "6 - A new generation of solid particle and other high-performance receiver designs for concentrating solar thermal (CST) central tower systems." In: *Advances in Concentrating Solar Thermal Research and Technology.* Ed. by Blanco, M. J. and Santigosa, L. R. Woodhead Publishing Series in Energy, 2017, pp. 107–128. DOI: 10.1016/B978-0-08-100516-3.00006-X.

[15] Ermanoski, I., Siegel, N. P., and Stechel, E. B. "A new reactor concept for efficient solar-thermochemical fuel production." In: *Journal of Solar Energy Engineering* 135.3, 031002 (2013), pp. 1–10. DOI: 10.1115/1.4023356.

[16] Singh, A., Lapp, J., et al. "Design of a pilot scale directly irradiated, high temperature, and low pressure moving particle cavity chamber for metal oxide reduction." In: *Solar Energy* 157 (2017), pp. 365–376. DOI: 10.1016/j.solener.2017.08.040.

[17] Sakai, M. "How Should the Discrete Element Method Be Applied in Industrial Systems?: A Review." In: *KONA Powder and Particle Journal* 33 (2016), pp. 169–178. DOI: 10.14356/kona.2016023.

[18] Sandlin, M. J. "Experimental Verification of Numerical Models of Granular Flow Through Wire Mesh Screens." PhD thesis. Georgia Institute of Technology, 2017.

[19] Sandlin, M. and Abdel-Khalik, S. I. "A study of granular flow through horizontal wire mesh screens for concentrated solar power particle heating receiver applications – Part I: Experimental studies and numerical model development." In: *Solar Energy* 169 (2018), pp. 1–10. DOI: 10.1016/j.solener.2018.03.036.

[20] Sandlin, M. and Abdel-Khalik, S. I. "A study of granular flow through horizontal wire mesh screens for concentrated solar power particle heating receiver applications – Part II: Parametric model predictions." In: *Solar Energy* 174 (2018), pp. 1252–1262. DOI: 10.1016/j.solener.2018.04.042.

[21] Zanino, R., Ho, C. K., et al. "Preliminary discrete element modeling of a falling particle curtain for CSP central tower receivers." In: vol. 1734. 1. 2016. DOI: 10.1063/1.4949091.

[22] Morris, A. B., Ma, Z., et al. "Simulations of heat transfer to solid particles flowing through an array of heated tubes." In: *Solar Energy* 130 (2016), pp. 101–115. DOI: 10.1016/j.solener.2016.01.033.

[23] Bellan, S., Matsubara, K., et al. "CFD-DEM investigation of particles circulation pattern of two-tower fluidized bed reactor for beam-down solar concentrating system." In: *Powder Technology* 319 (2017), pp. 228–237. DOI: 10.1016/j.powtec.2017.06.060.

[24] Bellan, S., Gokon, N., et al. "Numerical and experimental study on granular flow and heat transfer characteristics of directly-irradiated fluidized bed reactor for solar gasification." In: *International Journal of Hydrogen Energy* 43.34 (2018). DOI: 10.1016/j.ijhydene.2018.06.033.

[25] Bellan, S., Kodama, T., et al. "Heat transfer and particulate flow analysis of a 30 kW directly irradiated solar fluidized bed reactor for thermochemical cycling." In: *Chemical Engineering Science* (2018). In press. DOI: 10.1016/j.ces.2018.09.012.

[26] Bellan, S., Matsubara, K., et al. "A CFD-DEM study of hydrodynamics with heat transfer in a gas-solid fluidized bed reactor for solar thermal applications." In: *International Journal of Heat and Mass Transfer* 116 (2018), pp. 377–392. DOI: 10.1016/j.ijheatmasstransfer.2017.09.015.

[27] Kloss, C., Goniva, C., et al. "Models, algorithms and validation for opensource DEM and CFD-DEM." In: *Progress in Computational Fluid Dynamics, an International Journal* 12.2 (2012), pp. 140–152. DOI: 10.1504/PCFD.2012.047457.

[28] *Concentrating Solar Power Projects*. National Renewable Energy Laboratory. URL: https://solarpaces.nrel.gov, Seen on 08/17/2018.

[29] Romero, M. and González-Aguilar, J. "7 - Next generation of liquid metal and other high-performance receiver designs for concentrating solar thermal (CST) central tower systems." In: *Advances in Concentrating Solar Thermal Research and Technology*. Ed. by Blanco, M. J. and Santigosa, L. R. Woodhead Publishing Series in Energy, 2017, pp. 129–154. DOI: 10.1016/B978-0-08-100516-3.00007-1.

[30] *GE's STF-D Series Reheat Steam Turbines*. General Electric. URL: https://www.ge.com/power/steam/steam-turbines/reheat, Seen on 09/13/2018.

[31] *Breakthroughs in Steam Conditions*. Mitsubishi Hitachi Power Systems, Ltd. URL: http://www.mhps.com/products/steamturbines/performance/index.html, Seen on 09/13/2018.

[32] Schrader, A. J., De Dominicis, G., et al. "Solar electricity via an Air Brayton cycle with an integrated two-step thermochemical cycle for heat storage based on Co3O4/CoO redox reactions III: Solar thermochemical reactor design and modeling." In: *Solar Energy* 150 (2017), pp. 584–595. DOI: 10.1016/j.solener.2017.05.003.

[33] Buck, R. and Giuliano, S. "Solar Tower System Temperature Range Optimization for Reduced LCOE." In: *SolarPACES2018* (Casablanca, Marocco). Oct. 3, 2018.

[34] Ho, C. K. "A review of high-temperature particle receivers for concentrating solar power." In: *Applied Thermal Engineering* 109, Part B (2016), pp. 958–969. DOI: 10.1016/j.applthermaleng.2016.04.103.

[35] Baumann, T. and Zunft, S. "Development and Performance Assessment of a Moving Bed Heat Exchanger for Solar Central Receiver Power Plants." In: *Energy Procedia* 69 (2015), pp. 748–757. DOI: 10.1016/j.egypro.2015.03.085.

[36] Diago, M., Iniesta, A. C., et al. "Characterization of desert sand to be used as a high-temperature thermal energy storage medium in particle solar receiver technology." In: *Applied Energy* 216 (2018), pp. 402–413. DOI: 10.1016/j.apenergy.2018.02.106.

[37] Smith, D. C. "Design and Optimization of Tube-Type Receiver Panels for Molten Salt Applications." In: *ASME Solar Energy Conference* (Maui, USA). Vol. 2. Apr. 1992, pp. 1029–1036.

[38] Vant-Hull, L. L. "The Role of "Allowable Flux Density" in the Design and Operation of Molten-Salt Solar Central Receivers." In: *Journal of Solar Energy Engineering* 124.2 (2002), pp. 165–169. DOI: 10.1115/1.1464124.

[39] *CARBOHSP. High-strength sintered bauxite proppant.* CARBO Ceramics Inc. 2010.

[40] Wu, W. "A Centrifugal Particle Receiver for High-temperature Solar Applications." PhD thesis. RWTH Aachen, 2015.

[41] Bauer, T., Breidenbach, N., et al. "Overview of molten salt storage systems and material development for solar thermal power plants." In: *World Renewable Energy Forum* (Denver, USA). Vol. 2. 2012, pp. 837–844.

[42] Tan, T., Chen, Y., et al. "Wind Effect on the Performance of Solid Particle Solar Receivers with and without the Protection of an Aerowindow." In: *Solar Energy* 83.10 (2009), pp. 1815–1827. DOI: 10.1016/j.solener.2009.06.014.

[43] Falcone, P., Hackett, C., and Noring, J. "Evaluation and application of solid thermal energy carriers in a high temperature solar central receiver system." In: *Proceedings of the Seventeenth Intersociety Energy Conversion Engineering Conference* (Los Angeles, USA). New York: Institute of Electrical and Electronics Engineers, Aug. 8, 1982, pp. 1498–1503.

[44] Falcone, P., Noring, J., and Hruby, J. *Assessment of a solid particle receiver for a high temperature solar central receiver system.* Technical report SAND85-8208. Livermore, USA: Sandia National Laboratories, Feb. 1985.

[45] Martin, J. and Vitko Jr, J. *ASCUAS: a solar central receiver utilizing a solid thermal carrier.* Technical report SAND82-8203. Livermore, USA: Sandia National Laboratories, Jan. 1982.

[46] Hruby, J. and Burolla, V. *Solid Particle Receiver Experiments: Velocity Measurements.* Technical report SAND84-8238. Livermore, USA: Sandia National Laboratories, Oct. 1984.

[47] Hruby, J., Steele, B., and Burolla, V. *Solid Particle Experiments: Radiant Heat Test.* Technical report SAND84-8251. Livermore, USA: Sandia National Laboratories, Dec. 1984.

[48] Hruby, J. *Technical feasibility study of a solid particle solar central receiver for high temperature applications.* Technical report SAND86-8211. Livermore, USA: Sandia National Laboratories, Mar. 1986.

[49] Hruby, J., Steeper, R., et al. "An experimental and numerical study of flow and convective heat transfer in a freely falling curtain of particles." In: *Journal of fluids engineering* 110.2 (1988), pp. 172–181. DOI: 10.1115/1.3243531.

[50] Rightley, M., Matthews, L., and Mulholland, G. "Experimental characterization of the heat transfer in a free-falling-particle receiver." In: *Solar Energy* 48.6 (1992), pp. 363–374. DOI: 10.1016/0038-092X(92)90045-C.

[51] Siegel, N. P., Ho, C. K., et al. "Development and Evaluation of a Prototype Solid Particle Receiver: On-Sun Testing and Model Validation." In: *Journal of Solar Energy Engineering* 132.2, 021008 (2010), pp. 1–8. DOI: 10.1115/1.4001146.

[52] Tan, T. and Chen, Y. "Review of study on solid particle solar receivers." In: *Renewable and Sustainable Energy Reviews* 14.1 (2010), pp. 265–276. DOI: 10.1016/j.rser.2009.05.012.

[53] Ho, C. K., Christian, J. M., et al. "Performance evaluation of a high-temperature falling particle receiver." In: *ASME 2016 10th International Conference on Energy Sustainability* (Charlotte, USA). ES2016-59238. American Society of Mechanical Engineers, June 26–30, 2016, pp. 1–8. DOI: 10.1115/ES2016-59238.

[54] Khalsa, S. S. S., Christian, J. M., et al. "CFD simulation and performance analysis of alternative designs for high-temperature solid particle receivers." In: *ASME 2011 5th International Conference on Energy Sustainability* (Washington, USA). ES2011-54430. American Society of Mechanical Engineers, 2011, pp. 687–693. DOI: 10.1115/ES2011-54430.

[55] Röger, M., Amsbeck, L., et al. "Face-down solid particle receiver using recirculation." In: *Journal of Solar Energy Engineering* 133.3, 031009 (2011). DOI: 10.1115/1.4004269.

[56] Ho, C. K., Khalsa, S. S., and Siegel, N. P. "Modeling on-sun tests of a prototype solid particle receiver for concentrating solar power processes and storage." In: *ASME 2009 3rd International Conference on Energy Sustainability* (San Francisco, USA). ES2009-90035. American Society of Mechanical Engineers, 2009, pp. 543–550. DOI: 10.1115/ES2009-90035.

[57] Gobereit, B., Amsbeck, L., et al. "Assessment of a falling solid particle receiver with numerical simulation." In: *Solar Energy* 115 (2015), pp. 505–517. DOI: 10.1016/j.solener.2015.03.013.

[58] Gobereit, B. "Theoretische und experimentelle Untersuchungen zur Weiterentwicklung von solaren Partikelreceivern." PhD thesis. RWTH Aachen, 2015.

[59] Ho, C. K., Christian, J. M., et al. "On-sun testing of an advanced falling particle receiver system." In: *AIP Conference Proceedings* 1734.1, 030022 (2016), pp. 1–8. DOI: 10.1063/1.4949074.

[60] Lee, T., Lim, S., et al. "Numerical simulation of particulate flow in interconnected porous media for central particle-heating receiver applications." In: *Solar Energy* 113 (2015), pp. 14–24. DOI: 10.1016/j.solener.2014.12.017.

[61] Lee, T., Shin, S., and Abdel-Khalik, S. I. "Parametric investigation of particulate flow in interconnected porous media for central particle-heating receiver." In: *Journal of Mechanical Science and Technology* 32.3 (2018), pp. 1181–1186. DOI: 10.1007/s12206-018-0221-x.

[62] Khayyat, A., Knott, R., et al. "Measurement of particulate flow in discrete structure particle heating receivers." In: *ASME 2015 9th International Conference on Energy Sustainability* (San Diego, USA). ES2015-49510. American Society of Mechanical Engineers, pp. 1–4. DOI: 10.1115/ES2015-49510.

[63] Ma, Z. and Zhang, R. "Solid particle thermal energy storage design for a fluidized-bed concentrating solar power plant." U.S. pat. req. US20130255667A1. 2013.

[64] Ma, Z., Glatzmaier, G., and Mehos, M. "Fluidized bed technology for concentrating solar power with thermal energy storage." In: *Journal of Solar Energy Engineering* 136.3, 031014 (2014). DOI: 10.1115/1.4027262.

[65] Martinek, J. and Ma, Z. "Granular Flow and Heat Transfer Study in a Near-Blackbody Enclosed Particle Receiver." In: *Journal of Solar Energy Engineering* 137.5, 051008 (2015), pp. 1–9. DOI: 10.1115/1.4030970.

[66] Martinek, J., Wendelin, T., and Ma, Z. "Predictive performance modeling framework for a novel enclosed particle receiver configuration and application for thermochemical energy storage." In: *Solar Energy* 166 (2018), pp. 409–421. DOI: 10.1016/j.solener.2018.03.051.

[67] Flamant, G. "Étude de Procedes Application á la Décarbonatation de la Calcite." PhD thesis. Université Paul Sabatier (Université de Toulouse III), 1978.

[68] Bachovchin, D., Archer, D., et al. *Design and testing of a fluidized-bed solar thermal receiver*. Tech. rep. Westinghouse R&D Center and Georgia Institute of Technology, 1980.

[69] Flamant, G., Olalde, G., and Gauthier, D. "High Temperature Solar Gas-Solid Receivers." In: *Alternative Energy Sources V. Part B: Solar Applications* (1983). Ed. by Veziroglu, T.

[70] Flamant, G., Gauthier, D., et al. "A 50 kW Fluidized Bed High Temperature Solar Receiver: Heat Transfer Analysis." In: *Journal of Solar Energy Engineering* 110.4 (1988), pp. 313–320. DOI: 10.1115/1.3268273.

[71] Flamant, G. "Theoretical and experimental study of radiant heat transfer in a solar fluidized-bed receiver." In: *AIChE Journal* 28.4 (1982), pp. 529–535. DOI: 10.1002/aic.690280402.

[72] Koenigsdorff, R. and Kienzle, P. "Results of and prospects for research on direct-absorption fluidized bed solar receivers." In: *Solar energy materials* 24.1-4 (1991), pp. 279–283. DOI: 10.1016/0165-1633(91)90068-V.

[73] Koenigsdorff, R. *Direkteinkopplung konzentrierter Solarstrahlung in eine zirkulierende Wirbelschicht*. Düsseldorf: VDI-Verlag, 1994.

[74] Bai, F., Zhang, Y., et al. "Thermal Performance of a Quartz Tube Solid Particle Air Receiver." In: *Energy Procedia* 49 (2014), pp. 284–294. DOI: 10.1016/j.egypro.2014.03.031.

[75] Zhang, Y., Bai, F., et al. "Experimental Study of a Single Quartz Tube Solid Particle Air Receiver." In: *Energy Procedia* 69 (2015), pp. 600–607. DOI: 10.1016/j.egypro.2015.03.069.

[76] Matsubara, K., Kazuma, Y., et al. "High-temperature Fluidized Receiver for Concentrated Solar Radiation by a Beam-down Reflector System." In: *Energy Procedia* 49 (2014). Proceedings of the SolarPACES 2013 International Conference, pp. 447–456. ISSN: 1876-6102. DOI: 10.1016/j.egypro.2014.03.048.

[77] Matsubara, K., Sakai, H., et al. "Numerical Modeling of a Two-tower Type Fluidized Receiver for High Temperature Solar Concentration by a Beam-down Reflector System." In: *Energy Procedia* 69 (2015), pp. 487–496. DOI: 10.1016/j.egypro.2015.03.057.

[78] Sarker, M. R. I., Saha, M., et al. "Recirculating metallic particles for the efficiency enhancement of concentrated solar receivers." In: *Renewable Energy* 96, Part A (2016), pp. 850–862. DOI: 10.1016/j.renene.2016.05.047.

[79] Kodama, T., Gokon, N., et al. "Particles fluidized bed receiver/reactor tests with quartz sand particles using a 100-kWth beam-down solar concentrating system at Miyazaki." In: *AIP Conference Proceedings* 1850.1, 100012 (2017). DOI: 10.1063/1.4984469.

[80] Kodama, T., Gokon, N., et al. "Particles fluidized bed receiver/reactor with a beam-down solar concentrating optics: 30-kWth performance test using a big sun-simulator." In: *AIP Conference Proceedings*. Vol. 1734. AIP Publishing. DOI: 10.1063/1.4949206.

[81] Zhang, H., Yuan, H., et al. "Particulate Immersed Boundary Method for complex fluid–particle interaction problems with heat transfer." In: *Computers & Mathematics with Applications* 71.1 (2016), pp. 391–407. DOI: 10.1016/j.camwa.2015.12.003.

[82] Zhang, H., Benoit, H., et al. "Particle circulation loops in solar energy capture and storage: Gas–solid flow and heat transfer considerations." In: *Applied Energy* 161 (2016), pp. 206–224. DOI: 10.1016/j.apenergy.2015.10.005.

[83] Zhang, H., Benoit, H., et al. "High-efficiency solar power towers using particle suspensions as heat carrier in the receiver and in the thermal energy storage." In: *Renewable Energy* 111 (2017), pp. 438–446. DOI: 10.1016/j.renene.2017.03.101.

[84] Wu, W., Amsbeck, L., et al. "Proof of Concept Test of a Centrifugal Particle Receiver." In: *Energy Procedia* 49 (2014), pp. 560–568. DOI: 10.1016/j.egypro.2014.03.060.

[85] Ebert, M., Amsbeck, L., et al. "Upscaling, Manufacturing and Test of a Centrifugal Particle Receiver." In: *ASME 2016 10th International Conference on Energy Sustainability* (Charlotte, USA). ES2016-59252. June 26–30, 2016, pp. 1–7. DOI: 10.1115/ES2016-59252.

[86] Kodama, T. and Gokon, N. "Thermochemical cycles for high-temperature solar hydrogen production." In: *Chemical Reviews* 107.10 (2007), pp. 4048–4077. DOI: 10.1021/cr050188a.

[87] Ho, C. K., Christian, J., et al. "Highlights of the high-temperature falling particle receiver project: 2012 - 2016." In: *AIP Conference Proceedings*. Vol. 1850. American Institute of Physics Inc. DOI: 10.1063/1.4984370.

[88] Ma, Z., Mehos, M., et al. "Development of a Concentrating Solar Power System Using Fluidized-bed Technology for Thermal Energy Conversion and Solid Particles for Thermal Energy Storage." In: *Energy Procedia* 69 (2015), pp. 1349–1359. DOI: 10.1016/j.egypro.2015.03.136.

[89] Buck, R., Amsbeck, L., et al. "Solarstrahlungsempfängervorrichtung und Verfahren zur solaren Erhitzung von Warmeträgermedium." German pat. DE102010062367A1. 2010.

[90] Wu, W., Trebing, D., et al. "Prototype testing of a centrifugal particle receiver for high-temperature concentrating solar applications." In: *Journal of Solar Energy Engineering* 137.4, 041011 (2015). DOI: 10.1115/1.4030657.

[91] Flesch, R. "Windeinfluss auf Cavity-Receiver für solare Turmkraftwerke." PhD thesis. RWTH Aachen, 2016.

[92] Grobbel, J. "Entwicklung und numerische Untersuchung von Maßnahmen zur Reduktion konvektiver Verluste von Cavity-Receivern solarthermischer Turmkraftwerke." Master thesis. 2014.

[93] Säck, J. P., Breuer, S., et al. "High temperature hydrogen production: Design of a 750 KW demonstration plant for a two step thermochemical cycle." In: *Solar Energy* 135 (2016), pp. 232–241. DOI: 10.1016/j.solener.2016.05.059.

[94] Marxer, D., Furler, P., et al. "Solar thermochemical splitting of CO2 into separate streams of CO and O2 with high selectivity, stability, conversion, and efficiency." In: *Energy & Environmental Science* 10.5 (2017), pp. 1142–1149. DOI: 10.1039/C6EE03776C.

[95] Ermanoski, I. "Cascading pressure thermal reduction for efficient solar fuel production." In: *International Journal of Hydrogen Energy* 39.25 (2014), pp. 13114–13117. DOI: 10.1016/j.ijhydene.2014.06.143.

[96] Ermanoski, I., Miller, J., and Allendorf, M. "Efficiency maximization in solar-thermochemical fuel production: challenging the concept of isothermal water splitting." In: *Physical Chemistry Chemical Physics* 16.18 (2014), pp. 8418–8427. DOI: 10.1039/C4CP00978A.

[97] Ermanoski, I., Grobbel, J., et al. "Design and construction of a cascading pressure reactor prototype for solar-thermochemical hydrogen production." In: *AIP Conference Proceedings* 1734.1, 120001 (2016), pp. 1–8. DOI: 10.1063/1.4949203.

[98] Chueh, W. C., Falter, C., et al. "High-flux solar-driven thermochemical dissociation of CO2 and H2O using nonstoichiometric ceria." In: *Science* 330.6012 (2010), pp. 1797–1801. DOI: 10.1126/science.1197834.

[99] Cho, H. S., Myojin, T., et al. "Solar Demonstration of Thermochemical Two-step Water Splitting Cycle Using CeO2/MPSZ Ceramic foam Device by 45kWth KIER Solar Furnace." In: *Energy Procedia* 49 (2014), pp. 1922–1931. DOI: 10.1016/j.egypro.2014.03.204.

[100] Agrafiotis, C., Roeb, M., et al. "Solar water splitting for hydrogen production with monolithic reactors." In: *Solar Energy* 79.4 (2005), pp. 409–421. DOI: 10.1016/j.solener.2005.02.026.

[101] Kaneko, H., Miura, T., et al. "Rotary-Type Solar Reactor for Solar Hydrogen Production with Two-step Water Splitting Process." In: *Energy & Fuels* 21.4 (2007), pp. 2287–2293. DOI: 10.1021/ef060581z.

[102] Diver, R. B., Miller, J. E., et al. "Testing of a CR5 solar thermochemical heat engine prototype." In: *ASME 2010 4th International Conference on Energy Sustainability* (Phoenix, USA). Vol. 2. ASME, pp. 97–104. DOI: 10.1115/ES2010-90093.

[103] Lapp, J. and Lipiński, W. "Transient Three-Dimensional Heat Transfer Model of a Solar Thermochemical Reactor for H2O and CO2 Splitting Via Nonstoichiometric Ceria Redox Cycling." In: *Journal of Solar Energy Engineering* 136.3, 031006 (2014), pp. 1–11. DOI: 10.1115/1.4026465.

[104] Grena, R. "Thermal simulation of a single particle in a falling-particle solar receiver." In: *Solar Energy* 83.8 (2009), pp. 1186–1199. DOI: 10.1016/j.solener.2009.02.001.

[105] Miller, J. E., McDaniel, A. H., and Allendorf, M. D. "Considerations in the Design of Materials for Solar-Driven Fuel Production Using Metal-Oxide Thermochemical Cycles." In: *Advanced Energy Materials* 4.2, 1300469 (2014). DOI: 10.1002/aenm.201300469.

[106] Meier, A., Ganz, J., and Steinfeld, A. "Modeling of a novel high-temperature solar chemical reactor." In: *Chemical Engineering Science* 51.11 (1996), pp. 3181–3186. DOI: 10.1016/0009-2509(96)00217-5.

[107] Kodama, T., Enomoto, S.-i., et al. "Application of an internally circulating fluidized bed for windowed solar chemical reactor with direct irradiation of reacting particles." In: *Journal of Solar Energy Engineering* 130.1, 014504 (2008), pp. 1–4. DOI: 10.1115/1.2807213.

[108] Kodama, T., Gokon, N., et al. "Particle fluidized bed receiver/reactor with a beam-down solar concentrating optics: Performance test of two-step water splitting with ceria particles using 30-kWth sun-simulator." In: *AIP Conference Proceedings* 2033.1, 130009 (2018). DOI: 10.1063/1.5067143.

[109] Oles, A. S. and Jackson, G. S. "Modeling of a concentrated-solar, falling-particle receiver for ceria reduction." In: *Solar Energy* 122 (2015), pp. 126–147. DOI: 10.1016/j.solener.2015.08.009.

[110] Koepf, E., Advani, S. G., et al. "A novel beam-down, gravity-fed, solar thermochemical receiver/reactor for direct solid particle decomposition: Design, modeling, and experimentation." In: *International Journal of Hydrogen Energy* 37.22 (2012), pp. 16871–16887. DOI: 10.1016/j.ijhydene.2012.08.086.

[111] Grobbel, J., Lapp, J. L., et al. "Solarstrahlungsreceiver zur solaren Bestrahlung von Feststoffpartikeln, eine Industrieanlage mit einem Solarstrahlungsreceiver, sowie ein Verfahren zur solaren Bestrahlung von Feststoffpartikeln." German pat. DE102016216733.2. 2016.

[112] Grobbel, J., Brendelberger, S., et al. "Heat transfer in a directly irradiated ceria particle bed under vacuum conditions." In: *Solar Energy* 158 (2017), pp. 737–745. DOI: 10.1016/j.solener.2017.10.022.

[113] Felinks, J. "Wärmerückgewinnung aus Partikeln mittels kugelförmiger Wärmeträgermedien in solaren thermochemischen Kreisprozessen." PhD thesis. RWTH Aachen, 2017.

[114] Brendelberger, S. and Sattler, C. "Concept analysis of an indirect particle-based redox process for solar-driven H2O/CO2 splitting." In: *Solar Energy* 113 (2015), pp. 158–170. DOI: 10.1016/j.solener.2014.12.035.

[115] Richter, S., Brendelberger, S., et al. "Partikelmischungsreaktor zur Reduktion von Ceroxid in solaren thermochemischen Kreisprozessen zur Wasserstoffproduktion." Poster presentation. Dechema Jahrestreffen Reaktionstechnik 2016 zusammen mit der ProcessNet-Fachgruppe Mischvorgänge (Würzburg,Germany). May 2–4, 2016. URL: https://elib.dlr.de/108871/.

[116] Evans, G., Houf, W., et al. "Gas-particle flow within a high temperature solar cavity receiver including radiation heat transfer." In: *Journal of Solar Energy Engineering* 109.2 (1987), pp. 134–142. DOI: 10.1115/1.3268190.

[117] Meier, A. "A predictive CFD model for a falling particle receiver/reactor exposed to concentrated sunlight." In: *Chemical Engineering Science* 54.13–14 (1999), pp. 2899–2905. DOI: 10.1016/S0009-2509(98)00376-5.

[118] Chen, H., Chen, Y., et al. "Computational Fluid Dynamics Modeling of Gas-Particle Flow Within a Solid-Particle Solar Receiver." In: *Journal of Solar Energy Engineering* 129.2 (2007), pp. 160–170. DOI: 10.1115/1.2716418.

[119] Kim, K., Siegel, N., et al. "A study of solid particle flow characterization in solar particle receiver." In: *Solar Energy* 83.10 (2009), pp. 1784–1793. DOI: 10.1016/j.solener.2009.06.011.

[120] Kim, K., Moujaes, S. F., and Kolb, G. J. "Experimental and simulation study on wind affecting particle flow in a solar receiver." In: *Solar Energy* 84.2 (2010), pp. 263–270. DOI: 10.1016/j.solener.2009.11.005.

[121] Mills, B., Ho, C. K., et al. "Novel particle release patterns for increased receiver thermal efficiency." In: vol. 1850. 1. 2017. DOI: 10.1063/1.4984378.

[122] Marti, J., Haselbacher, A., and Steinfeld, A. "A numerical investigation of gas-particle suspensions as heat transfer media for high-temperature concentrated solar power." In: *International Journal of Heat and Mass Transfer* 90 (2015), pp. 1056–1070. DOI: 10.1016/j.ijheatmasstransfer.2015.07.033.

[123] Wang, F., Bai, F., et al. "Numerical Simulation of Quartz Tube Solid Particle Air Receiver." In: *Energy Procedia* 69 (2015), pp. 573–582. DOI: 10.1016/j.egypro.2015.03.066.

[124] Ansart, R., García-Triñanes, P., et al. "Dense gas-particle suspension upward flow used as heat transfer fluid in solar receiver: PEPT experiments and 3D numerical simulations." In: *Powder Technology* 307 (2017), pp. 25–36. DOI: 10.1016/j.powtec.2016.11.006.

[125] Baumann, T. and Zunft, S. "Theoretical and experimental investigation of a Moving Bed Heat Exchanger for Solar Central Receiver Power Plants." In: *Journal of Physics: Conference Series* 395, 012055 (2012). DOI: 10.1088/1742-6596/395/1/012055.

[126] Dreißigacker, V., Zunft, S., and Müller-Steinhagen, H. "A thermo-mechanical model of packed-bed storage and experimental validation." In: *Applied Energy* 111 (2013), pp. 1120–1125. DOI: 10.1016/j.apenergy.2013.03.067.

[127] Sassine, N., Donzé, F.-V., et al. "Thermal stress numerical study in granular packed bed storage tank." In: *Granular Matter* 20.3, 44 (2018). DOI: 10.1007/s10035-018-0817-y.

[128] Grobbel, J., Brendelberger, S., et al. "Calibration of parameters for DEM simulations of solar particle receivers by bulk experiments and surrogate functions." In: *Powder Technology* (2019). DOI: 10.1016/j.powtec.2019.11.028.

[129] O'Sullivan, C. *Particulate discrete element modelling. A Geomechanics Perspective*. Vol. 4. Applied Geotechnics. London and New York: Taylor & Francis, 2011.

[130] Plimpton, S. "Fast Parallel Algorithms for Short-Range Molecular Dynamics." In: *Journal of Computational Physics* 117.1 (1995), pp. 1–19. DOI: 10.1006/jcph.1995.1039.

[131] Schäfer, J., Dippel, S., and Wolf, D. E. "Force schemes in simulations of granular materials." In: *Journal de physique I* 6.1 (1996), pp. 5–20. DOI: 10.1051/jp1:1996129.

[132] Kruggel-Emden, H., Simsek, E., et al. "Review and extension of normal force models for the Discrete Element Method." In: *Powder Technology* 171.3 (2007), pp. 157–173. DOI: 10.1016/j.powtec.2006.10.004.

[133] Tsuji, Y., Tanaka, T., and Ishida, T. "Lagrangian numerical simulation of plug flow of cohesionless particles in a horizontal pipe." In: *Powder Technology* 71.3 (1992), pp. 239–250. DOI: 10.1016/0032-5910(92)88030-L.

[134] Antypov, D. and Elliott, J. A. "On an analytical solution for the damped Hertzian spring." In: *EPL (Europhysics Letters)* 94.5, 50004 (2011). DOI: 10.1209/0295-5075/94/50004.

[135] Di Renzo, A. and Di Maio, F. P. "Comparison of contact-force models for the simulation of collisions in DEM-based granular flow codes." In: *Chemical Engineering Science* 59.3 (2004), pp. 525–541. DOI: 10.1016/j.ces.2003.09.037.

[136] Di Renzo, A. and Di Maio, F. P. "An improved integral non-linear model for the contact of particles in distinct element simulations." In: *Chemical Engineering Science* 60.5 (2005), pp. 1303–1312. DOI: 10.1016/j.ces.2004.10.004.

[137] Ai, J., Chen, J.-F., et al. "Assessment of rolling resistance models in discrete element simulations." In: *Powder Technology* 206.3 (2011), pp. 269–282. DOI: 10.1016/j.powtec.2010.09.030.

[138] Brilliantov, N. V., Spahn, F., et al. "Model for collisions in granular gases." In: *Physical Review E* 53.5 (1996), pp. 5382–5392. DOI: 10.1103/PhysRevE.53.5382.

[139] Schwager, T. and Pöschel, T. "Coefficient of restitution and linear–dashpot model revisited." In: *Granular Matter* 9.6 (2007), pp. 465–469. DOI: 10.1007/s10035-007-0065-z.

[140] Silbert, L. E., Ertaş, D., et al. "Granular flow down an inclined plane: Bagnold scaling and rheology." In: *Physical Review E* 64.5, 051302 (2001). DOI: 10.1103/PhysRevE.64.051302.

[141] Zhang, H. and Makse, H. "Jamming transition in emulsions and granular materials." In: *Physical Review E* 72.1, 011301 (2005). DOI: 10.1103/PhysRevE.72.011301.

[142] Zhong, W., Yu, A., et al. "DEM/CFD-DEM Modelling of Non-spherical Particulate Systems: Theoretical Developments and Applications." In: *Powder Technology* 302 (2016), pp. 108–152. DOI: 10.1016/j.powtec.2016.07.010.

[143] Kruggel-Emden, H., Rickelt, S., et al. "A study on the validity of the multi-sphere Discrete Element Method." In: *Powder Technology* 188.2 (2008), pp. 153–165. DOI: 10.1016/j.powtec.2008.04.037.

[144] Peters, J. F., Kala, R., and Maier, R. S. "A hierarchical search algorithm for discrete element method of greatly differing particle sizes." In: *Engineering Computations* 26.6 (2009), pp. 621–634. DOI: 10.1108/02644400910975423.

[145] Wensrich, C. M. and Katterfeld, A. "Rolling friction as a technique for modelling particle shape in DEM." In: *Powder Technology* 217 (2012), pp. 409–417. DOI: 10.1016/j.powtec.2011.10.057.

[146] Lai, C. G. and Wilmanski, K. *Surface Waves in Geomechanics: Direct and Inverse Modelling for Soils and Rocks*. Vol. 481. CISM International Centre for Mechanical Sciences. Wien: Springer, 2005.

[147] Thornton, C. *Granular dynamics, contact mechanics and particle system simulations. A DEM study*. Vol. 24. Particle Technology Series. Cham: Springer, 2015. DOI: 10.1007/978-3-319-18711-2.

[148] Li, Y., Xu, Y., and Thornton, C. "A comparison of discrete element simulations and experiments for 'sandpiles' composed of spherical particles." In: *Powder Technology* 160.3 (2005), pp. 219–228. DOI: 10.1016/j.powtec.2005.09.002.

[149] Grima, A. P. and Wypych, P. W. "Discrete element simulations of granular pile formation: Method for calibrating discrete element models." In: *Engineering Computations* 28.3 (2011), pp. 314–339. DOI: 10.1108/02644401111118169.

[150] Coetzee, C. J. "Review: Calibration of the discrete element method." In: *Powder Technology* 310 (2017), pp. 104–142. DOI: 10.1016/j.powtec.2017.01.015.

[151] Lommen, S., Schott, D., and Lodewijks, G. "DEM speedup: Stiffness effects on behavior of bulk material." In: *Particuology* 12 (2014), pp. 107–112. DOI: 10.1016/j.partic.2013.03.006.

[152] Timoshenko, S. and Goodier, J. N. *Theory of elasticity*. New York: McGraw-Hill, 1970.

[153] Morris, A., Pannala, S., et al. "Development of soft-sphere contact models for thermal heat conduction in granular flows." In: *AIChE Journal* 62.12 (2016), pp. 4526–4535. DOI: 10.1002/aic.15331.

[154] Nasato, D. S., Goniva, C., et al. "Coarse graining for large-scale DEM simulations of particle flow - An investigation on contact and cohesion models." In: *Procedia Engineering*. Vol. 102, pp. 1484–1490. DOI: 10.1016/j.proeng.2015.01.282.

[155] Thakur, S. C., Ooi, J. Y., and Ahmadian, H. "Scaling of discrete element model parameters for cohesionless and cohesive solid." In: *Powder Technology* 293 (2016), pp. 130–137. DOI: 10.1016/j.powtec.2015.05.051.

[156] Lu, L., Morris, A., et al. "Extension of a coarse grained particle method to simulate heat transfer in fluidized beds." In: *International Journal of Heat and Mass Transfer* 111 (2017), pp. 723–735. DOI: 10.1016/j.ijheatmasstransfer.2017.04.040.

[157] Hilton, J. E. and Cleary, P. W. "Comparison of non-cohesive resolved and coarse grain DEM models for gas flow through particle beds." In: *Applied Mathematical Modelling* 38.17–18 (2014), pp. 4197–4214. DOI: 10.1016/j.apm.2014.02.013.

[158] Kuwagi, K., Takeda, H., and Horio, M. "The similar particle assembly (SPA) model, an approach to large-scale discrete element (DEM) simulation." In: *Fluidization XI - Present and Future for Fluidization Engineering* (2004), pp. 243–250.

[159] Mokhtar, M. A., Kuwagi, K., et al. "Validation of the similar particle assembly (SPA) model for the fluidization of Geldart's group A and D particles." In: *AIChE Journal* 58.1 (2012), pp. 87–98. DOI: 10.1002/aic.12568.

[160] Radl, S., Radeke, C., et al. "Parcel-based approach for the simulation of gas-particle flows." In: *8th International Conference on CFD in Oil & Gas, Metallurgical and Process Industries* (Trondheim, Norway). June 21–23, 2011.

[161] Feng, Y. T. and Owen, D. R. J. "Discrete element modelling of large scale particle systems - I: exact scaling laws." In: *Computational Particle Mechanics* 1.2 (2014), pp. 159–168. DOI: 10.1007/s40571-014-0010-y.

[162] Pöschel, T., Saluena, C., and Schwager, T. "Scaling properties of granular materials." In: *Physical Review E* 64.1, 011308 (2001). DOI: 10.1103/PhysRevE.64.011308.

[163] Sakai, M. and Koshizuka, S. "Large-scale discrete element modeling in pneumatic conveying." In: *Chemical Engineering Science* 64.3 (2009), pp. 533–539. DOI: 10.1016/j.ces.2008.10.003.

[164] Sakai, M., Yamada, Y., et al. "Large-scale discrete element modeling in a fluidized bed." In: *International Journal for Numerical Methods in Fluids* 64.10-12 (2010), pp. 1319–1335. DOI: 10.1002/fld.2364.

[165] Sakai, M., Abe, M., et al. "Verification and validation of a coarse grain model of the DEM in a bubbling fluidized bed." In: *Chemical Engineering Journal* 244 (2014), pp. 33–43. DOI: 10.1016/j.cej.2014.01.029.

[166] Lu, L., Xu, J., et al. "EMMS-based discrete particle method (EMMS–DPM) for simulation of gas–solid flows." In: *Chemical Engineering Science* 120 (2014), pp. 67–87. DOI: 10.1016/j.ces.2014.08.004.

[167] Bierwisch, C. S. "Numerical Simulations of Granular Flow and Filling." PhD thesis. Albert-Ludwigs-Universität Freiburg im Breisgau, 2009.

[168] Queteschiner, D., Lichtenegger, T., et al. "Multi-level coarse-grain model of the DEM." In: *Powder Technology* 338 (2018), pp. 614–624. DOI: 10.1016/j.powtec.2018.07.033.

[169] Cundall, P. A. and Strack, O. D. L. "A discrete numerical model for granular assemblies." In: *Geotechnique* 29.1 (1979), pp. 47–65. DOI: 10.1680/geot.1979.29.1.47.

[170] Sudbrock, F., Kruggel-Emden, H., et al. "Convective Drying of Agitated Silica Gel and Beech Wood Particle Beds—Experiments and Transient DEM-CFD Simulations." In: *Drying Technology* 33.15-16 (2015), pp. 1808–1820. DOI: 10.1080/07373937.2015.1026982.

[171] Li, J. and Mason, D. J. "Application of the discrete element modelling in air drying of particulate solids." In: *Drying Technology* 20.2 (2002), pp. 255–282. DOI: 10.1081/DRT-120002542.

[172] Kharaghani, A., Metzger, T., and Tsotsas, E. "A proposal for discrete modeling of mechanical effects during drying, combining pore networks with DEM." In: *AIChE Journal* 57.4 (2011), pp. 872–885. DOI: 10.1002/aic.12318.

[173] Metzger, T. and Tsotsas, E. "Network models for capillary porous media: application to drying technology." In: *Chemie Ingenieur Technik* 82.6 (2010), pp. 869–879. DOI: 10.1002/cite.201000023.

[174] Tatemoto, Y. and Sawada, T. "Numerical Analysis of Drying Characteristics of Wet Material Immersed in Fluidized Bed of Inert Particles." In: *Drying Technology* 30.9 (2012), pp. 979–988. DOI: 10.1080/07373937.2012.675604.

[175] Sahni, E. K. and Chaudhuri, B. "Contact drying: A review of experimental and mechanistic modeling approaches." In: *International Journal of Pharmaceutics* 434.1 (2012), pp. 334–348.

[176] Azadi, P., Yan, N., and Farnood, R. "Discrete element modeling of the transient heat transfer and toner fusing process in the Xerographic printing of coated papers." In: *Computers & Chemical Engineering* 32.12 (2008), pp. 3238–3245. DOI: 10.1016/j.compchemeng.2008.05.018.

[177] Kruggel-Emden, H., Wirtz, S., et al. "Modeling of granular flow and combined heat transfer in hoppers by the discrete element method (DEM)." In: *Journal of Pressure Vessel Technology* 128.3 (2006), pp. 439–444. DOI: 10.1115/1.2218349.

[178] Mahmoudi, A. H., Hoffmann, F., and Peters, B. "Application of XDEM as a novel approach to predict drying of a packed bed." In: *International Journal of Thermal Sciences* 75 (2014), pp. 65–75. DOI: 10.1016/j.ijthermalsci.2013.07.016.

[179] Van Lew, J. T., Ying, A., and Abdou, M. "A discrete element method study on the evolution of thermomechanics of a pebble bed experiencing pebble failure." In: *Fusion Engineering and Design* 89.7–8 (2014), pp. 1151–1157. DOI: 10.1016/j.fusengdes.2014.04.066.

[180] Hou, Q., Li, J., and Yu, A. "CFD-DEM Study of Heat Transfer in the Reduction Shaft of Corex." In: *Steel research international* 86.6 (2015), pp. 626–635. DOI: 10.1002/srin.201400367.

[181] Hou, Q., E, D., et al. "DEM-based virtual experimental blast furnace: A quasi-steady state model." In: *Powder Technology* 314 (2017), pp. 557–566.

[182] Bluhm-Drenhaus, T., Simsek, E., et al. "A coupled fluid dynamic-discrete element simulation of heat and mass transfer in a lime shaft kiln." In: *Chemical Engineering Science* 65.9 (2010), pp. 2821–2834. DOI: 10.1016/j.ces.2010.01.015.

[183] Pennec, F., Alzina, A., et al. "A combined finite-discrete element method for calculating the effective thermal conductivity of bio-aggregates based materials." In: *International Journal of Heat and Mass Transfer* 60 (2013), pp. 274–283. DOI: 10.1016/j.ijheatmasstransfer.2013.01.002.

[184] Wang, Y., Wang, S., et al. "Numerical modeling of porous flow in fractured rock and its applications in geothermal energy extraction." In: *Journal of Earth Science* 26.1 (2015), pp. 20–27. DOI: 10.1007/s12583-015-0507-1.

[185] Azmir, J., Hou, Q., and Yu, A. "Discrete particle simulation of food grain drying in a fluidised bed." In: *Powder Technology* 323 (2018), pp. 238–249. DOI: 10.1016/j.powtec.2017.10.019.

[186] Moussa, R. B., Guessasma, M., et al. "Thermal Radiation Contribution to Metal Dust Explosions." In: *Procedia Engineering* 102 (2015), pp. 714–721. DOI: 10.1016/j.proeng.2015.01.172.

[187] Zhou, H., Flamant, G., and Gauthier, D. "DEM-LES simulation of coal combustion in a bubbling fluidized bed Part II: coal combustion at the particle level." In: *Chemical Engineering Science* 59.20 (2004), pp. 4205–4215. DOI: 10.1016/j.ces.2004.01.070.

[188] Liu, D., Chen, X., et al. "Simulation of char and propane combustion in a fluidized bed by extending DEM–CFD approach." In: *Proceedings of the Combustion Institute* 33.2 (2011), pp. 2701–2708. DOI: 10.1016/j.proci.2010.06.070.

[189] Chaudhuri, B., Muzzio, F. J., and Tomassone, M. S. "Experimentally validated computations of heat transfer in granular materials in rotary calciners." In: *Powder Technology* 198.1 (2010), pp. 6–15. DOI: 10.1016/j.powtec.2009.09.024.

[190] Krause, B., Liedmann, B., et al. "Coupled three dimensional DEM-CFD simulation of a lime shaft kiln-Calcination, particle movement and gas phase flow field." In: *Chemical Engineering Science* 134 (2015), pp. 834–849. DOI: 10.1016/j.ces.2015.06.002.

[191] Cheng, C. and Zhang, X. "Modeling of Interior Ballistic Gas-Solid Flow Using a Coupled Computational Fluid Dynamics-Discrete Element Method." In: *Journal of Applied Mechanics* 80.3, 031403 (2013). DOI: 10.1115/1.4023313.

[192] Hobbs, A. "Simulation of an aggregate dryer using coupled CFD and DEM methods." In: *International Journal of Computational Fluid Dynamics* 23.2 (2009), pp. 199–207. DOI: 10.1080/10618560802680971.

[193] Swasdisevi, T., Tanthapanichakoon, W., et al. "Prediction of gas-particle dynamics and heat transfer in a two-dimensional spouted bed." In: *Advanced Powder Technology* 16.3 (2005), pp. 275–293. DOI: 10.1163/1568552053750215.

[194] Kaneko, Y., Shiojima, T., and Horio, M. "DEM simulation of fluidized beds for gas-phase olefin polymerization." In: *Chemical Engineering Science* 54.24 (1999), pp. 5809–5821. DOI: 10.1016/S0009-2509(99)00153-0.

[195] Li, J. and Mason, D. J. "A computational investigation of transient heat transfer in pneumatic transport of granular particles." In: *Powder Technology* 112.3 (2000), pp. 273–282. DOI: 10.1016/S0032-5910(00)00302-8.

[196] Tsuji, Y., Kawaguchi, T., and Tanaka, T. "Discrete particle simulation of two-dimensional fluidized bed." In: *Powder Technology* 77.1 (1993), pp. 79–87. DOI: 10.1016/0032-5910(93)85010-7.

[197] Das, S., Deen, N. G., and Kuipers, J. A. M. "A DNS study of flow and heat transfer through slender fixed-bed reactors randomly packed with spherical particles." In: *Chemical Engineering Science* 160 (2017), pp. 1–19. DOI: 10.1016/j.ces.2016.11.008.

[198] Kruggel-Emden, H., Kravets, B., et al. "Direct numerical simulation of coupled fluid flow and heat transfer for single particles and particle packings by a LBM-approach." In: *Powder Technology* 294 (2016), pp. 236–251. DOI: 10.1016/j.powtec.2016.02.038.

[199] Vargas, W. L. and McCarthy, J. J. "Heat conduction in granular materials." In: *AIChE Journal* 47.5 (2001), pp. 1052–1059. DOI: 10.1002/aic.690470511.

[200] Vargas, W. L. and McCarthy, J. J. "Conductivity of granular media with stagnant interstitial fluids via thermal particle dynamics simulation." In: *International Journal of Heat and Mass Transfer* 45.24 (2002), pp. 4847–4856. DOI: 10.1016/S0017-9310(02)00175-8.

[201] Batchelor, G. K. and O'brien, R. "Thermal or electrical conduction through a granular material." In: *Proceedings of the Royal Society of London. A. Mathematical and Physical Sciences* 355 (1977), pp. 313–333. DOI: 10.1098/rspa.1977.0100.

[202] Malone, K. F. and Xu, B. H. "Determination of contact parameters for discrete element method simulations of granular systems." In: *Particuology* 6.6 (2008), pp. 521–528. DOI: 10.1016/j.partic.2008.07.012.

[203] Zhao, Y., Jiang, M., et al. "Particle-scale simulation of the flow and heat transfer behaviors in fluidized bed with immersed tube." In: *AIChE Journal* 55.12 (2009), pp. 3109–3124. DOI: 10.1002/aic.11956.

[204] Figueroa, I., Vargas, W. L., and McCarthy, J. J. "Mixing and heat conduction in rotating tumblers." In: *Chemical Engineering Science* 65.2 (2010), pp. 1045–1054. DOI: 10.1016/j.ces.2009.09.058.

[205] Shi, D., Vargas, W. L., and McCarthy, J. J. "Heat transfer in rotary kilns with interstitial gases." In: *Chemical Engineering Science* 63.18 (2008), pp. 4506–4516. DOI: 10.1016/j.ces.2008.06.006.

[206] Gui, N., Yan, J., et al. "DEM simulation and analysis of particle mixing and heat conduction in a rotating drum." In: *Chemical Engineering Science* 97 (2013), pp. 225–234. DOI: 10.1016/j.ces.2013.04.005.

[207] Nguyen, V. D., Cogné, C., et al. "Discrete modeling of granular flow with thermal transfer: Application to the discharge of silos." In: *Applied Thermal Engineering* 29.8–9 (2009), pp. 1846–1853. DOI: 10.1016/j.applthermaleng.2008.09.009.

[208] Komossa, H., Wirtz, S., et al. "Heat transfer in indirect heated rotary drums filled with monodisperse spheres: Comparison of experiments with DEM simulations." In: *Powder Technology* 286 (2015), pp. 722–731. DOI: 10.1016/j.powtec.2015.07.022.

[209] Di Maio, F. P., Di Renzo, A., and Trevisan, D. "Comparison of heat transfer models in DEM-CFD simulations of fluidized beds with an immersed probe." In: *Powder Technology* 193.3 (2009), pp. 257–265. DOI: 10.1016/j.powtec.2009.03.002.

[210] Zehner, P. and Schlünder, E. U. "Einfluß der Wärmestrahlung und des Druckes auf den Wärmetransport in nicht durchströmten Schüttungen." In: *Chemie Ingenieur Technik* 44.23 (1972), pp. 1303–1308.

[211] Cheng, G., Yu, A., and Zulli, P. "Evaluation of effective thermal conductivity from the structure of a packed bed." In: *Chemical Engineering Science* 54.19 (1999), pp. 4199–4209. DOI: 10.1016/S0009-2509(99)00125-6.

[212] Li, J., Mason, D. J., and Mujumdar, A. S. "A numerical study of heat transfer mechanisms in gas–solids flows through pipes using a coupled CFD and DEM model." In: *Drying Technology* 21.9 (2003), pp. 1839–1866. DOI: 10.1081/DRT-120025511.

[213] Zhou, H., Flamant, G., et al. "Simulation of Coal Combustion in a Bubbling Fluidized Bed by Distinct Element Method." In: *Chemical Engineering Research and Design* 81.9 (2003), pp. 1144–1149. DOI: 10.1205/026387603770866308.

[214] Sun, J. and Chen, M. M. "A theoretical analysis of heat transfer due to particle impact." In: *International Journal of Heat and Mass Transfer* 31.5 (1988), pp. 969–975. DOI: 10.1016/0017-9310(88)90085-3.

[215] Zhou, Z., Yu, A., and Zulli, P. "Particle scale study of heat transfer in packed and bubbling fluidized beds." In: *AIChE Journal* 55.4 (2009), pp. 868–884. DOI: 10.1002/aic.11823.

[216] Zhou, Z., Kuang, S., et al. "Discrete particle simulation of particle–fluid flow: model formulations and their applicability." In: *Journal of Fluid Mechanics* 661 (2010), pp. 482–510. DOI: 10.1017/S002211201000306X.

[217] Gan, J., Zhou, Z., and Yu, A. "Particle scale study of heat transfer in packed and fluidized beds of ellipsoidal particles." In: *Chemical Engineering Science* 144 (2016), pp. 201–215. DOI: 10.1016/j.ces.2016.01.041.

[218] Gan, J., Zhou, Z., and Yu, A. "Effect of particle shape and size on effective thermal conductivity of packed beds." In: *Powder Technology* 311 (2017), pp. 157–166. DOI: 10.1016/j.powtec.2017.01.024.

[219] Oschmann, T. and Kruggel-Emden, H. "A novel method for the calculation of particle heat conduction and resolved 3D wall heat transfer for the CFD/DEM approach." In: *Powder Technology* 338 (2018), pp. 289–303. DOI: 10.1016/j.powtec.2018.07.017.

[220] Zhang, H. W., Zhou, Q., et al. "A DEM study on the effective thermal conductivity of granular assemblies." In: *Powder Technology* 205.1 (2011), pp. 172–183. DOI: 10.1016/j.powtec.2010.09.008.

[221] Tsory, T., Ben-Jacob, N., et al. "Thermal DEM–CFD modeling and simulation of heat transfer through packed bed." In: *Powder Technology* 244 (2013), pp. 52–60. DOI: 10.1016/j.powtec.2013.04.013.

[222] Feng, Y. T., Han, K., et al. "Discrete thermal element modelling of heat conduction in particle systems: Basic formulations." In: *Journal of Computational Physics* 227.10 (2008), pp. 5072–5089. DOI: 10.1016/j.jcp.2008.01.031.

[223] Rickelt, S., Wirtz, S., and Scherer, V. "A New Approach to Simulate Transient Heat Transfer Within the Discrete Element Method." In: 48272 (2008), pp. 221–230. DOI: 10.1115/PVP2008-61522.

[224] Rickelt, S., Kruggel-Emden, H., et al. "Simulation of Heat Transfer in Moving Granular Material by the Discrete Element Method With Special Emphasis on Inner Particle Heat Transfer." In: 43574 (2009), pp. 961–971. DOI: 10.1115/HT2009-88605.

[225] Brosh, T. and Levy, A. "Modeling of Heat Transfer in Pneumatic Conveyer Using a Combined DEM-CFD Numerical Code." In: *Drying Technology* 28.2 (2010), pp. 155–164. DOI: 10.1080/07373930903517482.

[226] Oschmann, T., Schiemann, M., and Kruggel-Emden, H. "Development and verification of a resolved 3D inner particle heat transfer model for the Discrete Element Method (DEM)." In: *Powder Technology* 291 (2016), pp. 392–407. DOI: 10.1016/j.powtec.2015.12.008.

[227] Forgber, T., Mohan, B., et al. "Heat transfer rates in sheared beds of inertial particles at high Biot numbers." In: *Granular Matter* 19.1, 14 (2017). DOI: 10.1007/s10035-016-0695-0.

[228] Oschmann, T. and Kruggel-Emden, H. "Numerical and experimental investigation of the heat transfer of spherical particles in a packed bed with an implicit 3D finite difference approach." In: *Granular Matter* 19.3, 47 (2017). DOI: 10.1007/s10035-017-0711-z.

[229] Forgber, T. and Radl, S. "A novel approach to calculate radiative thermal exchange in coupled particle simulations." In: *Powder Technology* 323 (2018), pp. 24–44. DOI: 10.1016/j.powtec.2017.09.014.

[230] Wu, H., Gui, N., et al. "Numerical simulation of heat transfer in packed pebble beds: CFD-DEM coupled with particle thermal radiation." In: *International Journal of Heat and Mass Transfer* 110 (2017), pp. 393–405. DOI: 10.1016/j.ijheatmasstransfer.2017.03.035.

[231] Amberger, S., Kloss, C., and Pirker, S. "Using Ray Tracing to Model Thermal Radiation in LIGGGHTS." Presentation at the LAMMPS Users' Workshop and Symposium (Albuquerque, USA). Aug. 7–8, 2013. URL: https://lammps.sandia.gov/workshops/Aug13/Amberger/presentation.pdf.

[232] Al-Arkawazi, S. "Modeling the heat transfer between fluid-granular medium." In: *Applied Thermal Engineering* 128 (2018), pp. 696–705. ISSN: 1359-4311. DOI: 10.1016/j.applthermaleng.2017.09.064. URL: http://www.sciencedirect.com/science/article/pii/S1359431117344307.

[233] Chaudhuri, B., Muzzio, F. J., and Tomassone, M. S. "Modeling of heat transfer in granular flow in rotating vessels." In: *Chemical Engineering Science* 61.19 (2006), pp. 6348–6360. DOI: 10.1016/j.ces.2006.05.034.

[234] Zehner, P. "Experimentelle und theoretische Bestimmung der effektiven Wärmeleitfähigkeit durchströmter Kugelschüttungen bei mässigen und hohen Temperaturen." PhD thesis. Universität Karlsruhe, 1972.

[235] Goniva, C., Kloss, C., et al. "Influence of rolling friction on single spout fluidized bed simulation." In: *Particuology* 10.5 (2012), pp. 582–591. DOI: 10.1016/j.partic.2012.05.002.

[236] Bauer, R. *Effektive radiale Wärmeleitfähigkeit gasdurchströmter Schüttungen mit Partikeln unterschiedlicher Form und Größenverteilung: mit 7 Tafeln.* Düsseldorf: VDI-Verlag, 1977.

[237] Zehner, P. and Schlünder, E. U. "Wärmeleitfähigkeit von Schüttungen bei mäßigen Temperaturen." In: *Chemie Ingenieur Technik* 42.14 (1970), pp. 933–941. DOI: 10.1002/cite.330421408.

[238] Verein deutscher Ingenieure. *VDI-Wärmeatlas.* 11th ed. Berlin and Heidelberg: Springer, 2013. DOI: 10.1007/978-3-642-19981-3.

[239] Van Antwerpen, W., Du Toit, C. G., and Rousseau, P. G. "A review of correlations to model the packing structure and effective thermal conductivity in packed beds of mono-sized spherical particles." In: *Nuclear Engineering and Design* 240.7 (2010), pp. 1803–1818. DOI: 10.1016/j.nucengdes.2010.03.009.

[240] Martin, H. "Wärme- und Stoffübertragung in der Wirbelschicht." In: *Chemie Ingenieur Technik* 52.3 (1980), pp. 199–209. DOI: 10.1002/cite.330520303.

[241] Nasr, K., Viskanta, R., and Ramadhyani, S. "An Experimental Evaluation of the Effective Thermal Conductivities of Packed Beds at High Temperatures." In: *Journal of Heat Transfer* 116.4 (1994), pp. 829–837. DOI: 10.1115/1.2911455.

[242] Budama, V. K., Johnson, N. G., et al. "Thermodynamic development and design of a concentrating solar thermochemical water-splitting process for co-production of hydrogen and electricity." In: *International Journal of Hydrogen Energy* 43.37 (2018), pp. 17574–17587. DOI: 10.1016/j.ijhydene.2018.07.151.

[243] Bulfin, B., Call, F., et al. "Oxidation and Reduction Reaction Kinetics of Mixed Cerium Zirconium Oxides." In: *The Journal of Physical Chemistry C* 120.4 (2016), pp. 2027–2035. DOI: 10.1021/acs.jpcc.5b08729.

[244] Bulfin, B., Call, F., et al. "Thermodynamics of CeO2 thermochemical fuel production." In: *Energy & Fuels* 29.2 (2015), pp. 1001–1009. DOI: 10.1021/ef5019912.

[245] Butcher, J. C. and Goodwin, N. *Numerical methods for ordinary differential equations*. Vol. 2. Wiley Online Library, 2008.

[246] Amberger, S., Pirker, S., and Kloss, C. "Thermal Radiation Modeling Using Ray Tracing in LIGGGHTS." In: *6th International Conference on Discrete Element Methods* (Golden, USA). Aug. 5–6, 2013.

[247] Howell, J., Menguc, M., and Siegel, R. *Thermal Radiation Heat Transfer, 5th Edition*. 5th ed. Taylor & Francis, 2010.

[248] Ahlbrink, N., Belhomme, B., et al. "STRAL: Fast Ray Tracing Software With Tool Coupling Capabilities for High-Precision Simulations of Solar Thermal Power Plants." In: *Proceedings of the SolarPACES 2012 conference* (Marrakesh, Marocco). Sept. 11–14, 2012.

[249] Aguinsky, L. F. "Modelling Radiative Heat Transfer in Solar Thermochemical Particle Receivers." Master thesis. RWTH Aachen, 2018.

[250] Eberly, D. H. *3D game engine design: a practical approach to real-time computer graphics*. CRC Press, 2006.

[251] Möller, T. and Trumbore, B. "Fast, Minimum Storage Ray-Triangle Intersection." In: *Journal of Graphics Tools* 2.1 (1997), pp. 21–28. DOI: 10.1080/10867651.1997.10487468.

[252] Barnes, T. *Fast, Branchless Ray/Bounding Box Intersections*. May 2, 2011. URL: https://tavianator.com/fast-branchless-raybounding-box-intersections/, Seen on 12/17/2018.

[253] Blanco, M. J., Amieva, J. M., and Mancillas, A. "The Tonatiuh Software Development Project: An Open Source Approach to the Simulation of Solar Concentrating Systems." In: 42142 (2005), pp. 157–164. DOI: 10.1115/IMECE2005-81859.

[254] Mahan, J. R. *Radiation Heat Transfer: A Statistical Approach*. Wiley, June 2002. 504 pp. ISBN: 978-0-471-21270-6.

[255] Scherer, V., Wirtz, S., et al. "Simulation of Reacting Moving Granular Material in Furnaces and Boilers An Overview on the Capabilities Of the Discrete Element Method." In: *Energy Procedia* 120 (2017), pp. 41–61. DOI: 10.1016/j.egypro.2017.07.154.

[256] Schlünder, E. U. "Heat transfer to packed and stirred beds from the surface of immersed bodies." In: *Chemical Engineering and Processing: Process Intensification* 18.1 (1984), pp. 31–53. DOI: 10.1016/0255-2701(84)85007-2.

[257] Bauer, R. and Schlünder, E. U. "Effective radial thermal conductivity of packings in gas flow. Part I. Convective transport coefficient." In: *International Chemical Engineering* 18.2 (1978), pp. 180–188.

[258] Schneider, C. A., Rasband, W. S., and Eliceiri, K. W. "NIH Image to ImageJ: 25 years of image analysis." In: *Nature Methods* 9.7 (2012), pp. 671–675. DOI: 10.1038/nmeth.2089.

[259] *Representation of results of particle size analysis - Part 2: Calculation of average particle sizes/diameters and moments from particle size distributions*. Standard. Geneva, Switzerland: International Organization for Standardization, 2014.

[260] Trebing, D. "Strömung von Granulaten im Zentrifugal-Partikelreceiver." In press. PhD thesis. RWTH Aachen, 2019.

[261] Touloukian, Y. S. and Buyco, E. H. *Thermophysical properties of matter. The TPRC data series*. A Comprehensive Compilation of Data by the Thermophysical Properties Research Center (TPRC), Purdue University. Vol. 5: *Specific heat - Nonmetalics solids*. Ed. by Touloukian, Y. S. Ed. by Ho, C. New York: IFI Plenum, 1970.

[262] Touloukian, Y. S., Powell, R. W., et al. *Thermophysical properties of matter. The TPRC data series*. A Comprehensive Compilation of Data by the Thermophysical Properties Research Center (TPRC), Purdue University. Vol. 2: *Thermal Conductivity - Nonmetallic Solids*. Ed. by Touloukian, Y. S. Ed. by Ho, C. New York: IFI Plenum, 1970.

[263] Farmer, I. *Strata Mechanics*. Vol. 23. Thermal Conductivity. Elsevier Science, 1982, p. 211. Google Books: zj-wEwTyiCIC.

[264] Farmer, I. *Strata Mechanics*. Vol. 32. Developments in Geotechnical Engineering. Elsevier Science, 1982, p. 279. Google Books: dcJAAQAAQBAJ.

[265] Marigo, M. and Stitt, E. H. "Discrete Element Method (DEM) for Industrial Applications: Comments on Calibration and Validation for the Modelling of Cylindrical Pellets." In: *KONA Powder and Particle Journal* 32 (2015), pp. 236–252. DOI: 10.14356/kona.2015016.

[266] Henninger, M. "Parameter Calibration for Discrete Element Method Simulations of Solar Particle Receivers with Bulk Experiments." Bachelor thesis. RWTH Aachen, 2017.

[267] Lim, G. H. "On the conveying velocity of a vibratory feeder." In: *Computers & Structures* 62.1 (1997), pp. 197–203. DOI: 10.1016/S0045-7949(96)00223-4.

[268] Schulze, D. *Pulver und Schüttgüter. Fließeigenschaften und Handhabung*. Springer Vieweg, 2014. DOI: 10.1007/978-3-642-53885-8.

[269] Li, Q., Feng, M., and Zou, Z. "Validation and Calibration Approach for Discrete Element Simulation of Burden Charging in Pre-reduction Shaft Furnace of COREX Process." In: *ISIJ international* 53.8 (2013), pp. 1365–1371. DOI: 10.2355/isijinternational.53.1365.

[270] Benvenuti, L., Kloss, C., and Pirker, S. "Identification of DEM simulation parameters by Artificial Neural Networks and bulk experiments." In: *Powder Technology* 291 (2016), pp. 456–465. DOI: 10.1016/j.powtec.2016.01.003.

[271] Do, H. Q., Aragón, A. M., and Schott, D. L. "A calibration framework for discrete element model parameters using genetic algorithms." In: *Advanced Powder Technology* 29.6 (2018), pp. 1393–1403. DOI: 10.1016/j.apt.2018.03.001.

[272] Rackl, M. and Hanley, K. J. "A methodical calibration procedure for discrete element models." In: *Powder Technology* 307 (2017), pp. 73–83. DOI: 10.1016/j.powtec.2016.11.048.

[273] Atkins, P. W. and Paula, J. de. *Physikalische Chemie*. Wiley, 2013, p. 1284. ISBN: 978-3-527-33247-2.

[274] Thelen, M., Willsch, C., et al. "Hochauflösendes optisches Messsystem zur schnellen Erfassung von Flussdichte-Kennfeldern." Poster presentation. 19. Kölner Sonnenkolloquium 2016 (Köln, Germany). July 6, 2016. URL: https://elib.dlr.de/108819/.

[275] Niehoff, A. G., Thomey, D., et al. "Thermodynamic Model of a Solar Receiver for Superheating of Sulfur Trioxide and Steam at Pilot Plant Scale." In: *ASME 2016 10th International Conference on Energy Sustainability* (Charlotte, USA). American Society of Mechanical Engineers, June 26–30, 2016. DOI: 10.1115/ES2016-59167.

[276] Howell, J. R. and Mengüç, M. P. "Radiative transfer configuration factor catalog: A listing of relations for common geometries." In: *Journal of Quantitative Spectroscopy and Radiative Transfer* 112.5 (2011), pp. 910–912. DOI: 10.1016/j.jqsrt.2010.10.002.

[277] Planas Almazan, P. "Accuracy of Monte Carlo ray-tracing thermal radiation calculations: A practical discussion." In: *Sixth European Symposium on Space Environmental Control Systems*. Vol. 400. 1997, p. 579.

[278] Kwapinska, M., Saage, G., and Tsotsas, E. "Continuous versus discrete modelling of heat transfer to agitated beds." In: *Powder Technology* 181.3 (2008), pp. 331–342. DOI: 10.1016/j.powtec.2007.05.025.

[279] Incropera, F. P. and Dewitt, D. P. *Introduction to Heat Transfer*. 4th ed. New York: John Wiley & Sons, 2002. ISBN: 0471386499.

[280] Metalcor GmbH. *Datenblatt 2.4663*. URL: http://www.metalcor.de/datenblatt/103/, Seen on 12/17/2018.

[281] Hänel, D. *Computational Fluid Dynamics I+II*. Lecture script. Aerodynamisches Institut, RWTH Aachen. URL: http://www.aia.rwth-aachen.de/vlueb/vl/numerische_stroemungsmechanik_i/material/cfdI+II_2.pdf.

[282] Touloukian, Y. S. and DeWitt, D. P. *Thermophysical properties of matter. The TPRC data series*. A Comprehensive Compilation of Data by the Thermophysical Properties Research Center (TPRC), Purdue University. Vol. 8: *Thermal Radiative Properties - Nonmetallic Solids*. Ed. by Touloukian, Y. S. Ed. by Ho, C. New York: IFI Plenum, 1972.

A Appendix

A.1 Effective Properties in Contact Force Model

The effective (or reduced) properties in the contact force model are calculated as follows:

$$\frac{1}{Y_{\mathrm{red}}} = \frac{1-\nu_1^2}{Y_1} + \frac{1-\nu_2^2}{Y_2} \tag{A.1}$$

$$\frac{1}{G_{\mathrm{red}}} = \frac{2(2-\nu_1)(1+\nu_1)}{Y_1} + \frac{2(2-\nu_2)(1+\nu_2)}{Y_2} \tag{A.2}$$

$$\frac{1}{R_{\mathrm{red}}} = \frac{1}{R_1} + \frac{1}{R_2} \tag{A.3}$$

$$\frac{1}{m_{\mathrm{red}}} = \frac{1}{m_1} + \frac{1}{m_2} \tag{A.4}$$

A.2 Derivation of Maximum Thermal DEM Time Step

The particle-particle heat transfer scheme from equation (4.27), which also can be written as

$$T_j^{n+1} = T_j^n + \sigma \sum_{i=1}^{N_{\mathrm{con}}} \left(T_i^n - T_j^n\right) \qquad , \qquad \sigma = \frac{H_{\mathrm{c}} \Delta t}{m_j c_{\mathrm{p},j}} \tag{A.5}$$

was tested for stability with the von-Neumann analysis, a method to determine the stability of numerical schemes and described in [281]. The notation of this reference was used. The error function of a difference equation is written as a Fourier series

$$\varepsilon(x,y,z,t) = \sum_{k_{\mathrm{min}}}^{k_{\mathrm{max}}} V\left(t,k_x,k_y,k_z\right) e^{I(k_x x + k_y y + k_z z)} \tag{A.6}$$

with the amplitudes $V(t,k_x,k_y,k_z)$ and wave numbers k_x,k_y and k_z. The variable I denotes the imaginary unit $\sqrt{-1}$ here. The error function at particle i at time step n is

$$\varepsilon_i^n = \sum_{k_{\mathrm{min}}}^{k_{\mathrm{max}}} V^n e^{I(k_x x_i + k_y y_i + k_z z_i)} \tag{A.7}$$

Inserting this into the difference equation (A.5) leads to

$$\begin{aligned}
&V^{n+1}e^{I(k_x x_j+k_y y_j+k_z z_j)} = V^n e^{I(k_x x_j+k_y y_j+k_z z_j)} \\
&\quad + \sigma \sum_{i=1}^{N_{\text{con}}} \left(V^n e^{I}(k_x x_i + k_y y_i + k_z z_i) - V^n e^{I(k_x x_j+k_y y_j+k_z z_j)} \right) \\
\Leftrightarrow &V^{n+1} = V^n + \sigma \sum_{i=1}^{N_{\text{con}}} \left(V^n e^{I(k_x(x_i-x_j)+k_y(y_i-y_j)+k_z(z_i-zj)} - V^n \right) \\
\Leftrightarrow &V^{n+1} = V^n(1-\sigma N_{\text{con}}) + \sigma \sum_{i=1}^{N_{\text{con}}} (V^n e^{I(k_x(x_i-x_j)+k_y(y_i-y_j)+k_z(z_i-zj))} \\
\Rightarrow &G := \frac{V^{n+1}}{V^n} = 1 - \sigma N_{\text{con}} + \sigma \sum_{i=1}^{N_{\text{con}}} (e^{I(k_x(x_i-x_j)+k_y(y_i-y_j)+k_z(z_i-zj))}) \\
&\quad = 1 - \sigma N_{\text{con}} + \sigma \sum_{i=1}^{N_{\text{con}}} \cos(k_x(x_i-x_j)+k_y(y_i-y_j)+k_z(z_i-z_j)) \\
&\qquad + I\sigma \sum_{i=1}^{N_{\text{con}}} \sin(k_x(x_i-x_j)+k_y(y_i-y_j)+k_z(z_i-z_j))
\end{aligned} \tag{A.8}$$

For stability, the norm of the error amplification factor G has to be less than one:

$$G \leq 1 \tag{A.9}$$

In our case it follows that

$$\begin{aligned}
|G|^2 = &\left[(1-\sigma N_{\text{con}}) + \sigma \sum_{i=1}^{N_{\text{con}}} \cos(k_x(x_i-x_j)+k_y(y_i-y_j)+k_z(z_i-z_j)) \right] \\
&+ \left[\sigma \sum_{i=1}^{N_{\text{con}}} \sin(k_x(x_i-x_j)+k_y(y_i-y_j)+k_z(z_i-z_j)) \right]^2 \\
=&(1-\sigma N_{\text{con}})^2 + 2(1-\sigma N_{\text{con}})\sigma \sum_{i=1}^{N_{\text{con}}} \cos(\Theta_i) \\
&+ \left[\sigma \sum_{i=1}^{N_{\text{con}}} \cos(\Theta_i) \right]^2 + \left[\sigma \sum_{i=1}^{N_{\text{con}}} \sin(\Theta_i) \right]^2
\end{aligned}$$

$$
\begin{aligned}
=&(1-\sigma N_{\mathrm{con}})^2 + 2(1-\sigma N_{\mathrm{con}})\sigma \sum_{i=1}^{N_{\mathrm{con}}} \cos(\Theta_i) \\
&+ \sigma^2 \left[\sum_{i=1}^{N_{\mathrm{con}}} \sum_{m=1}^{N_{\mathrm{con}}} \cos(\Theta_i)\cos(\Theta_m) \right] \\
&+ \sigma^2 \left[\sum_{i=1}^{N_{\mathrm{con}}} \sum_{m=1}^{N_{\mathrm{con}}} \sin(\Theta_i)\sin(\Theta_m) \right] \\
\\
=&(1-\sigma N_{\mathrm{con}})^2 + 2(1-\sigma N_{\mathrm{con}})\sigma \sum_{i=1}^{N_{\mathrm{con}}} \cos(\Theta_i) \\
&+ \sigma^2 \left[\sum_{i=1}^{N_{\mathrm{con}}} \cos^2(\Theta_i) + \sum_{i\neq m}^{N_{\mathrm{con}}} \cos(\Theta_i) cos(\Theta_m) \right] \\
&+ \sigma^2 \left[\sum_{i=1}^{N_{\mathrm{con}}} \sin^2(\Theta_i) + \sum_{i\neq m}^{N_{\mathrm{con}}} \sin(\Theta_i)\sin(\Theta_m) \right] \\
\leq&(1-\sigma N_{\mathrm{con}})^2 + 2(1-\sigma N_{\mathrm{con}})\sigma \sum_{i=1}^{N_{\mathrm{con}}} \cos(\Theta_i) \\
&+ \sigma^2 \left[N_{\mathrm{con}} + \sum_{i\neq m}^{N_{\mathrm{con}}} \cos(\Theta_i)\cos(\Theta_m) + \sin(\Theta_i)\sin(\Theta_m) \right] \\
\\
=&(1-\sigma N_{\mathrm{con}})^2 + 2(1-\sigma N_{\mathrm{con}})\sigma \sum_{i=1}^{N_{\mathrm{con}}} \cos(\Theta_i) \\
&+ \sigma^2 \left[N_{\mathrm{con}} + \underbrace{\sum_{i\neq m}^{N_{\mathrm{con}}} \cos(\Theta_i - \Theta_m)}_{N^2-N \text{ terms}} \right] \\
\leq&(1-\sigma N_{\mathrm{con}})^2 + 2(1-\sigma N_{\mathrm{con}})\sigma \sum_{i=1}^{N_{\mathrm{con}}} \cos(\Theta_i) + \sigma^2 N_{\mathrm{con}}^2 \\
=&(1-\sigma N_{\mathrm{con}})^2 + 2(1-\sigma N_{\mathrm{con}})\sigma \sum_{i=1}^{N_{\mathrm{con}}} \cos(\Theta_i) + \sigma^2 N_{\mathrm{con}}^2
\end{aligned}
\tag{A.10}
$$

Case a) $\sigma N_{\mathrm{con}} > 1$. We look at the case of $\Theta_i = \pi$.

$$\begin{aligned} |G(\Theta_i = \pi)|^2 &= (1 - \sigma N_{\mathrm{con}})^2 - 2(1 - \sigma N_{\mathrm{con}})\sigma N_{\mathrm{con}} + \sigma^2 N_{\mathrm{con}}^2 \\ &= 1 - 4\sigma N_{\mathrm{con}} + 4(\sigma N_{\mathrm{con}})^2 \\ &= (1 - 2\sigma N_{\mathrm{con}})^2 \\ &> 1 \end{aligned} \tag{A.11}$$

The condition is not fulfilled, so that the scheme is unstable for $\sigma N_{\mathrm{con}} > 1$. Case b) $\sigma N_{\mathrm{con}} \leq 1$

$$\begin{aligned} |G| &\leq (1 - \sigma N_{\mathrm{con}})^2 + 2(1 - \sigma N_{\mathrm{con}})\sigma N_{\mathrm{con}} + \sigma^2 N_{\mathrm{con}}^2 \\ &= 1 - 2\sigma N_{\mathrm{con}} + 2(\sigma N_{\mathrm{con}})^2 + 2\sigma N_{\mathrm{con}} - 2(\sigma N_{\mathrm{con}})^2 \\ &= 1 \end{aligned} \tag{A.12}$$

The condition is fulfilled for all Θ_i, so that the scheme is stable for $\sigma N_{\mathrm{con}} \leq 1$. It follows for the time step

$$\begin{aligned} \sigma = \frac{H_{\mathrm{c}} \Delta t}{m c_p} &\leq \frac{1}{N_{\mathrm{con}}} \\ \Rightarrow \Delta t &\leq \frac{m c_p}{H_{\mathrm{c}} N_{\mathrm{con}}} \end{aligned} \quad . \tag{A.13}$$

A.3 Particle Property Data

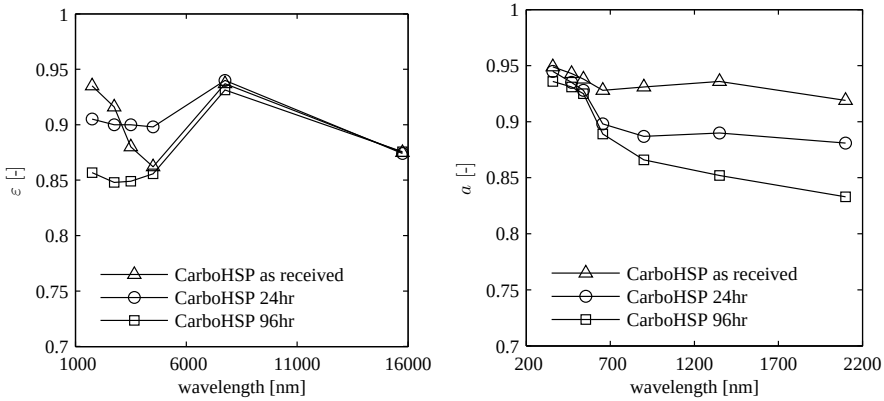

(a) Hemispherical emissivity (b) Hemispherical absorptivity

Figure A.1: Wavelength dependent emissivity and absorptivity of CarboHSP bauxite particles, measured by Siegel and figures obtained from Wu [40]

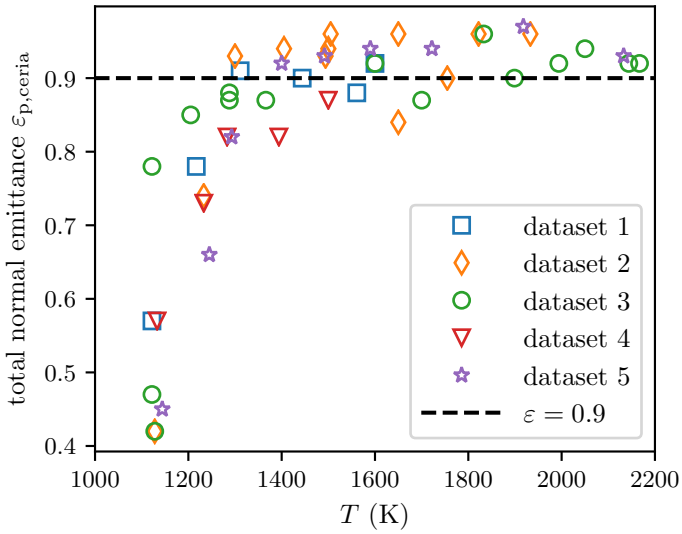

Figure A.2: Total normal emittance of ceria, data given in [282]

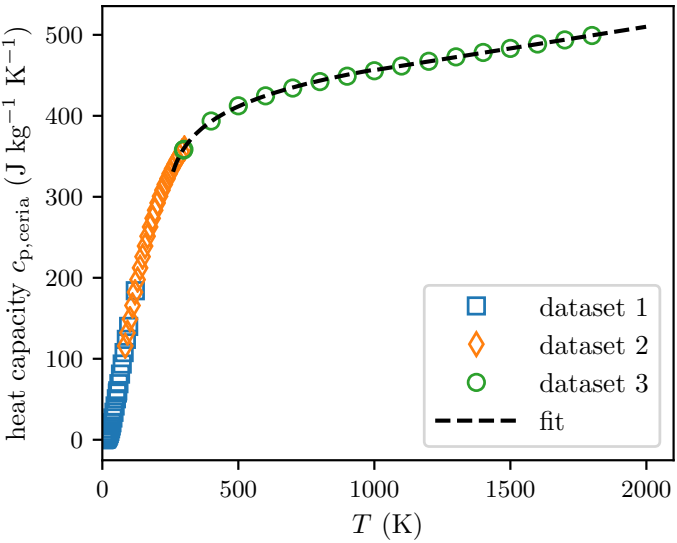

Figure A.3: Specific heat of ceria, literature data [261] and fit

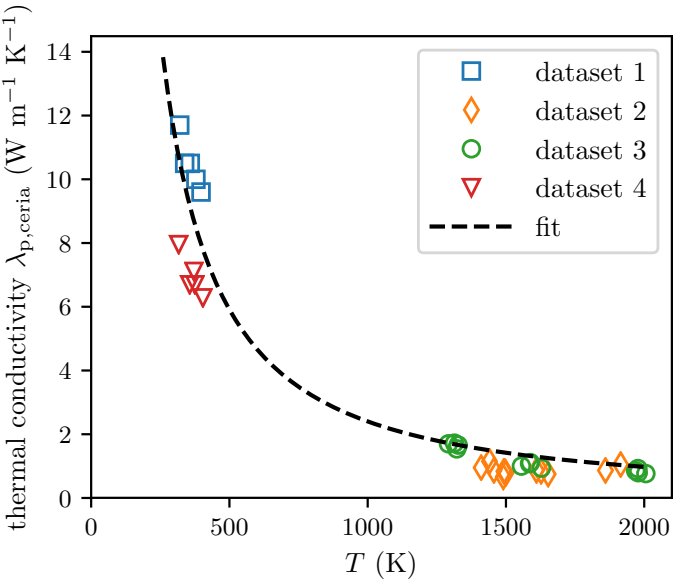

Figure A.4: Thermal conductivity of ceria, literature data [262] and fit

A.4 Vacuum Experiment Parameters

The parameters for the simulation of the vacuum experiment are listed in table A.1.

Table A.1: Parameters for the simulation of the vacuum experiment, already published in [112]

Parameter	Label	Baseline value	Unit	Source	Max. error estimation
Heat capacity ceria	$c_{\mathrm{p,ceria}}(T)$	$235.2(T - 229.6\ \mathrm{K})^{0.09955}$ for $T < 1000$ K $0.05362T + 402.8$ for $T > 1000$ K	W kg^{-1} K^{-1}	fit to [261]	2 %
Solid thermal conductivity ceria	$\lambda_s(T)$	$19070T^{-1.3}$	W m^{-1} K^{-1}	fit to [262]	10 %
Density ceria particles	ρ	6636	kg m^{-3}	[⋆]	2 %
Mean Sauter diameter	d	277	μm	[⋆]	6 %
Bed void space	ϕ	0.4		[⋆]	-
Insulation heat capacity	$c_{\mathrm{p,ins}}$	1130	W kg^{-1} K^{-1}	[+]	10 %
Insulation thermal conductivity	$\lambda_{\mathrm{ins}}(T)$	$0.00015T + 0.04903$ for $T < 1273$ K	W m^{-1} K^{-1}	[+]	20 %
Flux density on bed	$q_{\mathrm{solar}}(t,r)$	see fig. 6.9	W m^{-2}	[⋆]	5 %
Initial temperature	$T(t = 0)$	from experiment	K	[⋆]	1 %
Space temperature enclosure	T_{amb}	300	K	[⋆]	1 %
Absorptivity bed	α_{bed}	0.9			10 %
Emissivity bed	$\varepsilon_{\mathrm{bed}}$	0.9		[282]	10 %
Emissivity Insulation	$\varepsilon_{\mathrm{ins}}$	0.78		[282]	2 %
Cooling plate temperature	T_{bottom}	from experiment	K	[⋆]	1 %
Film coefficient	$h(p,T)$	correlation, equations found in [238], p. 759	W m^{-2} K^{-1}	[238]	30 %
Transmissivity window	τ	0.90			-
Insulation outer diameter	d_{ins}	300	mm	[⋆]	-
Particle bed diameter	d_{bed}	83	mm	[⋆]	-
Particle bed height	h_{bed}	20	mm	[⋆]	5 %
Position thermocouple TC5	h_{TC5}	2.12	mm	[⋆]	24 %
shape factor	C_{f}	1.25		[238]	-
flattening coefficient	φ	0.001		[238]	-

[⋆] own measurement [+] manufacturer data

A.5 Error Analysis for the Vacuum Experiment Simulations

This section has already been published in [112]. There are numerous parameters involved in the simulation of the vacuum experiment in section 6.1.2. To have an idea about the implications of them on the results, a parameter study was conducted. A base case is defined with the parameters in table A.1. The parameters are varied by an estimated error margin and the deviation in temperature was noted. Then the two worst case scenarios were simulated, first with all maximum errors leading to a higher temperature and then with all maximum errors leading to a lower temperature. A typical result is shown in figure A.5 for an ambient pressure case. It shows that the uncertainty in the parameter values can cause an error in the temperature of about 15 % which corresponds to about 100 K in the peak point of the graph. This error is mostly caused by the uncertainty in absorptivity and emissivity; if this uncertainty is excluded from the analysis, the error is reduced to the grey band in figure A.5. As mentioned the shown error margins are a worst case scenario; with high

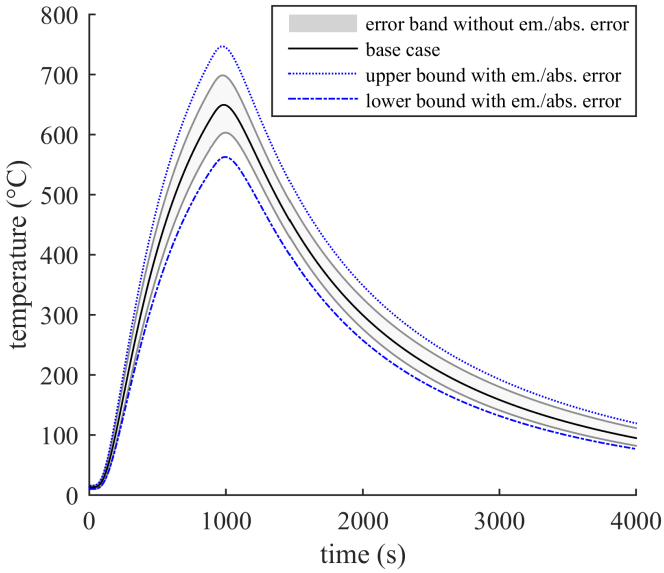

Figure A.5: Maximum uncertainty in T_{TC5} for an ambient pressure case if all errors in table A.1 are at their maximum value

probability the errors will not be at their highest extent and each of them will also not influence the measurement in the same direction. Rather some of them will cause a temperature rise while others cause a temperature drop, so that the overall error is smaller than in the worst case scenario. However, the uncertainty should be kept in mind when interpreting the results of the vacuum experiment.

A.6 Funnel Mass Flows in Horizontal Conveyor Experiments

The funnel mass flows influence the outcome of the horizontal conveyor experiments and simulations in chapter 5.2. Therefore they were measured by pouring particles through the funnels on a scale and measuring the mass over time. It turned out that some of the funnels, even though they were nominally the same size, had significantly different mass flows. A reason for this could be production tolerances or previous usage of the funnels, where they might be deformed. That is why different mass flows for the experiments are listed in table A.2. The experiments with the particle-laminated plate were conducted with a different funnel than the experiments on steel and the Al_2O_3 insulation board done by Henninger [266].

Table A.2: Funnel mass flows in horizontal conveyor experiments

Particles	Funnel nominal diameter	Particle mass	Experiments on steel and Al_2O_3 [266]	Experiments on particle-laminated plate
Carbo HSP13	7.5 mm	348 g	24.16 g/s	18.97 g/s
SG10H	7.5 mm	301 g	23.78 g/s	20.15 g/s
SG05H	7.5 mm	295 g	31.67 g/s	40.16 g/s
Carbo HSP16/30	7.5 mm	312 g	23.89 g/s	21.27 g/s
Carbo HSP20/40	7.5 mm	304 g	25.83 g/s	22.99 g/s
Carbo HSP30/60	7.5 mm	310 g	29.0 g/s	26.12 g/s
Ceria	7.5 mm	285 g	57.09 g/s	46.35 g/s